



<https://theses.gla.ac.uk/>

Theses Digitisation:

<https://www.gla.ac.uk/myglasgow/research/enlighten/theses/digitisation/>

This is a digitised version of the original print thesis.

Copyright and moral rights for this work are retained by the author

A copy can be downloaded for personal non-commercial research or study,  
without prior permission or charge

This work cannot be reproduced or quoted extensively from without first  
obtaining permission in writing from the author

The content must not be changed in any way or sold commercially in any  
format or medium without the formal permission of the author

When referring to this work, full bibliographic details including the author,  
title, awarding institution and date of the thesis must be given

Enlighten: Theses

<https://theses.gla.ac.uk/>  
[research-enlighten@glasgow.ac.uk](mailto:research-enlighten@glasgow.ac.uk)

# **Nonlinearities and all-optical switching in semiconductor laser amplifiers**

**Ivan Evans**

*7/6/99*

Submitted to the faculty of Engineering of the University of Glasgow for  
the degree Doctor of Philosophy

ProQuest Number: 10644196

All rights reserved

INFORMATION TO ALL USERS

The quality of this reproduction is dependent upon the quality of the copy submitted.

In the unlikely event that the author did not send a complete manuscript and there are missing pages, these will be noted. Also, if material had to be removed, a note will indicate the deletion.



ProQuest 10644196

Published by ProQuest LLC (2017). Copyright of the Dissertation is held by the Author.

All rights reserved.

This work is protected against unauthorized copying under Title 17, United States Code  
Microform Edition © ProQuest LLC.

ProQuest LLC.  
789 East Eisenhower Parkway  
P.O. Box 1346  
Ann Arbor, MI 48106 – 1346

# Abstract

The nonlinear properties of semiconductor laser amplifiers have been investigated, particularly at the transparency bias point, in the InGaAsP/InP and GaAs/AlGaAs material systems.

An all-solid-state F-centre laser system has been developed. It consisted of a diode-pumped Nd:YLF laser mode-locked at 77 MHz repetition rate, producing pulse durations of 6-20 ps with an average power of 2.2 W. The Nd:YLF laser synchronously pumps the F-centre laser producing pulse widths as short as 4ps with average powers of 200 mW. The available wavelength tuning range was from 1.45  $\mu\text{m}$  to 1.55  $\mu\text{m}$ . The Nd:YLF pump laser, although not designed to do so, Kerr lensed mode-locked. The reason for this unexpected behaviour was investigated and was shown to be due to the unusual laser cavity design. Thermal lensing is shown have a significant impact on the cavity stability and is believed to degrade the laser performance.

The nonlinear coefficient,  $n_2$ , has been measured by self-phase-modulation, for pulses of picosecond duration in a 5QW InGaAsP laser amplifier at a wavelength of 1.5  $\mu\text{m}$ . Subsequently a pump-probe study, showed the likely origin of this nonlinearity was carrier heating. The pump-probe studies have also shown that this nonlinearity saturates for mW power levels at the pulse durations used. The gain saturation caused by carrier heating is modelled and the calculated saturation powers relate well to the pump-probe data. The mechanism that causes the effective saturation of the nonlinearity is therefore attributed to carrier heating induced gain saturation.

For the first time an integrated active asymmetric Mach-Zehnder interferometer laser amplifier has been fabricated in the AlGaAs/GaAs material system. This structure has been characterised as a laser and tested as an all-optical switch at the transparency bias point. The Mach-Zehnder was switched with pulses of 100 fs duration corresponding to a pulse energy of 3pJ. The device shows inferior performance to passive waveguide and fibre all-optical switches, in the area of switching contrast.

Similar active amplifier switches in the nonlinear directional coupler configuration also show better characteristics. The poor performance of the Mach-Zehnder used here is believed to be due to arm asymmetries caused by gain saturation or fabrication variations.

A detailed model of the switching characteristics is presented. However it was not possible to use the model to deduce key material parameters because the model provided a good fit to the experimental data across a wide matrix of parameters, up to 100% variation in  $n_2$ ,  $\alpha$  and  $\beta$ .

# Acknowledgements

I was a young man with ideals and principles before I started working on this project, now many years later only some of these virtues remain. But it hasn't all been black, I must thank Charlie Ironside for his support over the years interleaved with very occasional nagging. Thanks must also go to Robin Thompson of Nortel in Harlow for his help and supply of optical amplifiers, lensed fibres and wafers.

Also I am grateful to the Electronics Department technical staff for their help in and around the cleanroom, for building all the obscure electronic and mechanical jobs I thought I might need and to the dry Etching group for the use of their facilities. I am also indebted to Craig Hamilton and Patsy Miller for sharing the joy of the F-centre laser and to Jim Gray for his help in the optics labs.

Thanks to my current work colleagues in Oxford for their support and friendship and not complaining when I decided to monopolise the printers, before I decided to invest in one myself.

Finally and predictably thanks to my parents for their part in funding this endeavour and keeping me from living in a cardboard box, surely if they had the choice to do it all again they would never have children.

# Contents

<b>1</b>	<b>Introduction</b>	<b>1</b>
1.1	Nonlinear optics	2
1.11	All-optical switching	2
1.2	Nonlinearities in semiconductor laser amplifiers-review	4
<b>2</b>	<b>Semiconductor lasers and amplifiers</b>	<b>12</b>
2.1	Introduction	12
2.2	Applications	13
2.3	Laser structures	14
2.31	Lateral confinement structures	14
2.32	Bulk and quantum-well lasers	15
2.33	Nonlinear effects and transparency in lasers	20
<b>3</b>	<b>Fabrication of semiconductor laser amplifiers</b>	<b>26</b>
3.1	Introduction	26
3.2	Fabrication process	26
3.21	Sample preparation	26
3.22	Lithography	26
3.23	Dry etching	27
3.3	Laser fabrication	28
3.31	Broad area oxide stripe lasers and material characterisation	29
3.32	Ridge waveguide lasers	31
3.33	Fabrication of the asymmetric Mach-Zehnder interferometer	32
3.34	InGaAsP / InP laser fabrication	36
3.35	Device mounting	37

3.4	<b>Conclusions</b>	37
<b>4</b>	<b>Experimental laser system</b>	<b>40</b>
4.1	<b>Introduction</b>	40
4.2	<b>Diagnostics</b>	41
4.3	<b>Diode-pumped Nd:YLF laser system</b>	43
4.31	Nd:YLF CW and FM mode-locked operation	45
4.32	Mode-locking Techniques and Kerr lens mode-locking	46
4.33	Nd:YLF Kerr lens mode-locked operation-experimental	51
4.34	Nd:YLF Kerr lensed mode-locked operation-analysis	54
4.35	Thermal lensing effects and an improved Nd:YLF laser system	59
4.4	<b>F-centres</b>	64
4.41	KCl:Tl F-centre	66
4.42	Experimental KCl:Tl laser system	67
4.43	Future work: improved KCL:Tl laser system	71
4.5	<b>Conclusions</b>	74
<b>5</b>	<b>Linear and nonlinear properties of InGaAsP optical amplifiers</b>	<b>79</b>
5.1	<b>Introduction</b>	79
5.2	<b>Laser amplifier details</b>	79
5.21	Device characteristics	80
5.22	Anti-Reflection coatings	82
5.23	Coupling arrangement	84
5.24	Transparency	85
5.3	<b>Amplifier gain saturation</b>	85
5.31	Amplifier modelling	88
5.32	Injection locking	93
5.4	<b>Self-phase-modulation</b>	94

5.41	Experimental spectral broadening in an InGaAsP amplifier	95
<b>5.5</b>	<b>Pump-Probe experiment</b>	<b>98</b>
5.51	Experimental pump-probe arrangement	99
5.52	Results	101
5.53	Modelling of carrier heating at transparency	105
5.54	Discussion and conclusion	111

## **6 Active integrated GaAs/AlGaAs nonlinear**

	<b>Mach-Zehnder interferometer</b>	<b>116</b>
<b>6.1</b>	<b>Introduction</b>	<b>116</b>
<b>6.2</b>	<b>Nonlinear Mach-Zehnder interferometer</b>	<b>117</b>
6.21	Design of the integrated asymmetric Mach-Zehnder interferometer	120
<b>6.3</b>	<b>Linear characterisation of the Mach-Zehnder interferometer</b>	<b>125</b>
6.31	BPM model	125
6.32	AMZI Lasing characteristics	128
<b>6.4</b>	<b>All-optical switching of the AMZI-experimental</b>	<b>131</b>
6.41	Experimental details	131
6.42	AMZI switching results	133
<b>6.5</b>	<b>All-optical switching of the AMZI-analysis and discussion</b>	<b>134</b>
6.51	Comparison with other work in amplifiers at transparency	134
6.52	Analysis of the AMZI switching characteristics	137
6.53	Unified AMZI switching model	146
6.54	Critical assessment of fit with model	151
<b>6.6</b>	<b>Practical applications of semiconductor optical amplifiers at the transparency bias point</b>	<b>156</b>
<b>6.7</b>	<b>Conclusions</b>	<b>161</b>

<b>7</b>	<b>Summary and conclusions</b>	<b>166</b>
	<b>Appendix</b>	<b>174</b>
Appendix I	Wafers used	174
Appendix II	Laser characterisation	181
Appendix III	BNR devices	184
Appendix IV	ABCD matrix model	190
Appendix V	Computer programmes	194
Appendix VI	Error analysis of AMZI switching response and uncertainty in the modelled AMZI response	220

# Chapter 1

## Introduction

In the modern world, electronic and optical communications play a pivotal and perhaps vital role. This leads to a seemingly inexhaustible demand for more transmission capacity. One aspect of this is the drive to exploit the large and as yet under-utilised bandwidth available in optical fibre. Subsequently there is huge interest in developing new technologies and techniques that can enhance transmission capacities.

An important component in such optical systems is the light source, the semiconductor laser, the properties of which have an important influence on attainable transmission rates. Improvements in the understanding of the nonlinear optical properties of semiconductor lasers may allow higher modulation speeds to be attained and could point to which material types offer the best performance. In the ultrahigh speed transmission systems of the next century semiconductor laser amplifiers could play an increasingly wider role, providing more complex functions than just the optical source. Semiconductor laser amplifiers, because of their strong nonlinear optical properties, are contenders for all-optical signal processing elements such as all-optical switches, wavelength converters, multiplexers and demultiplexers

This thesis focuses primarily on the ultrafast nonlinearities in the InGaAsP/InP laser material system at a wavelengths around  $1.5\mu\text{m}$  and the demonstration of an active asymmetric Mach-Zehnder interferometer (AMZI) laser amplifier all-optical switch in GaAs/AlGaAs, at a wavelength of  $0.86\mu\text{m}$

The remainder of this chapter gives a brief background to nonlinear optics, all-optical switching and reviews the recent work on the nonlinear properties of semiconductor laser amplifiers.

## 1.1 Nonlinear optics

For modest light intensities the optical properties of materials are independent of light intensity. Nonlinear optics<sup>1</sup> is concerned with the situation where the light intensity is sufficient to interact with the propagation medium and alter the materials properties.

It is the interaction of an electric field with the charged particles which compose the material that leads to nonlinear optical phenomena. The effect of this radiation on the material is described by a polarisation vector,  $P$ , which is expressed as,

$$P = \epsilon_0 \cdot \chi \cdot E = \epsilon_0 \cdot (\chi^{(1)} E + \chi^{(2)} E^2 + \chi^{(3)} E^3 + \dots) \quad (1.1)$$

where  $\epsilon_0$  is the free space permittivity,  $E$  is the electric field,  $\chi^{(1)}$  is the linear susceptibility and the terms  $\chi^{(2)}$ ,  $\chi^{(3)}$  are the nonlinear susceptibilities.  $D$  is the electric field displacement vector which is expressed as,

$$D = \epsilon_0 \cdot E + P \quad (1.2)$$

The quadratic  $\chi$  term gives rise to frequency mixing, in the simplest case frequency doubling and the electrooptic (Pockels) effect. The cubic term can produce four-wave mixing, two-photon absorption, Raman processes and leads to an intensity-dependent refractive index. This intensity-dependent refractive index leads to many useful processes. Considering only the  $\chi^3$  term the refractive index becomes,

$$n = n_0 + n_2 I \quad (1.3)$$

where  $n_0$  is the linear refractive index,  $I$  is the light intensity and  $n_2$  is the nonlinear index.

### 1.11 All-optical switching

The intensity dependent refractive index, produced by the third order nonlinearities is generally referred to as the optical Kerr effect. Kerr like materials can be utilised to form all-optical switches<sup>2</sup>. In an all-optical switch the light signal can be switched or manipulated by another control light signal without recourse to electronics. As the Kerr

effect is an electronic process, involving the interaction of radiation with the bound electrons which compose the material, it recovers virtually instantaneously. Kerr based all-optical switching therefore offers the potential for faster switching and hence higher data transmission rates in communication systems.

Many variants of all-optical switch are possible and some employ geometries that are familiar from conventional integrated optical switches. Some key configurations are the Mach-Zehnder interferometer and the nonlinear directional coupler (NLDC). In Chapter 6 the nonlinear Mach-Zehnder is described in detail. The NLDC consists of two parallel waveguides which interact due to their close proximity. The optical modes of this system can be viewed as two orthogonal super modes, which are composites of the modes of the original waveguides. When both of these modes are excited a periodic transfer of power, or beating, between waveguides occurs because of the difference in the effective indices of the supermodes. One important property of the directional coupler is that complete power transfer, between guides, only occurs when both guides are identical, or more strictly phase matched. Similarly the greater the asymmetry between guides the less the power transfer. The NLDC uses the nonlinear index changes to destroy the coupler symmetry and hence frustrate power transfer between waveguides. At low light intensities the refractive index of both guides is identical and the interaction length can be selected so that the signal in one guide couples over to the other. At higher optical intensities the coupler is no longer symmetric, because of self induced index changes, and most of the signal remains in the input guide. Further configurations<sup>3</sup> such as Fabry-Perot cavities, Bragg gratings, nonlinear X switches and other mode interference devices are possible.

All-optical switching has been realised in various materials with Kerr like responses. Optical fibre, although it has a small nonlinearity, can be successfully utilised because its low linear losses makes long lengths possible. Switching has been demonstrated in a fibre nonlinear loop mirror<sup>4</sup>, a version of the Mach-Zehnder interferometer. Optical switching has also been realised in semiconductor waveguides, in AlGaAs, at a wavelength corresponding to half the band gap<sup>5</sup>. These devices also exploited a Kerr based nonlinearity with an ultrafast recovery time; this nonlinearity is also weak and peak powers of the order of Watts are required. The half band gap operation is important to reduce the degrading effects of two-photon absorption.

Nonlinear effects resonant to the band edge <sup>6</sup> are on the other hand far larger, but are slower because of the large interband recovery time.

One goal underlying much of the work in nonlinear optics, in particular all-optical switching investigations; is to identify a material system which offers a large optical nonlinearity, which recovers with an ultrafast time constant, and can be used to form a suitable waveguiding geometry. The development of ultrafast all-optical elements with low optical power requirements is the ultimate goal.

## **1.2 Nonlinearities in semiconductor laser amplifiers-review**

Recently nonlinear effects observed in semiconductor laser amplifiers have aroused much interest. Improved understanding of these nonlinear processes would improve understanding of direct laser modulation dynamics, pulsed and mode-locked semiconductor lasers <sup>7</sup>. The nature of these nonlinearities also merits examination, because if suitable, they could be utilised to produce all-optical processing elements such as optical routers, multiplexers, demultiplexers, frequency shifters and pulse shapers <sup>8</sup>.

A brief overview of some of the recent work in this area now follows, as well as some of the potential applications.

A phenomenon that is well understood is the interband nonlinearity associated with saturation of gain for an amplifier at high bias currents, or absorption saturation for a device at low drive current. This occurs because of the finite number of carriers in the conduction or valence bands and the non zero interband carrier recovery time. Strong stimulated emission or absorption shifts therefore alters the equilibrium carrier populations. If an optical signal of sufficient intensity is propagated through an amplifier structure, saturation will occur as the number of occupied states in the conduction or valence band are reduced, and correspondingly the devices gain or loss saturates. Saturation power levels are generally in the submilliwatt regime and depend on the material and device structure. The relatively low saturation levels lead to the concept of flared amplifiers and lasers, where the intensity is reduced by an expanded waveguide region <sup>9</sup>, allowing higher output powers. Loss saturation can be utilised to form self

switching devices such as Q-switched and mode-locked diode lasers<sup>10</sup>. These devices employ a short section that is unbiased or reverse biased, which acts as a saturable absorber. In the saturable absorber a pulse sees less absorption than a c.w. signal as the higher peak intensity saturates the absorption, the device therefore preferentially supports pulsed operation. These effects can also be utilised for pulse shaping, where the trailing pulse edge experiences saturation induced by the leading edge<sup>11,12</sup>. The time constant associated with these interband effects is in the nanosecond regime.

Gain nonlinearities have an important bearing on laser modulation dynamics. Discrepancies between experimental and theoretical studies have shown that the interband gain saturation effects described above do not fully describe laser modulation dynamics<sup>13-15</sup>, there are some other effects involved. To account for this discrepancy an additional nonlinear gain is generally introduced in the modulation literature by the use of a term which compresses the gain at high light intensities<sup>16</sup>, but takes no account of the mechanism behind these effects. The simplest representation of this is to employ a saturation parameter  $\varepsilon$ , which compresses the laser gain for high optical powers, as shown below,

$$g = a \cdot \frac{(n - n_t)}{(1 - \varepsilon \cdot P)} \quad (1.4)$$

where  $g$  is the gain term,  $a$  is the slope of the gain carrier density relationship,  $n$  is the carrier density,  $n_t$  is the carrier density at transparency and  $P$  is the photon density in the active region. Carrier induced refractive index changes are generally introduced, in the modulation literature, via the linewidth enhancement factor,  $\alpha$ , which relates an induced change in the material refractive index to a corresponding change in its gain. The linewidth enhancement factor is expressed as,

$$\alpha = \frac{\text{Re}(\chi)}{\text{Im}(\chi)} = -2k_0 \left( \frac{\delta n / \delta N}{\delta g / \delta N} \right) \quad (1.5)$$

where  $\chi$  is the susceptibility,  $k_0$  is the vacuum wavenumber,  $n$  is the refractive index,  $g$  is the gain or absorption of the medium and  $N$  is the carrier density. This parameter is one of the key pointers to a semiconductor lasers modulation performance. The

magnitude of  $\alpha$  is dependent on device structure<sup>17-19</sup>, which shows there is potential for its optimisation. The linewidth enhancement factor is a manifestation of the Kramers-Krönig dispersion relations<sup>1</sup> which relate the real and imaginary components of the refractive index to each other, over frequency space. Equations 1.4 and 1.5 indicate the two empirical parameters that are key in describing laser dynamics, at the onset of this thesis the nonlinear physical processes that gave rise to the observed modulation and saturation behaviour were not well understood. The nonlinear properties of semiconductor amplifiers merited attention because of their important bearing on laser modulation and saturation behaviour.

The nature of these ultrafast nonlinearities have been investigated in the time domain by pump-probe studies and in the frequency domain by four-wave mixing (FWM)<sup>20-23</sup>. FWM occurs because of the non zero value of the  $\chi^3$  nonlinear susceptibility and is a useful method of obtaining information on nonlinear processes without requiring the use of short pulse laser systems. The experimental data is somewhat inconclusive, but indicates that several processes exist with time constants in the 100 fs regime<sup>24</sup>. FWM in amplifiers may also be utilised in demultiplexers or frequency translators<sup>8</sup> in the high speed optical systems of the future.

Pump-probe studies have been carried out on a range of different structures in the AlGaAs and InGaAsP laser systems<sup>25-32</sup>, mainly in the small signal regime. These studies employ short, typically 100 fs, pulses from mode-locked lasers to probe the nonlinearities in the time domain. Several mechanisms have been observed, the relative magnitudes of which depend on the laser structures involved and the pulse durations used. The origin of these nonlinearities is still under investigation, but a consensus appears to be emerging. Both gain and refractive index nonlinearities have been studied. Several ultrafast features have been observed, including two-photon absorption (TPA) and carrier heating effects that exhibit a delayed turn on. The time constants attributed to these effects are not resolved for TPA and are around 1ps for the carrier heating. When the refractive index dynamics are observed<sup>32</sup> these components are seen to have effective  $n_2$ 's of opposite signs. These nonlinear effects are described further in the next chapter.

All-optical switching has been demonstrated in amplifiers biased at transparency in the directional coupler configuration in the AlGaAs material system<sup>33</sup> and in

InGaAsP Quaternary material<sup>34,35</sup>. If these nonlinearities are to be successfully utilised there are many areas which require detailed analysis including: TPA signal attenuation, likely device throughput, saturation of the nonlinearity, the interplay between these competing nonlinearities, optimum switching pulsewidth, preferred device structures, the gain components of the nonlinearity and their role in degrading switch performance. The motive for examining the all-optical switching performance of amplifiers at transparency, in particular, is that they may prove a compromise option that lies somewhere between the fast, but weak, Kerr nonlinearities (seen in optical fibre and in AlGaAs at half the band gap) and the strong, but slow recovering effects of resonant interband nonlinearities.

It was from these perspectives that the nonlinear properties of semiconductor laser amplifiers were investigated.

In this thesis a pump-probe study is performed on InGaAsP/InP laser amplifiers at around 1.5  $\mu\text{m}$  using a synchronously pumped F-centre laser as the light source. Although this does not have sufficiently short pulses to reveal information on the ultrafast effects described above, it will excite the nonlinearities associated with carrier heating, which can be perhaps more readily utilised, as the other effects are only dominant for subpicosecond pulse widths. These studies are performed in the small and large signal regimes to investigate the saturation intensity of the nonlinearity.

An active asymmetric Mach-Zehnder interferometer has been constructed in AlGaAs/GaAs laser material and demonstrated as an all-optical switch. Its performance and limitations are investigated.

## References

- 1 P. N. Butcher, D. Cotter, “The elements of nonlinear optics”, Cambridge University Press, 1990
- 2 M. N. Islam, “Ultrafast switching with nonlinear optics”, *Physics Today*, 1994
- 3 G. I. Stegeman, E. M. Wright, “All-optical waveguide switching”, *Optical and Quantum Electronics*, vol. 22, p. 95, 1990
- 4 K. J. Blow, K. Smith, “ Nonlinear loop mirror devices and applications”, *BT Technol. J.*, vol. 11, no. 2, p. 99, 1993
- 5 K. Al-hemyari, C. N. Ironside, J. S. Aitchison, G. T. Kennedy, R. S. Grant, W. Sibbett, “Ultrafast all-optical switching in GaAlAs integrated interferometer in 1.55 $\mu$ m spectral region”, *Electron. Lett.*, vol. 28, p. 1090, 1992
- 6 K. Al-hemyari, C. N. Ironside, J. S. Aitchison, “Resonant nonlinear optical properties of GaAs/GaAlAs single quantum-well waveguide and an integrated asymmetric Mach-Zehnder interferometer”, *IEEE Journal of Quantum Electronics*, vol. 28, no. 10, p. 2051, 1992
- 7 M. Willatzen, T. Takahashi, Y. Arakawa, “Nonlinear gain effects due to carrier heating and spectral holeburning in strained quantum well lasers”, *IEEE Transactions Photonics Technology Letters*, vol. 4, no. 7, p. 682, 1992
- 8 Ludwig, Raybon, “Measurements of frequency converted signals using four-wave mixing in a semiconductor laser amplifier at 1, 2.5, 5 and 10 GB/s”, *Electron. Lett.*, vol. 30, no. 4, p. 338, 1994
- 9 J. Walpole, E. S. Kintzer, S. R. Chinn, C. A. Wang, L. J Missaggia, “High power strained layer InGaAs / AlGaAs tapered travelling wave amplifier”, *Appl. Phys. Lett.*, vol 61, no. 7 , p.740, 1992
- 10 D. J. Derickson, R. J. Helkey, A. Mar, J. R. Karin, J. G. Wasserbaur, J. E. Bowers, “Short pulse generation using multisegment mode-locked semiconductor lasers”, *IEEE Journal of Quantum Electronics*, vol. 28 no. 10, p. 2186, 1992
- 11 N. J. Frigo, “Ultrashort pulse propagation in saturable media: a simplified physical model”, *IEEE Journal of Quantum Electronics*, vol. 19, no. 4, p. 511,

1983

- 12 M. Tohyama, R. Takahashi, T. Kamiya, "A scheme of picosecond pulse shaping using gain saturation characteristics of semiconductor laser amplifiers", *IEEE Journal of Quantum Electronics*, vol. 27, no. 9, p. 2201, 1991
- 13 Y. Arakawa, T. Takahashi, "Effect of nonlinear gain on modulation dynamics in quantum well lasers", *Electronics Lett.*, vol. 25, no. 2, p. 169 1989
- 14 L. Olofsson, T. G. Brown, "On the linewidth enhancement factor in semiconductor lasers", *Appl. Phys. Lett.*, vol. 57, no. 26, p. 2773, 1990
- 15 T. L. Koch, R. A. Linke, "Effect of nonlinear gain reduction on semiconductor laser wavelength chirping", *Appl. Phys. Lett.*, vol. 48, no. 10, p. 613, 1986
- 16 G. P. Agrawal, G. H. Duan, P. Gallion, "Influence of refractive index nonlinearities on modulation noise properties of semiconductor lasers", *Electronics Lett.*, vol. 28, no. 19, p.773, 1992
- 17 M. Osinski, J. Buus "Linewidth broadening factor in semiconductor lasers- an overview", *IEEE Journal of Quantum Electronics*, vol. 23, no. 1, p. 9, 1987
- 18 R. Raghuraman, N. Yu, R. Englemann, H. Lee, C. L. Shieh, "Spectral dependence of differential gain. mode shift and linewidth enhancement factor in a InGaAs-GaAs strained layer single quantum-well laser operated under high injection conditions", *IEEE Journal Of Quantum Electronics*, vol. 29, no. 1, p. 69, 1993
- 19 W. W. Chow, S. W. Koch, M. Sargent III, C. Ell, "Many body effects on the linewidth enhancement factor in quantum-well lasers", *Appl. Phys. Lett.*, vol. 58, no. 4, p. 328, 1991
- 20 A. D'Ottavi, A. Macozzi, S. Scotti, F. C. Romeo, F. Martelli, P. Spano, R. Dall'Ara, J. Eckner, G. Guekos, "Four-wave mixing efficiency in travelling wave semiconductor optical amplifiers at high saturation", *Appl. Phys. Lett.*, vol. 67, no. 19, p. 2753, 1995
- 21 A. Uskov, J. Mork, J. Mark, M. C. Tathham, G. Sherlock, "Terahertz four-wave mixing in semiconductor optical amplifiers experiment and theory", *Appl. Phys. Lett.* vol. 65, no. 8, p. 944, 1994
- 22 K. Kikuchi, M Amano, "Analysis of origin of nonlinear gain in 1.5 $\mu$ m semiconductor active layers by highly nondegenerate four-wave mixing", *Appl.*

- Phys. Lett., vol. 64, no. 5, p. 548, 1994
- 23** C. B. Kim, E. T. Peng, C. B. Su, W. Rideout, G. H. Cha, "Measurement of 50fs nonlinear gain time constant in semiconductor lasers", IEEE Photonics Technology Letters, vol. 4, no. 9, p. 969, 1992
- 24** R. Nierzke, P. Pankin, W. Elsässer, E. O. Göbel, "Four-wave mixing in GaAs/AlGaAs semiconductor lasers", IEEE Journal of Quantum Electronics, vol. 25, no. 6, p. 9, 1989
- 25** M. P. Kesler, E. P. Ippen, "Subpicosecond gain dynamics in GaAlAs laser diodes", Appl. Phys. Lett., vol. 51, no. 22, p. 1765, 1987
- 26** J. Mark, J. Mørk, "Subpicosecond gain dynamics in InGaAsP optical amplifiers: experiment and theory", Appl. Phys. Lett., vol. 61, no. 19, p. 2281, 1992
- 27** J. Mørk, A. Mecozzi, "Response function for gain and refractive index dynamics in active semiconductor waveguides", Appl. Phys. Lett., vol. 65, no. 14, p. 1736, 1994
- 28** C. T. Hultgren, D. J. Dougherty, E. P. Ippen, "Above and below band femtosecond nonlinearities in active AlGaAs waveguides", Appl. Phys. Lett., vol. 61, no. 23, p. 2767, 1992
- 29** C. K. Sun, H. K. Choi, C. A. Wang, J. G. Fujimoto, "Studies of carrier heating in InGaAs/AlGaAs strained layer quantum-well diode lasers using a multiple pump-probe technique", Appl. Phys. Lett., vol. 62, no. 7, p. 747, 1993
- 30** J. Mark, N. Tessler, G. Eisenstein, J. Mørk, "Broadband femtosecond pump-probe set-up operation at 1300 and 1500nm", Appl. Phys. Lett, vol. 64, no. 15, p. 1899, 1994
- 31** J. Mørk, J. Mark, C. P. Seltzer, "Carrier heating in InGaAsP laser amplifiers due to two-photon absorption", Appl. Phys. Lett, vol. 64, no. 17, p. 2206, 1994
- 32** K. Hall, G. Lenz, A. M. Darwish, E. P. Ippen, "Subpicosecond gain and index nonlinearities in InGaAsP diode lasers", Optics Communications, vol. 11, p. 589, 1994
- 33** S. G. Lee, B. P. McGinnis, R. Jin, J. Yumoto, H. M. Gibbs, R. Binder, S. W. Koch, N. Peyghambarian, "Subpicosecond switching in a current injected GaAs / AlGaAs multiple-quantum-well nonlinear directional coupler", Appl. Phys. Lett., vol. 64, no. 4, p. 454, 1994

- 34 D. M. Atkin, M. J. Adams, "Optical switching in the twin-guide travelling-wave laser amplifier", *IEE Proc.*, vol. 140, no. 5, p. 296, 1993
- 35 D. A. O. Davies, M. A. Fisher, D. J. Elton, S. D. Perrin, M. J. Adams, G. T. Kennedy, R. S. Grant, P. D. Roberts, W. Sibbett, "Nonlinear switching in InGaAsP laser amplifier directional couplers biased at transparency", *Electron. Lett.*, vol. 29, no. 19, p. 1710, 1993

## **Chapter 2**

### **Semiconductor lasers and amplifiers**

#### **2.1 Introduction**

Lasing action in semiconductors was first demonstrated in 1962. The device consisted of a forward biased GaAs p-n junction with two polished facets forming the cavity mirrors. Lasing occurred at the junction where electrons and holes recombined. These early devices were of limited practical application, as threshold currents were high and room temperature operation was not feasible.

In order to reduce lasing thresholds double heterostructure devices were developed, where the active layer is sandwiched between two layers with a lower refractive index, which also have different band gaps. This double heterostructure forms a slab waveguide leading to increased efficiency as more light is confined to the active region. In addition to the improved optical confinement, the band gap step improves the confinement of electrons and holes to the active region. The realisation of such structures requires the lattice constants of the “sandwich layers” to be closely matched, otherwise defects will degrade the devices performance.

Early laser structures were formed from AlGaAs / GaAs layers but a wide range of materials now exist encompassing the ultraviolet to the far infra-red regions. Of primary interest to telecommunications are quaternary laser structures formed from InP/ InGaAsP layers which can produce laser action at  $1.31\mu\text{m}$  and  $1.55\mu\text{m}$ , which correspond to the spectral regions where optical fibre shows low attenuation. Initially a wavelength around  $1.31\mu\text{m}$  was used, as lasers were easier to produce at this wavelength. Now most new fibre systems are deployed around  $1.55\mu\text{m}$  utilising the lower loss that this wavelength experiences, although ordinarily dispersion is worse at  $1.55\mu\text{m}$ .

## **2.2 Applications**

The semiconductor laser because of its compact nature and source of coherent light has numerous applications, however only those relevant to telecommunications are described in this section.

Semiconductor lasers provide the source of light for optical fibre transmission systems. In order to transmit information they must be modulated, the simplest way of achieving this is to modulate the laser drive current and hence the light intensity. This in itself causes a number of problems. According to the Kramers-Krönig relations <sup>1</sup>, a change in a material's absorption, such as one induced when a laser is modulated, will also cause a change in the refractive index. The ratio of the rate of change of the real and imaginary parts of the complex refractive index is termed the linewidth enhancement factor as defined in Chapter 1. For telecommunications applications, the laser linewidth requires tight control as dispersion in optical fibre can limit maximum data transmission rates. Wavelength division multiplexing (WDM) schemes also require tight wavelength control. Because of these tight wavelength requirements simple Fabry-Perot laser structures formed between cleaved facets are not suitable for high transmission rates over long distances as they produce a broad linewidth and rarely lase in a single frequency mode, particularly when modulated. For this reason semiconductor lasers incorporating a Bragg grating either DFB (distributed-feedback) or DBR (distributed Bragg reflector) lasers are employed. However even in these structures, the modulation induced refractive index changes will tune the grating and broaden the linewidth. Two alternative approaches are to employ a modulator external to the laser cavity or ensure the grating region is outside the laser amplifying region either by engineering the band gap or forming an extended external cavity, possibly a fibre grating. Another area where semiconductor lasers have received attention is where they are employed as optical amplifiers to regenerate a signal. Semiconductor optical amplifier structures are ostensibly the same as semiconductor laser structures, the difference being that amplifiers employ AR coated or angled facets or both to prevent laser action occurring. Amplifiers offer potentially high gains of 40dB and wide bandwidths of 40nm. To date the widespread use of semiconductor amplifiers has been limited because of their polarisation sensitivity. This is highly undesirable as standard

single mode optical fibres do not maintain a particular polarisation and the resultant polarisation through a length of fibre is highly sensitive to environmental factors. However recently less polarisation sensitive semiconductor amplifier structures have been developed <sup>2</sup>.

## 2.3 Laser structures

In this section the basics and concepts of some important semiconductor laser structures are introduced.

### 2.3.1 lateral confinement structures

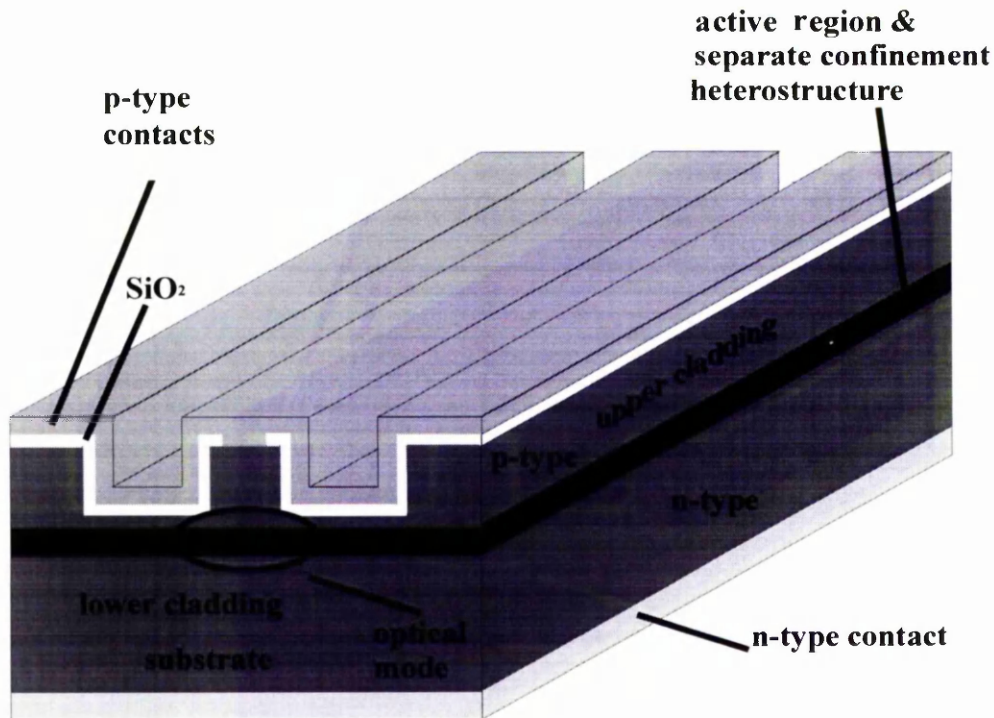


*Fig. 2.1 A generic ridge waveguide structure.*

As mentioned in the introduction, laser efficiency is enhanced by providing a waveguiding double heterostructure. Equally so, an optically confining structure in the other plane will reduce thresholds and if correctly designed can produce a largely single-mode output which is important for fibre coupling efficiencies. One technique is to

embed a segment of the double heterostructure within two surrounding layers. Such devices are called buried heterostructure (BH) lasers and generally involve two material growth stages with an etch stage in between. The optical mode within BH laser structures is strongly confined, hence lasing thresholds are lowered.

A technique allowing easier fabrication and only one growth step is to produce a more weakly guided structure such as a ridge waveguide or a rib structure. The lasers employed in this project were of the ridge waveguide structure, a generic diagram of which is shown above in Fig. 2.1.

The lateral confinement in the ridge waveguide structure is provided by the effective index step produced by the ridge. If suitably designed this structure can be tailored to only support the zero order mode or produce a largely single mode laser output. The structures forming the laser active region are now briefly described.

### **2.32 Bulk and quantum-well lasers**

Until recently most laser structures employed an active region composed of a single material, typically 0.1 $\mu\text{m}$  thick, the term bulk is applied to such devices. Many of the laser properties are determined by the electronic band structure of the active region. The band structure of crystalline solids is complicated with multiple valence and conduction bands and various direct and indirect band minima<sup>3,4</sup>. However in semiconductor lasers most of the interactions of interest occur around the direct minima between conduction and valence bands. The band gap is generally simplified to a series of parabolic bands, as shown below in Fig. 2.2. The energy states of these parabolic bands are described by,

$$E(k) = \frac{\hbar^2 k^2}{4\pi \cdot m} \quad (2.1)$$

where  $k$  is the wave vector and  $m$  is the electron or hole effective mass, which is specific to the each subband. Because of the crystal anisotropy, certain directions are harder for holes to move in, this leads to the concept of the heavy hole (hh) and light hole (lh) bands. Spin orbit coupling gives rise to the split-off band. In bulk material the

density of states varies with the square root of the energy.

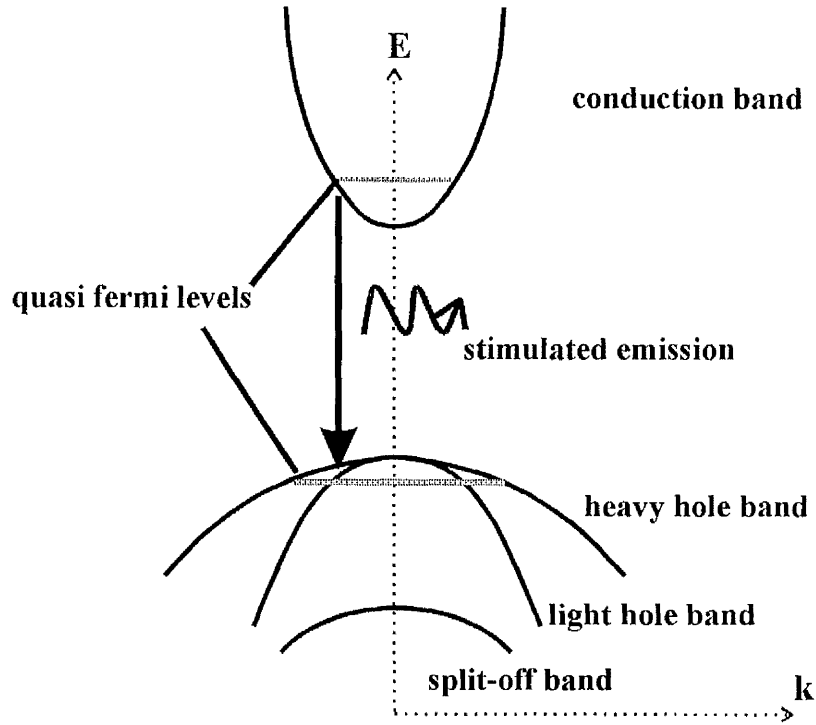


Fig. 2.2 Simplified band structure for a bulk laser. The  $k=0$  position is where the conduction and valence bands are closest, the heavy hole and light hole bands “touch” at this point.

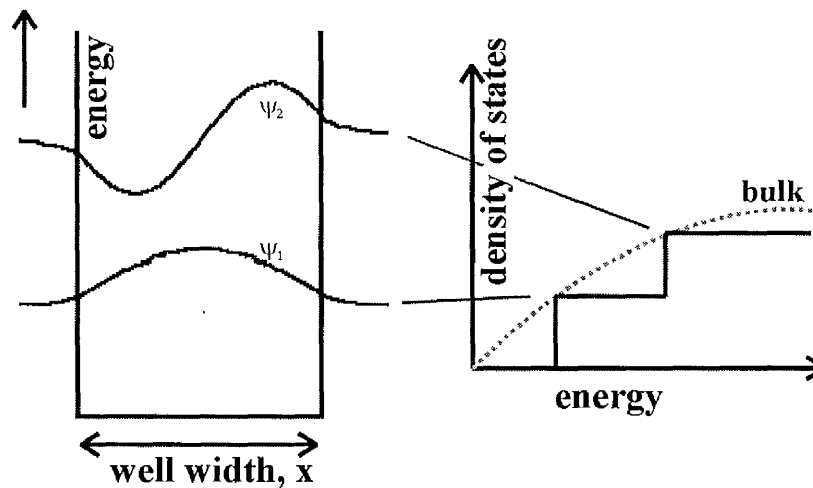


Fig. 2.3 The wave functions for the first two levels for an electron in a quantum well laser and a representation of the corresponding density of states.

In the early 70's it was realised that lasers incorporating thinner layers of around 10nm and less would offer superior performance characteristics. These lasers, termed quantum-well<sup>5,6</sup> (QW) employ thin layers of different band gaps. If sufficiently narrow

the energy states for an electron in a QW become a series of discrete levels as illustrated above. Fig 2.3 also shows that the density of states in a QW laser is modified from that in a bulk laser and does not continuously depend on energy. It is the quantisation of the energy levels in QW lasers that leads to many improvements over bulk structures.  $\psi_1(x)$  and  $\psi_2(x)$  are the wavefunctions for the first two states that an electron can occupy. The physical interpretation of the wavefunction is that  $|\psi(x)|^2$  represents the probability that the particle is found at that particular point.

QW structures are realised by interleaving different compositions of materials, generally materials from groups III-V of the periodic table are used for near infrared wavelengths. By altering the compositions that form these layers, the band gap energies can be controlled, some possible materials are  $\text{Al}_x\text{Ga}_{1-x}\text{As}$  in which the amount of aluminium and gallium is varied and  $\text{In}_{1-x}\text{Ga}_x\text{As}_y\text{P}_{1-y}$  in which the quantities of all the component elements are adjusted to provide the desired material properties. A possible QW structure is shown below in Fig 2.4, employing five  $\text{In}_{0.53}\text{GaAs}$  wells and  $\text{InGaAsP}$  quaternary layer barriers, the compositions are selected to provide a lattice match to  $\text{InP}$  with the quaternary layer chosen to have a band gap of  $1.26\mu\text{m}$ . This design employs  $4.5\text{nm}$  thick wells and  $12\text{nm}$  thick barriers, to give lasing wavelengths around  $1.53\mu\text{m}$ . Also illustrated are the variations in valence and conduction band across what would be the device active region, showing the potential barriers.

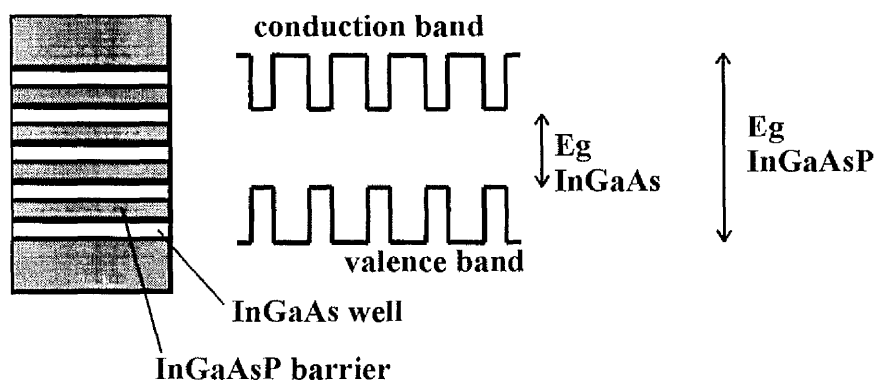
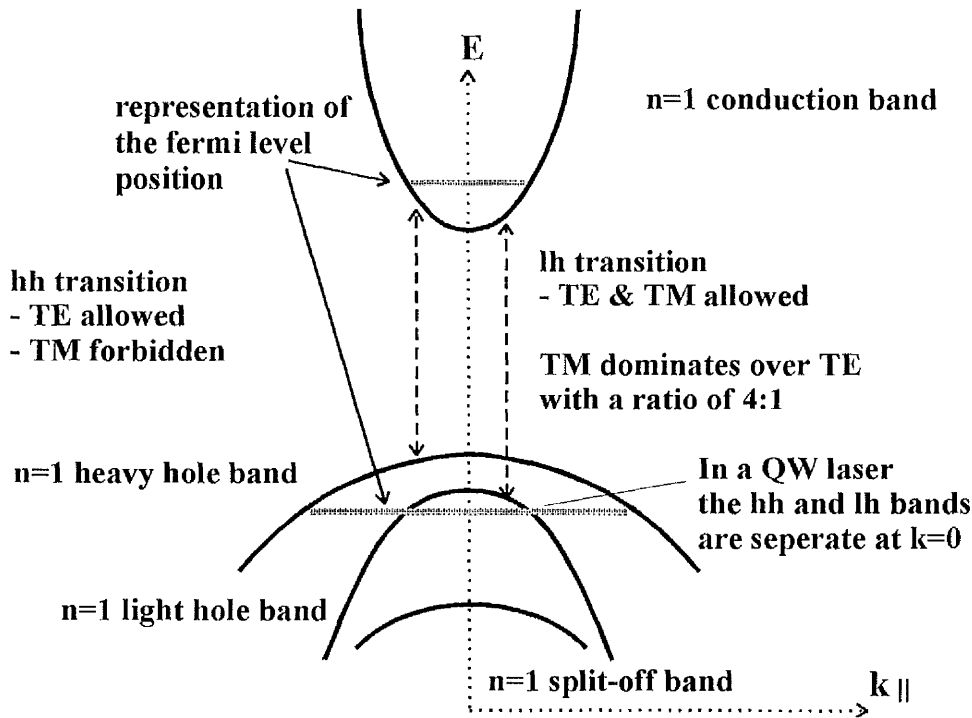


Fig. 2.4 A possible MQW InGaAsP laser structure and corresponding band gap.

The band structure is also significantly modified in a QW laser, as shown in Fig. 2.5. One significant difference between bulk and quantum well structures is that the heavy and light hole bands are no longer degenerate at  $k=0$  in the quantum well case, which means generally that the lh band plays little part in providing optical gain. Polarisation

selection is enhanced in QW structures as TE radiation (polarisation parallel to the plane of the well) interacts with or is emitted by both hh and lh bands whereas TM is only emitted by the conduction band-lh transition. This does not occur in bulk material as the carriers are not constrained in any particular direction. The selection rules also forbid transitions between different valence and conduction band states.



*Fig. 2.5 Simplified band structure for a quantum well laser, for momentum parallel to the well growth direction. An important point is the splitting of the hh and lh bands which leads to enhanced polarisation selection. Not shown is the repeated band structure due to the other electron and hole states, as illustrated in Fig 2.4.*

The band structure of Fig. 2.5. is repeated for the higher ( $n=2$ ,  $n=3\dots$ ) energy states, which form repeated valence and conduction bands with a greater band gap than the  $n=1$  case. Lasers operate predominantly on the  $n=1$  transition.

Initially lattice matching between layers was viewed as essential for producing devices with low defect counts and long life expectancies, but this view has been reappraised recently. Small amounts of lattice mismatch induced strain can further enhance laser performance<sup>7,8</sup> and indeed appropriate strain can have a positive effect on

suppressing defects<sup>9</sup>. Strained layer QW lasers are now the preferred choice for most applications. The addition of biaxial strain alters the material band structure, the net effect of this being to alter the separation between the hh and lh bands. Compressive strain lowers the lh band and tensile strain raises it, which can be useful in tuning the polarisation selection of lasers. The benefits of QW lasers is a detailed area which has been studied extensively. In order to exploit the advantages which follow from the 2-D density of states a QW laser must be carefully designed<sup>10</sup>. Well designed QW and strained QW structures are superior to bulk devices in many respects<sup>7-11</sup>. Some of these benefits are listed below:

- **Wavelength control:** The dimensions of the quantum well specify the wavelength at which the device operates, wavelength control is therefore improved over bulk devices.
- **New wavelength ranges:** A wider range of emission wavelengths is possible, particularly if strained layers are used.
- **Lasing threshold:** Because a given carrier density is required to achieve transparency, a thinner single QW active region requires less current to reach transparency. However this advantage is offset by the poor mode confinement. In practice it is often necessary to use multiple quantum wells with a separate confinement heterostructure. The 2-D density of states means that a high gain is available at the bottom of the band, unlike in a bulk laser where the lower energy states must be filled first, before a high gain is achieved. This is the key reason why threshold densities are reduced. At higher current densities in a MQW laser the  $n=1$  level saturates as injected carriers go into higher levels, which do not contribute to the lasing mode. As a result the gain saturation effects are more significant than in bulk structures, particularly for devices with fewer QW's.
- **Improved temperature performance:** There is a two fold explanation, the Fermi levels show less temperature dependence because of the 2-D density of states, and the limiting effects of intervalence band absorption and Auger recombination are reduced, because of modifications to the valence band.
- **Enhanced polarisation selection:** Because the lh and hh bands split and interact with each polarisation differently in QW structures, as illustrated in Fig 2.5, it is possible to use strained structures to further tune the polarisation selectivity.

- Modulation characteristics <sup>12</sup>: Modulation performance is improved because the differential gain  $\delta g/\delta n$  is higher in suitably designed QW structures, which leads to an increased relaxation oscillation frequency. The linewidth enhancement factor, which is important in linewidth broadening, is also reduced in QW lasers and further still in strained layer structures.

For these reasons QW lasers have replaced bulk devices for most applications.

### 2.33 Nonlinear effects and transparency in lasers

Some of the recent literature on the nonlinear properties of semiconductor laser amplifiers, relevant to this thesis, has been reviewed in the previous chapter. In this section some of these nonlinear processes are covered in more detail, with reference to some of the experimental studies presented later.

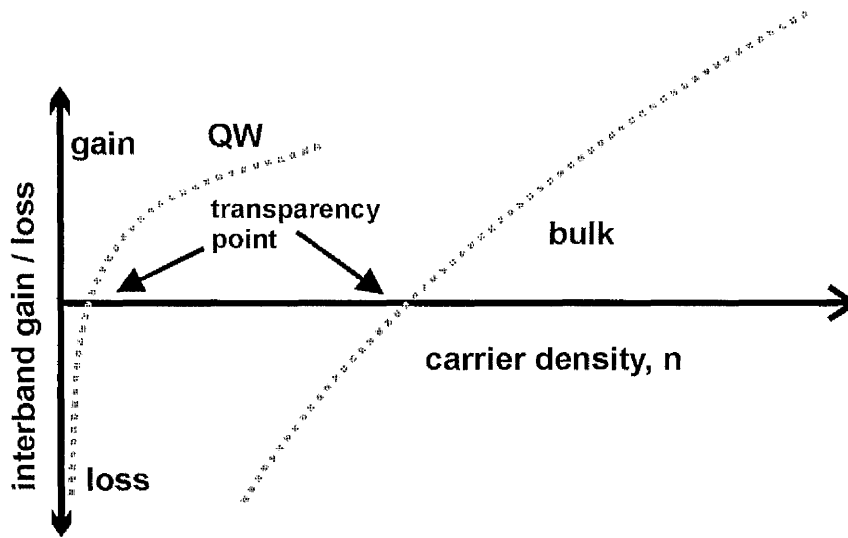


*Fig. 2.6 A diagrammatic representation of optical gain vs injected carrier density for a QW and a bulk semiconductor laser<sup>6</sup>. The transparency point is where stimulated emission exactly balances interband absorption. A linear relationship between gain and carrier density is often assumed for bulk devices.*

Any strong variations in carrier density in a laser amplifier will alter the balance between gain (stimulated emission) and loss (absorption), as suggested by Fig. 2.6. Correspondingly, strong variations in the optical intensity also perturb the carrier equilibrium, the net result being self-induced gain and phase changes in the optical signal. Therefore it should be noted that an intense pulse will saturate the absorption, subsequently experiencing more gain, when the device is biased below transparency in Fig. 2.6. Similarly, a gain reduction will be experienced by an intense pulse travelling in a medium biased above transparency. These interband variations in carrier density have a slow recovery time, of the order of nanoseconds. When the device lies exactly in-between gain and absorption, the transparency point is reached. At this point, although the net rate of interband transitions will be zero, there is still a substantial absorption loss due to free-carrier absorption. The transparency condition also varies with wavelength as illustrated in Fig. 2.7, meaning that for a given wavelength near the band gap, the transparency condition can be reached by adjusting the bias current or, for a given current, transparency will be seen at a certain wavelength.

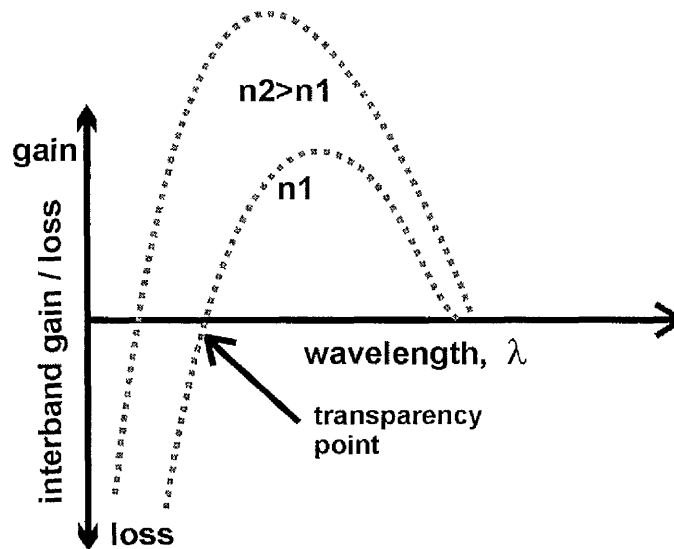


*Fig. 2.7 Representation of optical gain variation with wavelength for a given bias current in a QW laser. Increasing drive current will increase the peak gain and shift the characteristic to shorter wavelengths. Due to the density of states step features can be observed for higher current densities corresponding to the higher occupancy levels in the QW.*

The transparency point can readily be identified in an amplifier, by monitoring the sign of the small signal voltage bias variations which are induced by an injected optical signal. The optical signal alters the Fermi levels in the device, which translate to a bias voltage shift, when the amplifier is tuned past transparency these signal voltage variations change in sign. When a device is operated at transparency, the long lived interband nonlinearities are cancelled out leaving only ultrafast effects, this means that if suitably biased, amplifiers at transparency provide a useful medium for investigating and exploiting these ultrafast nonlinearities. Some of these ultrafast nonlinearities are now described.

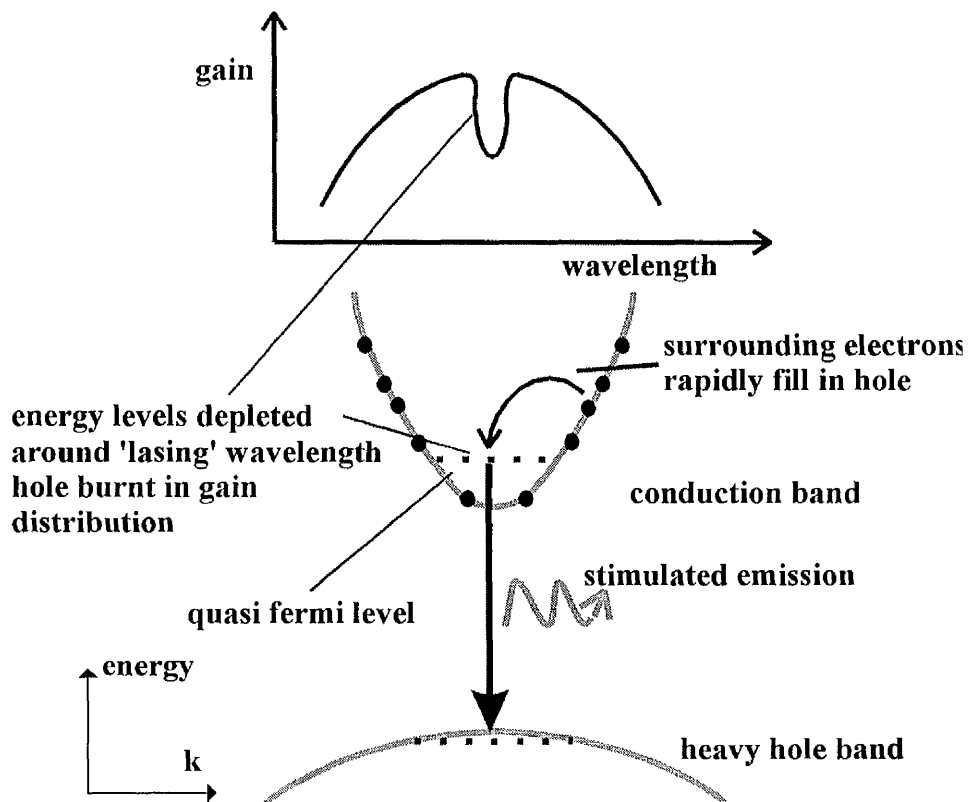


*Fig. 2.8 Illustration of spectral hole burning, a strong optical signal depletes the carrier concentration and causes a dip in the gain spectra, as illustrated above. The hole is rapidly filled in by surrounding carriers with a subpicosecond time constant.*

Any intense pulse propagating through a laser amplifier medium will see the slowly recovering interband effects mentioned above, associated with the depletion of the

carried density, corresponding to the wavelength of the optical signal. In addition, as shown in Fig. 2.8, there is a fast recovering intraband effect known as spectral hole burning, in which the passage of an intense optical pulse depletes the carrier distribution.

The ‘neighbouring’ carriers, however, quickly fill in this hole through phonon interaction. This process has a subpicosecond time constant. Although the hole fills in an ultrafast time scale and a new Fermi level is established, the distribution only recovers to its initial state in a time determined by the interband time constants. Spectral hole burning will have an identifiable signature depending on the laser amplifier bias conditions, in absorption an ultrafast increase in transmission will be induced, the opposite occurs when the device is biased in the gain region. At the transparency point, no ultrafast hole burning effects should occur.

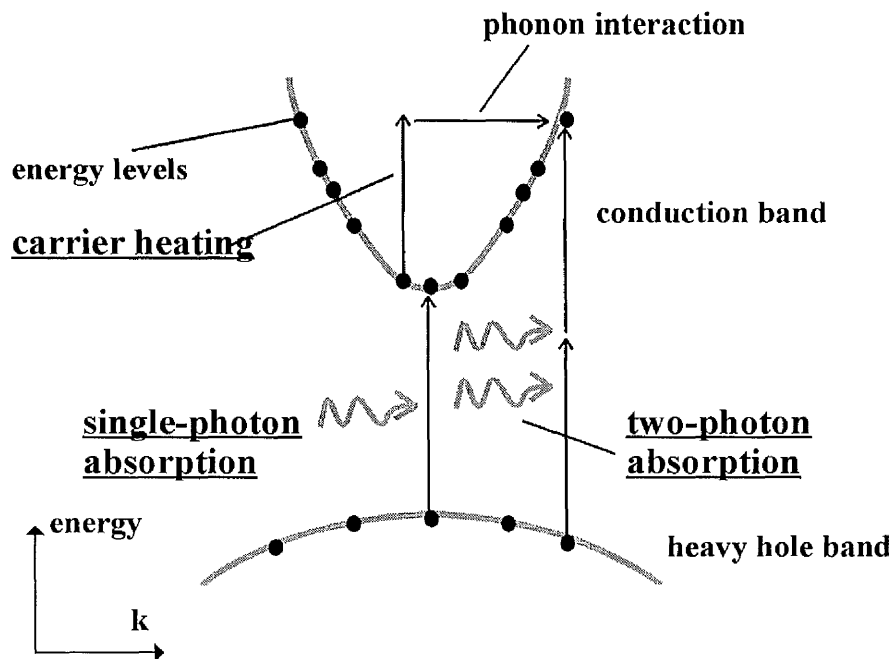


*Fig. 2.9 Illustration of carrier heating and two-photon absorption, two further ultra fast nonlinearities significant in amplifiers.*

Another ultrafast process is two-photon absorption, which is illustrated in Fig. 2.9. Here two photons can ‘simultaneously’ interact with an electron and excite it to a higher energy level. Two-photon absorption is an important loss mechanism at high peak optical intensities, one of its key signatures being its intensity squared dependence.

Also illustrated in Fig. 2.9 is a carrier heating, in general, this term can be given to any process that raises the Fermi level by exciting carriers to higher levels, or heating the distribution. Generally in this thesis we are concerned with the type of carrier heating where free carriers are excited to higher levels by free carrier absorption as illustrated below. Also possible is carrier cooling.

The nonlinear processes described here, their relevance to laser performance, applications and all-optical switching, represent the starting point for this thesis. The investigation of these effects in InGaAsP and AlGaAs laser amplifiers is described in later chapters. Of particular interest is which of the various nonlinear processes described here is dominant, for pulses in the picosecond regime. The magnitude and saturation of the nonlinearity seen by picosecond pulses is also investigated.

## References

- 1 D. C. Hutchins, M. Sheik-Bahae, D. J. Hagan, E. W. Van Stryland, "Kramers-Krönig relations in nonlinear optics", *Optical and Quantum Electronics*, vol. 24, p. 1, 1992
- 2 A. Godefrey, J. C. Keromnes, G. Joulie, P. Lamouer, "1.55 $\mu$ m polarisation insensitive optical amplifier with strain balanced superlattice active layer" *IEEE Photonics Technology Lett.*, vol. 7, no. 5, p. 473, 1995
- 3 J. H. Davies, "The physics of low dimensional semiconductors", Cambridge University Press, 1998
- 4 C. F. Klingshirn, "Semiconductor Optics", Springer, 1997
- 5 G. P. Agrawal, N. K. Dutta, "Semiconductor Lasers", 2nd ed., Chapter 9, Van Nostrand Reinhold 1993
- 6 A. Yariv, "Quantum electronics", John Wiley, 1988
- 7 M. Willatzen, T. Takahashi, Y. Arakawa, "Nonlinear gain effects due to carrier heating and spectral holeburning in strained quantum well lasers", *IEEE Photonics Technology Letters*, vol. 4, no. 7, p. 682, 1992
- 8 Y. Huang, S. Arai, K. Komori, "Theoretical linewidth enhancement factor  $\alpha$  of Ga<sub>1-x</sub>In<sub>x</sub>As/GaInAsP/InP strained quantum well structures", *IEEE Photonics Technology Letters*, vol. 5, no. 2, p. 142, 1993
- 9 P. S. Zory ed., "Quantum well lasers", Chapters 1 and 8, Academic Press 1993
- 10 E. Kapon ed., "Semiconductor lasers 1", Chapter 1, Academic Press 1999
- 11 Y. Arakawa, A Yariv, "Quantum well lasers gain, spectra, dynamics", *IEEE Journal of Quantum Electronics*, vol. 22, no. 9, p.1887, 1986
- 12 N. Storkfelt, M. Yamaguchi, B. Mikkelsen, K. E. Stubkjaer, "Recombination constants and  $\alpha$  factor in 1.5 $\mu$ m MQW optical amplifiers taking carrier overflow into account", *Electronics Lett.*, vol. 28, no. 19, p. 1774, 1992

## **Chapter 3**

### **Fabrication of semiconductor laser amplifiers**

#### **3.1 Introduction**

A large proportion of the devices described in the later chapters of this thesis, in particular the asymmetric Mach-Zehnder laser amplifier, were fabricated in the class 10000 clean room at Glasgow University, using fairly standard photolithographic techniques<sup>1-3</sup>. In addition the dry etching, plasma deposition and metal deposition facilities were also widely used. The majority of devices produced were in the GaAs/AlGaAs material system. Although much work was done in the InGaAsP/InP quaternary system, ridge waveguide lasers of acceptable quality could not be produced. Therefore the long wavelength lasers which were used in this thesis were supplied in bar form by Nortel. The AlGaAs wafers used were grown by molecular beam epitaxy (MBE)<sup>4,5</sup> at Glasgow and produced devices that lased around 0.86 $\mu\text{m}$ . The quaternary wafers were grown by metal-organic chemical vapour deposition (MOCVD)<sup>4,5</sup> at the University of Sheffield and by Nortel at Harlow and produced devices that lased around 1.5 $\mu\text{m}$ . Full details of the wafers grown are given in Appendix I.

In this chapter a brief overview of the fabrication techniques used to produce semiconductor laser chips is given.

#### **3.2 Fabrication processes**

##### **3.21 Sample preparation**

Semiconductor processing is done in clean environments where the quantity and size of airborne contaminants are controlled. The devices fabricated in this project were processed within class 100 cabinets in a class 10000 clean room. It is necessary to

ensure the surface of the wafer is clean and free from contamination at all times. A four-stage cleaning process was used before each processing step, consisting of: trichloroethane (later Opticlear for safety reasons), acetone, methanol and deionised water. The procedure used was to place the samples in each of these solutions in sequence in an ultrasonic agitator for 5 minutes. After the cleaning process the samples were blow dried with dry nitrogen and briefly baked in an oven to remove any residual moisture.

### **3.22 Lithography**

Contact photolithography <sup>1,3</sup> was used to pattern structures for laser waveguides and more elaborate devices. The Shipley S1400 series of resists were used. Generally S1400-17 was used for fine geometries as it formed a thin film around 0.5 $\mu$ m thick. S1400-31, which forms a film around 2 $\mu$ m thick, was used for larger features and to produce a tougher resist to withstand some etches. The resists were evenly deposited onto the sample surface, which was then spun for typically 30 seconds at 4000 r.p.m. Prior to resist deposition a solvent was used to promote adhesion. The resist was then baked in an oven at 90° C for 30 minutes to remove solvents ready for patterning. The samples were aligned to the mask and exposed to U.V. light. Exposure times varied according to the resist type used and the size of the features involved. The exposed areas of the resist were removed by immersion in a 1:1 water, developer solution for 75 seconds, ready for the next step. If a tough resist was required a post bake was used after development.

### **3.23 Dry etching**

Generally, wet etching is isotropic and produces undercut etch profiles. Etch depths are also difficult to control accurately unless etch stop layers are used. For most waveguide fabrication dry etching was employed as it can produce near vertical etch profiles, with better controlled etch depths. In most dry etching the reactive gases are ionised to form a plasma. The ions are then accelerated onto a plate holding the sample. By using appropriate etch conditions; near vertical low damage etch profiles can be obtained. Reactive ion etching (RIE) <sup>1,3,6</sup> was the technique used for most of this work. For GaAs/AlGaAs a SiCl<sub>4</sub> etch process <sup>7</sup> was used on an Oxford Plasmatech RIE 80. For

InP/InGaAsP a CH<sub>4</sub>:H etch process was used on an Electro Tech 340 machine, this is described later. An in-situ interferometer monitor was employed to control etch depths. The etch depths were measured with a surface profiler to verify the accuracy of the in-situ monitor.

### 3.3 Laser fabrication

The specific techniques used to produce the laser structures in this project are now outlined. Initially, broad area gain guided structures were fabricated to characterise new wafers; their fabrication is first described. The procedures for fabricating RWL structures and the techniques used for producing the asymmetric Mach-Zehnder interferometer (AMZI) laser amplifiers of Chapter 6 are then described. Finally InP / InGaAsP fabrication and device mounting techniques are outlined.

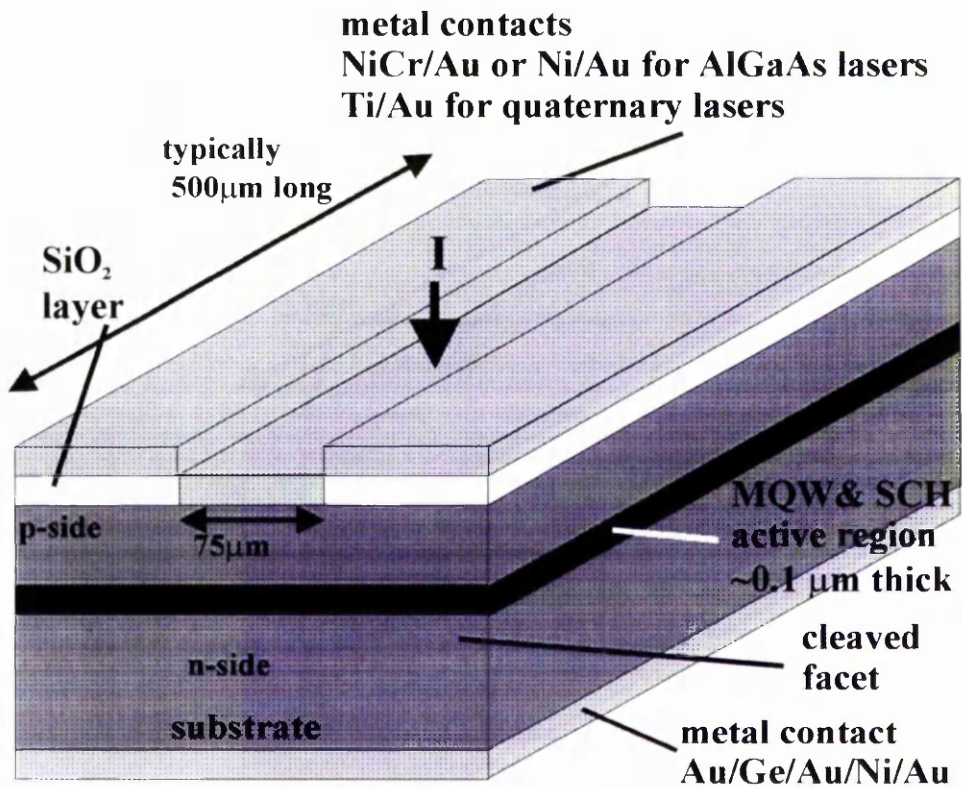


Fig. 3.1 'Generic' oxide stripe laser.

### **3.31 Broad area oxide stripe lasers and material characterisation**

The fabrication of oxide stripe lasers provided a quick and convenient method of characterising new laser material<sup>8</sup>. The characterisation data provides information on lasing wavelengths, device thresholds and slope efficiencies allowing a decision to be made on whether the material is suitable for further use, or is poor and should be abandoned.

Fig. 3.1 shows a generic oxide stripe structure. A window in the SiO<sub>2</sub>, through which current is injected, defines the laser cavity. Mirror facets are formed by cleaving along a crystallographic plane.

The fabrication procedure for GaAs/AlGaAs lasers is now outlined. The laser active region, the p and n regions and the contact layers were laid down in the material growth steps. In order to make a simple gain guided structure, essentially only a window which defines the pumped area need be formed. A layer of 200nm of plasma enhanced chemical vapour deposition (PECVD) SiO<sub>2</sub> was first deposited on the sample p-side. Photolithography was used to pattern a resist mask above the SiO<sub>2</sub>, allowing a 75µm wide window in the SiO<sub>2</sub> to be etched using buffered HF. The p-type contacts were then deposited.

The metalisation scheme and semiconductor contact layer<sup>9,10</sup> play an important part in determining the devices electrical characteristics. Contacts which have a negligible resistance irrespective of voltage bias are known as ohmic or non rectifying. Generally for lasers ohmic contacts are desirable, in order to minimise device bias voltage. The work function difference between the metal and semiconductor determines the nature of the contact. In an n-type contact, if the metal work function is greater, a potential barrier is created between the metal and semiconductor, corresponding to a step in the conduction band at the interface, forming a Schottky barrier. An ohmic contact results if the semiconductor has the larger work function. The opposite is true for a p-type contact. For a highly doped semiconductor contact layer (doping concentration of typically 10<sup>18</sup> to 10<sup>19</sup> cm<sup>-3</sup>) ohmic contacts can be achieved, irrespective of the work function differences, because a thinner potential barrier results. If the barrier is sufficiently thin electrons have a significant probability of quantum-mechanically tunnelling through it. For low resistance ohmic contacts, an evaporated

gold alloy was used; for the p-type contacts to GaAs, Ni/Au or NiCr/Au was preferred. The initial layer of Ni or NiCr provided the adhesion and allowed an ohmic contact and the gold provided a thicker low resistance contact pad suitable for wire or solder bonding. For devices requiring wire bonding NiCr/Au was preferred. Ti/Au contacts are also possible but are not necessarily ohmic to p-type GaAs because of the small work function of Ti. However an ohmic contact is possible, through quantum tunnelling, as noted previously. Ti/Au contacts were used in quaternary laser structures as they provided good adhesion (to InGaAs) and performance. The thicknesses were 70nm of Ti and 150nm of Au for Ti/Au and 40nm of Ni or NiCr and 150nm Au for Ni/Au and NiCr/Au. For wire bonding thicker (1 $\mu$ m) gold layers were used. Following this the substrate was lapped using AlO<sub>3</sub> powder until it was 150 $\mu$ m thick. A 1:2 water / ammonia solution was used to deoxidise the n-side, prior to evaporation. The n-side contacts were then deposited, an Au/Ge/Au/Ni/Au alloy being used with thickness of 14nm, 14nm, 14nm, 11nm and 150nm respectively. The n-side was usually annealed for 30 seconds at 350°C. The devices were then cleaved into bars forming the optical facets and then cut into individual chips. The techniques used to fabricate InGaAsP/ InP lasers were very similar.

After the fabrication steps were complete the lasers were diced into chips, of varying length, generally lengths of 300, 500, 700, 900, 1100 and 1500  $\mu$ m were used. These chips were tested on a pulsed test set up with a 200:1 duty cycle, the L-I and V-I characteristics were automatically recorded by a Labview programme. The advantages of the pulsed test is that it does not require the chips to be bonded onto a mount and temperature stabilised, which would be necessary if a c.w. drive current was used. The characterisation process generally involves the testing of broad area lasers of various lengths, from this the threshold of what would be an infinite length device can be obtained; this is one key measure of the material quality. Other parameters that can be calculated are the internal quantum efficiency and the losses at transparency. The obtained characterisation data for the wafers used is listed in Appendix II. Typical thresholds for infinite lengths in AlGaAs broad area lasers were 300 A cm<sup>-2</sup>. Calculated losses at transparency ranged from 6.6 to 17cm<sup>-1</sup>. All the wafers grown for this thesis were deemed to be of suitable quality for subsequent RWL fabrication.

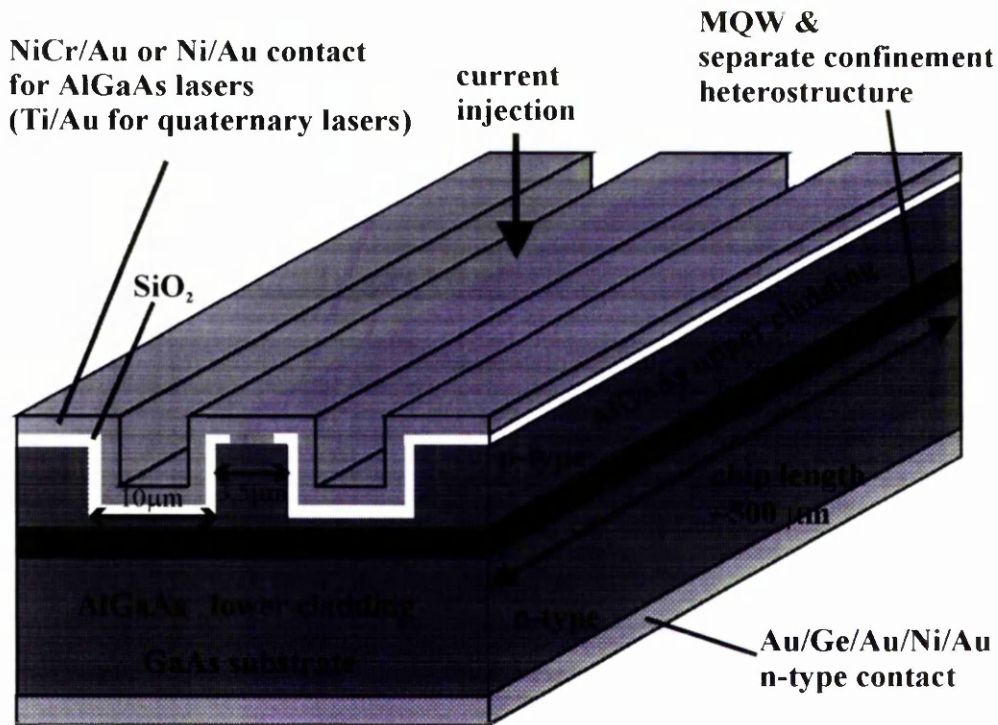


Fig. 3.2 Ridge waveguide laser structure.

### 3.32 AlGaAs Ridge waveguide laser fabrication

The AMZI laser amplifiers, described later in Chapter 6 were fabricated in the ridge waveguide structure, which can be used to produce single mode waveguides. Fig 3.2 shows a schematic of a complete GaAs/AlGaAs ridge waveguide laser (RWL). The structure is formed by partially etching through the upper cladding region to form a narrow ridge which provides lateral confinement. The fabrication steps are described below.

#### 1. Formation of the ridge structure.

- PECVD deposition of 200nm SiO<sub>2</sub> on the sample p-side surface, this is later used as a mask for the AlGaAs etch.
- Photolithography to form the resist mask for the SiO<sub>2</sub> etch.

- $C_2F_6$  RIE etching of  $SiO_2$  to pattern the  $SiO_2$ , forming the mask for the GaAs/AlGaAs etch. Strip resist.
  - $SiCl_4$  RIE etching of AlGaAs to form the ridge waveguide structure.
  - Removal of the  $SiO_2$  mask layer with a buffered HF solution.
2. Formation of a  $SiO_2$  layer with windows on top of the ridges. This ensures that the injected current is confined to the areas intended.
- PECVD deposition of 200nm  $SiO_2$ .
  - Photolithography to form the mask for the current window.
  - HF wet etching of a  $\sim 1.5\mu m$  wide window in the  $SiO_2$ , on top of the ridge. Strip resist.
3. Substrate thinning and contact deposition.
- Removal of the p-side gallium oxide layer with 1:1 HCl,  $H_2O$  or 1:1  $NH_3$ ,  $H_2O$  solution for 60 seconds.
  - Evaporation of the Ni/Au or NiCr/Au p-side contact.
  - Thinning of the substrate to  $<150\mu m$  thick (hand lapping using  $9\mu m$   $AlO_3$  powder).
  - Removal of the n-side gallium oxide layer using a 1:1  $NH_3$ ,  $H_2O$  solution.
  - Evaporation of the Au/Ge/Au/Ni/Au n-type contact.
4. Cleaving into individual laser chips.

### **3.33 Fabrication and testing of symmetric Mach-Zehnder interferometers**

As part of this project a range of integrated asymmetric Mach-Zehnder interferometer laser amplifiers were fabricated in GaAs/AlGaAs. A diagram of these devices is shown in Fig 3.3 and SEM pictures are shown in Fig 3.4-6. Although the fabrication techniques were broadly similar to those described for RWLs, several different process steps were

required to form these more complicated structures.

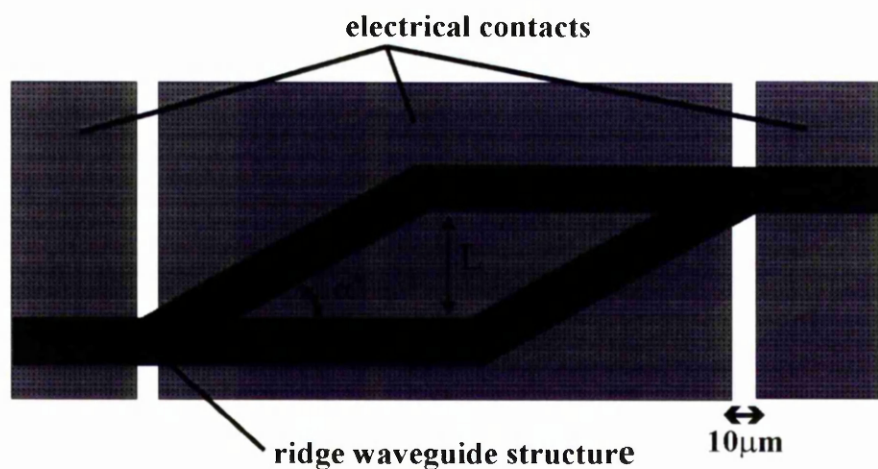


*Fig. 3.3 AMZI laser amplifier structure.*

Photolithography has a limited resolution determined by the wavelength of the light used to expose the resist, the mask to sample distance (when contact printing is used), the resist thickness and the feature resolution on the mask plate itself. The contact lithography techniques used made fabrication of structures  $< 1\mu\text{m}$  difficult. There is inevitably a loss of resolution, this was particularly obvious at the ‘tip’ of the Y junction as is shown in Fig. 3.4. If appropriate steps are not taken, significantly blunted Y junctions can be produced, causing back reflections and losses. Also the point of the Y junction can break up, causing scattering. In order to produce Y junctions that were not overly blunted the original nichrome master mask plates were used. These plates were formed by e-beam lithography and consequently have good resolution. It was also necessary to underexpose the pattern in order to produce sharp Y branches. Where an exposure time of 3.5s was normally used for a  $3.5\mu\text{m}$  geometry, this was reduced to 3.1s to produce less blurred Y branches. Ensuring a good contact between mask and sample was also important.

To produce multiple contacts on the AMZI p-side, the lift-off process was used. Prior to contact evaporation, thick layers of resist are patterned in the areas where spaces in the contact layer are required.

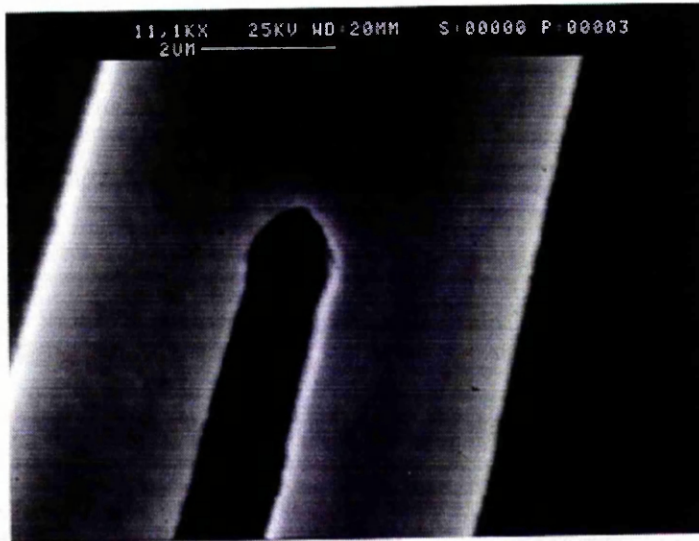


Fig. 3.4 Blunting of a Y branch tip to  $\sim 1\mu\text{m}$ .

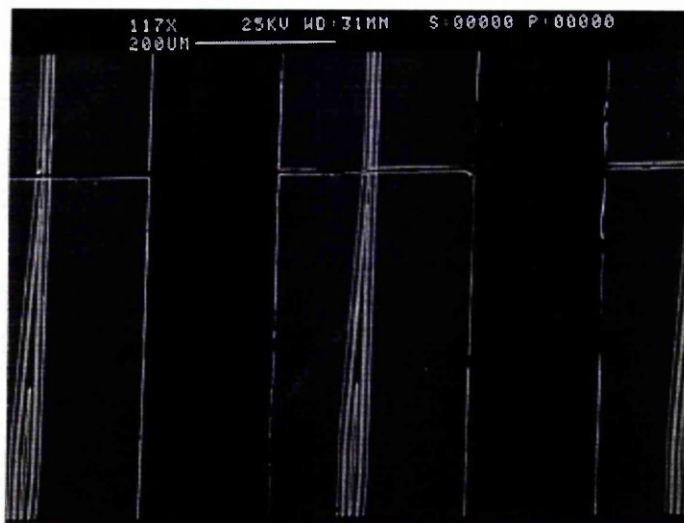
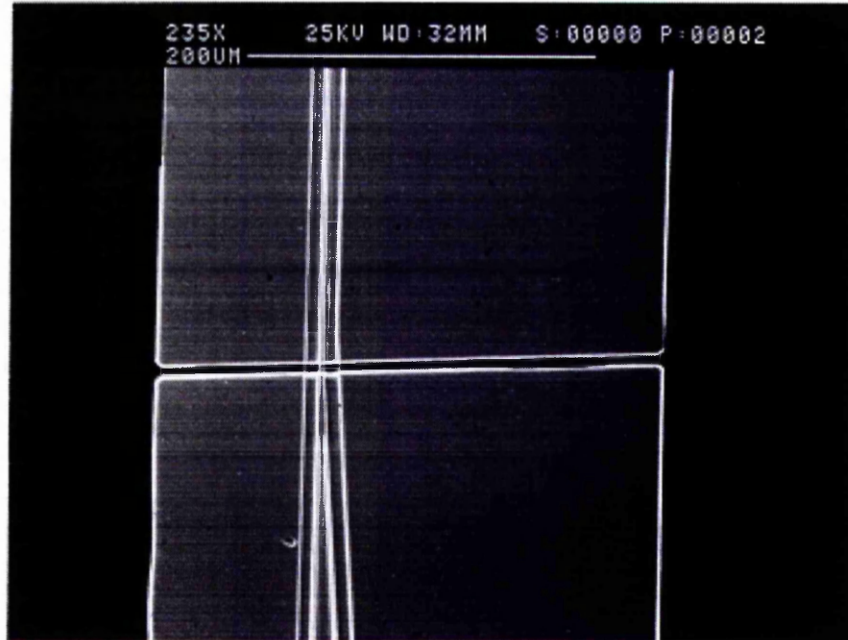


Fig. 3.5 Three adjacent AMZIs showing the separate input and Mach-Zehnder contacts.

After evaporation the samples were soaked in acetone, which removes the resist and ‘lifts off’ the metal layer on top. To enhance this process a 15 minute chlorobenzene soak was used half way through the initial resist baking, prior to photolithography. The chlorobenzene soak leads, upon development, to a more undercut resist profile, which facilitates lift-off. For successful lift-off it is important not to over post-bake the resist.

A post-development-bake of 5 minutes was used. It was also important to ensure that the sample, and hence the resist, was not heated in the metal deposition stage. Ammonia was not used here as an oxide removal etch, as it attacks the resist. Hydrochloric acid was used instead. In order to produce contacts that could be wire bonded, a NiCr/Au p-side contact was used for the AlGaAs AMZI lasers.



*Fig. 3.6 A closer view of the split contact between input waveguide and the Mach-Zehnder, showing the 10 $\mu$ m separation.*

Fig 3.6 shows a SEM of the split contact on an AMZI. Due of the high resistivity of the MBE grown GaAs/AlGaAs structures, a 10 $\mu$ m gap between contacts provided sufficient isolation and no additional passivation was required. Measurements gave in excess of 300  $\Omega$  isolation.

The Mach-Zehnders and adjacent Fabry-Perot lasers were tested using the pulsed test set up, described in Section 3.31, allowing good devices to be selected for mounting. Thresholds were typically around 10mA for 500 $\mu$ m long Fabry-Perot devices, but larger for the long AMZI sections. The AMZI was fabricated from wafer B454, a 4QW structure, primarily because of it's availability. Further details of the AMZI's lasing performance is given in Section 6.32.

### 3.34 InGaAsP/InP laser fabrication

In the course of this project, quaternary laser structures were fabricated. The techniques were broadly similar to those described previously. The main fabrication differences were: the native oxide removal etches were not believed to be necessary in the InGaAsP/InP material system, Ti/Au p-type contacts were used, a different etch chemistry was required for InGaAsP/InP RWL and it was important to ensure the ridge side walls were oxide “passivated”.

Broad area lasers were first produced to characterise the material, the results of which are described in Appendix II. Ridge waveguide structures were then formed using a CH<sub>4</sub>:H<sub>2</sub> dry etch which etches both InP and InGaAsP. Similar CH<sub>4</sub>:H<sub>2</sub> dry etches have been shown to provide near vertical anisotropic etch profiles <sup>6,11</sup>. The process <sup>12,13</sup> used an Electro-Tech 340 reactive ion etcher and the parameters are outlined in the table below.

Parameter	Value
gas flow	3.5 sccm CH <sub>4</sub> , 2.6 sccm H <sub>2</sub>
pressure	14 mtorr
r.f. power	100 W
d.c. bias	-850 V

*Table 3.1 Methane hydrogen InP/ InGaAsP dry etch.*

During the CH<sub>4</sub>:H<sub>2</sub> dry etch a polymer formed on the sample, which was removed immediately after the etch, using an oxygen plasma. For a total ridge etch of typically 1.4µm, 1µm was dry etched using the above process and the remainder wet etched using a 3:1 orthophosphoric acid / hydrochloric acid solution, which etched InP at ~1µm per minute, using InGaAsP as an etch stop. The wet etch was necessary because the dry etch alone produces considerable surface damage leaving rough surfaces.

A great deal of time was spent trying to produce devices using this process, but no lasers of acceptable quality were produced. Subsequently, this process, although it produced structures which looked visually acceptable, was found, because of the high ion energies, to cause damage to the laser active region, killing the luminescence <sup>14,15</sup>. An alternative etch chemistry <sup>16</sup> based on bromine was also tried, but this also proved

unsuccessful. Later alternative lower damage etch processes were developed<sup>14,15</sup>, but not at a time that could be utilised in this project. Dry etching is the preferred technique for waveguide fabrication as there is little mask undercut and near vertical etch profiles can be obtained irrespective of the crystallographic orientation, but with hindsight, at the time, a better solution would have been to solely wet etch the laser structures.

### **3.35 Device mounting**

Devices requiring to be operated c.w. were mounted on gold plated copper blocks with indium solder preforms. The blocks were designed to allow access to both facets. During mounting the block was initially heated to ~180°C and covered in a flux solution to prevent the indium oxidising. An indium ball of a size appropriate to the device being mounted was placed on the mount, left for a few minutes to heat up and then agitated until it melted into a pool. The laser amplifier chips were then positioned on top of the indium pool, p-side up in the case of the AMZI's. The mount was then cooled leaving a securely attached laser. Subsequently the block was left in a solution of trichloroethane to remove any flux traces and then rinsed in acetone and methanol.

## **3.4 Conclusions**

The fabrication techniques described allowed good quality single mode RWL structures to be produced in GaAs/AlGaAs. The ridge waveguide geometry allows complex structures such as Y branch splitters and combiners to be realised and results in low thresholds. In the AMZI structure, separate contacts are provided for each section, with sufficient isolation to allow all sections to be biased independently. The techniques described have been used to produce an integrated Mach-Zehnder laser amplifier structure, the characterising and testing of which is described in a later chapter. Originally the intention was also to construct the AMZI in the InGaAsP/InP material system for 1.5µm operation but the dry etching process in existence at the time did not allow devices of suitable quality to be produced.

## References

- 1 S. M. Sze (ed), "VLSI technology", McGraw-Hill, 1988
- 2 S. M. Sze, "Semiconductor devices physics and technology", John Wiley, 1985
- 3 P. Rai-Choudhury, "Handbook of microlithography, micromachining and microfabrication", vol. 1 microlithography, vol. 3 microfabrication.
- 4 G. P. Agrawal, N. K. Dutta "Semiconductor lasers", 2nd ed. Chapter 4 , Van Nostrand Reinhold, 1993
- 5 Kenichi Iga, Susumu Kinoshita, "Process technology for semiconductor lasers", Springer-Verlag, 1996
- 6 S. J. Pearton, "Dry etching techniques and chemistries for III-V semiconductors", Materials Science and Engineering B-Solid State Materials for Advanced Technology, vol. 10, no. 3, p. 187, 1991
- 7 S. K. Murad, S. P. Beaumont, C. D. W. Wilkinson, "Selective and nonselective RIE of GaAs/ AlGaAs in SiCl<sub>4</sub> plasma", Microelectronic Eng., vol. 23, p. 357, 1994
- 8 J. F. Martins-Filho, "Monolithic colliding pulse mode-locked quantum-well lasers", Chapter 3, Ph.D. Thesis, University of Glasgow, 1995
- 9 A. Piotrowska, A. Guivarch, G. Pelous, "Ohmic contacts to III-V compound semiconductors- a review of fabrication techniques", Solid-State electronics, vol. 26, no. 3, p 179, 1983
- 10 A. G. Baca, F. Ren, J. C. Zolper, R. D. Briggs, S. J. Pearton, "A survey of ohmic contacts to III-V compound semiconductors", Thin Solid Films, vol. 308, p. 599, 1997
- 11 J. W. McNabb, H. G. Graighead, H. Temkin, R. Logan, "Anisotropic reactive ion etching of InP in methane hydrogen based plasmas", Journal of Vacuum Science and Technology B., vol. 9, no 6, p. 3535, 1991
- 12 M. A. Foad, C. D. W. Wilkinson, C. Dunscomb, R. H. Williams, "CH<sub>4</sub>/H<sub>2</sub> - a universal reactive ion etch for III-Vi semiconductors", Appl. Phys. Lett., vol. 60, no. 20, p 2531, 1992
- 13 Andrew McKee, "Photoabsorption induced disordering of InGaAs-InGaAsP multiple Quantum well structures for optoelectronic integration ", Ph.D Thesis,

University of Glasgow, 1996

- 14 Stewart Duncan McDougall, "Monolithic colliding pulse mode-locking of AlGaAs/GaAs and InGaAs/InGaAsP quantum well lasers", Ph.D Thesis, University of Glasgow, 1997
- 15 B. C. Qui, B. S. Ooi, A. C. Bryce, S. Hicks, C. D. W. Wilkinson, R. M. De la Rue, J. H. Marsh, "Reduced damage reactive ion etching process for fabrication of InGaAsP/InGaAs multiple quantum well ridge waveguide lasers", Journal of Vacuum Science and Technology B, vol. 14, no. 4, p.1818, 1998
- 16 S. K. Murad, S. P. Beaumont, M. Holland, C. D. W. Wilkinson, "Selective reactive ion etching of InGaAs and InP over InAlAs in SiCl<sub>4</sub>/SiF<sub>4</sub>/HBr plasmas", Journal of Vacuum Science and Technology B, vol. 13, no. 6, p.2344, 1995

# Chapter 4

## Experimental laser system

### 4.1 Introduction

In this section, a description of the experimental laser system developed and used to perform most of the experiments on optical amplifiers at 1.5  $\mu\text{m}$  is given. The laser system consisted of a FM mode-locked diode-pumped Nd:YLF laser producing pulses of 20-40 ps FWHM duration at 77 MHz repetition rate. This was used to synchronously pump a KCl:Tl F-centre (aka colour centre) laser. This provided a c.w. or mode-locked tuneable optical source at around 1.5  $\mu\text{m}$ . This was, to our knowledge, the first diode-pumped F-centre laser developed.

The Nd:YLF laser and its performance is described. An interesting, but unintended property of this laser was its ability to Kerr lens mode-lock (KLM). In this chapter the reasons for this are analysed and it is shown that, because of the unusual cavity configuration, the Kerr medium is the LiNbO<sub>3</sub> phase modulator. Some problems with the current Nd:YLF pump laser are discussed and their possible solutions identified. The F-centre laser is then described and finally some suggestions for improving the complete system performance are discussed, but first, a description of some of the diagnostic equipment used is given.

The author is indebted to Craig Hamilton for his work on the same Nd:YLF and F-centre laser system<sup>1</sup>, his work set up and characterised the F-centre laser's c.w. performance. The initial demonstration of the FM mode-locked and KLM synchronously pumped F-centre laser was by Craig Hamilton, subsequently the autocorrelation system was set up by the author. The author's contribution is the refinement and use of the system as a tool to perform a series of experiments and the characterisation and analysis of the mode-locking mechanism and its stability. The laser

was run daily over a period of 2-3 months and its performance noted in terms of pulsewidth and stability for KLM and FM mode-locking. Consequently the limitations of the system became evident, the quantification and ABCD matrix analysis of the laser's KLM, thermal instability and the suggested improved system are the author's own work. Considerable time was spent trying to optimise the existing laser cavity, in particular: experimentation with various mirror positions, the inclusion of an adjustable aperture, the use of an active feedback system to adjust the cavity length, variation of the phase modulator position and drive power. The F-centre laser was modified for the coupled cavity or additive-pulse mode-locked configuration, with a length of fibre forming a subsidiary cavity, in order to produce subpicosecond pulses. However there was insufficient time to characterise this configuration in detail.

## **4.2 Diagnostics**

A brief description of some of the more elaborate diagnostic equipment required to monitor and characterise the lasers performance is now given.

The simplest method of monitoring the output of a pulsed laser is with an oscilloscope and high speed detector, chosen for the appropriate wavelength range. Such detectors are generally suitable for monitoring pulse repetition rates of up to 50 GHz although specialist devices can operate faster. Whilst this technique can be used to monitor pulse trains from typical mode-locked solid state lasers with repetition rates of around 100 MHz, it provides little information on pulse durations shorter than 100 ps, which is typically the combined oscilloscope and detector time constant.

A standard technique for measuring short pulse durations is second harmonic generation (SHG) autocorrelation, where the laser signal is split in two and a variable delay is applied to one pulse. These two pulses are then recombined and focused on a nonlinear crystal which generates a SHG signal. By monitoring the SHG signal as a function of relative pulse delay, it is possible to obtain information on the pulsewidth, providing the pulse shape is known. The obtained SHG signal is maximised when both pulses overlap perfectly and quickly decays either side of maximum overlap as SHG has

an intensity squared dependence. Table 4.1 shows the conversion factors to translate the autocorrelation FWHM into a pulsewidth FWHM.

Pulse Shape	$t_p / t$
$e^{-t^2}$	$\sqrt{2}$
$\sec^2(t)$	1.543

Table 4.1 Relationship between autocorrelation FWHM,  $t_p$  and the pulse FWHM,  $t$ .

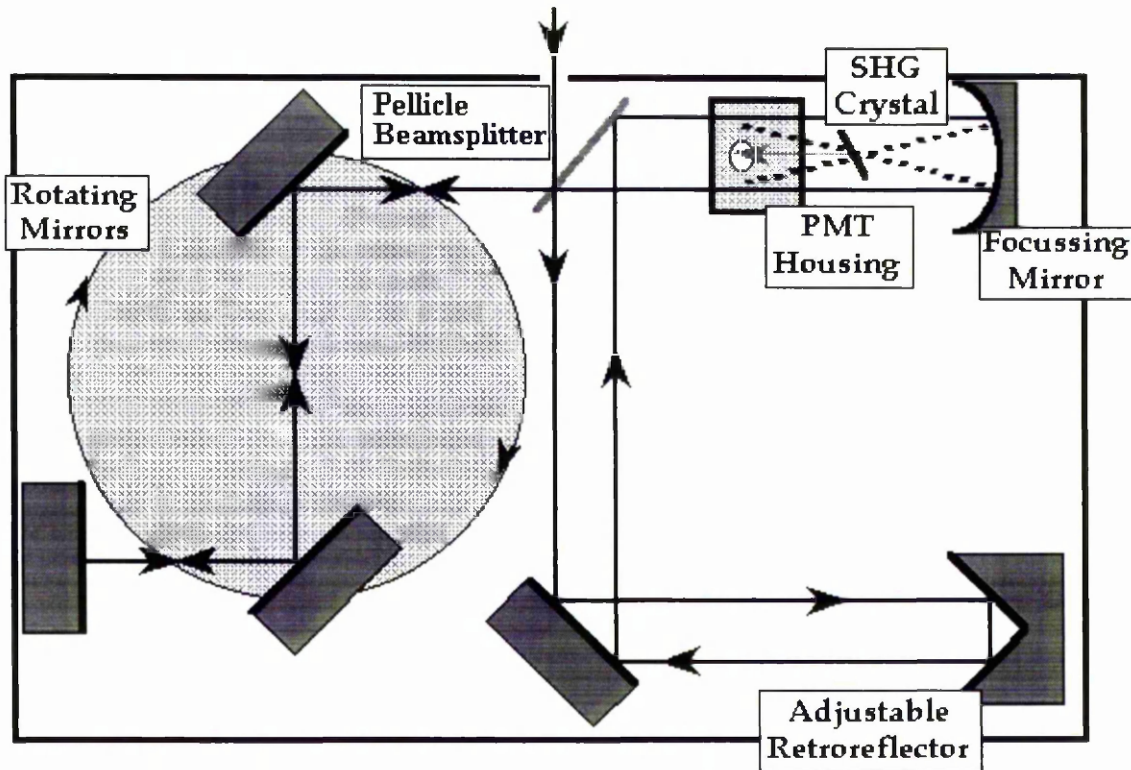


Fig. 4.1 Schematic of the autocorrelator used for pulsewidth measurements.

There are several variants of autocorrelator, the phasematching can be of type II where the two pulses are orthogonally polarised or more usually type I, where both pulses have the same polarisation. Two possible configurations exist, the collinear autocorrelator, where the two pulses travel through the crystal along the same optical path and the non-collinear or background free arrangement, where the paths of the two pulses intersect within the crystal and then diverge, the generated SHG travels at an angle that bisects the paths formed by the two pulses.

The autocorrelator used here was a Femtochrome FR-103 IR, a schematic of which is shown above in Fig. 4.1. The autocorrelator employs type I phase matching and a non-collinear geometry which provides a background free autocorrelation. The device is designed for measuring ultrashort pulses, so to prevent pulse broadening the mirrors are metal coated and a thin pellicle beamsplitter is used. The nonlinear medium is a 100 $\mu\text{m}$  thick  $\text{LiIO}_3$  crystal which can be used in the wavelength range 0.9  $\mu\text{m}$  to 1.6  $\mu\text{m}$ , if a suitable fundamental blocking filter is used. Rather than using a loud speaker, which can only translate a small amount, or a PZT stage, which would introduce positioning uncertainties, a continually rotating mirror geometry is used, which produces a continually varying path length corresponding to an optical delay of between 0 and 120 ps. The time delay produced varies linearly with the parallel mirror assembly angle for the small angular changes involved. A micrometer controlled retroreflector is provided in the other arm to provide a calibration check.

The technique used to align the system, was to first block the stationary arm and adjust the signal from the other arm through the aperture, onto the photomultiplier tube. The crystal angle, focus point and input polarisation are then adjusted to maximise the SHG signal. Following this, a small amount of further adjustment is required to obtain an autocorrelation signal.

### **4.3 Diode-pumped Nd:YLF laser system**

The pump laser for the  $\text{KCl:Tl}$  laser was a diode-pumped Nd:YLF laser developed by Microlase Optical Systems.

Diode-pumping <sup>2</sup> has come to the fore in recent years because of the development of high power diode sources, which have many advantages over more traditional flashlamp-pumps. Laser diodes can be precisely tuned to match the absorption band of the gain medium, whereas flashlamp-pumping is an inefficient process, as only a small proportion of the white light pumps the required transition, the rest is dissipated as heat. This heat dissipation itself causes problems and water cooling systems are required to remove excess heat from the laser rod and flashlamp chamber in

high power systems. These cooling systems are bulky, expensive and result in noisier laser operation compared to their diode-pumped equivalent.

A more short pulse laboratory workhorse laser is the Nd:YAG but more recently new materials have been developed, in particular Nd:YLF, which in many respects is similar to Nd:YAG but offers some advantages. Both obviously employ the rare earth neodymium ion, YAG (yttrium aluminium garnet) and YLF (YLiF<sub>4</sub>) are the host materials. A comparison between Nd:YAG and Nd:YLF is shown in Table 4.2 below.

	Nd:YAG	Nd:YLF
<b>Lasing Wavelength</b>	1.064 $\mu$ m	1.047 $\mu$ m
<b>Pump Wavelength</b>	0.810 $\mu$ m	0.797 $\mu$ m
<b>Upper State lifetime</b>	250 $\mu$ s	450 $\mu$ s
<b>Gain cross section</b>	6.5 $\times 10^{-19}$ cm <sup>2</sup>	1.8 $\times 10^{-19}$ cm <sup>2</sup>
<b>Fluorescence linewidth</b>	6cm <sup>-1</sup>	12cm <sup>-1</sup>

Table 4.2 Comparison between Nd:YAG and Nd:YLF.

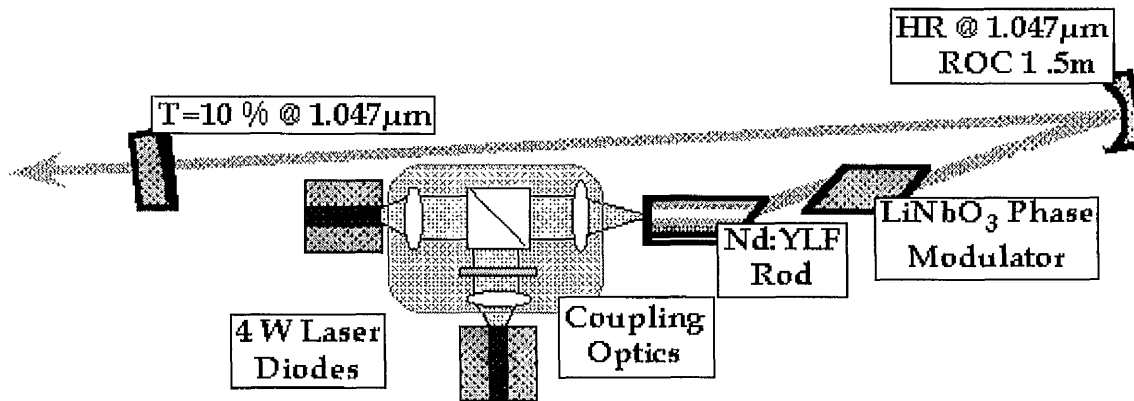


Fig. 4.2 Mode-locked diode-pumped Nd:YLF laser.

From Table 4.2 it can be seen that Nd:YAG and Nd:YLF offer similar performance, although Nd:YAG is better suited for high power lasers because of its larger gain cross section, Nd:YLF has the potential for supporting shorter pulses because of its larger linewidth. Also, Nd:YLF possesses better thermal properties and less attention has to be paid to thermal lensing effects, which can be a source of instability. For these reasons a diode-pumped Nd:YLF<sup>2,3</sup> system was chosen rather than the more typical mainframe flashlamp-pumped Nd:YAG.

A schematic of the experimental laser system is shown in Fig. 4.2 above. The

rod is pumped by two 4 Watt AlGaAs laser diodes (supplied by SDL) which are temperature tuned to the Nd:YLF absorption line. One of the diode's polarisation is rotated by 90 degrees, allowing the pump beams to be combined at a polarising beamsplitter and following this are some beam shaping optics which define the pump beam size within the rod and hence the pumping efficiency <sup>4</sup>. The rod is 1cm long and end pumped. One end is Brewster cut and the other flat, which is HR coated at 1.047  $\mu\text{m}$  to form one of the three cavity mirrors. Astigmatic compensation for the Brewster-angled rod surface is provided in the cavity dog leg angle. A 1.5 m radius of curvature (ROC) mirror positioned 77 cm from the rod surface defines the beam waist within the rod which is estimated to be 300  $\mu\text{m}$  ( $1/e^2$  radii) from ABCD matrix calculations, which are discussed later. The final mirror is formed by a 10 % output coupler. Frequency modulation is provided by a 2.5 cm long Brewster-angled LiNbO<sub>3</sub> electro-optic phase modulator, which was located about 4 cm from the rod. The beam size here is relatively small so a modulator with a small aperture can be used, without requiring any additional optics. The laser repetition rate is set by a fixed frequency oscillator at 77.74 MHz.

#### **4.31 Nd:YLF c.w. and FM mode-locked operation**

When operated at full power with pump diode currents of 5.5 and 5.25 A, output powers of up to 2.2 W were routinely obtained from the Nd:YLF laser, with single-mode beam profiles.

When mode-locked, the average power was virtually the same as the c.w. case. The modulation voltage applied to the phase modulator was adjusted for shortest pulses, as too much power tended to produce broader pulses, also at high powers the modulator driver generated some higher harmonics, rather than a pure sine wave. Continually monitoring with a fast detector showed that the mode-locked pulse train laser tended to hop phase by 180 degrees and only by slightly adjusting the cavity mirrors and length could this be eliminated and the most stable shortest pulses obtained.

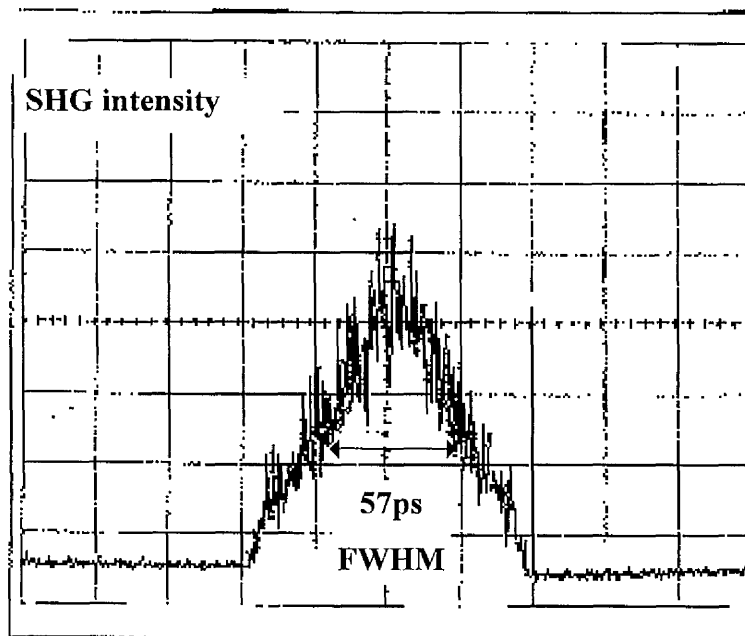


*Fig. 4.3 Autocorrelation of Nd:YLF laser when FM mode-locking. FWHM autocorrelation width of 57 ps, pulsewidth of 40 ps.*

The shortest pulses measured were 20 ps FWHM, which is significantly shorter than those obtained from typical lamp pumped Nd:YAG systems<sup>5</sup>, which produce pulses in the 60-100 ps regime. Fig. 4.3 shows an autocorrelation of a FM mode-locked pulse, in this case for a pulsewidth of 40 ps duration.

#### **4.32 Mode-locking techniques<sup>6</sup> and Kerr lens mode-locking**

Mode-locking is the name given to a powerful range of techniques which enable the optical power within a laser cavity to be “forced” into periodic pulses in the time domain. This is useful because these pulses can be ultra-short, down to femtoseconds in duration, giving high peak powers. These high peak power pulses have a range of applications in the nonlinear optics field. In this section a brief overview of mode-locking is given, followed by a listing of the principal mode-locking techniques.

Most lasers support many longitudinal optical modes, as they have a large gain bandwidth compared to the cavity Fabry-Perot mode spacing. If unperturbed these modes exhibit random phase relationships, in other words the modes are not in phase with each other. The output in the time domain is therefore the random sum of all the

oscillating modes. An interesting behaviour occurs when the individual cavity modes are forced to be in-phase with each other or mode-locked. When this occurs regular pulses are produced in the time domain, with a pulse spacing corresponding to the cavity round trip time, or a submultiple. The origin of this pulse train can be understood by considering the fourier transform of the optical spectrum, which gives periodic pulses in the time domain, with a pulse width proportional to  $1/\nu_p$ , where  $\nu_p$  is the spectral envelope or bandwidth. As many lasers have a broad bandwidth, mode-locked pulsewidths are significantly shorter than those obtained through other techniques. When mode-locking is initiated, by what ever method, the laser cavity is altered to favour the passage of pulses, preferentially favouring the shortest. This allows pulse durations to approach the theoretical limit, for a given gain material. The ultimate pulse duration, for a given bandwidth, is known as the transform limit. For a transform limited gaussian pulse Equation 4.1 links the pulsewidth and the bandwidth,

$$t_p \cdot \Delta\nu_p \approx 0.441 \tag{4.1}$$

where  $t_p$  is the FWHM pulsewidth in the time domain and  $\Delta\nu_p$  is the FWHM spectral bandwidth. In practice not all of the cavity modes can be phase-locked, and with some mode-locking methods significant frequency chirp is experienced, however some mode-locked lasers approach the transform limit.

There are several techniques of attaining mode-locking, some of the main methods are outlined in the table shown below.

<b>Active mode-locking</b>	
The laser is forced to mode-lock by an applied modulation	
<b>Mode-locking method</b>	<b>Summary</b>
<b>Amplitude modulation (AM)</b>	Intuitively this is the simplest method to understand. The loss of the laser cavity is modulated, either by modulating the gain medium or by an additional modulator which is introduced into the cavity. In solid state lasers one method of achieving AM mode-locking is through synchronously pumping. In this scheme one laser, usually FM mode-locked, pumps another. If the cavities are matched in length, the pumped laser mode-locks. The advantage of this scheme

	is that pulse shortening occurs, the final pulsewidth is shorter than that obtained with FM mode-locking alone.
<b>Frequency modulation (FM)</b>	In traditional solid state lasers an acousto-optic or electro-optic modulator is introduced into the laser cavity. When this is modulated at a frequency of $c/2L$ mode-locking occurs. This was the method traditionally used for the mode-locking of mainframe lamp-pumped Nd:YAG lasers. Although recently the lasers themselves have evolved into compact diode pumped systems, the FM mode-locking techniques remain essentially the same.
Generally these techniques do not reach the transform limit. Particularly for systems with a large gain bandwidth, these techniques are generally only useful for picosecond pulse generation. For shorter durations alternative methods have to be employed.	

<b>Passive mode-locking</b>	
<p>These methods do not force the laser to mode-lock through an externally applied modulation, instead they rely on an element within the laser cavity, a saturable absorber, which has a lower optical loss for an intense optical signal. These systems therefore favour pulsed operation and, because the saturable absorber action increases for shorter pulsewidths, they are superior over active mode-locking in obtaining the minimum pulse duration for a given gain medium. They are also less sensitive to cavity length fluctuations, as in general, they do not require to be phase-locked to an external oscillator.</p> <p>In recent years, in parallel with the development of new laser materials, several new mode-locking techniques have been developed <sup>7,8</sup> these techniques form the last three mode-locking methods described here.</p>	
<b>Traditional saturable absorber</b>	<p>Traditionally a dye jet provided the saturable absorber action. These schemes are limited by the recovery time of the dye and the optical intensity on the dye. This necessitates tightly focused beams and colliding pulse schemes.</p> <p>This technique is limited by the availability of a dye at the desired wavelength.</p>
<b>Additive pulse (APM) or coupled cavity</b>	Developed from the soliton laser <sup>9</sup> , in this scheme the light in a subsidiary cavity is arranged to interfere with the main cavity signal. A nonlinear medium, usually a short length of optical fibre (typically 20cm) forms part of the subcavity. The laser utilises nonlinear self-phase-modulation in the fibre. When the length of the subcavity is suitably adjusted, the phase relationship between the cavities means that the pulses from the subcavity interfere with the pulse in the main cavity, constructively in the centre of the pulse and destructively at the pulse wings; short pulse operation results. One disadvantage of

	<p>this system is that it is necessary to accurately control the cavity lengths to within a fraction of a wavelength. This is accomplished with an electronic feedback loop, which relies on the variation of the average output power that occurs when the cavities are detuned.</p> <p>This technique has been successfully applied to a wide range of solid state lasers including: Ti:sapphire, Nd:YAG and Nd:YLF. In some F-centre lasers APM is not self starting and synchronous pumping is still used to initiate it.</p>
<p><b>Kerr lens mode-locking (KLM)</b></p>	<p>Following its discovery in 1991 Kerr lens mode-locking <sup>10</sup> revolutionised the field, providing a simple means of ultra-short pulse generation. KLM is arguably the preferred method for obtaining femtosecond laser pulses, as it does not require the phase-locking of the cavity to an external modulator or interferometric length control.</p> <p>This technique also relies on nonlinear self-phase-modulation (SPM), which in an unguided medium gives rise to self-focusing. It is this self-focusing which leads to an effective saturable absorber action; if an aperture is suitably placed within the laser cavity, short pulses, which experience more self-focusing, will on passage through the aperture, experience less loss. The cavity therefore favours short pulse operation. In order to exploit KLM the laser cavity must be suitably designed. The nonlinear element is often the gain medium and the aperture within the cavity should be positioned so that the SPM induced changes in the beam waist result in a lower round trip loss. In order to maximise the effects of self focusing it is necessary to detune the cavity from what would be the position of maximum stability for c.w. operation.</p> <p>KLM has been successfully utilised in a wide range of laser materials including Ti:sapphire, Cr:LiSAF, Nd:YAG, Nd:YLF and Cr:forsterite. Some gain materials, Ti:sapphire for example, have a sufficient nonlinearity to give self focusing. Other materials do not, then an additional nonlinear element is required. A natural “soft aperture” is provided in some gain materials, formed by the overlap between lasing and pump beams. KLM is normally not self starting, usually some form of cavity perturbation is necessary to initiate it.</p>
<p><b>antiresonant semiconductor saturable absorber mirror</b></p>	<p>This technique uses a resonant nonlinearity in specifically tailored semiconductor material, which forms one of the cavity mirrors. The saturable absorber mirror is a multi-layered structure, grown by MBE, sandwiched between two high reflecting surfaces, forming a thin Fabry-Perot etalon. Either a</p>

	<p>metalized surface or Bragg reflector is used to form the mirrors. The Fabry-Perot cavity is operated at anti-resonance, to reduce the intensity in the medium (hence reducing the likelihood of damage), this also importantly raises the saturation intensity, favouring shorter pulses. This technique has been used in isolation and in combination with other techniques, to achieve mode-locking in picosecond and femtosecond lasers</p>
--	---

Table 4.3 Mode-locking methods

Of importance to the Nd:YLF laser used in this thesis is KLM, as described in the table above. Fig 4.4 gives a diagrammatic explanation of Kerr lens mode-locking, for a three mirror cavity. There are several key elements necessary in order to obtain KLM, which are discussed below:

- **Kerr medium.** A essential element for KLM is a medium within the laser cavity which provides self-focusing of the optical beam, effectively introducing an additional lens into the cavity, which is only seen by short pulses. This self-focusing alters the laser resonator, changing the beam width.
- **Cavity design.** In order to exploit the self-focusing, the cavity should be designed so the self-focusing introduced by the nonlinear Kerr lens leads to a large variation in the beam width. In practice this means that the laser resonator is designed to be close to the instability limit. Instead of the resonator design of Figure 4.4, usually a four mirror resonator is used with two curved mirrors. By moving the relative mirror positions of the curved mirrors the cavity can be adjusted to be near the instability limit.
- **Hard or soft aperture.** To encourage the mode-locking an appropriately sized aperture should be placed in the cavity, at a position where the Kerr lens induced beam size variations are maximised. The aperture preferentially lets past high intensity signals. Apertures can either be a physical hard aperture or an effective

soft aperture formed by the overlap between pump and lasing beams.

- **Self starting.** Not all KLM lasers self start, if this is the case the laser cavity requires to be perturbed in order to initiate mode-locking.

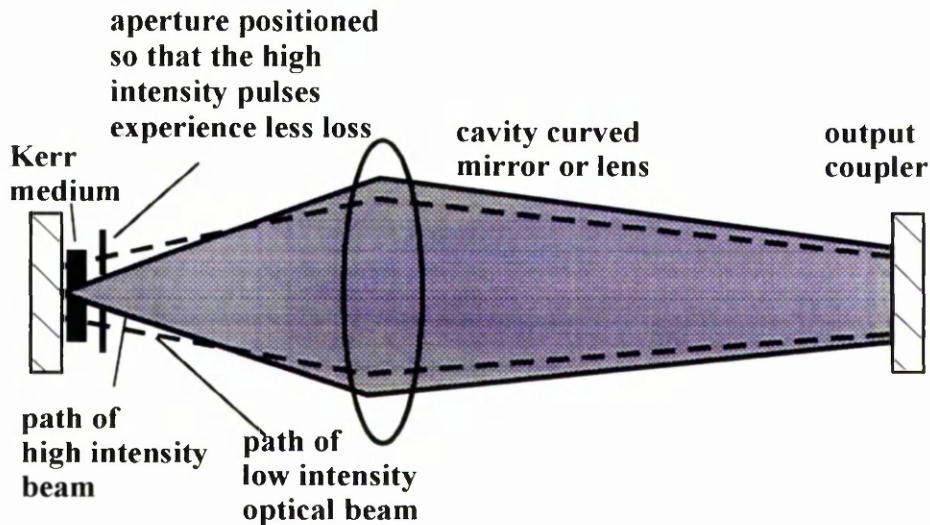


*Fig. 4.4 Diagrammatic illustration of Kerr lens mode-locking in a three mirror cavity. Shorter pulses experience mode self-focusing and will therefore have a narrower beam waist at certain positions in the cavity, this is where the placing of an aperture will promote KLM. The gain medium is not shown, but in many lasers the laser rod itself forms the Kerr medium.*

The next section describes the KLM behaviour, as observed and analysed in the experimental Nd:YLF laser.

#### **4.33 Nd:YLF Kerr lens mode-locked operation-experimental**

The laser system, whilst designed to FM mode-lock would, if suitably adjusted, undergo sudden pulse shortening caused by what was attributed to Kerr lensing. When initiated KLM would cause the pulsewidths suddenly to shorten from 20-30 ps to typically 6 ps

FWHM as shown below in Fig. 4.5, this went along with a sudden 3 % increase in average power.

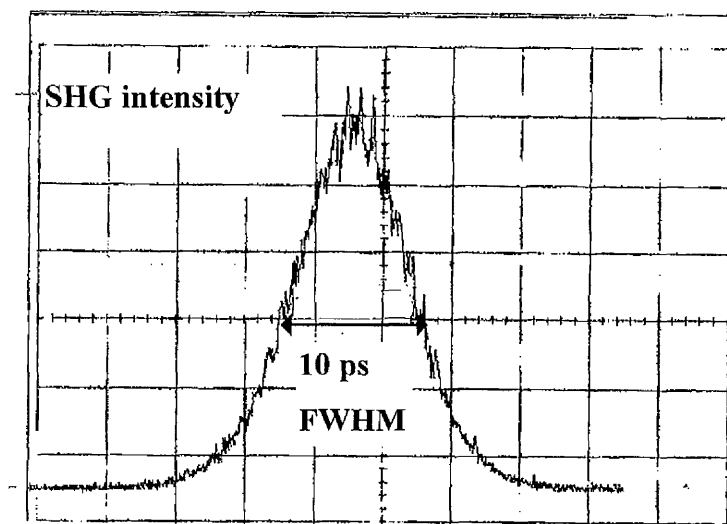
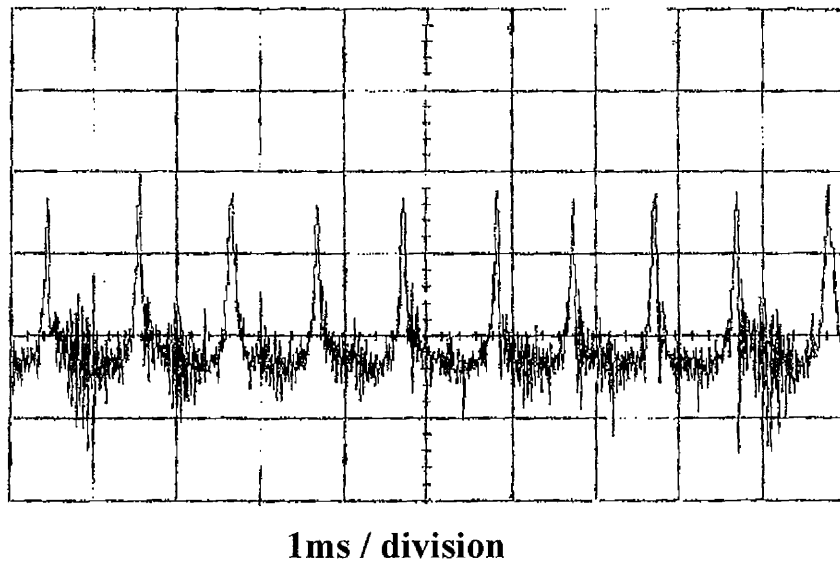


Fig. 4.5 Autocorrelation of Nd:YLF laser when Kerr lens mode-locking. FWHM autocorrelation width of 10 ps, pulsewidth of 6.5 ps.

Although the average power suddenly increased when KLM was initiated, it was necessary to detune the laser cavity slightly from the position of maximum average output power in order to promote KLM. The KLM operation was readily identified, even without autocorrelation, as a green 2nd harmonic signal, generated within the LiNbO<sub>3</sub> phase modulator, would markedly change in intensity when KLM was initiated. The average powers obtained with KLM were typically 1.7 W or less.

The KLM operation allowed the laser to produce significantly shorter pulse durations. With the aim of allowing these shorter pulses to be obtained routinely, the KLM behaviour was further investigated. The KLM did not self-start, as is not uncommon and was the case in the first lasers in which KLM was observed. In order to initiate the KLM it was necessary to adjust the cavity, either by adjusting the output coupler, one of the internal elements or just vibrating the optical bench. Once initiated the laser would continue to KLM for a time varying between minutes and several hours, however if left unadjusted a beating effect was observed between the KLM and the phase modulator driver frequency as shown in Fig. 4.6. The cavity length required constant adjustment if this was to be avoided. Fig. 4.7 shows the laser drifting over a five minute period when

KLM, monitored by observing the SHG signal produced in the  $\text{LiNbO}_3$  phase modulator. If the drive to the phase modulator was removed, the KLM stopped virtually instantaneously, similarly KLM proved impossible to initiate without the phase modulator driver switched on. As illustrated above in Fig. 4.4 the KLM process relies on an aperture in the cavity. Although there is no hard aperture in the cavity, several effects such as the overlap between the pump and lasing beams in the rod or effects in the phase modulator can produce an effective aperture. Subsequently an adjustable aperture was experimented with, this is described in more detail in Section 4.34. An attempt was also made to actively stabilise the cavity length by using the green 2nd harmonic signal, generated within the phase modulator, to drive a feedback loop controlling the position of one of the cavity mirrors. Initial experiments proved unsuccessful and time was not available to pursue this further.



*Fig. 4.6 Low frequency beating between the Kerr lens mode-locking frequency and the phase modulator driving frequency. Observed when the green second harmonic signal is monitored.*

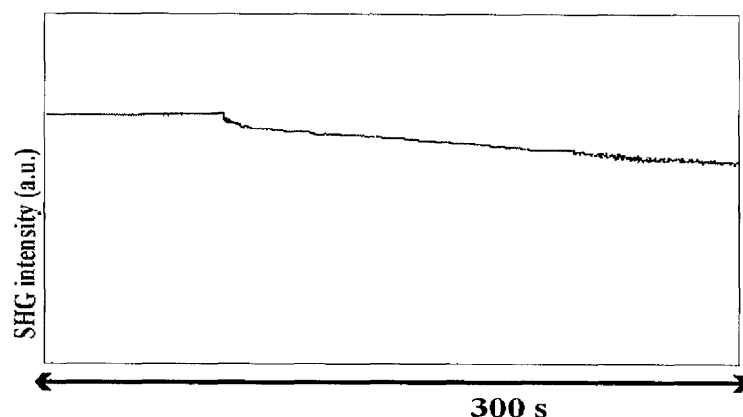


Fig. 4.7 Cavity drift over time as shown by the intensity of a SHG signal over five minutes.

#### 4.34 Nd:YLF Kerr lens mode-locked operation-analysis

Following the results outlined above, showing that the KLM was difficult to control; the Nd:YLF cavity was analysed using an ABCD matrix approach<sup>11-17</sup>, detailed in Appendix IV and the origin of the self-focusing nonlinearity was investigated.

KLM has been observed in Ti:sapphire and Cr:LiSAF lasers<sup>10,12,18</sup>, where the Kerr medium is the gain material, but in Nd:YLF and Nd:YAG the nonlinear index,  $n_2$  is small<sup>19</sup> ( $6 \times 10^{-16} \text{ cm}^2 \text{ W}^{-1}$  for Nd:YAG and  $1.7 \times 10^{-16} \text{ cm}^2 \text{ W}^{-1}$  for Nd:YLF) and for diode-pumped geometries the beam waist in the rod is quite large. For these reasons KLM has mainly been achieved in Nd:YLF lasers using an introduced Kerr medium such as Schott glass, typically SF 56<sup>20,21</sup>. For these reasons it was thought unlikely that the Nd:YLF rod was the nonlinear medium.

Following further analysis, the  $\text{LiNbO}_3$  phase modulator was identified as the likely Kerr medium as its  $n_2$  is an order of magnitude larger than that of the gain medium. The quoted nonlinear indices<sup>19</sup>,  $n_2$ , are  $1.7 \times 10^{-16} \text{ cm}^2 \text{ W}^{-1}$  for Nd:YLF and  $9 \times 10^{-16} \text{ cm}^2 \text{ W}^{-1}$  for  $\text{LiNbO}_3$ . The phase modulator is also significantly longer than the rod and therefore will induce more self-focusing. The unusual cavity arrangement, with the phase modulator located next to the Nd:YLF rod means the beam size in the  $\text{LiNbO}_3$  is similar to that in the rod (ABCD matrix calculations, described next, give only a 1 % change in beam size between rod and modulator). Although there is no hard aperture in the cavity, the overlap between pump and cavity modes provides a 'soft aperture'<sup>6</sup>. Also the phase modulator has an associated aperture and aperturing effects have been

attributed to thermal lens aberrations <sup>22</sup> in similar laser systems.

In order to investigate the laser behaviour further, an ABCD matrix approach was used to look at the boundaries of stability in the cavity and model the effects of self-focusing. The parameters used in the ABCD matrix models, listed in Appendix V, are shown below.

Parameter	Description	Value
$L_{rod}$	Nd:YLF rod length	1cm
$n_{rod}^{19}$	refractive index of the Nd:YLF rod	1.8
$L_{phase}$	length of the LiNbO <sub>3</sub> phase modulator	2.5 cm
$n_{phase}^{19}$	refractive index of the LiNbO <sub>3</sub> phase modulator	2.2
$R_2$	radius of curvature of the cavity dog leg mirror	1.5 m
$L$	the cavity length, adjusted to mode-lock at 77.74 MHz	1.948 m
$L_1$	distance between the rod and the phase modulator	4 cm
$L_2$	distance between the phase modulator and curved mirror	69.95 cm
$L_3$	distance between the curved mirror and output coupler	1.14 m
$w_0$	the beam radius in the Kerr medium, calculated	308 $\mu$ m
$n_2^{19}$	nonlinear index of the LiNbO <sub>3</sub> rod	$9 \times 10^{-16} \text{ cm}^2 \text{ W}^{-1}$
$t_p$	FWHM pulsewidth	6 ps
$P_{av}$	the power in the laser cavity	20 W
$f_{sf}$	The focal length of the Kerr lens, this is discussed later	

*Table 4.4 Parameters used in the ABCD matrix model of the Nd:YLF laser cavity. The dimensions given are with reference to the cavity configuration shown in Fig. 4.2.*

The results of the linear stability analysis, for varying positions,  $L_3$ , of the curved cavity mirror are shown below, in Fig. 4.8. The  $1/e^2$  beam radius was calculated to be 307  $\mu$ m in the rod, 930  $\mu$ m at the curved mirror and 779  $\mu$ m at the output coupler, for the cavity configuration used.

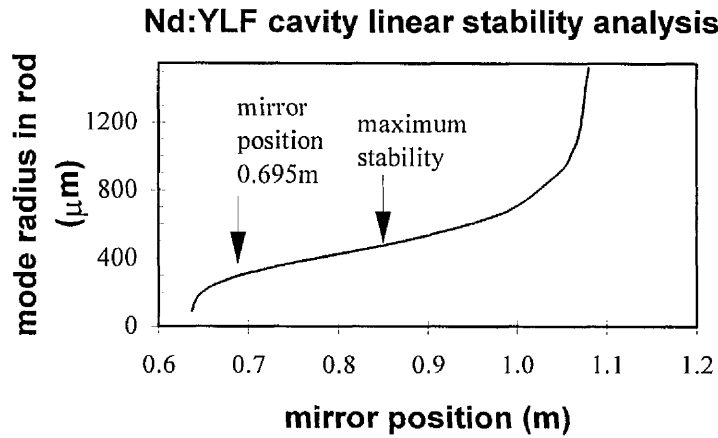


Fig. 4.8 Linear stability analysis for the Nd:YLF laser cavity for various positions of the focusing mirror. The two extremes of the graph are the boundaries of instability.

As shown in Fig. 4.8 the position of the focusing mirror has been designed to produce a beam radius in the rod allowing maximum pumping efficiency, rather than producing the most stable cavity configuration. It must be borne in mind that although it looks as if the cavity is close to the instability limit, the distances involved are large, around 5 cm.

The effects of the Kerr lens can be readily modelled if the self-induced index change across the pulse area is approximated to a quadratic, as shown below,

$$\begin{aligned}
 n(x) &\approx n_0 + n_2 I_0 \left( 1 - \frac{2x^2}{w_0^2} \right) \approx (n_0 + n_2 I_0) \left( 1 - \frac{2n_2 I_0 x^2}{w_0^2 \cdot n_0} \right) \\
 &\approx n_0 \left( 1 - \frac{2n_2 I_0 x^2}{w_0^2 \cdot n_0} \right)
 \end{aligned} \tag{4.2}$$

where  $x$  is the distance from the pulse centre,  $w_0$  is the beam waist,  $I_0$  is the peak optical intensity and  $n_2$  is the nonlinear index. The characteristic ABCD matrix of a medium of length  $L$  with an quadratic index variation of  $n = n_0(1 - 2x^2 / b^2)$  is given by Equation 4.3<sup>14,15</sup>.

$$\begin{bmatrix} a & b \\ c & d \end{bmatrix} = \begin{bmatrix} \cos(2 \cdot L / b) & \frac{2}{b} \cdot \sin(2 \cdot L / b) \\ -\frac{2}{b} \cdot \sin(2 \cdot L / b) & \cos(2 \cdot L / b) \end{bmatrix} \quad (4.3)$$

The focal length,  $f$ , of a medium described by the characteristic ABCD matrix is given by  $f = -1/c$ , where  $c$  is the third matrix element. Using the index variation described by 4.2 and applying the small angle approximation, the following expression is obtained.

$$\frac{-1}{c} = \frac{n_0 \cdot w_0^2}{4 \cdot n_2 \cdot I_0 \cdot L} \quad (4.4)$$

When the air to dielectric interfaces are included the following expression is obtained for the Kerr lens<sup>5,22</sup>.

$$f_{Kerr} = \frac{w_0^2}{4 \cdot n_2 \cdot I_0 \cdot L} \quad (4.5)$$

For the parameters shown in Table 4.4, assuming a peak intensity of  $3.06 \times 10^7 \text{ W cm}^{-2}$ , corresponding to a 6 ps FWHM pulse duration, the calculated focal length of the Kerr lens was 32 m. The Kerr lensing ABCD matrix model<sup>13</sup> starts with the beam waist for the c.w. case and uses this to calculate a first solution for the Kerr lens, which is refined during successive iterations (trips around the cavity) until the solution converges. The calculated size change caused by this Kerr lens is a 0.5 % decrease in the beam waist in the rod. Although the Kerr lens is weak, because of the unusual cavity design with the relatively weak focusing mirror, it does have some influence. This modelled 0.5 % change in mode size is small compared to that seen in other KLM lasers; a change in the beam waist of 1.9 % was modelled in a KLM diode-pumped Nd:YAG laser by Lui et al<sup>22</sup>. Some of the parameters of the Nd:YLF laser, such as the exact cavity length, are only estimated to an accuracy of +/-5 cm, the amount of self-focusing may therefore be underestimated. Fig 4.9 shows that a 5 cm shift in the mirror, from the assumed position causes a significant effect and enhances the Kerr lensing, giving an enhanced mode

waist change  $\delta w/w$  of 1.5 %.

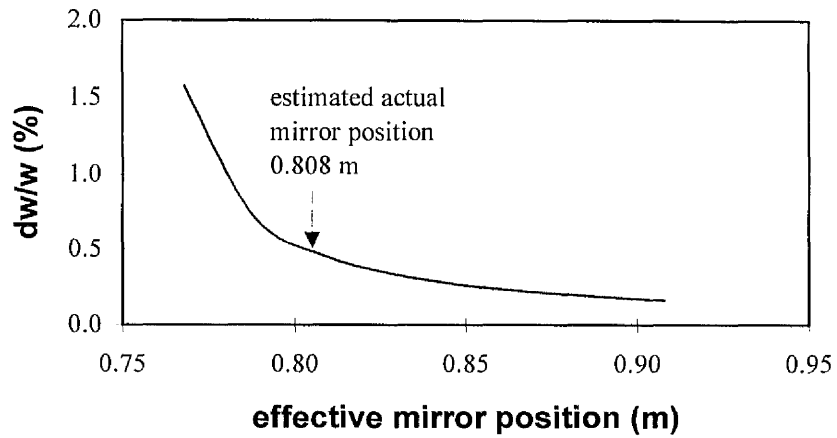


Fig. 4.9 Kerr induced change in the beam waist in the rod, for various curved mirror positions.

In the next section it is also shown that thermal lensing in the rod, plays a significant role in this particular laser cavity, and its effects should not be ignored.

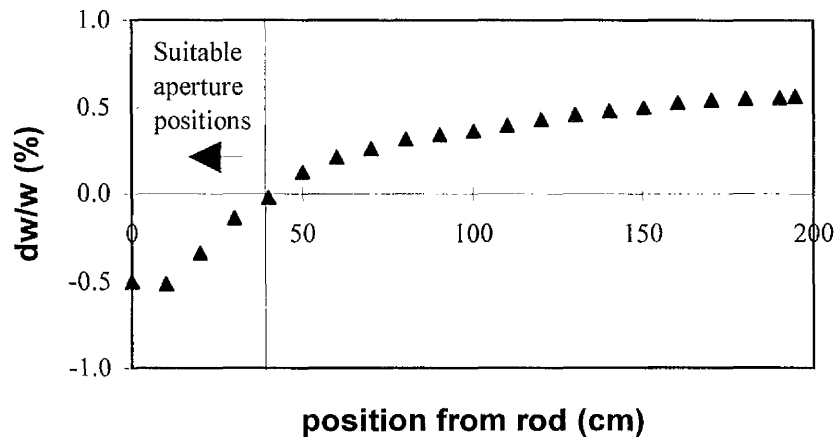


Fig. 4.10 Calculation of the Kerr lens induced change on beam size across the cavity.

One method of promoting KLM would be to include a hard aperture in the cavity. This was experimented with, but despite the systematic trial of a variable width slit in various cavity positions, no improvement in KLM operation was observed. The ABCD matrix model was used to map suitable positions in the cavity, for the inclusion

of a slit, that is, positions where the beam waist is reduced because of self-focusing. Fig. 4.10 illustrates the results of this analysis. Suitable positions are close to the laser rod, with the beam showing the biggest reduction in size inside the rod. This explains why the experimental trials with an adjustable slit failed; it was impossible to place the slit in the optimum position, next to the laser rod, as this position was occupied by the phase modulator.

To conclude, in this section it has been shown that the Kerr lensing behaviour is explained if the  $\text{LiNbO}_3$  is considered as the Kerr medium. This is a peculiarity which is specific to this laser, because of its unusual cavity design with the modulator adjacent to the rod and the long cavity length. This gives a small beam waist in the modulator, which results in significant self-focusing. The analysis also shows that the optimum position for an aperture would be in the rod, leading to the conclusion that the effective aperture in the cavity is a 'soft' aperture in the rod, or possibly the phase modulator which is nearby. The ABCD matrix model with the estimated cavity parameters gives a 0.5 % reduction in the mode size due to the Kerr lens, although it should be noted that the cavity lengths are only roughly known to within  $\pm 5$  cm, from measurement and the mode size variation may lie in the range 0.2-1.5 % if the outer limits of the measurement uncertainty are taken. This small variation may explain why the KLM was not self-starting and would not continue after the r.f. power to the phase modulator was switched off. In order to promote KLM, without redesigning the laser, the position of the curved mirror should be moved closer to the rod, nearer the instability limit. This would however alter the beam waist in the rod, reducing the pumping efficiency.

#### **4.35 Thermal lensing effects and an improved Nd:YLF laser system**

The diode-pumped Nd:YLF laser system, described above, showed a number of improvements over traditional flashlamp-pumped Nd:YAG systems, notably in the area of reduced amplitude fluctuations. However, there were a number of problems with the system, in particular the uncontrollable nature of the KLM and a stability problem that was attributed to thermal effects in the laser rod, following analysis and discussions with the laser manufacturers. This stability problem manifested itself primarily when the

laser was operating mode-locked, if left unattended the pulses would tend to broaden as the cavity length drifted. This occurred within a time frame of minutes, in order to produce useful pulsewidths when either FM mode-locked or KLM the cavity required continual adjustment. These problems are now analysed and some solutions are suggested.

The laser in its present configuration presents several problems for controllable KLM operation, in particular the dual function of the LiNbO<sub>3</sub> (as the Kerr medium and phase modulator) and the beating between the oscillator frequency and KLM oscillation frequency. The previous stability analysis has suggested that to enhance KLM the curved mirror should be moved closer to the rod. An alternative solution would be to rearrange the cavity, moving the phase modulator to a position in the cavity where the beam size is larger, and so less self-focusing would occur. This would allow another Kerr material, such as an appropriate Schott glass<sup>20</sup>, to be employed as the Kerr medium. A hard aperture could then be included, in a suitable position. Finally to prevent the beating problems a regenerative technique<sup>23</sup> could be employed, actively adjusting the cavity length to phase-lock the KLM frequency to a reference oscillator.

Alternatively the KLM could be abandoned altogether and FM mode-locked operation used. To remove the tendency of the laser to KLM would also require the removal of the phase modulator to a position in the cavity with a larger beam size.

Material	Parameter	Value	Reference
Nd:YAG	K, thermal conductivity	14 W m <sup>-1</sup> K <sup>-1</sup>	19
Nd:YAG	dn/dT,	7 x 10 <sup>-6</sup> K <sup>-1</sup>	19
Nd:YLF	K, thermal conductivity	6 W m <sup>-1</sup> K <sup>-1</sup>	19
Nd:YAG	dn <sub>o</sub> /dT, ordinary axis	-2 x 10 <sup>-6</sup> K <sup>-1</sup>	19
	dn <sub>e</sub> /dT, extraordinary axis	-4 x 10 <sup>-6</sup> K <sup>-1</sup>	

Table 4.5 Thermal properties of Nd:YAG and Nd:YLF.

One remaining problem with the Nd:YLF laser was an instability caused by pump induced thermal focusing in the laser rod. These instabilities occur because small

fluctuations in the thermal focal length result in corresponding beam waist size fluctuations. Thermal focusing is more commonly a problem in Nd:YAG, which is one of the worst mediums for thermal lensing <sup>5</sup> and usually it is necessary to account for these thermal effects in the cavity design. The key thermal properties of both Nd:YAG and Nd:YLF are shown in Table 4.5 above. According to the laser manufacturers, thermal effects were not included when the Nd:YLF laser cavity used here was designed.

There are several possible thermal effects <sup>17,24-26</sup> involved: the thermal gradients and constraining of the rod can result in stress birefringence, the length of the rod will vary in width with thermal expansion as the temperature will vary from the rod centre to edge and finally there is the pump induced temperature change in the rod which in turn changes the refractive index. Here we consider only the thermal lensing due to the pump induced index changes, as this is usually the most significant effect. With this pumping geometry a quadratic temperature distribution is expected over the pumped area with a logarithmic distribution over the remaining area of the rod. If uniform heating is assumed over the pump beam area, the effective thermal lens is given by <sup>24,26,27</sup>,

$$f_{th} = \frac{2 \cdot \pi \cdot K \cdot w_o^2}{\frac{dn}{dt} \cdot \alpha \cdot P} \quad (4.6)$$

where  $w_o$  is the radius of the pump beam,  $\alpha$  is the fraction of pump power absorbed,  $P$  is the pump power,  $K$  and  $dn/dt$  are thermal parameters as described in the table above. Note that Equation 4.6 is similar to the expression for the thermal lens where the entire rod is pumped uniformly <sup>17</sup>, except that  $w_o$  would be by the rod radius. If we assume that 20 % of the pump power is absorbed, resulting in heat generation and a pump radius of 300  $\mu\text{m}$ , a thermal lens of focal length 1.06 m is obtained. Because  $dn/dt$  is negative in Nd:YLF the thermal lens caused defocusing. Including this thermal lens in the ABCD matrix model results in a large change in beam waist, 397  $\mu\text{m}$  including the thermal lens compared to 307  $\mu\text{m}$  without.

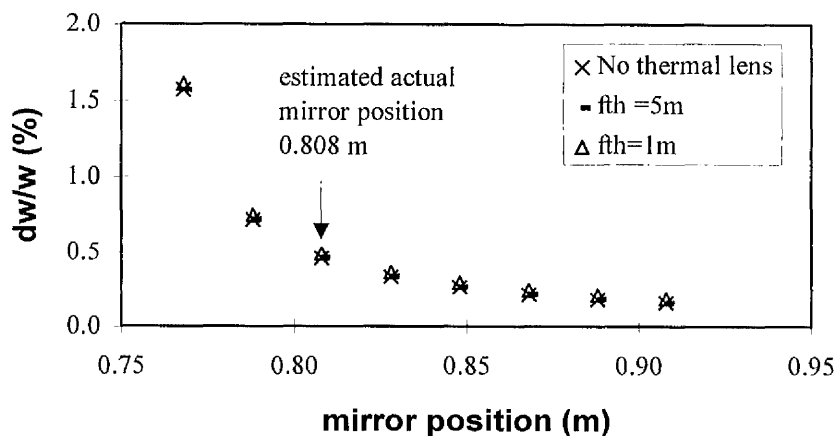


Fig. 4.11 The effect of a range of assumed values of thermal lens on the self-focusing. Little difference is observed.

Fig. 4.11 shows that although the thermal effects tend to move the cavity closer towards the instability limit, which would be likely to favour KLM, little difference in the fractional change of the beam waist in the rod,  $\delta w/w$ , is observed as thermal defocusing tends to increase the mode radius in the rod, which leads to a weaker Kerr lens.

It is difficult to reduce thermal lens variations in lasers to less than 1 %<sup>5</sup>. In order to provide stable KLM the cavity should be designed so that  $\delta w_{\text{thermal}}$ , the thermally induced beam size variation at the aperture is small. In this cavity this is not the case as the Kerr medium and soft aperture in the laser rod are close together. One method of reducing the laser's sensitivity to these fluctuations would be to reduce its cavity length and therefore employ a stronger focusing curved mirror. Another alternative would be to design a more complicated cavity, with additional mirrors which minimised susceptibility to thermal lens changes.

The Nd:YLF laser was one of the first prototype lasers supplied by Microlase Optical Systems and it was designed to mode-lock at 77 MHz corresponding to a cavity length of 1.948 m, as this is a similar repetition rate to that of traditional lamp-pumped systems. Later systems from Microlase<sup>28</sup> used a shorter cavity of 1.23 m which corresponds to a 122 MHz repetition rate. One effect of reducing the cavity length is that a 'stronger' focusing mirror is required, this means the cavity is less susceptible to the effects of the thermal lens and mirror angular misalignment<sup>6</sup>. Using the ABCD matrix model, a possible shorter cavity was designed, which could employ a 75 cm

ROC curved mirror located 55 cm from the rod. The sensitivity to length variations of the thermal lens was calculated for the existing YLF cavity and the proposed shorter cavity, assuming a thermal lens of focal length 1.06 m, as calculated. Figs 4.12 and 4.13 show the calculated variations in the beam waist for small variations in the length of the thermal lens. The gradient of Fig. 4.13 is much shallower indicating much better resistance to thermal variations. For example, the ABCD analysis shows that the present cavity shows a beam waist variation of 2.5 % for a 5 % change in the thermal focal length whilst the proposed shorter cavity design shows only a 0.07 % change. The analysis also shows that the inclusion of the calculated thermal lens in the present Nd:YLF cavity moves nearer to the instability boundary.

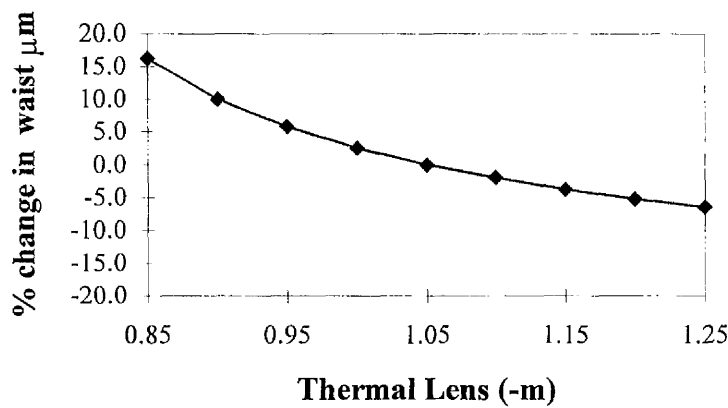


Fig. 4.12 Beam waist variation with thermal lens length variation for the present Nd:YLF cavity.

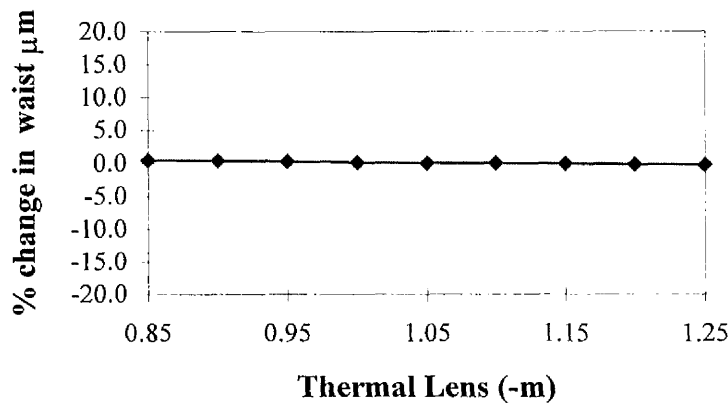


Fig. 4.13 Beam waist variation with thermal lens length variation for a proposed shorter laser cavity.

The ABCD matrix stability parameter,  $m=(a+b)^2/4$  is 0.85 without inclusion of the thermal lens and 0.94 with the lens. Here a value greater than one represents an unstable cavity. The pushing of the cavity nearer the instability limit by the thermal lens shows that it can make a significant impact. The proposed smaller cavity, because it is in the centre of the stability region, will not suffer these problems.

## 4.4 F-centres

Certain alkali halide F-centres (or colour centres) can be used to create broadly tuneable lasers<sup>29-31</sup>. Using a suitable range of hosts, laser action can be provided across a wide portion of the infra-red spectrum. These lasers are homogeneously broadened, mainly through the strong coupling of the F-centres to the surrounding crystal lattice and its phonons. This provides a wide pump and gain bandwidth, offering the potential for short pulse formation.

F-centres are formed when defects are introduced into alkali halide crystals. The simplest case is the F-centre, where an electron trap is produced when a halide ion vacancy is introduced into the lattice, as illustrated in Fig. 4.14(a). Another case, shown in Fig. 4.14(b), is called the  $F_2^+$  centre and occurs when a single electron is trapped by adjacent halide vacancies.

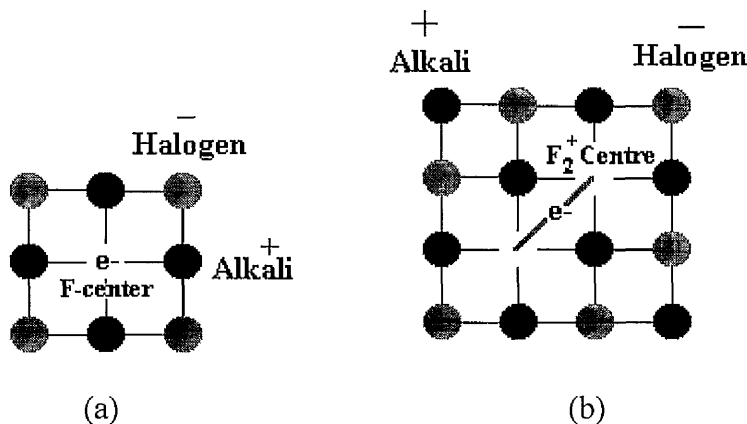


Fig. 4.14 F-centre defects a) left, the simple F centre, an electron trapped by an anion (halide ion) vacancy and b) right, the  $F_2^+$  centre produced by two adjacent vacancies.

The pumping cycle of the system <sup>30</sup>, as illustrated in the energy level diagram of Fig. 4.15, is a four-step process. The first step occurs when an electron absorbs radiation, raising it from the ground state to one of the p-like higher states. Upon excitation the system rapidly relaxes and following an interaction with a lattice phonon, there is a corresponding adjustment of the wavefunction and the ground state effectively rises. The system is now in the relaxed-excited state (RES). This interaction with a lattice phonon leads to a Stokes shift between the absorption and emission bands. The remaining steps are radiative emission, after which the system returns back to its normal configuration through phonon emission.

The simple F-centre is of little use in lasers, and although the  $F_2^+$  centre does lase, more useful laser materials can be produced through the introduction of lattice impurities. These impurities offer several advantages, in producing new tuning ranges, pump bands and improving the shelf life of the materials. There are two types of important laser centres which use introduced impurities, the  $F_A(II)$  centre, where a halide ion vacancy containing a trapped electron is adjacent to an introduced impurity metal ion. The other F-centre is the  $F_B(II)$  centre in which two impurities are present. Fig. 4.15 shows the normal and relaxed state of the  $F_A(II)$  centre.

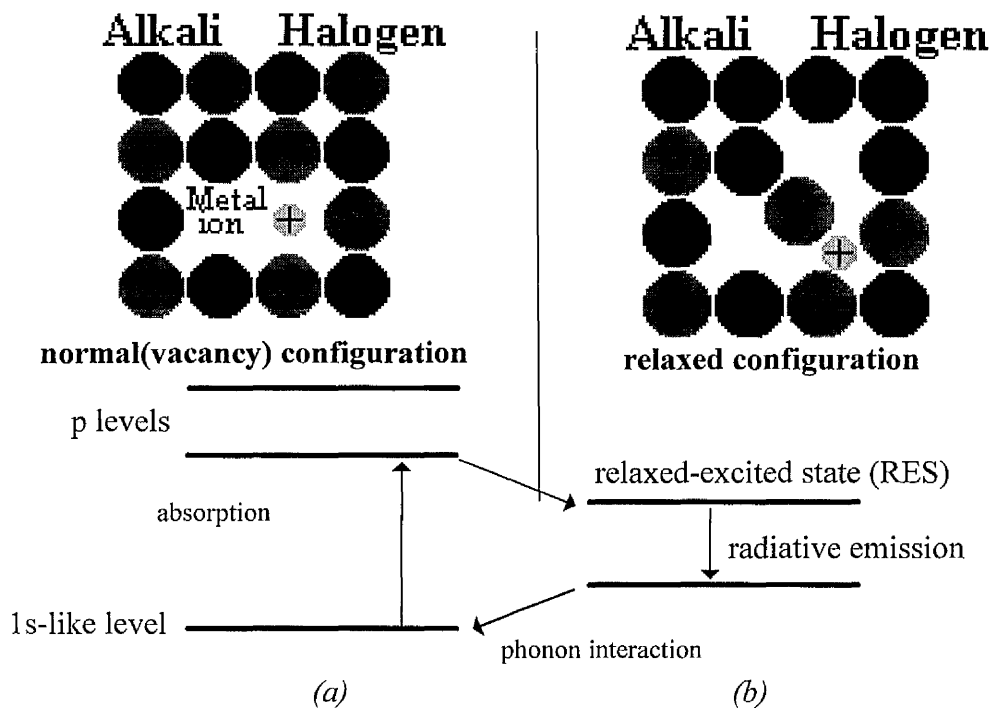


Fig. 5.15 Configuration of  $F_A(II)$  centre and typical F-centre associated energy levels for a) the normal configuration and b) the relaxed excited state.

The use of F-centres has several associated problems.  $F_2^+$  centres have a limited shelf life. Over time orientational bleaching occurs, in which the axis of the centre becomes rotated, consequently reducing pump efficiencies. It is possible to reduce this using multi-wavelength pump schemes<sup>31</sup> and low temperatures to slow down these effects. Even so, there is still a tendency for the centres to move through the crystal and eventually aggregate, becoming non-laser-active. The association of impurity ions in the  $F_A(II)$  centre tends to anchor and stabilise the defects. However, to increase longevity the crystals are usually stored and operated at liquid nitrogen temperatures (77 K) and kept in the dark. Operation at cold temperatures also increases the quantum efficiency of luminescence.

F-centre formation<sup>31</sup> is a complicated process that needs to be precisely controlled in order to produce crystals of high optical quality. The process usually used to produce laser active centres involves several main steps. First a crystal with an appropriate impurity concentration is grown, simple F-centres are then created by additive coloration or radiation damage. The additive coloration process involves placing the crystal in a vapour of the alkali metal, which diffuses into the crystal. In certain crystals the additive coloration process is not suitable, then a radiation damage process, usually an electron beam, is used. This is done at low temperatures typically  $-100^\circ\text{C}$  to prevent aggregation of the defects. The F-centres are then ionised by a brief exposure to light. The crystals are then heated close to room temperature to aggregate the defects into laser active centres. The creation of centres with impurity ions is a slightly more complicated process.

The F-centre laser employed in this project used KCl:Tl crystals supplied by the University of Utah, which were produced by the irradiation process.

#### **4.41 KCl:Tl F-centre**

KCl:Tl lasers are broadly tuneable around  $1.5\ \mu\text{m}$ , have a large gain bandwidth capable of supporting pulses of subpicosecond duration and compared to other laser sources around  $1.5\ \mu\text{m}$  they offer more flexibility. A laser with a similar wavelength range is the NaCl:OH F-Centre<sup>32</sup>, but this is slightly more complicated as the F-centres require

pumping at an additional wavelength to reorientate the axis of the laser centre. NaCl:OH offers the advantage of a longer shelf life as the OH ions stabilise the defects unlike in KCl:Tl which fades over a period of months.

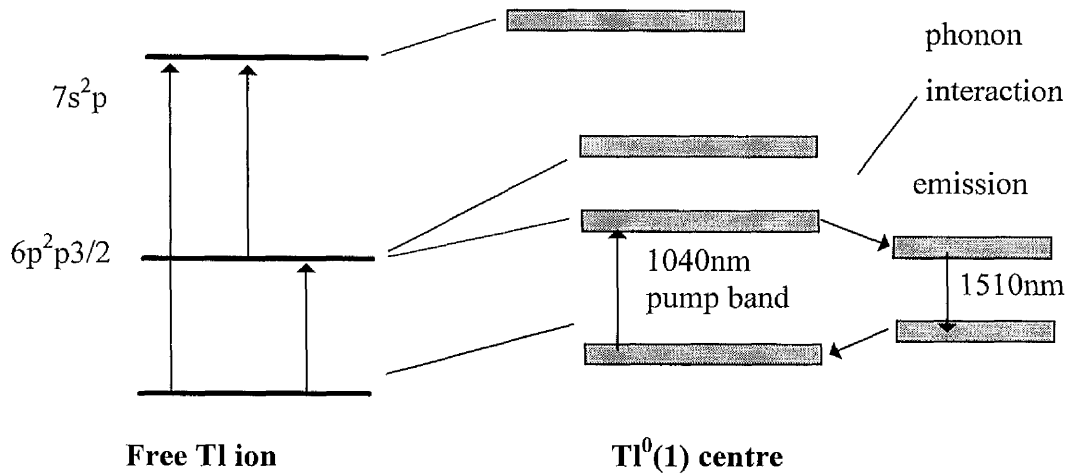


Fig. 4.16 Energy levels of an isolated thallium ion and the Tl<sup>0</sup>(1) centre.

The KCl:Tl F-centre consists of a neutral thallium ion Tl<sup>0</sup> adjacent to a halogen vacancy<sup>33,34</sup> in a KCl salt crystal. The energy levels of this system are closely related to those of an isolated thallium ion because the electron is localised at the thallium ion. However, the neighbouring lattice alters the energy levels somewhat, Fig. 4.16, above, shows the comparison between the energy levels for thallium and the Tl<sup>0</sup>(1) centre<sup>35</sup>. As illustrated the pump band is around 1040 nm, suitable for pumping with neodymium ion based lasers and the maximum luminescence is centred at 1510 nm. Other important parameters of KCl:Tl are a relatively long upper state lifetime of 1.6 μs and a luminescence FWHM of 150 nm.

#### 4.42 Experimental KCl:Tl laser system

The main component of the laser system was a St. Andrews University built liquid nitrogen cryostat, shown in Fig. 4.17, which keeps the laser crystal cold, prolonging its useful life. The cryostat cooled the crystal via a cold finger assembly which was connected to the liquid nitrogen chamber, a needle valve controlled whether the nitrogen was connected to the cold finger or not. In order to prevent high rates of liquid nitrogen

evaporation there is a vacuum jacket around the nitrogen chamber, so in this sense the cryostat was like a large Thermos flask. The vacuum in the jacket was maintained for long periods of time using a SORB pump. This was a type of sorption or getter pump which operates by the absorption and trapping of gas molecules at low temperatures in an 'active' material in the pump. Unlike other similar systems, the crystal chamber just contains the crystal assembly and not any of the cavity mirrors. A three-way valve allowed the crystal chamber to be evacuated and in normal operation it was connected to the vacuum space inside the jacket. Fig. 4.18 shows the area around the laser head. Two Brewster windows allowed access to the chamber in which a vacuum was maintained. The crystal was also positioned at the Brewster angle. The cryostat maintained the temperature of the cold finger for up to 36 hours without needing to be refilled. However after long periods of use, about six months, the SORB pump became saturated and cold spots and condensation were produced on the cryostat.

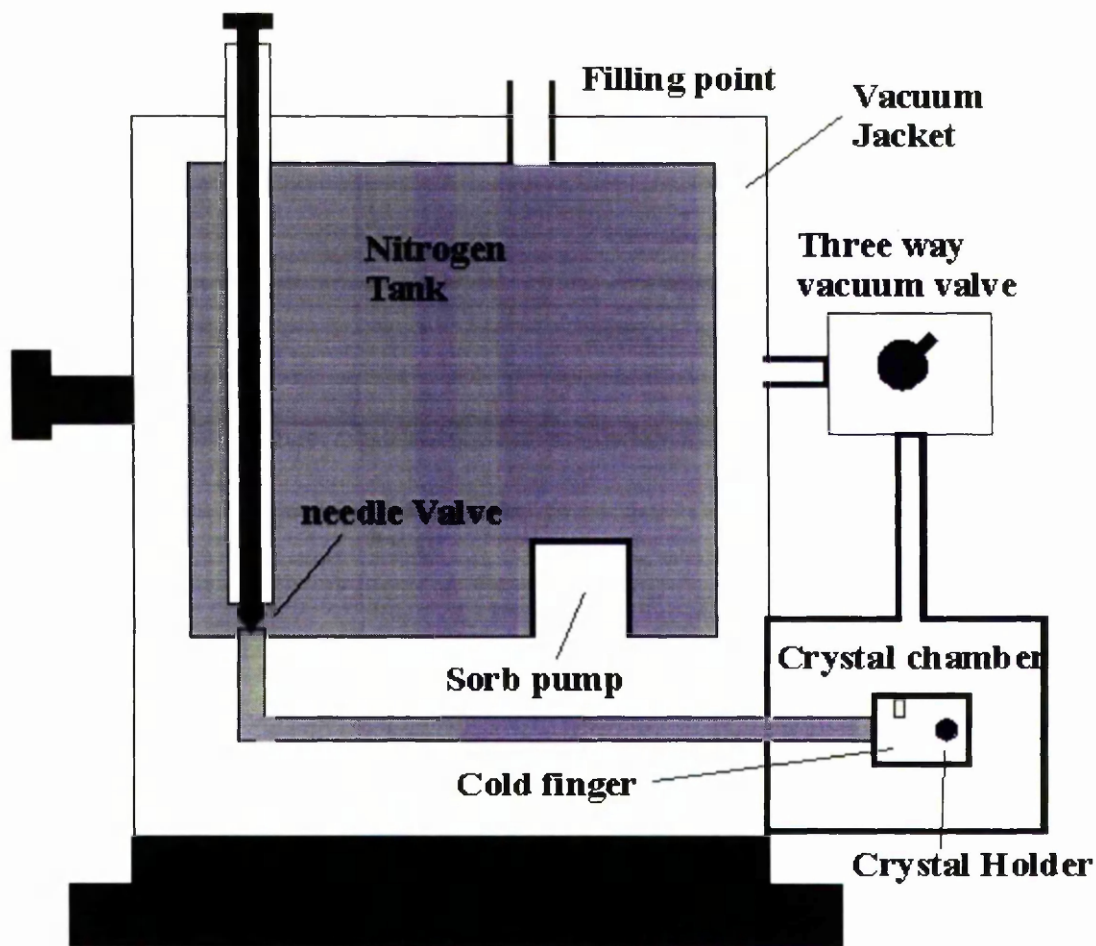


Fig. 4.17 A simplified diagram of the F-centre laser cryostat.

This was a sign that the SORB pump needed to be regenerated, which was done by either heating the SORB pump or by pumping out the jacket area for a period of two days. The crystal was first removed and the nitrogen left to evaporate.

A diagram of the laser cavity and pumping arrangement is shown in Fig. 4.19. The five mirror cavity used was similar to established dye laser cavities, the pump laser was the Nd:YLF as described previously. There was a slight offset between the pump and lasing axes and with careful alignment it was possible to avoid feedback into the pump laser from the 45 degree mirror. The two focusing mirrors around the laser head provided a small beam waist of around  $30\ \mu\text{m}$  within the crystal. The additional 1m ROC mirror positioned 0.5 m from the output coupler improved the cavity stability when the cavity is extended for synchronously pumping. Tuning was via a birefringent filter. For synchronously pumping, the cavity length was adjusted to that of the Nd:YLF pump laser via a translation stage on the output coupler, until short pulses were obtained.

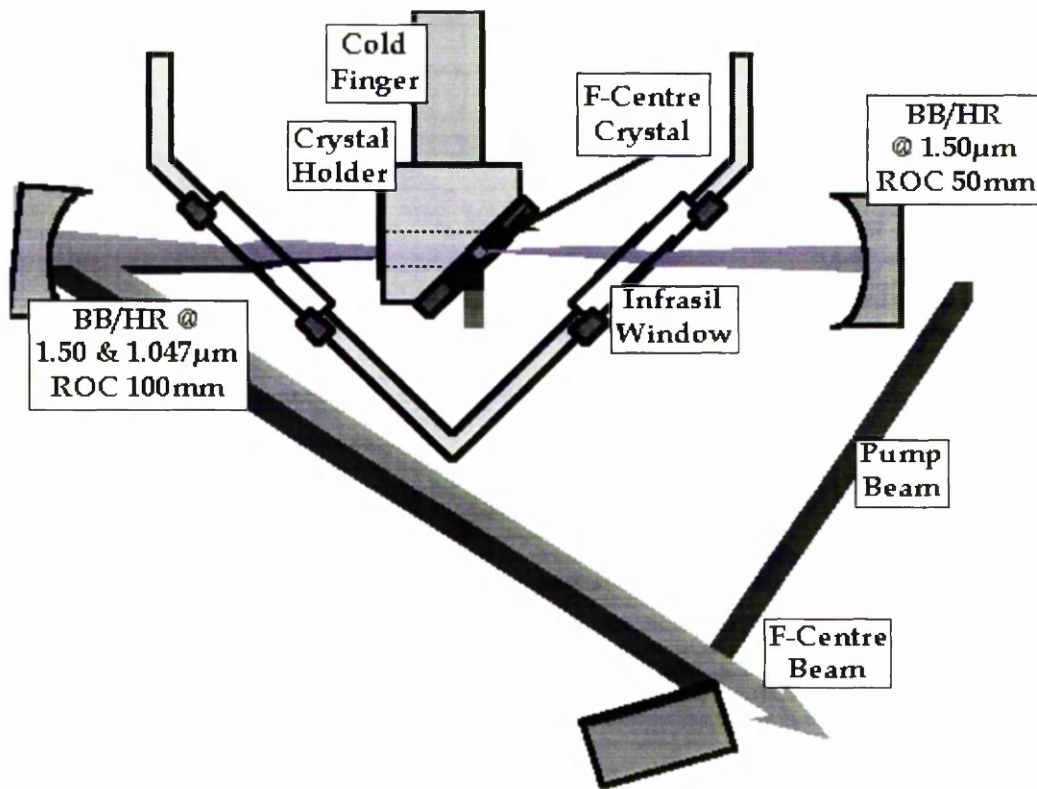


Fig. 4.18 F-centre laser cryostat crystal chamber showing pump and lasing

beams.

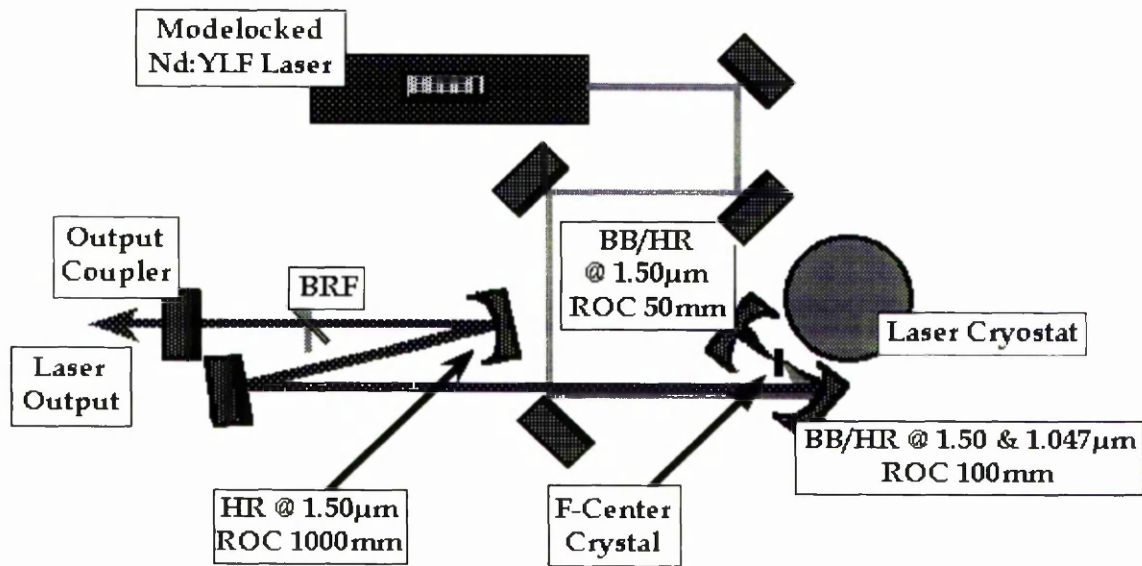
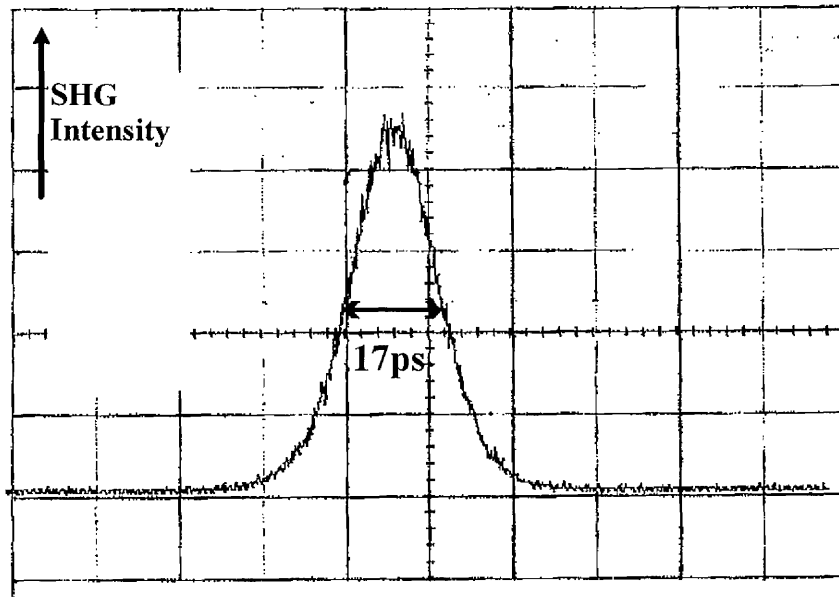


Fig. 4.19 Synchronously pumped F-centre cavity and pumping arrangement.

The KCl:TI laser<sup>1</sup> produced powers of 200 mW when operated c.w. or pulsed (for a new good quality crystal) at 1.5  $\mu\text{m}$  for 2 W pump power. A 25 % output coupler was found to provide the maximum output power. Threshold was obtained for around 200 mW pump power. The tuning range was in excess of 100 nm around 1.5  $\mu\text{m}$ . It was noticed that by introducing an aperture into the Nd:YLF cavity an improvement in F-centre power could often be obtained, this may be because the aperture produces a more compact pump beam in the F-centre crystal which overlaps more efficiently with the F-centre beam waist. When mode-locked, through synchronously pumping, the laser produced pulses at best of 10 ps FWHM when pumped with a 30 ps pump pulse and 4 ps when pumped with a 6 ps pulse. The autocorrelation of the FM mode-locked system is shown in Fig. 4.20. As the laser wavelength was tuned away from its maximum power an increase in pulsewidth was observed. This occurs because KCl:TI has a relatively small gain cross section, for an F-centre, and the radiative decay time is long compared to the time between pulses, intense pump pulses and high intracavity power are required for the shortest pulses. When required c.w. operation was achieved by switching off the mode-locker in the Nd:YLF, which caused little beam misalignment because of the low powers involved, or adjusting the F-centre cavity length such that

pulses were no longer observed.



*Fig. 4.20 Autocorrelation of F-centre when synchronously pumped with the FM mode-locked YLF. Autocorrelation FWHM 17p, Pulsewidth FWHM 11 ps. Pulsewidth durations of 4ps FWHM for were achieved when the pump laser was KLM.*

#### 4.43 Future work- improved KCl:Tl laser system

In this section a description of the coupled-cavity or additive-pulse arrangement for producing subpicosecond pulses is given. Finally suggestions for improving the present KCl:Tl laser system are put forward and discussed.

Although the synchronously pumped laser produced pulses as short as 4 ps, shorter subpicosecond pulses would be desirable for nonlinear investigations. One recently developed mode-locking technique that has been successfully applied to F-centre lasers is additive-pulse or coupled-cavity mode-locking<sup>36-41</sup> as outlined in Table 4.3. This technique employs a nonlinear element in a subsidiary cavity, an optical fibre is most often used. When the length of the subsidiary cavity is correctly adjusted, pulse shortening occurs as the SPM of the subcavity pulse causes it to combine constructively with the centre of the pulse from the main cavity and destructively with the wings. In KCl:Tl lasers coupled cavity mode-locking is usually not self-starting<sup>37,40</sup>, but is usually initiated through synchronously pumping.

The coupled-cavity mode-locking of the KCl:TI laser was briefly investigated in the Michelson configuration<sup>40</sup>. The cavity arrangement used is illustrated below.

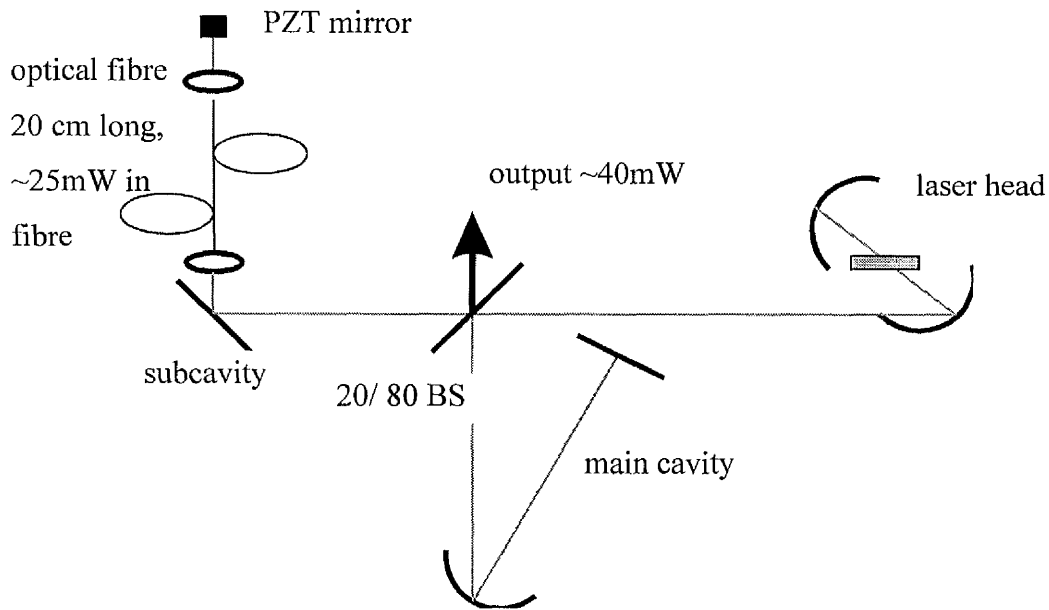


Fig. 4.21 Coupled-cavity arrangement used.

A 20cm long piece of Corning dispersion-shifted fibre was used in the subsidiary cavity. Index-matching gel was used to remove back-reflections from the fibre ends and its performance monitored by verifying that synchronous pumping was not degraded when the secondary cavity was unblocked, allowing light to couple into the fibre but blocking the return beam. A power of 25 mW was coupled into the fibre and a coupling ratio of 8:2 was used between the main and subcavities. Coupled-cavity mode-locking was initiated by monitoring the spectrum from the main cavity and adjusting the subsidiary cavity until substantial spectral broadening was observed. A spectrum of 6 nm FWHM was observed, as shown in Fig. 4.22. However coupled-cavity mode-locking could only be maintained for a few seconds and although short autocorrelations were observed there was insufficient time to capture the autocorrelations before coupled-cavity operation stopped.

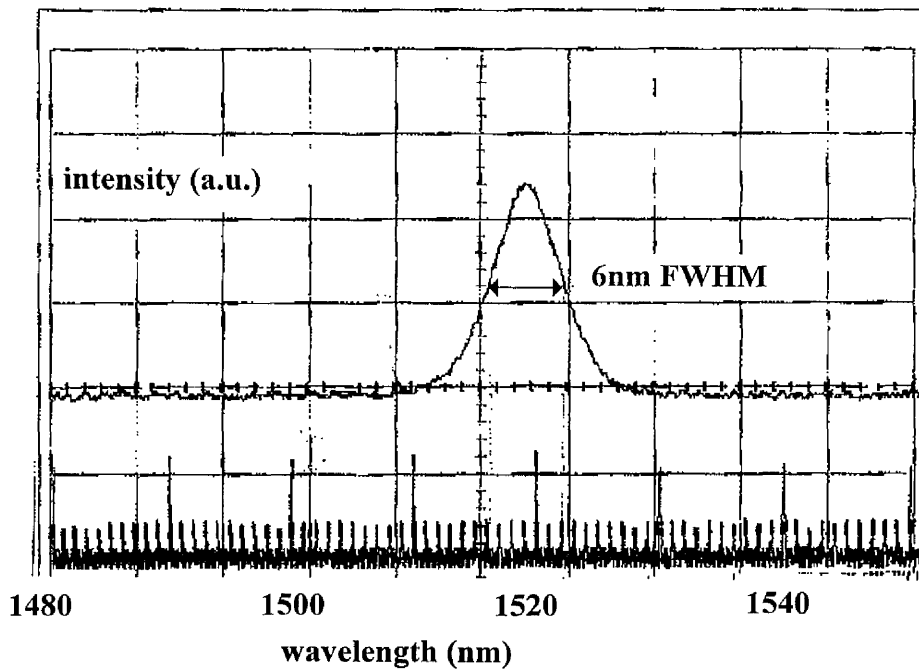


Fig. 4.22 Output spectrum of the coupled-cavity F-centre laser. The FWHM is 6nm. The trace below the spectrum is a reference output, from the spectrum analyser used, which is used to give the horizontal wavelength calibration.

A feedback system<sup>36</sup> was available to control the length of the subcavity but short pulse operation could not be sustained long enough to allow it to be used. The instability of the coupled-cavity mode-locking was attributed to the peak powers of the synchronously pumped pulses just being on the edge of the powers required to initiate the process. The tell tale signature of short pulse operation, spectral broadening, could only be obtained when both the pump and F-centre lasers were carefully optimised for maximum power. There was insufficient time to experiment with different configurations of fibre length and coupling ratios. If a time bandwidth product  $\delta t \cdot \delta f = 0.3$  is assumed for a sech squared pulse shape<sup>40</sup>, the obtained spectrum of FWHM 6 nm gives a  $\delta f = 790$  GHz, which suggests that a pulse width of  $\sim 380$  fs was obtained with the coupled cavity configuration.

As mentioned in Section 4.33 there were a number of problems with the Nd:YLF system used to pump the F-centre and this obviously reflects on the F-centre laser's performance. One solution offered was to reduce the length of the Nd:YLF cavity until

its repetition rate was around 120 MHz, which would require a corresponding decrease in the F-centre cavity length. Changing the cavity length would affect the mode waist inside the crystal and, if cavity stability were not to be sacrificed<sup>36</sup>, through the removal of the 1 m curved mirror, a slightly different curved mirror ROC or position should be employed.

## **4.5 Conclusions**

An all-solid state KCl:Tl F-centre laser system was developed, which was to our knowledge the first diode-pumped F-centre to be demonstrated. The system consisted of a diode-pumped Nd:YLF laser which was FM mode-locked and in turn synchronously pumped the F-centre. The pump laser showed comparable performance to flashlamp-pumped Nd:YAG lasers, with the advantages of smaller size and reduced noise that are products of diode-pumping and the use of Nd:YLF as the gain medium. The Nd:YLF laser is capable of producing shorter pulse durations because of the greater linewidth of Nd:YLF compared to Nd:YAG.

The laser, if suitably adjusted, would KLM producing pulses of 6 ps FWHM. This KLM operation has been attributed to the unusual cavity design with the LiNbO<sub>3</sub> phase modulator forming the Kerr medium. ABCD matrix calculations have shown that the Kerr lensing is weak, explaining why it did not continue without being driven by the r.f. signal on the phase modulator and why the KLM was not self-starting. These calculations also confirm that the optimum position for an aperture to promote KLM is at the laser rod and they indicate why experiments with an adjustable slit failed.

Whilst the Nd:YLF system showed ~1 % noise variation when operated c.w., a stability problem, attributed to the thermal lensing in the rod, limited the performance of the laser. Calculations show that the thermal lens moves the cavity nearer the instability limit, meaning that small fluctuations in the length of the thermal lens can lead to significant changes in beam waist. These thermal instabilities proved significant in limiting the performance and potential of the laser system.

Several suggestions are made to improve the laser cavity either by promoting KLM or by utilising FM mode-locking but significant cavity changes are required. A

shorter length cavity is shown to be less susceptible to thermal lens variations and would produce a resonator less sensitive to mirror angular variation.

This system with its broad tuning range and capability for short pulse generation is ideal for investigations into devices for telecomms applications at the long wavelength window around 1.5  $\mu\text{m}$ . In the next chapter the system has been used to investigate the linear and nonlinear properties of InP/ InGaAsP laser amplifiers.

## **References**

- 1 C. J. Hamilton, "Novel structures and fabrication techniques for the observation of solitons in AlGaAs", Ph.D thesis, University of Glasgow, 1995
- 2 G. P. A. Malcolm, A. I. Ferguson, "Mode-locking of diode laser pumped solid state lasers", *Optical and Quantum Electronics*, vol. 24, p. 705, 1992
- 3 P. A. Malcolm, M. Ebrahimzadeh, A. I. Ferguson, "Tuneable all-solid-state laser sources", *IEEE Journal of Quantum Electronics*, vol. 28, no. 4, p. 1170, 1992
- 4 Laporta, M. Brussard, "Design criteria for mode size optimisation in diode-pumped solid state lasers", *IEEE Journal of Quantum Electronics*, vol. 27, no. 10, p. 2319, 1991
- 5 Chung, A. E. Siegman, "Optical-Kerr-enhanced mode-locking of a lamp-pumped Nd:YAG laser", *IEEE Journal of Quantum Electronics*, vol. 31, no. 3, p. 582, 1995
- 6 W. Koechner, "Solid state laser engineering", Chapter 5, 9, Springer, 5th ed., 1999
- 7 U. Keller, "Ultrafast all-solid-state laser technology", *Appl. Phys. B*, vol. 58, p. 347, 1994
- 8 E. P. Ippen, "Principles of passive mode-locking", *Appl. Phys. B*, vol. 58, p. 159, 1994
- 9 L.F Mollenauer, R. H. Stolen, "The soliton laser", *Optics Letters*, vol. 9, p. 13, 1984
- 10 D. E. Spence, P. N. Kean, W. Sibbett, "60fs pulse generation from a self-mode-locked Ti:sapphire laser", *Optics Lett.*, vol. 16, p. 42, January 1991
- 11 D. Huang, M. Ulman, L. H. Acoli, H. A. Haus, J. G. Fujimoto, "Self-focusing-induced saturable loss for laser mode-locking", *Optics Lett.*, vol.17, no. 7, p. 511, 1992
- 12 Y. Chen, X. Zheng, T. Lai, X. Xu, D. Mo, W. Lin, "Resonators for self-mode-locking Ti:sapphire lasers without apertures", *Optics Lett.*, vol.17, no. 7, p. 511, 1992
- 13 V. Magni, G. Cerullo, S. De Silvestri, "Closed form gaussian beam analysis of resonators containing a Kerr medium for femtosecond lasers", *Optics Comm.*, vol. 101, p. 365, 1993

- 14 A. Yariv, "Quantum electronics", John Wiley, 3rd ed., 1989, Chapter 6
- 15 H. Kogelnik, "Imaging of optical modes-resonators with internal lenses", The Bell System Technical Journal, p. 455, March 1965
- 16 A. E. Siegman, "Lasers", Oxford University Press, 1986, Chapters 14-23
- 17 D. R. Hall, P. E. Jackson, "The physics and technology of laser resonators", Adam Hilger / IOP publishing, 1989, Chapter 11
- 18 M. J. P. Dymott, A. I. Ferguson, "Self-mode-locked diode-pumped Cr:LiSAF laser", Optics Lett., vol.19, no. 23, p. 1988, 1994
- 19 N. Nikogosian, "Handbook of properties of optical and laser related materials", Wiley, 1997
- 20 R. Lincoln, A. I. Ferguson, "All-solid-state self-mode-locking of a Nd:YLF laser", Optics Lett., vol.19, no. 24, p. 2119, 1994
- 21 G. P. A. Malcolm, A. I. Ferguson, "Self-mode-locking of a diode-pumped Nd:YLF laser", Optics Lett., vol. 16, no. 24, p. 24, 1991
- 22 X. Lui, C. J. Flood, D. R. Walker, H. M. Van Driel, "Kerr lens mode-locking of a diode-pumped Nd:YAG laser", Optics Lett., vol. 17, no. 19, p. 1361, 1992
- 23 J. W. Rodwell, D. M. Bloom, K. J. Weingarten, "Subpicosecond laser timing stabilisation", IEEE Journal of Quantum Electronics, vol. 25, no. 4, p. 817, 1989
- 24 D. Welford, D. M. Rines, B. J. Dinerman, R. Martinsen, " Observation of enhanced thermal lensing due to near gaussian pump energy deposition in a laser-diode side-pumped Nd:YAG laser", IEEE Journal of Quantum Electronics, vol. 28, no. 4, p. 1075, 1992
- 25 A. K. Cousins, "Temperature and thermal stress scaling in finite-length end-pumped laser rods", IEEE Journal of Quantum Electronics, vol. 28, no. 4, p. 1057, 1992
- 26 S. C. Tidwell, J. F. Seamans, M. S. Bowers, A. K. Cousins, "Scaling c.w. diode-end-pumped Nd:YAG lasers to high average powers", IEEE Journal of Quantum Electronics, vol. 28, no. 4, p. 997, 1992
- 27 J. Frauchinger, P. Albers, H. P. Weber, "Modelling of thermal lensing and higher order ring mode oscillation in end-pumped c.w. Nd:YAG lasers", IEEE Journal of Quantum Electronics, vol. 28, no. 4, p. 1046, 1992
- 28 Product spec. sheet for DM-1000 series of additive pulse mode-locked diode

pumped ND:YLF lasers, Microlase Optical Systems / Coherent Scotland, available from <http://www.microlase.co.uk>

- 29 J. Weber ed., "Handbook of laser science and technology vol. 1 lasers and masers", CRC press, 1982
- 30 F. Mollenauer, "Colour centre lasers", Methods of experimental physics, vol. 15 Quantum Electronics part B,1, 1979
- 31 F. Mollenauer, "Colour centre lasers", Laser Handbook, vol. 4, ed. M. L. Stich, M. Bass, Elsevier Science, 1985
- 32 E. Georgiou, J. F. Pinto, C. R. Pollock, "Optical properties and formation of oxygen-perturbed  $F_2^+$  color centre in NaCl", Phys. Rev. B, vol 35, p.7636, 1987
- 33 Goovaerts, J. Andriessen, S. V. Nistor, D. Schoemaker, "Electron-spin-resonance study of Tl atom defects in KCl and relativistic many-body analysis of the hyperfine structure", Phys. Rev. B, vol. 24, no. 1, p. 29, 1981
- 34 A. Aegerter, F. Luty, "The  $F_2^+$  centre in KCl crystals", Phys Stat. Sol. B, vol. 43, p. 245, 1971
- 35 F. Mollenauer, N. D. Vieira, L. Szeto, "Optical properties of the  $Tl^0(1)$  centre in KCl", Phys. Rev. B, vol. 27, no. 9, p. 5332, 1983
- 36 T. Kennedy, "Novel mode-locking techniques for colour-centre lasers", Ph.D thesis, University of St Andrews, 1993
- 37 X. Zhu, W. Sibbett, "Experimental study of the primary mode-locking parameters of coupled-cavity KCl:Tl colour-centre laser", J. Opt Soc. Am. B, vol. 7, no. 11, p. 2187, 1990
- 38 A. Haus, J. G. Fujimoto, E. P. Ippen, "Analytic theory of additive pulse and Kerr lens mode-locking", IEEE Journal of Quantum Electronics, vol. 28 no. 10, p. 2086, 1992
- 39 F. Krausz, M. E. Fermann, T. Brabec, P. F. Curley, M. Hofer, M. H. Ober, C Spielmann, E. Winter, A. J. Schmidt, "Femtosecond solid-state lasers", IEEE Journal of Quantum Electronics, vol. 28, no. 10, p. 2097, 1992
- 40 R. S. Grant, W. Sibbett, "Cavity configurations for coupled-cavity mode-locking", Optics Comm., vol. 86, p.177, 1991
- 41 W. Sibbett, R. S. Grant, D. E. Spence, "Broadly tuneable femtosecond solid-state laser sources", Appl. Phys. B., vol. 58, p. 171, 199

## **Chapter 5**

### **Linear and nonlinear properties of InGaAsP optical amplifiers**

#### **5.1 Introduction**

Semiconductor lasers in the InGaAsP material system have found widespread use as directly modulated pulse sources for high speed optical fibre telecommunications links and as pump sources for erbium-doped fibre amplifiers. However, InGaAsP laser amplifiers have proved inferior to fibre amplifiers at 1.55  $\mu\text{m}$  because of their polarisation sensitivity and low saturation powers, although recently less polarisation sensitive amplifiers have been developed<sup>1</sup> and flared amplifiers offer the prospects of increased saturation intensities. Another key area where semiconductor laser amplifiers could play an important role involves the utilisation of their strong optical nonlinear properties. As outlined in Chapter 1, these nonlinearities have potential for use in photonic switching and all-optical processing devices.

In this chapter some of the general characteristics of the amplifiers examined are presented and measured gain saturation characteristics for c.w. and pulsed inputs are related to an amplifier model. A pump-probe technique is used to examine the recovery times and magnitudes of the gain nonlinearities and the nonlinear coefficient,  $n_2$ , is measured using self phase modulation. The saturation of the carrier heating nonlinearity is investigated at transparency and this is related to a theoretical model of the carrier heating process.

#### **5.2 Laser amplifier details**

In this section the characteristics of the long wavelength semiconductor laser amplifiers

used in this thesis are described. The devices, which were used for all of the experiments in this chapter, were grown, fabricated and AR coated by BNR Europe Ltd at Harlow, because of difficulties experienced, at the time, in fabricating RWL structures at Glasgow. These devices were supplied in bar form, requiring only to be cleaved into chips and solder mounted. The devices were originally grown in a development programme for 1480nm erbium-doped fibre amplifier pumps and so the material gain peaks are around this wavelength.

The structures<sup>2</sup> were composed of 5 x 6nm thick GaInAs MQW's with Ga<sub>0.17</sub>In<sub>0.83</sub>As<sub>0.37</sub>P<sub>0.63</sub> barriers, lattice matched to InP. Horizontal optical confinement was provided by a RWL structure as described in Chapters 2 and 3. Ridge widths were 3µm and device lengths were 500µm. Both facets were AR coated for 1.5µm, using a multilayer dielectric coating. Before the devices were selected for AR coating, mounted laser chips from nearby on the wafer were tested, allowing devices with good L-I characteristics and suitable wavelengths to be chosen.

For c.w. operation the laser chips were mounted p-side down using indium solder on gold plated copper blocks, which were designed to allow access to both facets for lensed fibres or objective lenses. The blocks were temperature controlled.

## 5.21 Device characteristics

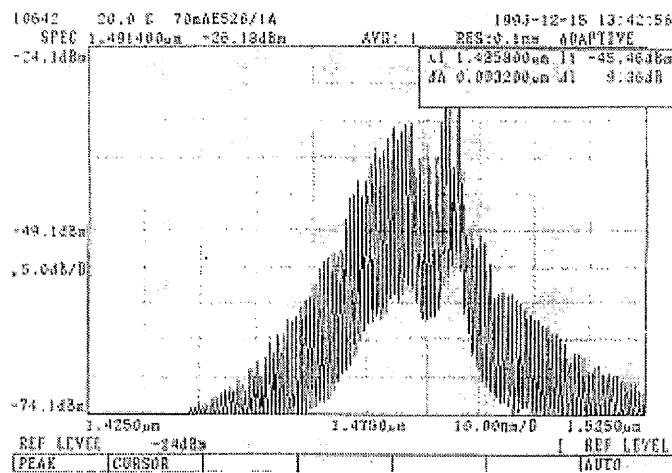


Fig 5.1 Spectrum at 70mA for a laser from wafer E526. Most of the investigations were performed on devices from this wafer. Amplifiers fabricated from this wafer are expected to be blue shifted by 10nm.

The BNR amplifiers used in this thesis were available from four wafers, providing gain peaks from 1470 to 1510nm, these devices were first characterised as lasers, as described in Appendix III. Devices from suitable wafers were then AR coated. Threshold currents for uncoated devices were typically 25-30mA, for a 500 $\mu$ m long device. The amplifiers which were used for the majority of the investigations, including the pump probe study were from wafer E526, which had a room temperature photoluminescence peak of 1483nm and a lasing centre wavelength of 1491nm. The spectrum of an uncoated device is shown in Fig. 5.1, above. It is important to note that there is a shift between the expected lasing wavelength, in an uncoated laser and the gain peak in an AR coated amplifier, which occurs because the carrier density in the laser becomes clamped above threshold. The gain peak of an amplifier was typically 10nm below the lasing wavelength of a similar uncoated device. This is illustrated in Fig. 5.3, for 1.55 $\mu$ m lasers and amplifiers with a 6 MQW strained layer active region, although these devices were not investigated as their gain wavelength was on the edge of the F-centre tuning range. Fig. 5.2 shows the corresponding L-I characteristics. Adjacent bars were selected from the wafer, one was cleaved into laser chips and the other was AR coated and cleaved into amplifier chips. The amplifiers of E526 showed a similar trend, although the appropriate spectra are not available to illustrate this.

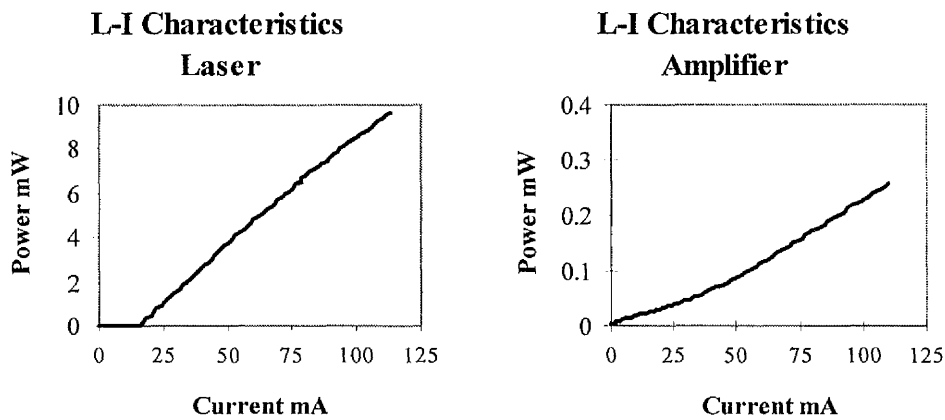
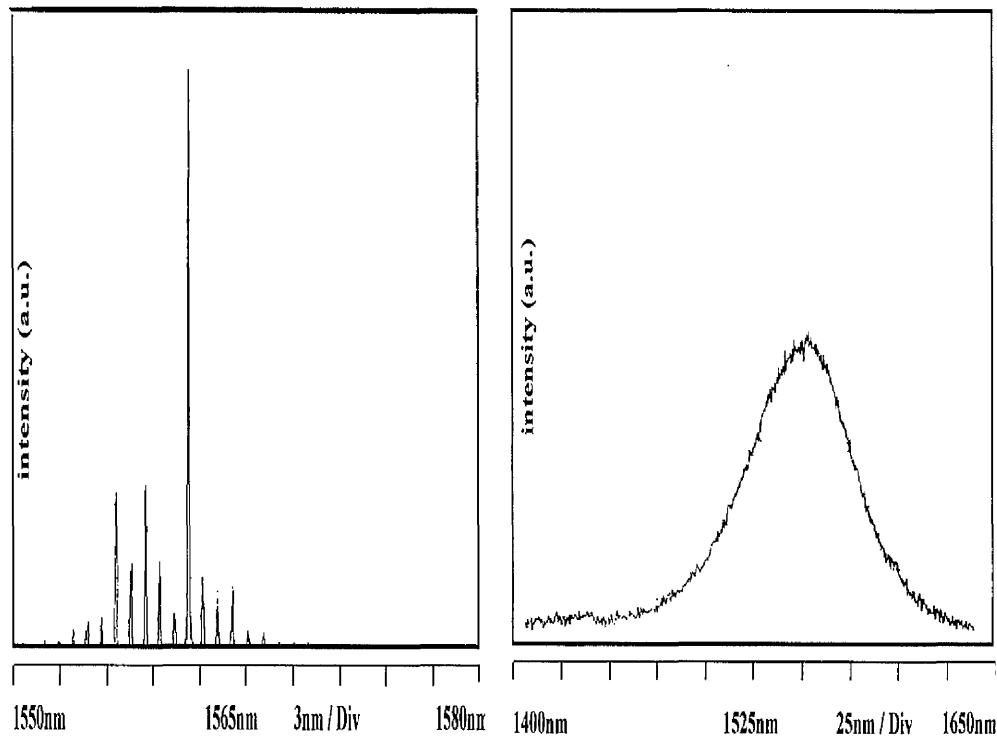


Fig. 5.2 Comparison between L-I characteristics for uncoated devices and AR coated devices from wafer E1007.



*Fig. 5.3 Spectral characteristics for uncoated laser, to the left and to the right an AR coated laser amplifier, from the same wafer (E1007), a shift of  $\sim 10\text{nm}$  is seen in centre wavelength. The drive current in both cases is  $50\text{mA}$ .*

## 5.22 Anti-reflection coatings

There are two different types of amplifier; travelling wave amplifiers, where facet reflectivities can be neglected and Fabry-Perot amplifiers, where facet reflectivities cannot be neglected and the resultant gain is therefore of a multi-pass nature. Whilst Fabry-Perot amplifiers offer large gain, they have a narrow bandwidth<sup>3</sup>. For this reason it is important to ensure the AR coatings are as good as possible and the residual reflectivities are low. For the experiments in this thesis it was necessary to use AR coatings, firstly to suppress lasing and secondly to produce a device which gives stable amplification.

A double layer<sup>4</sup> AR coating was deposited on the devices at BNR, the thickness of the layers were optically monitored, in situ, this allowed reflectivities as low as 0.1%,

when optimised. Fig. 5.4, shows that no lasing<sup>5</sup> is seen up to 150mA, higher currents were avoided in order to prolong the device's longevity. Device thresholds before coating would have been typically 25-30mA.

The value of these residual reflectivities can be estimated by examining the ripples in the gain spectrum<sup>6,7</sup>. Another technique involves using a cleaved fibre butted close to a coated facet to form a Fabry-Perot cavity<sup>8</sup>. In this case, the ripples in the spontaneous emission spectrum were measured. For a small single-pass gain reflectivity product, the peak-to-valley ratio of the gain ripples is given by<sup>7,9</sup>,

$$V = \left( \frac{1 + \sqrt{R_1 R_2 G}}{1 - \sqrt{R_1 R_2 G}} \right)^2 \quad (5.1)$$

where  $R_1$  and  $R_2$  are the facet reflectivities and  $G$  is the single-pass gain.

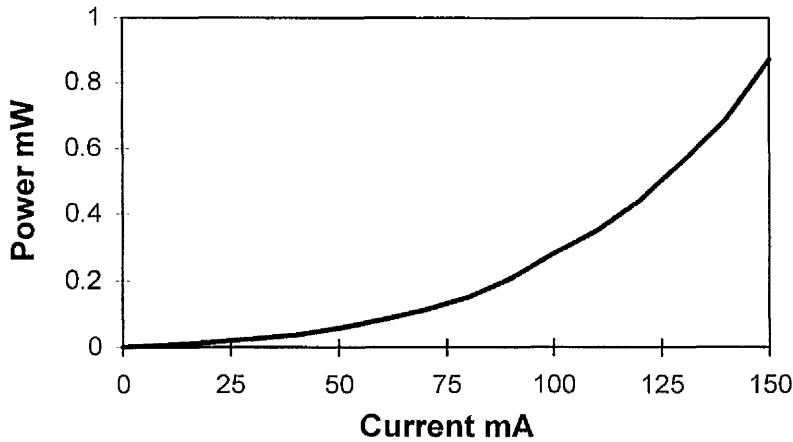


*Fig. 5.4 L-I characteristics for the amplifier used to estimate the AR coating reflectivities- no signs of lasing for currents up to 150mA.*

Fig. 5.5 shows ripples of 5% in the amplified spontaneous emission spectrum due to the residual facet reflectivities. Assuming the ripples in the spontaneous emission spectrum are the same magnitude as those in the gain spectrum and using the amplifier model (described later in this chapter) to estimate the single-pass gain at 50mA to be 14 for a 500 $\mu$ m device, the estimated residual reflectivity, from Fig. 5.5, is 0.17% at 1.5 $\mu$ m (the AR-coating wavelength). The spectra at 1.48 $\mu$ m exhibited larger gain ripples and a similar calculation again at 50mA drive current gives a reflectivity of 0.4%.

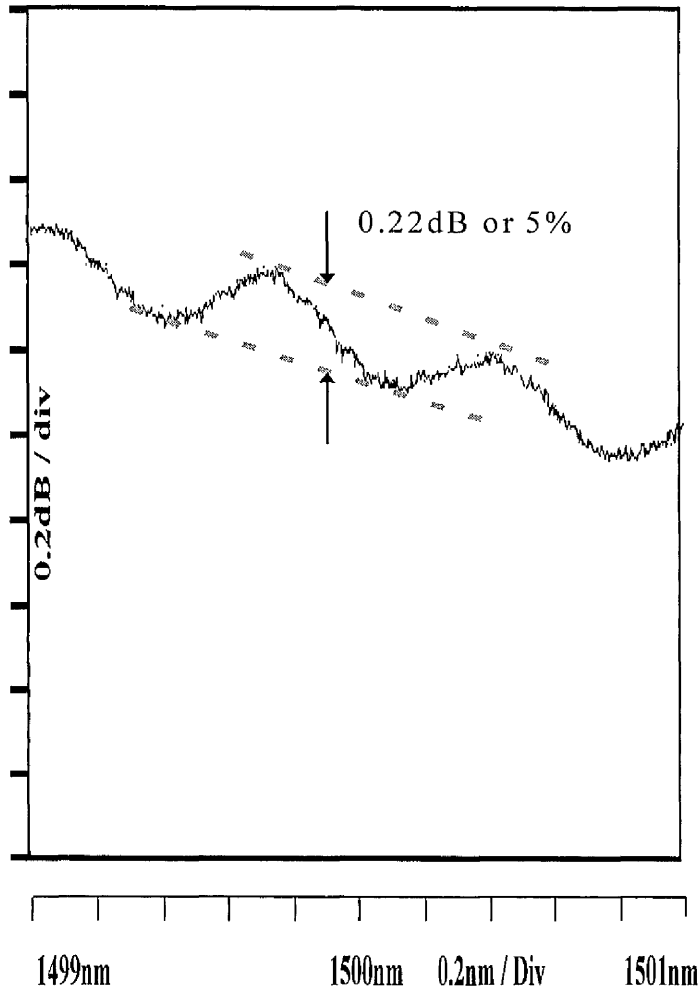


Fig. 5.5 Ripples in the spontaneous emission spectrum for an amplifier at 50mA. From this data the residual facet reflectivities were calculated.

### 5.23 Coupling arrangement

For most of the experiments described in this chapter the amplifier was maintained at a constant temperature via a thermo-electric cooler and a thermistor. The amplifier mount was placed on a micropositioner and input and output coupling was via objective lenses. The best technique for aiding coupling alignment was found to be chopping the input signal and then using a lock-in amplifier to monitor the photocurrent of the unbiased amplifier, whilst viewing the amplifier output on an infra-red camera. Using this technique the lock-in reading should reach a maximum when the maximum signal is coupled into the active region. A Melles Griot 45x lens with an NA of 0.7 was used as the input objective and a Newport F140B long working distance lens was used as the output objective. The input coupling efficiency was estimated to be 15% and the output

coupling efficiency was estimated to be 50%.

### 5.24 Transparency

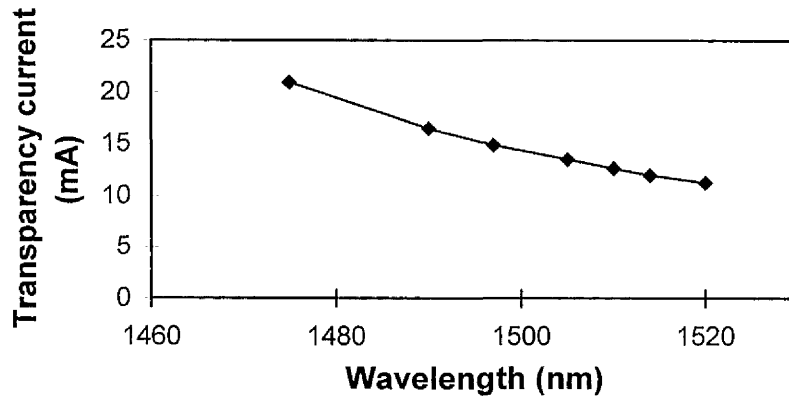


*Fig. 5.6 Transparency current variation with wavelength, for an amplifier from wafer E481.*

In semiconductor amplifiers the input signal can be amplified or attenuated depending on the amplifier bias, the point between these two conditions is termed transparency. At transparency, the current is such that interband absorption and stimulated emission cancel and so an injected signal produces no net changes to the Fermi levels. Although interband absorption and stimulated emission cancel at transparency, there will still be considerable losses due to waveguide scattering and free carrier absorption. Free carrier absorption losses are the most significant and are typically in the range  $20\text{-}40\text{ cm}^{-1}$ . The transparency point can be determined by chopping the input light and monitoring the amplifier terminal voltage with a lock-in amplifier, at transparency the lock-in signal is zero. The transparency current variation with wavelength is shown in Fig. 5.6, above.

### 5.3 Amplifier gain saturation

Although amplifiers are capable of providing large internal gains of greater than 30dB, the achievable gains are limited by poor coupling efficiencies and the low gain

saturation powers. The arrangement shown in Fig. 5.7 was used to examine the saturation behaviour of the amplifiers.

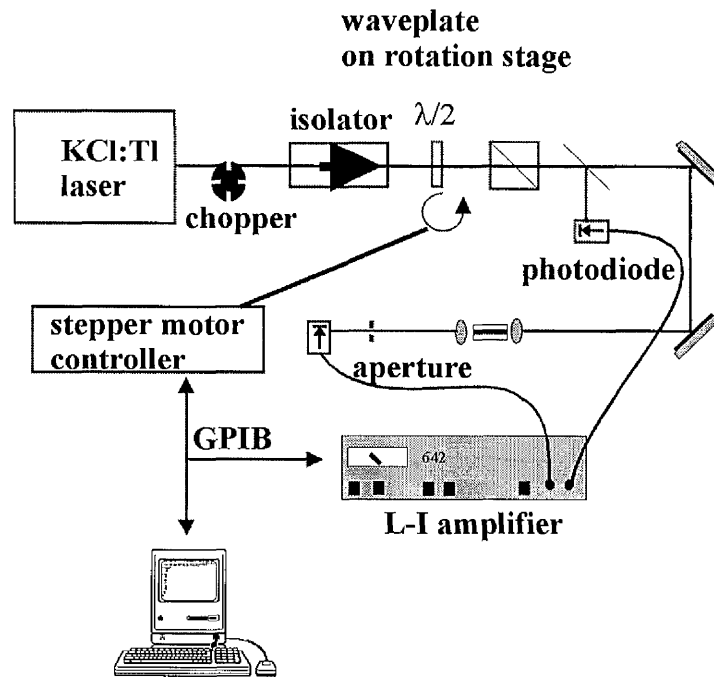


*Fig. 5.7 Experimental arrangement for examining gain saturation.*

The output from the F-centre laser was passed through a variable attenuator, provided by a half-waveplate and a polariser. A computer controlled rotation stage was used to turn the waveplate. A fraction of the signal was split onto a photodiode to monitor the input power level and the remainder was coupled into the optical amplifier. The output from the amplifier was focused through a small pinhole onto another photodiode. For each reading the computer rotates the waveplate and then captures the input and output signals from the lock-in amplifier.

Fig. 5.8, below shows the measured amplifier gain for various drive currents. When the amplifier was biased sufficiently within the absorption regime the effects of absorption saturation were observed. When the device was biased in between the gain and absorption regimes, at the transparency point, no saturation effects were observed.

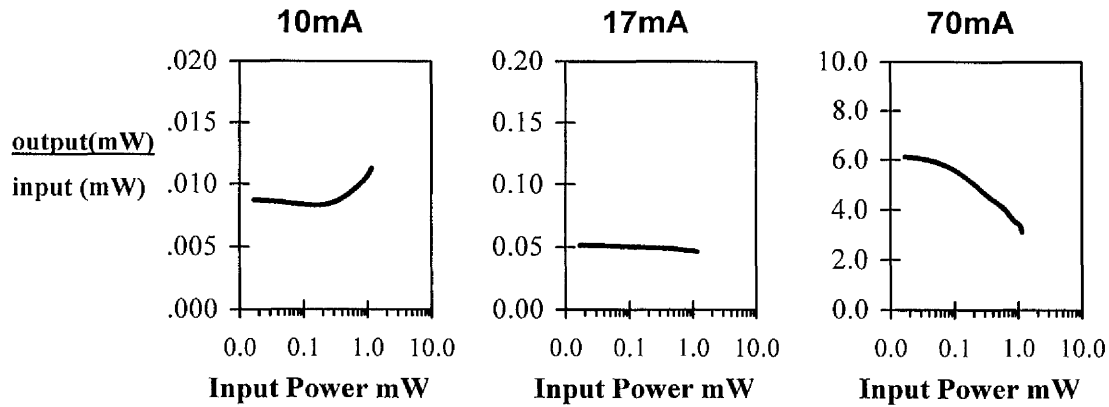


Fig. 5.8 Amplifier saturation for bias currents of 10mA (absorption), 17mA (transparency) and 70mA (gain).

The effects observed above are caused by the injected signal reducing the carrier density and hence gain.

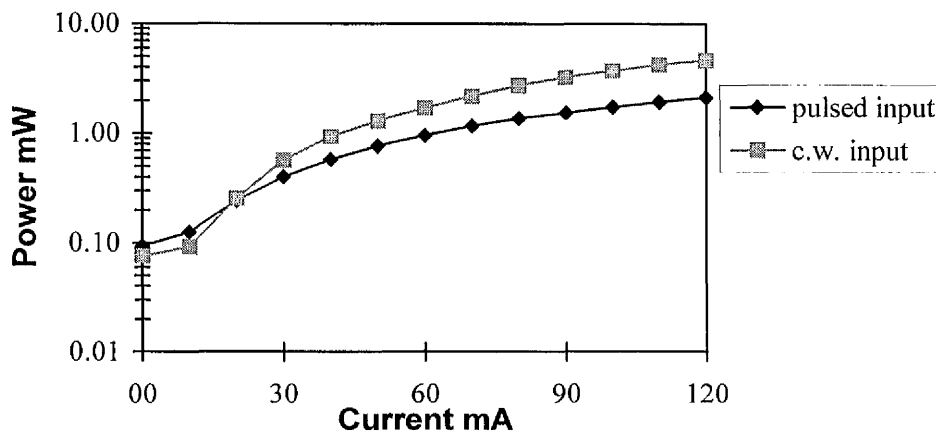


Fig. 5.9 Amplification of c.w. and pulsed inputs for different drive currents for 7mw input power.

The amplification for c.w. and pulsed inputs was compared for various drive currents as shown in Fig. 5.9 above. The pulses employed were of 30ps duration produced by synchronously pumping the F-centre laser. The effects observed occurred because for a pulsed input the pulse leading edge saturates the gain, reducing the amplification of the pulse's trailing edge. The opposite effect was observed when the device was biased in absorption. At transparency no significant amplification differences were observed for c.w. and pulsed inputs at the power levels used.

### 5.31 Amplifier modelling

Amplifiers and lasers can be accurately modelled using a rate equation approach<sup>10-17</sup>. A model was first developed to examine c.w. amplification and then expanded to include short pulse amplification. The programs were written in Mathematica and are listed in Appendix V. The basic rate equation used has the form<sup>18</sup>,

$$\frac{dn}{dt} = \frac{I}{qV} - R - \frac{g_o \cdot P}{h \cdot f \cdot w \cdot d} - \beta \cdot g_o \cdot S \quad (5.2)$$

where  $n$  is the carrier density,  $I$  is the current,  $q$  is the electron charge,  $R$  is the recombination rate,  $g_o$  represents the material gain,  $P$  is the power inside the device,  $h$  is Planck's constant,  $f$  is the optical frequency,  $w$  is the active region width and  $d$  is the active region thickness. Spontaneous emission is modelled<sup>10,13</sup> via the term  $\beta g_o S$ , where  $\beta$  is the overlap of the spontaneous emission with the amplified signal and  $S$  is the amplified spontaneous emission photon density averaged over the device length. The recombination rate term  $R$ ,

$$R = An + Bn^2 + Cn^3 \quad (5.3)$$

includes the effects of nonradiative, bimolecular and Auger recombination which have constants  $A$ ,  $B$  and  $C$  respectively. Cavity gain per unit length is expressed as,

$$g = \Gamma g_o - \alpha \quad (5.4)$$

where  $\Gamma$  is the modal confinement factor and  $\alpha$  is the linear loss term. The gain is often modelled using a linear approximation<sup>10-13</sup>,

$$g_o = a(n - n_t) \quad (5.5)$$

where  $a$  is the slope of the linear gain-carrier density relationship and  $n_t$  is the carrier density at transparency. For QW structures, however, a logarithmic approximation<sup>19</sup> is known to be more accurate, where the gain is given by,

$$g_o = \gamma \cdot \ln\left(\frac{n}{n_t}\right) \quad (5.6)$$

where  $\gamma$  is a fitting constant. Fig. 5.10 shown below compares the linear and logarithmic expressions. The parameter  $\gamma$  was chosen to match the published gain characteristics of similar BNR MQW lasers<sup>20</sup>, at a current significantly above threshold (100mA), the value used is also close to that quoted elsewhere for MQW lasers<sup>19</sup>.

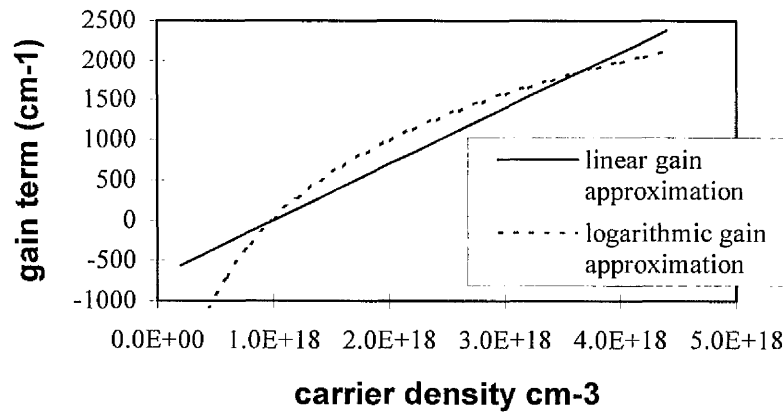


Fig. 5.10 Logarithmic and linear gain relations.

The amplification experienced by light in the amplifier travelling a distance L is then given by,

$$P_o = P_i \cdot e^{gL} \quad (5.7)$$

where  $P_i$  is the input power. The table below gives the values used to model the MQW InGaAsP amplifiers at 1.5 $\mu$ m.

Parameter	Description	Value	Reference
<b>A</b>	linear recombination rate	negligible at 25° C	<b>18</b>
<b>B</b>	bimolecular recombination constant	$10^{-10} \text{ cm}^3 \cdot \text{s}^{-1}$	<b>18,9,13</b>
<b>C</b>	Auger recombination constant	$4 \times 10^{-29} \text{ cm}^6 \cdot \text{s}^{-1}$	<b>18,9,13</b>
$\alpha$	linear loss term	$30 \text{ cm}^{-1}$	<b>9,13,10</b>
$\Gamma$	confinement factor	0.07	<b>20</b>
<b>d</b>	active region thickness	0.1 $\mu$ m	
<b>w</b>	active region width	3.5 $\mu$ m	

<b>l</b>	amplifier length	500 $\mu\text{m}$	
<b>a</b>	gain coefficient	$7 \times 10^{-16} \text{cm}^2$	<b>20</b>
$\gamma$	logarithmic gain coefficient	$1424 \text{cm}^{-1}$	<b>19</b>
<b>n<sub>t</sub></b>	transparency carrier density	$1 \times 10^{18} \text{cm}^{-3}$	<b>18,9,13</b>
<b>f</b>	optical frequency	$0.196 \times 10^{15} \text{Hz}$	
<b>q</b>	electron charge	$1.6 \times 10^{-19} \text{C}$	
<b>h</b>	Planck's constant	$6.625 \times 10^{-34} \text{Js}$	

Table 4.1 Parameters used in the amplifier model.

In the c.w. model the amplifier was split into small sections in which the gain was assumed to be linear. Equation 5.2 was used to calculate the carrier density in each section using the calculated amplified power from the preceding section. The gain in the section was then calculated from Equations 5.4 and 5.5 and was used to amplify the signal. Residual facet reflectivities were ignored in the model. Fig. 5.11 shows the modelled gain when spontaneous emission is ignored. This shows a similar saturation power to those found in measured devices: in Fig. 5.8, a 3dB point of 0.1mW for 70mA drive is found when a 10% coupling efficiency is assumed, which was similar to the modelled response

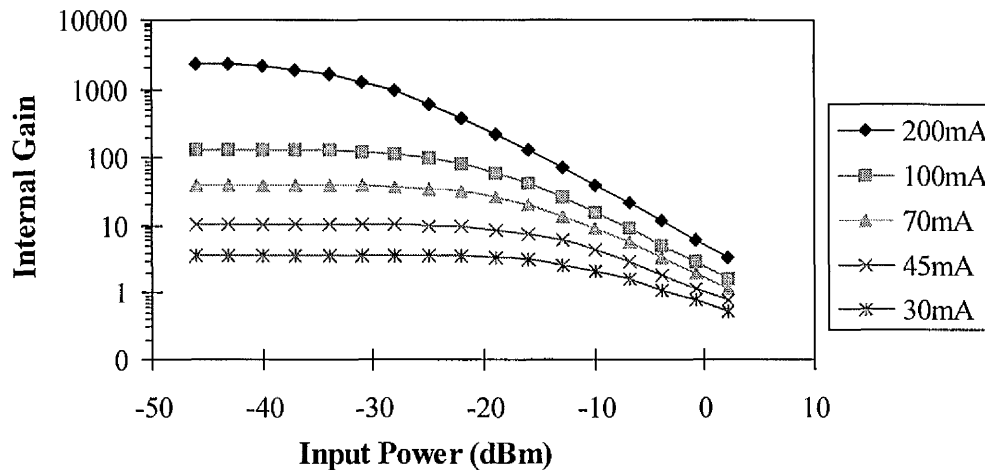


Fig. 5.11 Modelled amplifier gain against input power for various drive currents, neglecting the effects of spontaneous emission. Using the linear gain expression.

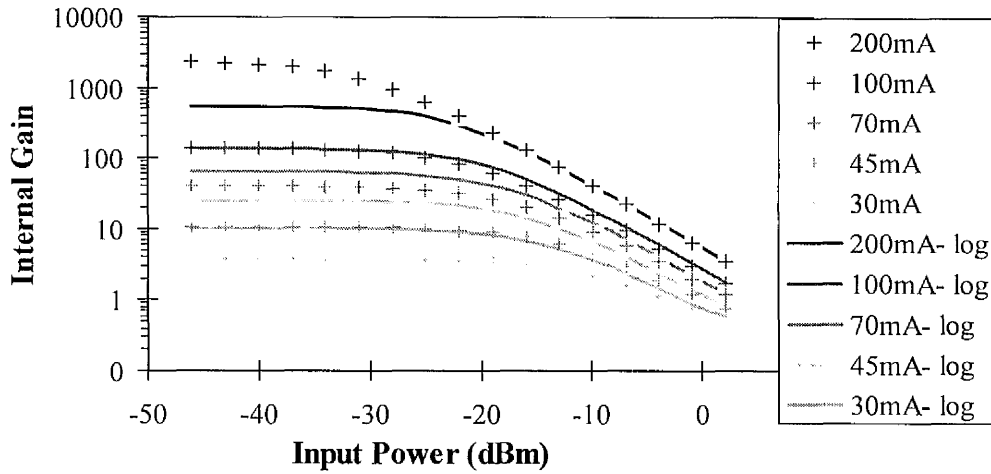


Fig. 5.12 Modelled amplifier gain against input power for various drive currents. The solid lines show the gain calculated using the logarithmic gain expression and the dotted lines indicate the results calculated for a linear expression.

A model for the effects of short pulse amplification was developed following the approach of Agrawal<sup>14</sup>. Using Equations 5. 1 and 5. 5, but discounting the spontaneous emission term, the following expression is obtained,

$$\frac{dg}{dt} = \frac{g_0 - g}{\tau_c} - \frac{gP}{E_{sat}} \quad (5.8)$$

where  $E_{stat} = h\omega\sigma/a$ ,  $\sigma = wd/\Gamma$  and  $\tau_c = n/R$  as defined in 5.3 . The small signal gain is given by  $g_0 = \Gamma a \cdot n_t (I/I_0 - 1)$  and  $I_0 = q \cdot V \cdot n_t / \tau_c$  which is the current at transparency. Equation 5.8 can be integrated to give,

$$g(t) = g_0 \cdot e \left( - \int_{-\infty}^t \frac{P}{E_{sat}} \cdot dt \right) \quad (5.9)$$

This expresses how the amplification changes over the pulse shape. This approach assumes that the optical pulses are significantly shorter than the carrier interband relaxation time and uses the linear expression for gain in terms of carrier density. Therefore Equation 5.5 is only valid for small signal variations in gain, in a device with

a nonlinear gain carrier density relationship, nevertheless it provides an illustration of self-induced pulse distortion. In the pulse amplification model the small-signal carrier density was calculated from 5.2, for a given current. From this  $\tau_c$  was calculated. The gain across the pulse was then calculated from 5.8. The graphs below, Fig. 5.13 and 5.14 show that substantial pulse shaping occurs for sufficiently intense pulses. When an amplifier is biased in the gain regime the leading edge of the pulse is sharpened and the trailing edge broadens, the opposite occurs for an amplifier biased below transparency.

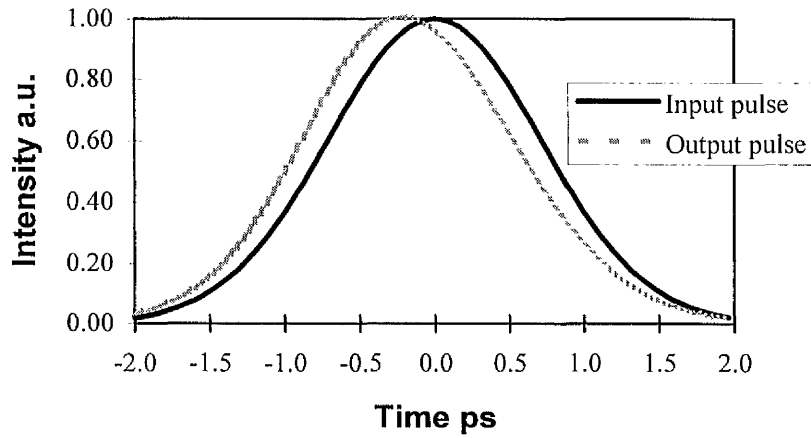


Fig. 5.13 Calculated pulse shaping for a 2ps FWHM pulse with pulse energy of 1pJ for 50mA bias.

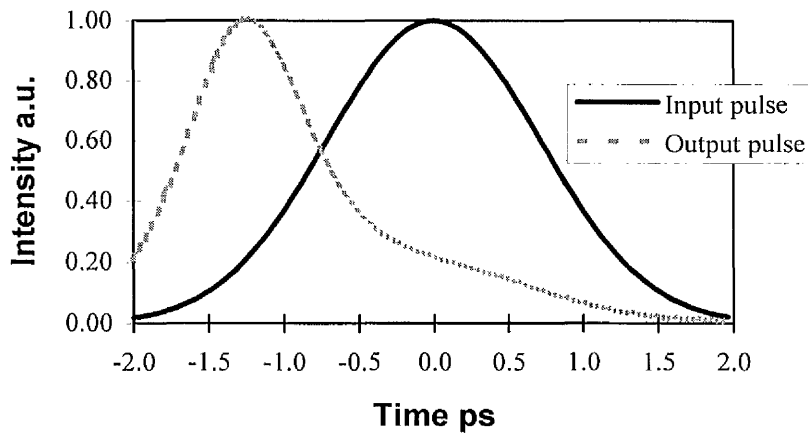


Fig. 5.14 Calculated pulse shaping for a 2ps FWHM pulse with pulse energy of 30pJ for 50mA bias.

### 5.32 Injection locking

During the course of the investigation of the gain saturation effects, an amplifier, (device E481 #5) was examined which had poor AR coatings and lased at 60mA. This compares to 30 mA for an uncoated device and a threshold of greater than 150mA (although devices were never driven sufficiently hard to prove that they did lase) for a successfully coated device. An interesting property of this device was observed when it was operated above threshold and used in a typical amplifier configuration, with light coupled from an external source, and the output monitored; if sufficient signal was coupled into the device it was possible to suppress lasing as shown in Fig. 5.15.

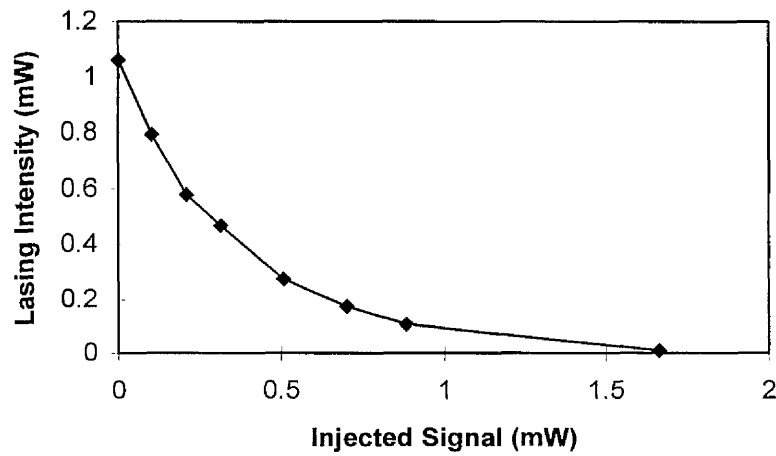


Fig. 5.15 Suppression of lasing by injected signal, for device E481 #5 at 70mA.

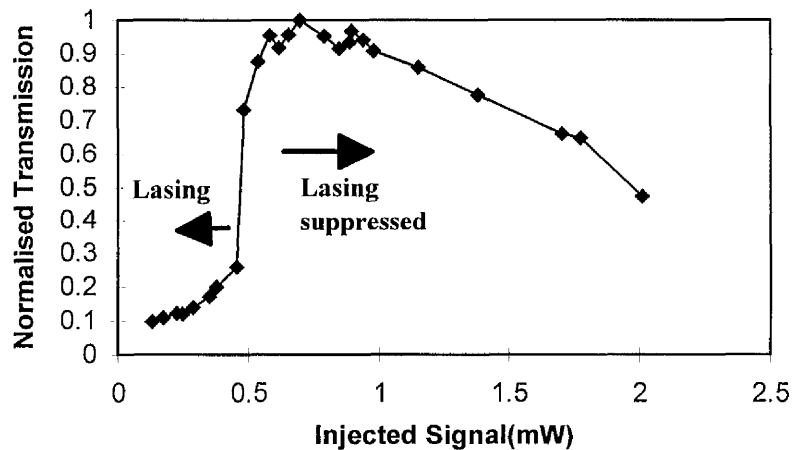


Fig. 5.16 Amplification experienced by an injected signal in an 'amplifier' above threshold, device E481 #5 at 70mA drive current.

It was possible to separate the lasing signal from the injected signal using a spectrum analyser as the lasing wavelength of the device was  $1.48\mu\text{m}$  and the injected signal was at  $1.5\mu\text{m}$ . Similarly if the gain of the ‘amplifier’ was monitored above threshold, a sharp transition in the gain was observed when the injected signal is sufficient to suppress lasing as shown in Fig. 5.16.

## 5.4 Self phase modulation

An optical pulse travelling through a medium with an intensity-dependent refractive index can experience induced phase changes over its duration. This process is called self-phase modulation (SPM) which leads to spectral broadening as frequency is the time derivative of phase. In a Kerr medium the refractive index is given by,

$$n = n_0 + n_2 \cdot I(t) \quad (5.10)$$

where  $n_0$  is the linear refractive index,  $n_2$  is the nonlinear coefficient and  $I$  is the optical intensity, which varies over the pulse. The instantaneous phase shift is given by,

$$\delta\phi(t) = \frac{2\pi \cdot l \cdot n_2 \cdot I(t)}{\lambda} \quad (5.11)$$

where  $l$  is the effective length of the medium and  $\lambda$  is the wavelength. For a gaussian input pulse of intensity,

$$I(t) = I_0 e^{-(t^2/\tau^2)} \quad (5.12)$$

the effects of self-phase modulation can be calculated by solving the equation<sup>21</sup>,

$$I_{out}(\omega) = \left| I_0^{1/2} \int_{-\infty}^{\infty} I(t)^{1/2} e^{i\delta\phi(t)} e^{-i(\omega-\omega_0)t} dt \right|^2 \quad (5.13)$$

this is the modulus squared of the Fourier transform of the pulse amplitude with a intensity dependent phase shift term. Which gives the intensity spectrum after self-phase modulation. For an instantaneously recovering refractive index the broadened pulse spectra for various phase shifts are shown below in Fig. 5.17.

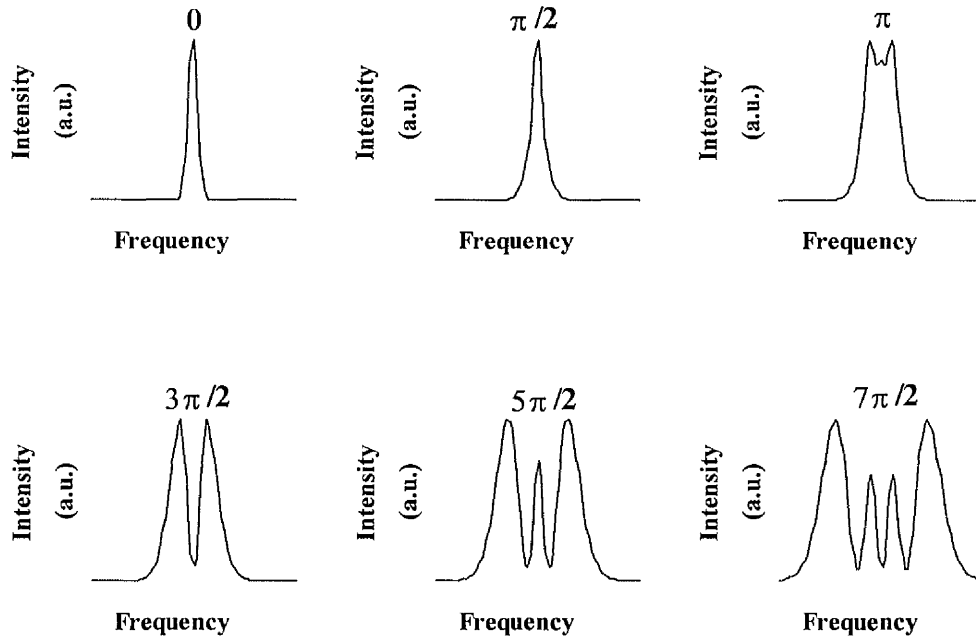


*Fig. 5.17 Calculated spectral broadening (after reference 21).*

The easily identifiable pulse spectra associated with a given phase shift allows spectral broadening to be used to estimate the nonlinear coefficient,  $n_2$ .

#### **5.41 Experimental spectral broadening in a InGaAsP amplifier**

An experimental arrangement similar to Fig. 5.7 was used, but in this case the output from the amplifier was coupled into a short length of multimode optical fibre which was connected to an Advantest spectrum analyser to monitor the spectral broadening. The laser pulses used were of duration 20ps FWHM which was significantly larger than the anticipated recovery time for an amplifier biased at transparency. The input polarisation

was TE. Devices from wafer E481, with a peak gain around  $1.47\mu\text{m}$  were used for these measurements. Fig. 5.18, below shows a low intensity pulse which is unbroadened upon transmission through the amplifier.

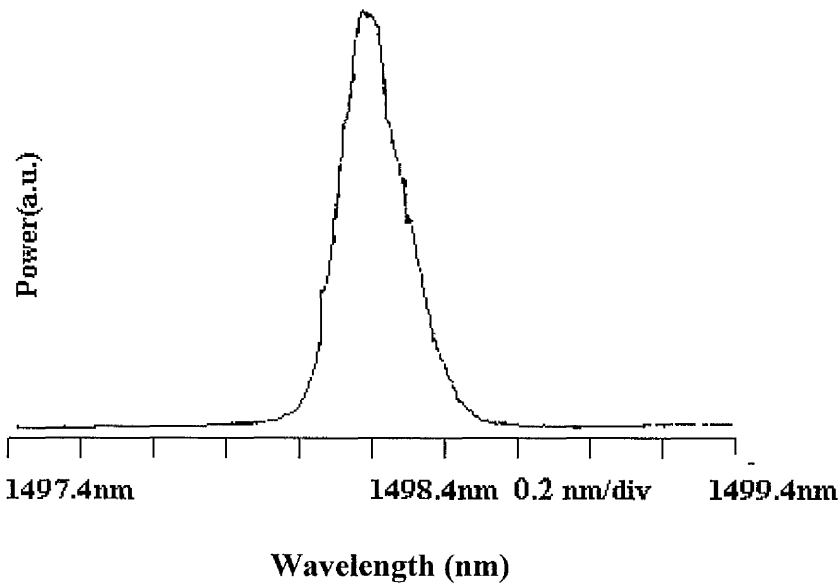


*Fig. 5.18 Low intensity unbroadened pulse.*

For a higher pulse intensities symmetric broadening occurred when the amplifier was biased at transparency.

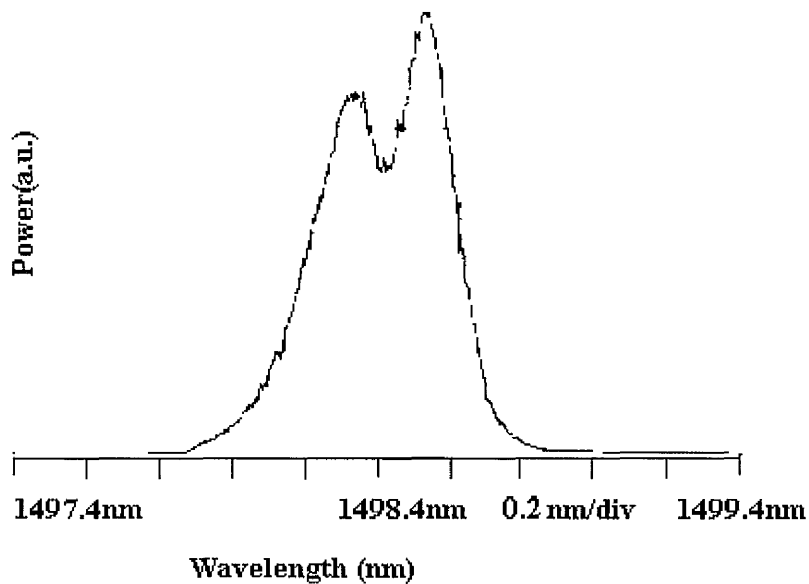


*Fig. 5.19 Spectral broadening at transparency  $\sim 3\pi/2$  phase shift for 6.2 mW coupled power.*

Fig. 5.19 shows the spectral characteristics associated with a  $3\pi/2$  phase shift. Asymmetric spectral broadening was observed when the amplifier was biased in the gain and absorption regimes as the gain recovery time was long compared to the pulse width. A broadened high intensity pulse is shown in Fig. 5.20. The sign of the asymmetric broadening is determined by the sign of the induced refractive index changes and so is opposite in the absorption and gain regimes.

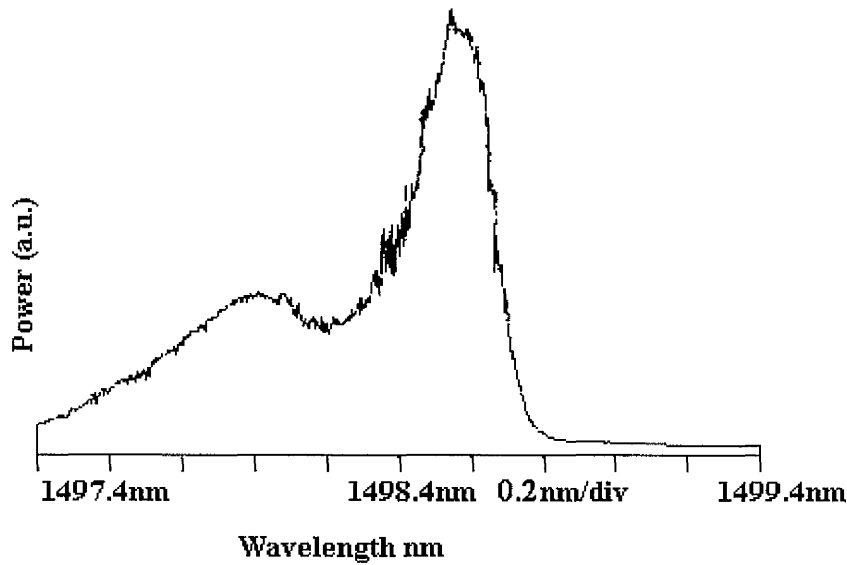


*Fig. 5.20 Asymmetric spectral broadening for an amplifier biased in absorption.*

From the data of Fig. 5.19 it is possible to estimate the nonlinear coefficient,  $n_2$  using Equation 5.11. Assuming the linear losses at transparency are  $40\text{cm}^{-1}$ , an effective modal area of  $2.8\mu\text{m}^2$  and a 15% coupling efficiency, the nonlinear index,  $n_2$  was calculated as  $2.39 \times 10^{-11} \text{ cm}^2 \text{ W}^{-1}$ . Comparing this value to other measurements in the literature; Grant et al <sup>22</sup> assumed a  $n_2$  of  $2 \times 10^{-11} \text{ cm}^2 \text{ W}^{-1}$  in an InGaAsP bulk device. A similar value of  $4 \times 10^{-11} \text{ cm}^2 \text{ W}^{-1}$  for TE input and  $2.5 \times 10^{-11} \text{ cm}^2 \text{ W}^{-1}$  for TM input was measured by Fisher et al <sup>23</sup> in a 4 MQW GaInAs / InGaAsP device. These measurements were also performed using the SPM method. Measurements performed in the time domain by pump probe studies<sup>24</sup> point to values an order of magnitude smaller of  $1 \times 10^{-12} \text{ cm}^2 \text{ W}^{-1}$ .

The  $n_2$  measured here by SPM in the 5 MQW InGaAsP ridge waveguide

amplifiers supplied by BNR Europe, shows a good agreement to values measured using the same technique, but there appears to be a discrepancy between the values calculated by SPM and  $n_2$  measurements in the literature estimated by pump probe methods. It should be noted that the main uncertainty in the values of  $n_2$  occurs because the coupling efficiency and modal area are not accurately known. The possible error in the calculated  $n_2$  could be up to a factor of 2.

## 5.5 Pump-probe experiment

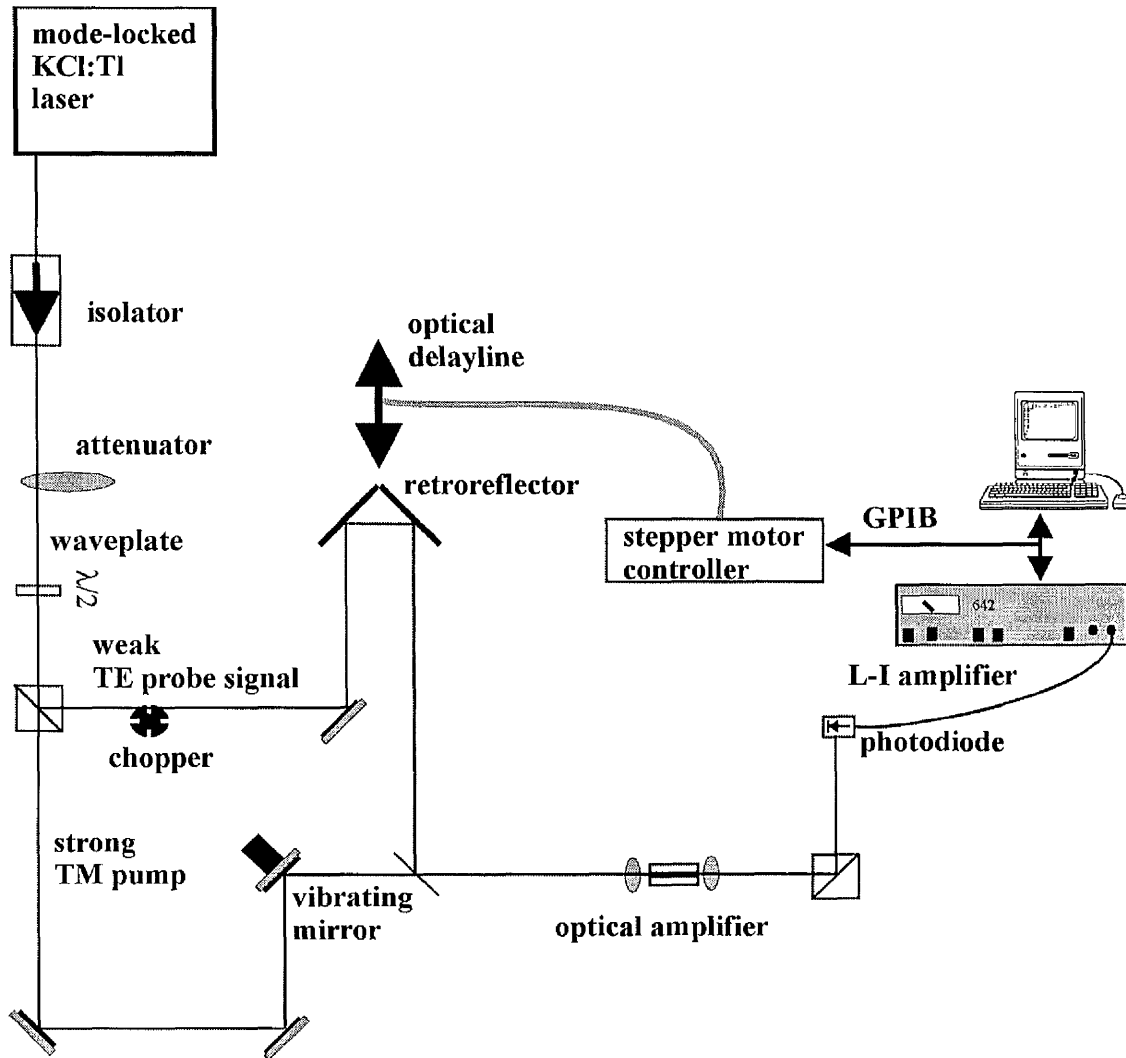


*Fig. 5.21 Pump-probe experimental arrangement.*

A widely used approach for examining gain and refractive index nonlinearities is the pump-probe interferometer technique, which can be used to obtain information about

the sign, magnitude and recovery time of optical nonlinearities. In one arrangement the light from a short pulse laser is split into orthogonally polarised high and low intensity components which form the two arms of the interferometer. The signals from each arm are then recombined in space and time and coupled into the nonlinear medium to be investigated. A retroreflector mounted on a stepper motor in one arm allows a controllable time delay between pulses. The intense pump pulse excites the nonlinearity, the effects of which can be monitored at the output by separating the orthogonally polarised weak probe signal. By adjusting the temporal overlap between pump and probe pulses a continual recording of the recovery dynamics of the nonlinearity can be provided.

### **5.51 Experimental pump-probe arrangement**

The experimental arrangement used is shown in Fig. 5.21 above. The output from a mode-locked KCl:Ti F-centre laser was passed through an optical isolator, after which an attenuator was used to reduce the laser power to the desired level. A half-waveplate and polariser were used to separate the signal into orthogonally polarised pump and probe pulses. The intensity of the probe was typically set to a factor of 20 times smaller than the pump, so that most of the observed nonlinearities were caused by the pump. The arm lengths were visually set to be of roughly equal length and pump and probe signals were then recombined collinearly at a beamsplitter. One method of setting the zero delay between pump and probe pulses is to monitor both signals with a fast photodiode and adjust the delay line until both pulses are observed to overlap, however this method is limited by the time constant of the detector and oscilloscope. The method finally used was to set the polarisation in both arms to be the same and look for interference fringes, where the signals recombine, using an I.R. camera. When the highest contrast fringes were observed, the zero delay position was located. The signals were coupled into the amplifier via an AR-coated objective lens. A high extinction ratio polariser allows pump and probe to be separated at the amplifiers output, ensuring the pump signal does not saturate the detector. The probe signal was then monitored via a photodiode and lock-in amplifier. A variable delay between probe and pump pulses was provided by a hollow retroreflector mounted on a stepper motor. It was important to ensure the signal is normally incident on the retroreflector or significant beam steering will occur as the retroreflector moves. By blocking the pump signal and monitoring the

probe it was possible to check that the translation of the retroreflector produces no beam misalignment.

In reality the above method proved problematic and considerable coherence noise was observed around zero delay. It was not possible to set pump and probe to be perfectly orthogonal and it was also likely that some polarisation scrambling occurred in the input objective. This noise around zero delay was overcome by placing a vibrating mirror in the pump arm. If the period of vibration is shorter than the lock-in time constant the coherence spike is averaged out.

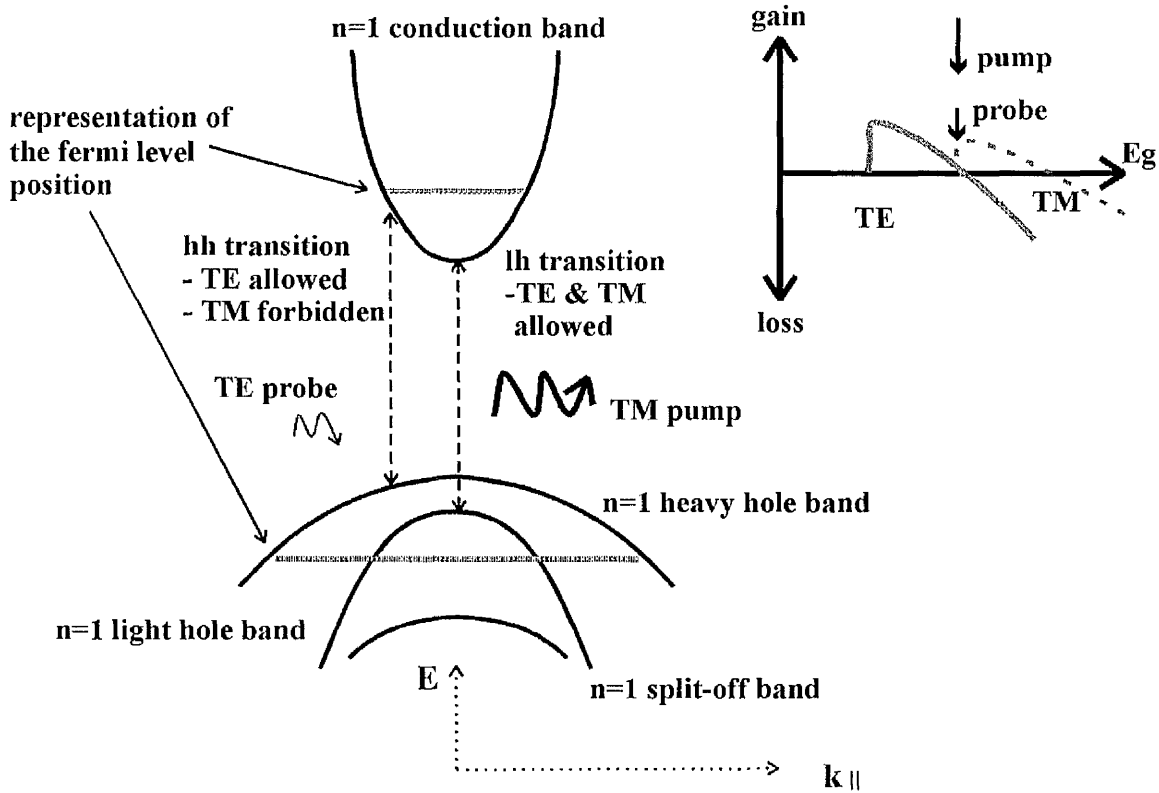


Fig. 5.22 Polarisation and wavelengths used for the pump-probe experiment on the lattice matched InGaAsP 5 MQW amplifiers, device E526. In relation to a) the band structure, for momentum parallel to the wells and b) the gain characteristics. The speak of the spontaneous emission is around 1500nm.

Experimentally it was more convenient to use a TE probe and a TM pump. This was because at 1500nm, which gives the shortest mode-locked pulses from the F-centre it was not possible to tune a TM input to the transparency point. This occurs as the gain peak is shifted towards shorter wavelengths for TM because of the polarisation selection

rules in QW structures. Fig. 5.22 shows where, in relation to the band gap, the experiments were performed. A device from wafer E526 was used for the experiments described in this section.

### 5.52 Pump-probe results

Fig. 5.23 shows the pump probe dynamics, for various amplifier drive currents from absorption through transparency into gain.

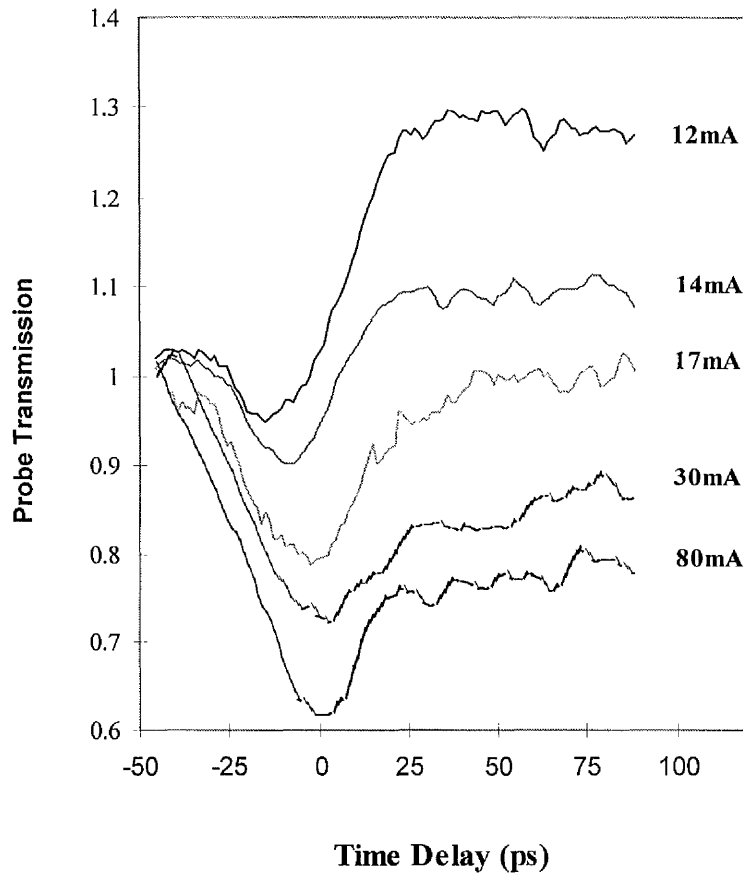


*Fig. 5.23 Experimental pump-probe data for different amplifier drive currents for 3mW input power. 17mA corresponds to transparency. The F-centre wavelength was tuned to 1500nm.*

The data show the fast recovering component observed elsewhere<sup>24</sup> and the long lived effects due to the interband effects arising from gain or absorption saturation. When the amplifier was biased deep in the absorption region, such as the 12mA data, the initial fast transient was swamped by the long lived effects. But at higher drive currents in the

gain regime the initial transient was always significant as the slow interband effects appear to saturate with increasing drive current. At 17 mA which was close to the transparency point no long lived effects were observed.

Following the observations from Fig. 5.23 that the long lived interband gain changes saturate with increasing drive current, it was decided to examine the long lived effects further. The delay line was adjusted so that the probe was fixed at 240 ps after the pump, and the pump induced change in probe transmission was monitored for different drive currents and pump powers.

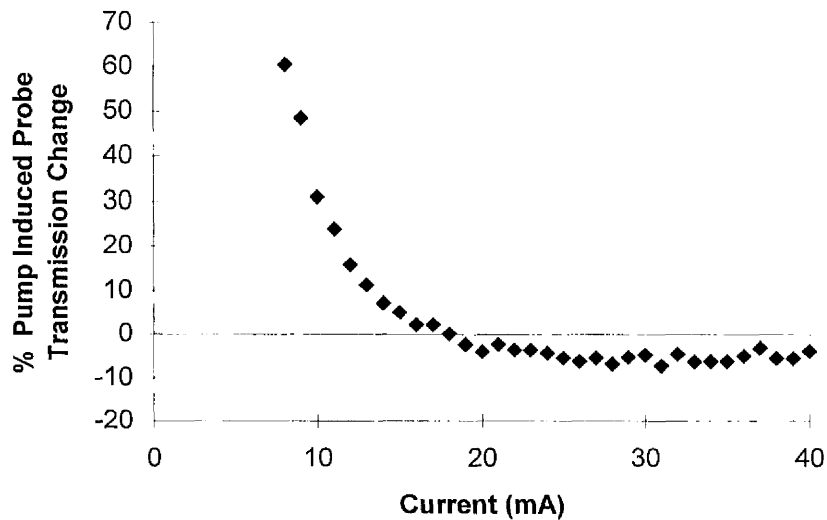


*Fig. 5.24 Long lived, pump induced probe changes for delay line fixed at 240ps after zero delay, at 1.5 μm for 3mW input power.*

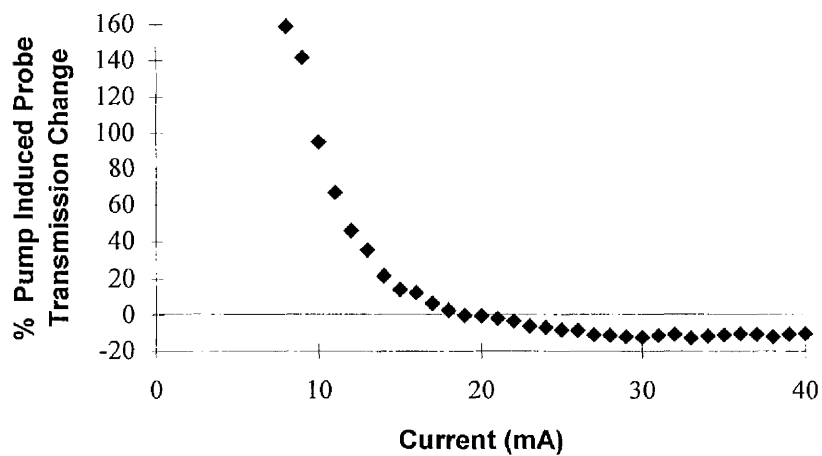


*Fig. 5.25 Long lived pump induced changes at a wavelength of 1.48 μm, for 3mW input power.*

Figures 5.24 and 5.25 show the long lived, nanosecond duration, transmission changes experienced by the probe at  $1.5\mu\text{m}$  and  $1.48\mu\text{m}$  for similar power pump signals. The smaller changes in absorption observed at  $1.5\mu\text{m}$  occur because the pump is nearer to the band edge and excites less transitions.

The effect seen in the above graphs, where for increasing currents above transparency the pump induced changes appear to level out, was because the TM pump was below or near the edge of the band gap and does not experience gain for high drive currents.

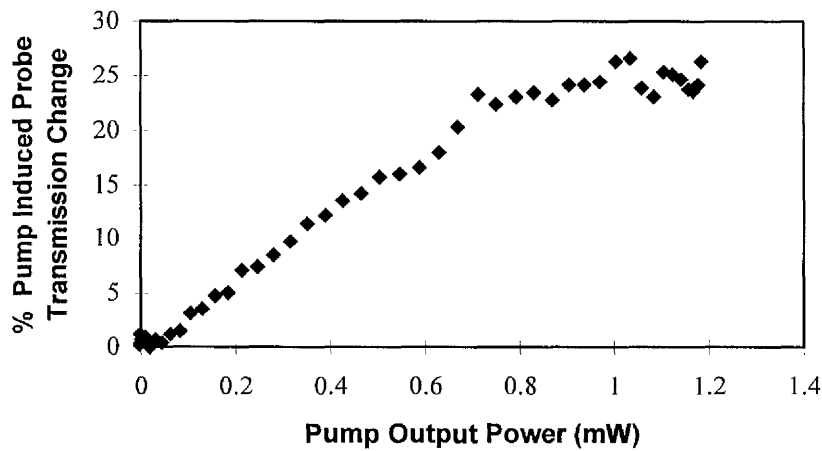


Fig. 5.26 Magnitude of the probe transient at zero delay with increasing pump powers at transparency, 17mA, showing saturation of carrier heating.

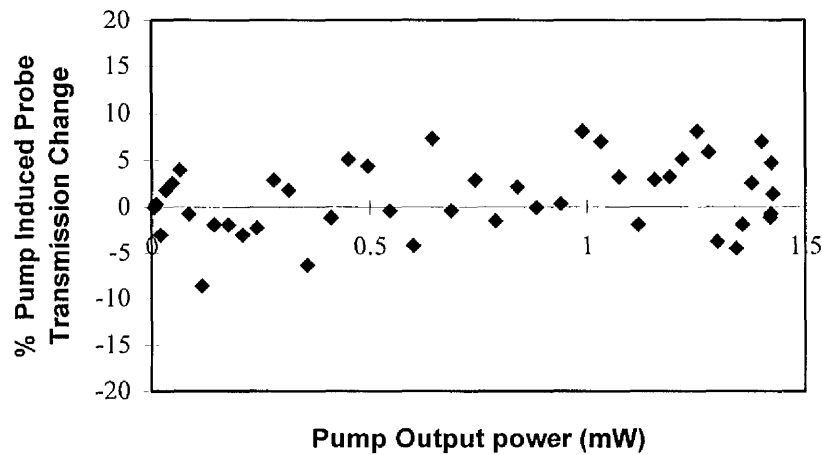


Fig. 5.27 Changes in the long lived transient for a similar bias current to Fig. 5.26.

Using a similar technique as described above, the size of the initial fast recovering probe transient seen at zero delay, was measured for various pump powers at the transparency point (17mA drive current). Although it should be noted that the transparency can be moved if sufficient power is coupled into the device. Fig. 5.26, above, shows the variation of the zero delay probe transient as a function of pump power at transparency. Similar traces were also observed above transparency at 30 and 40mA. The data show a linear variation which saturates. This suggests this effect was not caused by two-photon absorption, which would have a power squared dependence. The quickly recovering transients are consistent with carrier heating effects which have been observed to dominate over TPA for pulse durations  $>1\text{ps}$ <sup>24,25</sup>. For modest light intensities these effects saturate as is shown in Fig. 5.26, similar traces were obtained for a range of bias currents above and including transparency. Fig. 5.27 records the long lived transient at transparency. Although the data are noisy, because of pulse instability, it illustrates that the saturation effects observed in Fig. 5.26 are not caused by a significant non zero long lived transient washing out the quickly recovering transient. Again in order to verify that this saturation effect was not due to saturation of the pump signal, just the pump signal was examined. Fig. 5.28 shows that the pump does not experience saturation for the power levels used even when biased significantly above transparency.

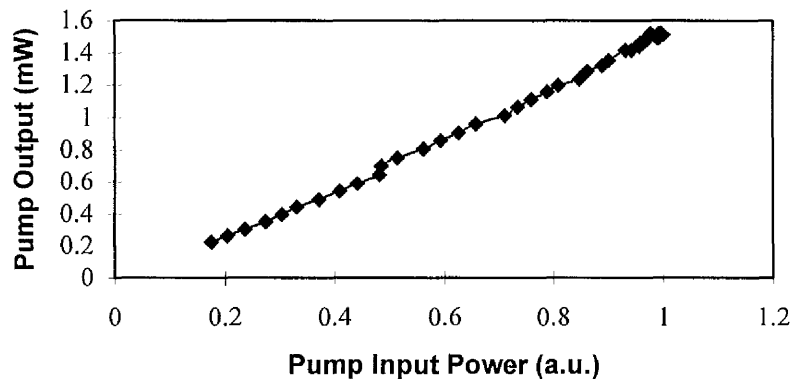


Fig. 5.28 Intensity of the TM pump before the amplifier plotted against the transmitted pump signal, indicating a linear variation (no saturation), for an amplifier biased at 40mA.

### 5.53 Modelling of carrier heating at transparency

Carrier heating in semiconductor lasers<sup>24-36</sup>, has been identified as the dominant cause of gain saturation. Following the pump-probe experiments described in the previous section, showing saturation of the carrier heating nonlinearity at high intensities (as shown in Fig. 5.26), a model was developed. The model is based on the approach of Uskov et al<sup>30</sup> and calculates the induced temperature changes of the carrier distribution at transparency, which allows the net gain to be calculated for a variety of pulsewidths and intensities.

The model suggests that for pulse widths and energies in the regimes used in this thesis, carrier heating induced gain saturation will occur for power levels in the mW regime.

The effects of nonlinear gain in laser amplifiers are generally included by a modification to the linear gain term of Equation 5.5<sup>28,30,36</sup>,

$$g_{nl} = \frac{(g_o + g_{tc} \cdot \Delta T_c + g_{tv} \cdot \Delta T_v) - \epsilon_{tpa} \cdot S^2}{1 + \epsilon_{shb} \cdot S} \quad (5.14)$$

where  $g_o$  is the linear gain term, as used in Equation 5.5,  $S$  is the photon density and  $g_{tc}$  and  $g_{tv}$  describe the temperature dependence of gain in the conduction band and valence bands respectively. Similarly  $\Delta T_c$  and  $\Delta T_v$  represent the temperature change of the electron and hole distributions from equilibrium. The lower  $(1 + \epsilon_{shb} \cdot S)$  term represents the nonlinear gain due to spectral hole burning, but at transparency the net spectral hole burning should be zero. Finally the  $\epsilon_{tpa}$  term allows the effects of two-photon absorption to be included. For the pulse durations used, the dominant nonlinearity is carrier heating and the two-photon term has therefore been neglected in the following analysis. The following expression can be used to calculate the optically induced temperature changes of the electron distribution,

$$\frac{\delta T}{\delta t} = h_c \cdot \left( \mu - E + \frac{\beta \cdot h \cdot f}{g_o} \right) \cdot v_g \cdot g_o \cdot S(t) - \frac{T - T_l}{\tau} \quad (5.15)$$

where  $T_l$  is the equilibrium lattice temperature,  $T$  is the perturbed carrier temperature,

$h_c^{-1} = (\delta U / \delta T)_n$  and  $\mu = (\delta U / \delta T)_T$ , where  $U$  is the energy density.  $E$  is the transition energy,  $\beta$  is the free carrier absorption coefficient,  $v_g$  is the group velocity of light and  $\tau$  is the interband temperature relaxation time. Equation 5.15 neglects the spontaneous recombination terms and the interband relaxation time, which is much longer than the pulse durations employed in the previous experiments and is not relevant at transparency. A similar expression exists for the temperature of the hole distribution, but here we just consider the electron distribution as it plays the dominant part<sup>28,30,33</sup>. At transparency Equation 5.15 can be simplified to the following expression,

$$\frac{\delta T}{\delta t} = h_c \cdot \beta \cdot h \cdot f \cdot v_g \cdot S(t) - \frac{T - T_l}{\tau} \quad (5.16)$$

This equation was solved numerically using a Mathematica programme, listed in Appendix V, for a range of pulse widths and powers. The temporal evolution of the carrier temperature was calculated following excitation by a ‘pump’ pulse at transparency. The parameter  $S(t)$ , the photon density across the pulse was modelled as a Gaussian. The net gain experienced by a pulse can also be calculated, by integrating over the temporal gain profile using a simplified version of Equation 5.14 shown below.

$$g_{nl} = g_0 + g_{tc} \cdot \Delta T_c + g_{tv} \quad (5.17)$$

At transparency the gain,  $g_0$ , is zero, therefore the issue of whether to use a logarithmic or linear gain, carrier density relation does not arise, although gain is assumed to vary linearly with temperature. At transparency there will be significant losses due to free carrier absorption. However in this simplified analysis these losses are ignored and the estimated saturation intensities will therefore be slightly underestimated. The parameters used in the model are the same as used in Section 5.31, Table 5.1. Additional parameters are listed below in Table 5.2.

Parameter	Description	Value	Reference
<b>pulse rep rate</b>		77 MHz	
$\beta$	free carrier absorption coefficient	800 m <sup>-1</sup>	<b>30</b>
$v_g$	group velocity	8.57 x 10 <sup>7</sup> ms <sup>-1</sup>	
$h_c$	$h_c^{-1} = (\delta U / \delta T)_n$ , where $U$ is the energy density	0.039 m <sup>3</sup> K J <sup>-1</sup>	<b>30</b>

$\tau$	electron intraband relaxation time	650 fs	<b>30,32</b>
$T_1$	equilibrium lattice temperature	300 K	
$g_{tc}$	gain variation with temperature	$-108 \text{ m}^{-1} \text{ K}^{-1}$	<b>30</b>

Table 5.2 Parameters used in the carrier heating model.

The following graphs show some of the results obtained from the carrier heating model.

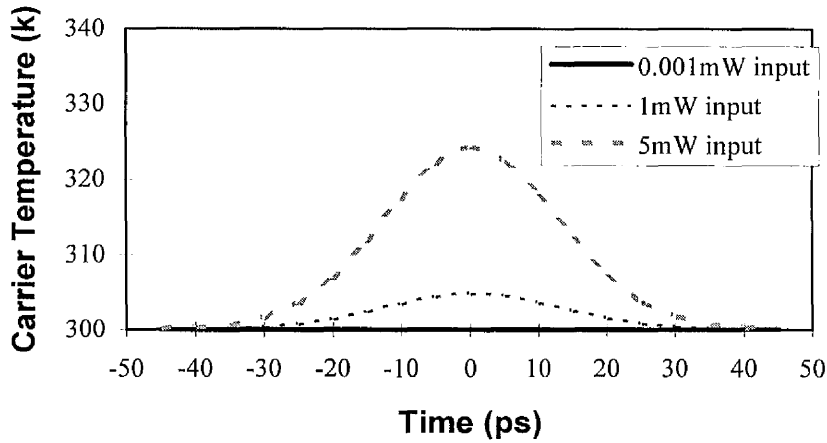


Fig. 5.29 Modelled induced temperature heating produced by a 30ps FWHM pulse for varying average powers.

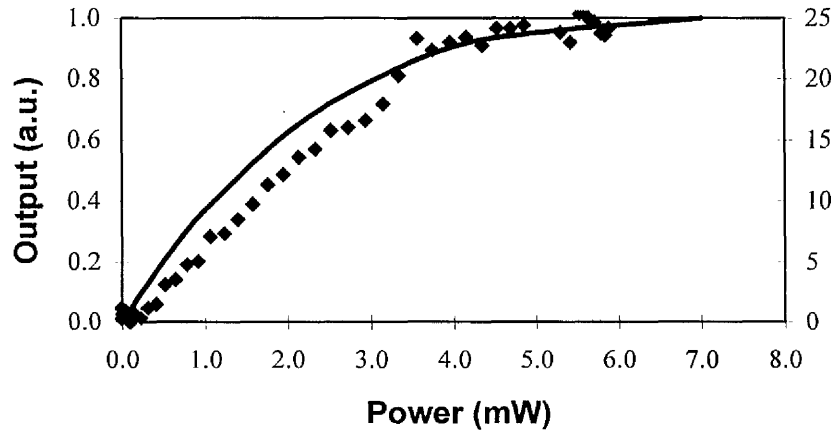
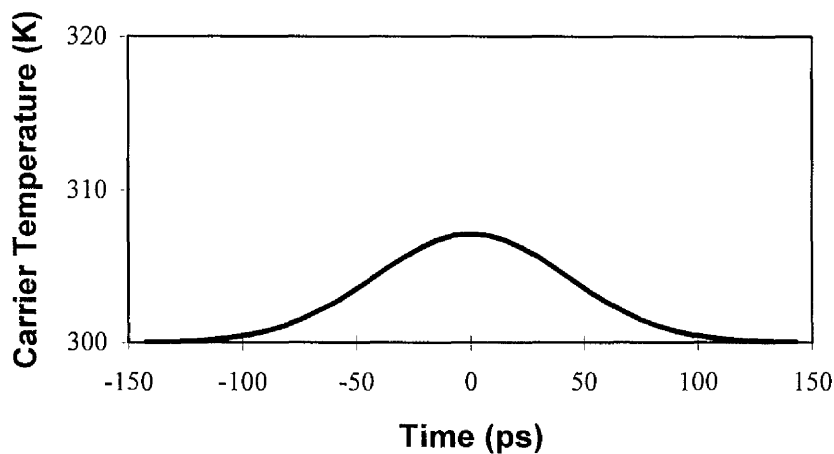


Fig. 5.30 Modelled saturation of the amplifier gain at transparency for 30ps FWHM pulsewidth at a repetition rate of 77MHz. The results of Fig 5.26 are overlaid, assuming a 20% coupling efficiency.

Fig. 5.29 shows that for powers in the milliwatt regime, for the pulse durations used, substantial heating of the distribution occurs. Fig. 5.30 shows how this heating translates into a gain saturation, which occurs for an average power of a few milliwatts, this is analogous to the experimental data of Fig. 5.26. If an output coupling efficiency of 20% is assumed both experimental and theory fit well, this is lower than the measured coupling efficiency of 50%, but it should be noted that the model ignores the linear losses which are significant, which explains this discrepancy. It should also be noted that the parameters shown in Table 5.2 are not accurately known, a good fit to the experimental data is therefore unlikely. However the shape of the experimental and calculated responses are well matched.



*Fig. 5.31 Carrier temperature changes induced by a pump pulse of 100ps FWHM, pulse energy 65pJ.*

The model was also used to analyse carrier heating for varying pulsewidths, for a fixed pulse energy of 65pJ, corresponding to an average power of 5mW at 77 MHz pulse repetition rate. Figures 5.31-5.34 show the carrier temperature for varying pulse durations. For an amplifier at transparency the shorter the pulse, the more significant the heating, the gain is therefore expected to be intensity dependent.

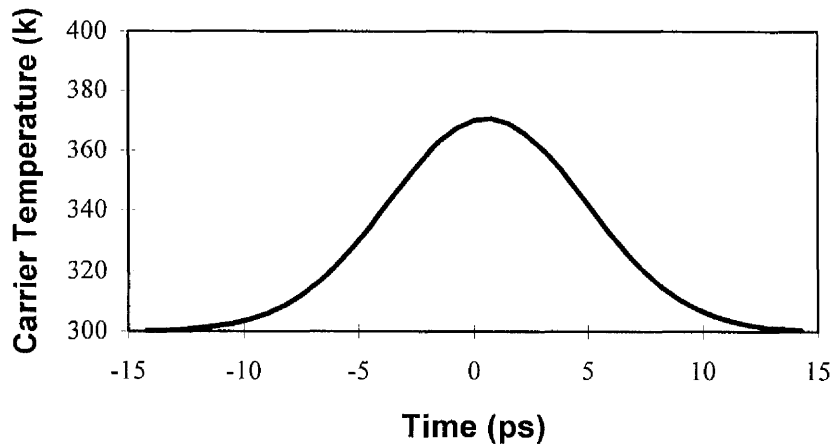


Fig. 5.32 Carrier temperature changes induced by a pump pulse of 10ps FWHM, pulse energy 65pJ.

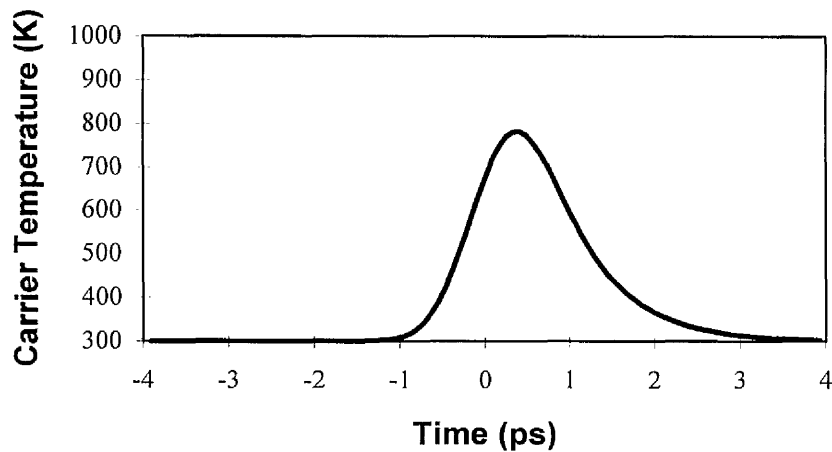


Fig. 5.33 Carrier temperature changes induced by a pump pulse of 1ps FWHM, pulse energy 65pJ.

The model was also used to compute the temperature changes for a pulse duration of 200fs, similar to the pulsewidths used in pump-probe studies elsewhere<sup>24,32</sup>. For pulses of this duration it is not valid to ignore two-photon absorption, nevertheless Fig. 5.34 neatly illustrates that the recovery time constant of the nonlinearity is limited by the  $\sim 0.5$ ps intraband relaxation time. The shape of the temperature distribution in Fig. 5.34 mirrors the gain changes seen in pump-probe studies, with a sharp falling edge and a slower recovery, with the distribution recovering in around 2ps.

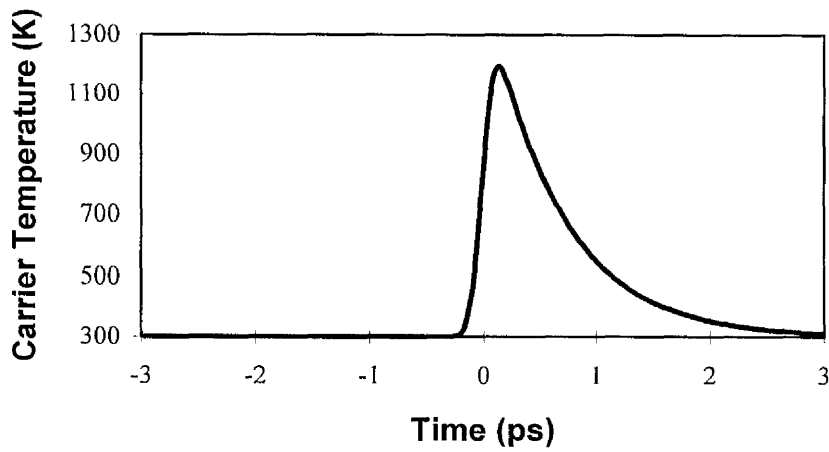


Fig. 5.34 Carrier temperature changes induced by a pump pulse of 0.2ps FWHM, pulse energy 65pJ. In reality two-photon absorption would be significant at these pulsewidths.

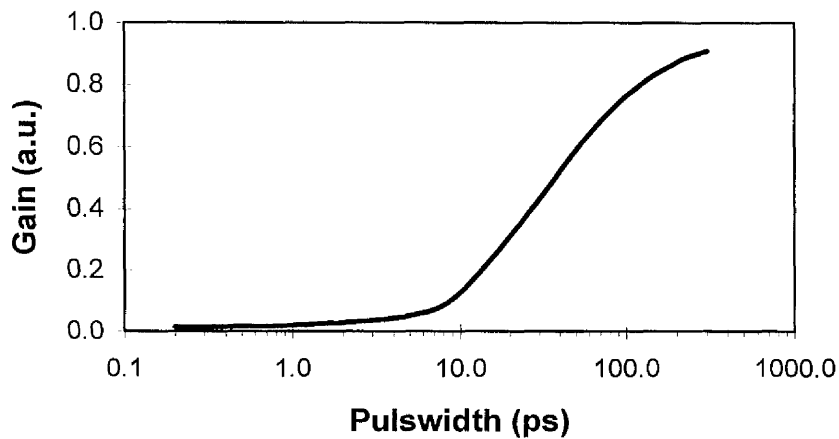


Fig. 5.35 Modelled gain for varying pulsewidths at transparency for an average power of 5mW, neglecting the effects of two-photon absorption. The unsaturated gain is one.

Fig. 5.35 shows how the temperature distributions of Figures 5.31-5.34 translate into gain, shorter pulsewidths will have a lower saturation power level at transparency. For pulse durations substantially shorter than the intraband relaxation time (0.65ps was used here) the gain becomes pulsewidth invariant, but in reality two-photon absorption cannot be ignored in these cases.

The model developed shows that carrier heating leads to a pulsewidth dependent

gain saturation. The model confirms that it was reasonable to conclude that carrier heating induced gain saturation at the transparency point occurs for an average power level of the order of a few mW inside the amplifier (for the pulse durations and energies used). The model also shows that this nonlinearity is likely to have a maximum recovery time of the order of 2ps which corresponds to a switching frequency of 500GHz.

#### **5.54 Discussion and conclusions**

The outcome of the pump-probe studies performed, indicated that, the SPM effects observed in Section 5.4 are predominantly caused by carrier heating. Carrier heating has been shown to be of considerable importance in semiconductor optical amplifiers<sup>24-29</sup> and leads to saturation effects. Many of the time-resolved studies reported in the literature<sup>24,25</sup> have used much shorter pulse durations, where the effects of TPA are more significant, these studies show that the phase shifts are accompanied by a TPA induced signal attenuation. However it seems likely that for practical amplifier applications pulse durations are more likely to be in the picosecond regime. The pump-probe and SPM studies performed here have shown that, for a pulse width of ~15ps, carrier heating effects are significant and can lead to large self-induced phase shifts at transparency, if intensities are sufficient. The data of Fig. 5.26 show that the carrier heating nonlinearity effectively saturates for modest power levels, because of the elevated temperature of the carrier distribution which reduces the gain. A model of gain saturation due to carrier heating at transparency has been developed which supports these experimental results. These saturation effects at transparency could have an important bearing on any devices utilising this nonlinearity, for example all-optical switches. It may be possible to develop an optimised geometry, which reduces switching power levels, by increasing the device length without badly compromising the insertion loss, which is length dependent. In other words there will be a trade off between the necessary switching power and device length (and hence insertion loss).

## References

- 1 A. Godefrey, J. C. Keromnes, G. Joulie, P. Lamouer, "1.55 $\mu\text{m}$  polarisation insensitive optical amplifier with strain balanced superlattice active layer", IEEE Photonics Technology Lett., vol. 7, no. 5, p. 473, 1995
- 2 B. S. Bhumbra, R. W. Glew, P. D. Green, G. D. Henshall, C. M. Lowney, J. E. Whiteaway, "High power operation of GaInAsP / GaInAs MQW ridge lasers emitting at 1.48 $\mu\text{m}$ ", Electronics Lett., vol. 26, no. 21, p. 1755, 1990
- 3 N. A. Olsson, "Semiconductor optical amplifiers", Proceedings of the IEEE, vol. 80, no.3 , p. 375, 1992
- 4 J. Macleod, "Thin film optical filters" 2<sup>nd</sup> Ed., Adam Hilger, 1986
- 5 J. O. Binder, G. D. Cormack, "Prediction of the gain versus injection current characteristics of individual semiconductor laser amplifiers", IEEE Journal of Lightwave Technology, vol. 8, no. 7, p. 1055, 1990
- 6 G. Eisenstein, R. M. Jopson, "Measurements of the gain spectra of near travelling-wave and Fabry Perot semiconductor optical amplifiers at 1.5  $\mu\text{m}$ ", Int. J. of Electronics, vol. 60, no. 1, p. 113, 1986
- 7 G. P. Agrawal, N. K. Dutta, "Semiconductor lasers", Chapter 11, 2nd ed, Van Nostrand Reinhold, 1993
- 8 R. P. Webb, W. J. Devlin, "Travelling-wave laser amplifier experiments at 1.5 $\mu\text{m}$ ", Electronics Lett., vol. 20, no. 17, p. 706, 1984
- 9 T. Mukai, Y. Yamamoto, "Gain, frequency bandwidth and saturation output power of AlGaAs DH laser amplifiers", IEEE Journal of Quantum Electronics, vol. 17, no. 6, p. 1028, 1981
- 10 J. A. Constable, I. H. White, A. N. Coles, D. G. Cunningham, "Harmonic and phase modulated distortion of analogue amplitude-modulated signals in bulk near travelling-wave semiconductor optical amplifiers", IEE Proceedings J, vol. 139, no. 6, p. 389, 1992
- 11 M. J. Adams, J. V. Collins, I. D. Henning, " Analysis of semiconductor optical amplifiers", IEE Proceedings J, vol. 132, no. 1, p.58, 1985
- 12 H. Schneider, J. D. Ralston, E. P. O'Reilly, S. Weisser, E. C. Larkins, "Gain

- switching in high speed semiconductor lasers: intermediate signal analysis”, *Appl. Phys. Lett.*, vol. 65, no. 6, p. 661, 1994
- 13 J. Wang, H. Olesen, K. E. Stubkjaer, “Recombination, gain and bandwidth characteristics of 1.3 $\mu$ m semiconductor laser amplifiers”, *Journal of Lightwave Technology*, vol. 5, no. 1, p. 184, 1987
  - 14 G. P. Agrawal, “Effect of gain dispersion on ultrashort pulse amplification in semiconductor laser amplifiers”, *IEEE Journal of Quantum Electronics*, vol. 27 no. 6, p.1843, 1991
  - 15 J. E. Bowers, B. R. Hemenway, A. H. Gnauck, D. P. Wilt, “High speed InGaAsP constricted mesa lasers”, *IEEE Journal of Quantum Electronics*, vol. 22, no.6, p. 833, 1986
  - 16 G. P. Agrawal, “Self phase modulation and spectral broadening of optical pulses in semiconductor laser amplifiers”, *IEEE Journal of Quantum Electronics*, vol. 25, no. 11, p. 2297, 1989
  - 17 G. P. Agrawal, “Effect of gain and index nonlinearities on single mode dynamics in semiconductor lasers”, *IEEE Journal of Quantum Electronics*, vol. 26, no. 11, p. 1901, 1990
  - 18 S. Ruiz Moreno, J. Guitart, “Practical method for modelling the nonlinear behaviour of a travelling wave semiconductor optical amplifier”, *IEE Proc. J*, vol. 140, no. 1, p. 39, 1993
  - 19 L. A. Coldren, S. W. Corzine, “Diode lasers and photonic integrated circuits”, Chapter 4, John Wiley, 1995
  - 20 J. E. A. Whiteaway, A. P. Wright, B. Garrett, G.H.B Thompson, J. E. Carroll, L. M. Zhang, C. F. Tsang, I. H. White, K. A. Williams, “Detailed large signal dynamic modelling of DFB laser structures and comparison with experiment”, *Optical and Quantum Electronics*, vol 26, no. 7, p. 917, 1994
  - 21 R. H. Stolen, C. Lin, “Self-phase-modulation in silica optical fibres”, *Phys. Rev. A*, vol 17, no. 4, p.1448, 1978
  - 22 R. S. Grant, W. Sibbett, “Observations of ultrafast nonlinear refraction in an InGaAsP optical amplifier”, *Appl. Phys. Lett.*, vol 58, no. 11, p. 1119, 1991
  - 23 M. A. Fisher, H. Wickes, G. T. Kenedy, R. S. Grant, W. Sibbett, “ Ultrafast nonlinear refraction in an active MQW waveguide”, *Electronics Lett.*, vol. 29,

no. 13 , p. 1185, 1993

- 24 K.L Hall, G. Lenz, A. M. Darwish, E. P. Ippen, "Subpicosecond gain and index nonlinearities in InGaAsP diode lasers", *Optics Communications*, vol. 111, p 589, 1994
- 25 M. Willatzen, J. Mark, J. Mørk, "Carrier temperature and spectral holeburning dynamics in InGaAsP quantum well laser amplifiers", *Appl. Phys. Lett.*, vol. 64, no. 2, p.143, 1994
- 26 M. Nidio, A. Suzuki, "Observation of carrier heating in a 1.5 $\mu$ m band multi-quantum-well semiconductor laser amplifier by time resolved measurement for amplified spontaneous emission spectrum", *Appl. Phys. Lett.*, vol. 65, no. 6, p. 681, 1994
- 27 A. Mecozzi, J. Mørk, "Saturation induced by picosecond pulses in semiconductor optical amplifiers", *J. Opt. Soc. Am. B*, vol. 14, no. 4, p. 761, 1997
- 28 C-Yi. Tsai, C-Yao. Tsai, R. M. Spencer, Y. Lo, L.F. Eastman, "Nonlinear gain coefficients in semiconductor lasers: effects of carrier heating", *IEEE Journal of Quantum Electronics*, vol. 32, no 2, p. 201, 1996
- 29 B. Gotatam, A. P. DeFonzo, "Theory of hot carrier effects on nonlinear gain in GaAs-GaAlAs lasers and amplifiers", *IEEE Journal of Quantum Electronics*, vol. 26, no. 10, p. 1689, 1990
- 30 Uskov, J. Mørk, J. Mark, "Theory of short-pulse gain saturation in semiconductor amplifiers", *IEEE Photonics Technology Lett.*, vol. 4, no. 5, p. 443, 1992
- 31 Uskov, J. Mørk, J. Mark, "Wave mixing in semiconductor laser amplifiers due to carrier heating and spectral-hole burning", *IEEE Journal of Quantum Electronics*, vol. 30, no. 9, p. 1769, 1994
- 32 J. Mørk, J. Mark, "Subpicosecond gain dynamics in InGaAsP optical amplifiers: Experiment and theory", *Appl. Phys. Lett.*, vol. 61, no. 19, p. 2281, 1992
- 33 J. Mørk, J. Mark, "Carrier heating in InGaAsP laser amplifiers due to two-photon absorption", *Appl. Phys. Lett.*, vol. 64, no. 17, p. 2206, 1994
- 34 J. Mørk, J. Mark, "Time resolved spectroscopy of semiconductor laser devices: experiments and modelling" *SPIE* , vol. 2399, p 146, 1995

- 35** P. J. Delfyett, A. Dienes, J. P. Hertage, M. Y. Hong, Y. H. Chang, “Femtosecond hybrid mode-locked semiconductor laser and amplifier dynamics”, Appl. Phys. B., vol. 58, p. 183, 1994
- 36** J. M. Tang, K. A. Shore, “Strong picosecond optical pulse propagation in semiconductor optical amplifiers at transparency”, IEEE Journal of Quantum Electronics, vol. 34, no. 7, p. 201, 1998

## Chapter 6

# Active integrated GaAs/AlGaAs nonlinear Mach-Zehnder interferometer

### 6.1 Introduction

The large nonlinearities present in semiconductor laser amplifiers can be utilised to form all-optical switching devices (for a review of all-optical switching see Chapter 1). Of particular interest is the case where the amplifier is biased at the transparency point, as described in detail in Chapter 5. In this regime the slow recovering inter-band nonlinearities are cancelled out, leaving only ultra-fast components<sup>1-4</sup>, which recover in a picosecond time scale. At present, all-optical switches have been realised in amplifiers at the transparency point in the nonlinear directional coupler (NLDC) configuration and in polarisation rotation switches. The asymmetric Mach-Zehnder interferometer (AMZI) configuration, although more complex to fabricate than the NLDC, offers the potential of lower switching powers<sup>5,6</sup> and similar devices have proved successful in the half bandgap regime<sup>7</sup> in passive GaAs/AlGaAs waveguides.

For these reasons an active AMZI laser amplifier was fabricated in the GaAs/AlGaAs laser material system. Various configurations were produced and characterised through measurement of lasing thresholds. The linear properties of these AMZI geometries were theoretically analysed, using a BPM method. The AMZI was all-optically switched with 100fs pulses from a self mode-locked Cr:LiSAF laser at 860nm, giving an effective nonlinear index,  $n_2$  of  $2 \times 10^{-12} \text{ cm}^2 \text{ W}^{-1}$ . This is to our knowledge the first time all-optical switching has been shown in an Mach-Zehnder using the nonlinearity present in laser amplifiers at transparency. A Mathematica program was developed to model the observed experimental switching behaviour. This model shows good agreement with the experiment and allows the values of the nonlinear index  $n_2$  and

the two-photon absorption coefficient,  $\beta$  to be estimated although the experimental uncertainties mean that an accurate estimate is not possible.

Finally in this chapter, improvements to the AMZI are suggested and its performance is compared with other all-optical switching devices.

## 6.2 Nonlinear Mach-Zehnder interferometer

The Mach-Zehnder interferometer is a familiar device in optics and is used in switching and sensor applications. In the Mach-Zehnder a beam of light is split into two paths, which later recombine. The useful property of the Mach-Zehnder occurs when the effective length of one arm is changed with respect to the other. This alters the interference between the two signals at the recombination point.

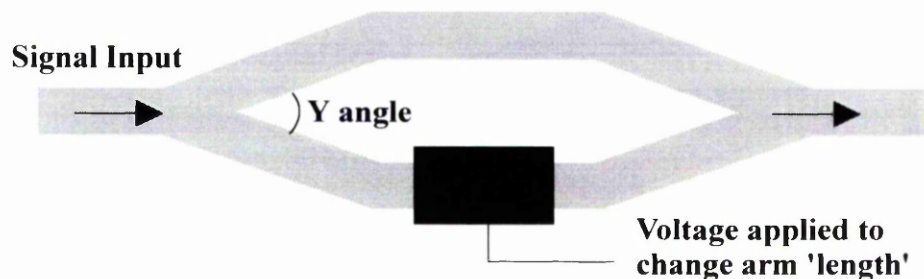


*Fig. 6.1 Linear integrated Mach-Zehnder interferometer.*

The integrated 'linear' version of the Mach-Zehnder switch, as shown above in Fig. 6.1, has long been used to form electro-optic switches<sup>8,9</sup>. Light is input into a waveguide and after propagating a certain distance it is split into two different paths, at a Y junction. The two arms then recombine to form a single waveguide again, switching off when there is a  $\pi$  phase shift between arms. This occurs because the two signals are  $\pi$  out of phase at the recombination point, the higher order 01 mode is therefore excited and, if the waveguide geometry is suitably designed, this will be radiated. The device therefore functions as a switch. There are several possible methods of obtaining the phase change between the two arms including: the electro-optic effect<sup>10</sup>, quantum-

confined stark effect <sup>11-13</sup>, Kerr effect and Franz-Keldysh effect. The power transmission characteristics of an ideal Mach-Zehnder show a cosine squared variation with arm phase change.

The nonlinear Mach-Zehnder differs from the device shown above in that the phase changes are self-induced or induced by an additional control pulse, using optical nonlinearities such as the third-order Kerr effect. By arranging the interferometer so that the light intensity is different in each arm, it is possible with sufficiently intense pulses to produce an all-optical switch <sup>5,6</sup>, as the pulses in each arm will undergo a different net self-induced phase change. Several design configurations are possible. The AMZI, shown later in Fig. 6.4, achieves the intensity variation between arms through an asymmetric Y junction which splits the power unevenly between arms. Another configuration employs a larger width waveguide in one arm and accordingly increases the guided mode area and decreases the intensity in that arm. Optical switching occurs when a  $\pi$  phase shift is induced between the two arms. The expression for the switching intensity of the all-optical AMZI is given by <sup>14</sup>,

$$I = \frac{\lambda}{2L(1-2\delta)n_2} \quad (6.1)$$

where L is the arm length,  $\lambda$  the optical wavelength,  $\delta$  is the arm power splitting ratio and  $n_2$  is the nonlinear index. In reality L will be an effective length accounting for the effects of linear losses, which are significant in amplifiers at transparency. The full expression including the linear loss term,  $\alpha$  is shown below.

$$I = \frac{\lambda}{2(1-2\delta)n_2} \cdot \frac{1}{\frac{\exp^{-\alpha L}}{\alpha} - \frac{1}{\alpha}} \quad (6.2)$$

The effects of linear losses have an influence on the switching power and also mean that there is a maximum arm length beyond which the switching power ceases to decrease. Fig. 6.2 shows the effects of linear losses on the switching intensity of a Mach-Zehnder using the values  $\lambda= 860\text{nm}$ ,  $n_2= 10^{-11} \text{ cm}^2 \text{ W}^{-1}$  and  $L=0.15\text{cm}$ . Even

substantial losses of around  $40\text{cm}^{-1}$  do not degrade switching intensities significantly, although the throughput will be poor.

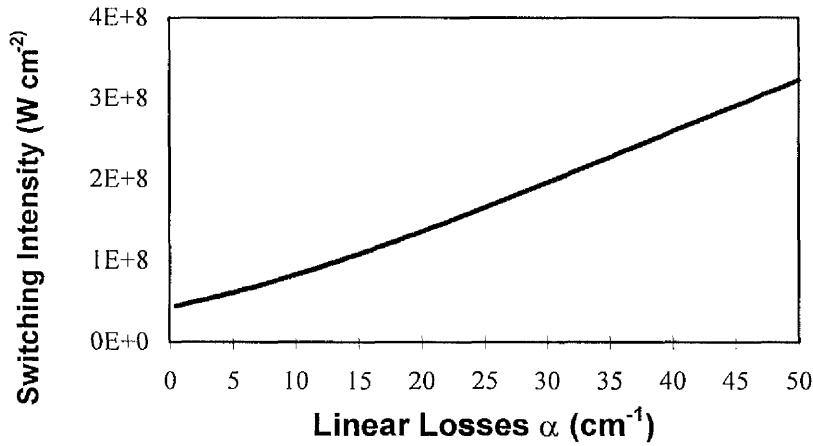


Fig. 6.2 Calculated switching power for varying linear losses of an all optical AMZI.

Using the same parameters and assuming a linear loss,  $\alpha$  of  $25\text{cm}^{-1}$ , the effect of varying device arm length on switching intensities has been calculated and is shown below in Fig. 6.3.

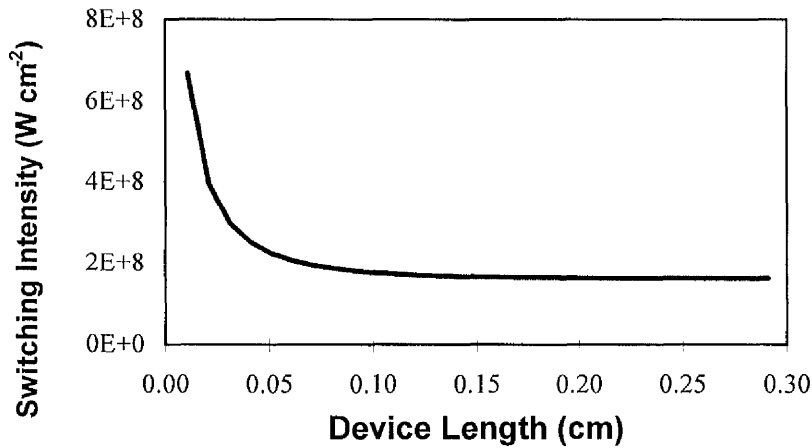


Fig. 6.3 Calculated switching power for different arm lengths in an all-optical AMZI, assuming a linear loss,  $\alpha$  of  $25\text{cm}^{-1}$ .

After a given length, no improvement in switching intensity is observed. This therefore imposes a limit on the maximum arm length that can be used to reduce switching powers. In addition, in a real device, switching behaviour is also likely to be degraded

by two-photon absorption and saturation of the nonlinearity. These factors are considered later.

### 6.21 Design of the integrated asymmetric Mach-Zehnder interferometer (AMZI)

A description of the integrated AlGaAs AMZI laser amplifier all-optical switch is now given. Fig. 6.4 shows a diagram of the AMZI configuration. The fabrication mask designed provided a range of splitting angles and arm lengths. Table 6.1 shows the various geometries available on the fabrication mask. The reasons for the designs chosen are outlined below.

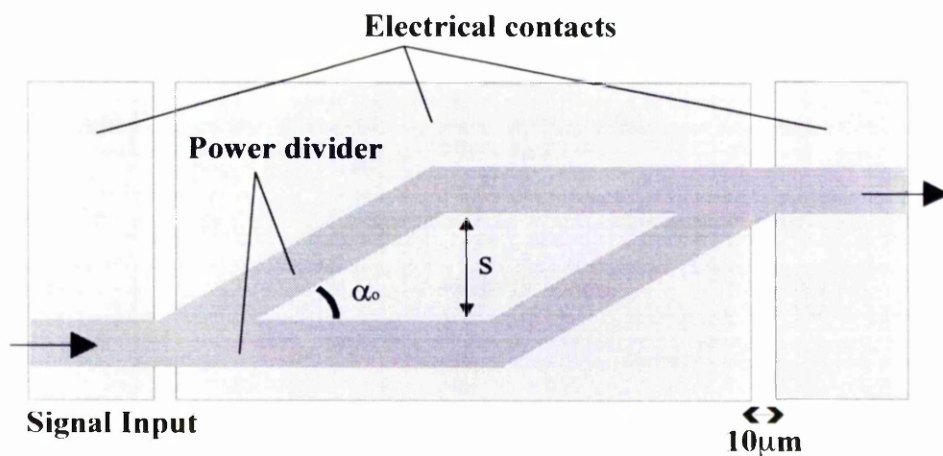


Fig. 6.4 Asymmetric Mach-Zehnder interferometer (AMZI) laser / amplifier.

Splitting angle degrees, $\alpha_0$	Total arm length	Arm separation, S
2	1.5mm	25 $\mu\text{m}$
3	1.5mm	25 $\mu\text{m}$
4	1.5mm	50 $\mu\text{m}$
3	1mm	25 $\mu\text{m}$
4	0.75mm	25 $\mu\text{m}$

Table 6.1 Parameters of the AMZI's fabricated.

A key design parameter is the length of the Mach-Zehnder arms. In general for all-optical switches it is desirable to maximise this length in order to reduce switching

intensities. However amplifiers at transparency have high linear losses due to free-carrier absorption. This imposes a limit on the Mach-Zehnder length that can be used before the linear losses limit switching improvement. Fig. 6.3 illustrates that lengths in excess of 1mm give no improvement, assuming an  $\alpha$  of  $25\text{cm}^{-1}$ . Longer length lasers also suffer from greater heat dissipation problems. For these reasons the maximum Mach-Zehnder arm length used was 1.5mm.

In order to provide an asymmetric power split, fairly large splitting angles of a few degrees are used. These large splitting angles ensure the Y branch is non-adiabatic and acts as an asymmetric power splitter rather than a modal evolution region which would result in a 50/50 split<sup>15-17</sup>. Larger bending angles also ensure that the region over which the evanescent fields interact strongly is short. The radiation losses of these asymmetric Y branches are relatively small, although at the recombination Y branch, power will be radiated mainly from the angled arm. In a real device some power loss will be associated with the blunted tip of the Y branch, a result of the limited lithographic resolution. Angle bends were utilised rather than S bends for ease of mask design and conservation of chip area. Although angle bends are more lossy for larger turn angles<sup>18</sup>, the device is expected to have considerable losses due to free-carrier absorption and the bending losses are estimated to be small compared to these. The analysis of the angled bends and Y branches employed is described later in Section 6.3.1.

A  $25\mu\text{m}$  minimum arm separation was selected to prevent excessive interaction between arms. The mask designed consisted of a range Mach-Zehnders in series with  $700\mu\text{m}$  of straight waveguide in between. This allowed the devices to be cleaved with up to  $700\mu\text{m}$  of straight waveguide after the recombining Y branch, which should be long enough to radiate any higher order slab or substrate modes that are excited.

It is important in the AMZI to ensure that the waveguiding structure rejects higher order modes. To this end, the waveguide geometry was modelled using Fwave, a finite difference 2D mode solver program developed within the department by Michael Taylor. Fwave can analyse multilayer waveguide geometries such as MQW structures. Table 6.2 shows the results of the Fwave analysis with reference to the ridge waveguide structure shown in Fig. 6.5. The modelling of mode 'cut off's' with a 2-D technique is not as clear cut as with the effective index method. When the higher order mode was observed not to be localised to the waveguide and would not yield a stable solution it

was judged to be 'cut-off'.

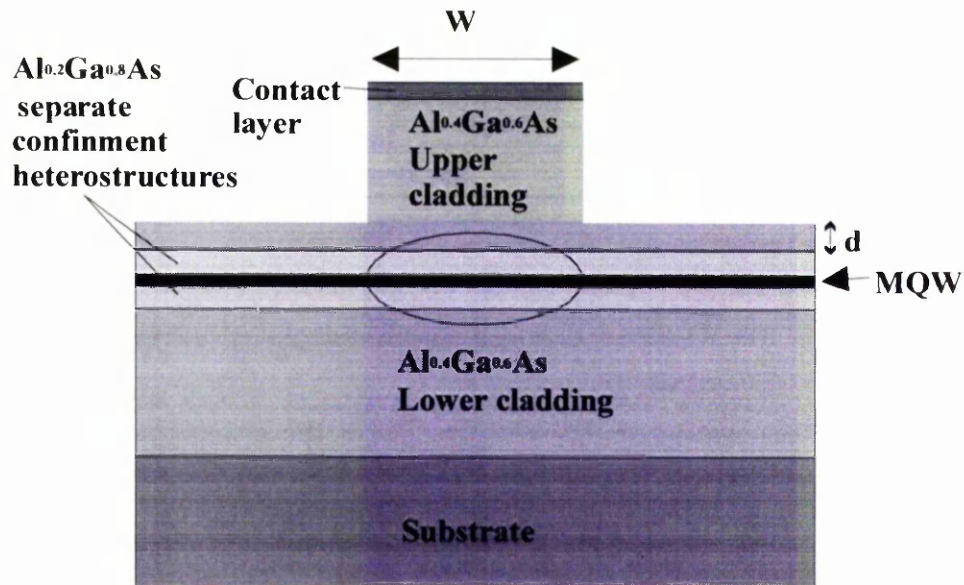


Fig. 6.5 AMZI ridge cross section for 860nm wavelength operation. The full structure details are given in Appendix I.

Unetched upper cladding depth, $d$	Ridge width, $W$	$TE_0$ supported	$TE_1$ supported	$TE_2$ supported
$0\mu\text{m}$	$3.5\mu\text{m}$	✓	✓	✓
$0.05\mu\text{m}$	$3.5\mu\text{m}$	✓	✓	✓
$0.1\mu\text{m}$	$3.5\mu\text{m}$	✓	✓	☠
$0.15\mu\text{m}$	$3.5\mu\text{m}$	✓	☠	☠
$0.2\mu\text{m}$	$3.5\mu\text{m}$	✓	☠	☠
$0.25\mu\text{m}$	$3.5\mu\text{m}$	✓	☠	☠

Table 6.2 Modes supported for various waveguiding geometries analysed using Fwave, a 2D finite difference mode solver.

The 2-D mode solver Fimmwave by Photon Design was later used to analyse the structure and Fig. 6.6 shows the obtained mode profiles.

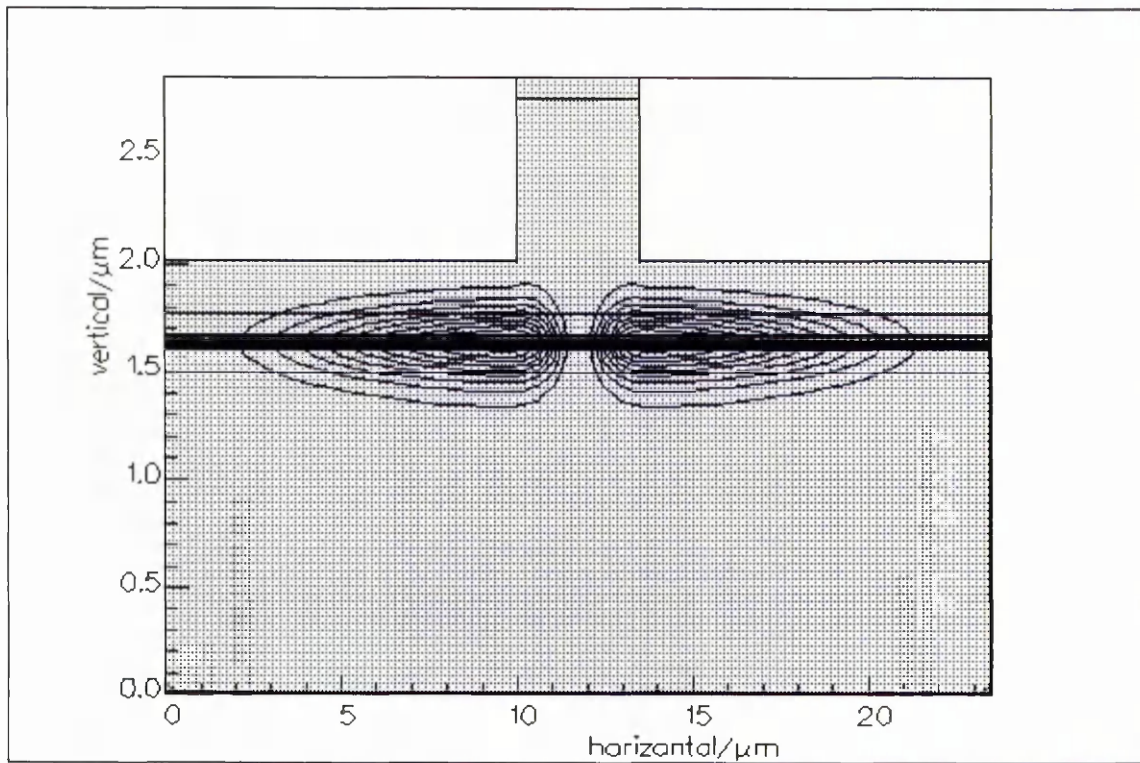
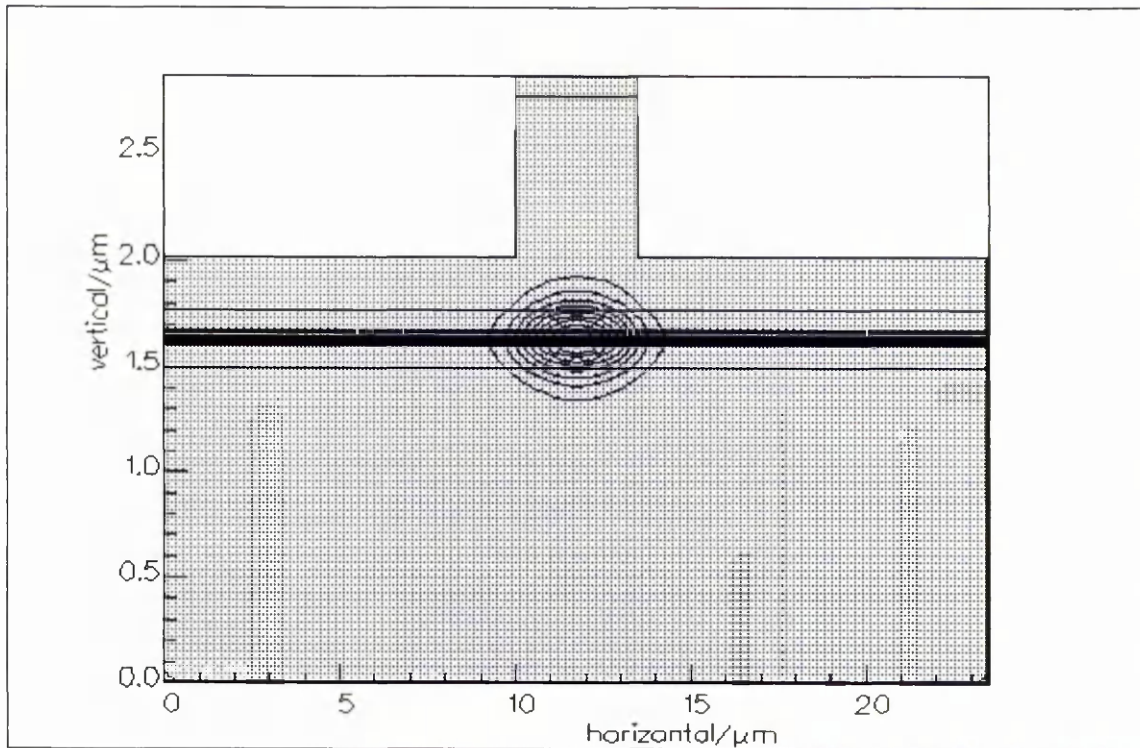
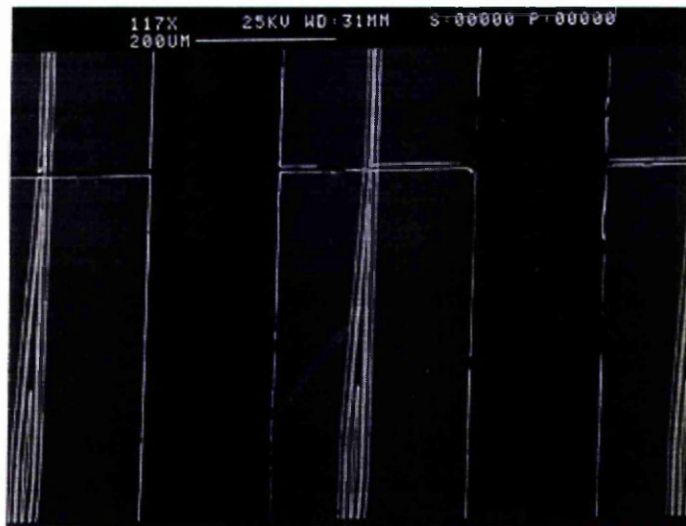


Fig. 6.6 Mode profiles of optical power for the zero order mode , top and the 1<sup>st</sup> order mode, bottom for a 3.5 wide guide with a dimension  $d=0.25\mu\text{m}$ , as defined in Fig. 6.5. The contour lines are at 10% spacing.

Fig. 6.6 illustrates that the 1<sup>st</sup> order mode is effectively a slab mode for the dimensions used and should radiate and suffer a large attenuation as it will be out with the pumped region. Following the F-wave analysis, typical geometries were a ridge width,  $w$  of  $3.5\mu\text{m}$  and a gap,  $d$  of  $0.2\text{-}0.25\mu\text{m}$  corresponding to an etch depth of  $0.85\text{-}0.9\mu\text{m}$ . A mask was also made with a waveguide width of  $2.5\mu\text{m}$ , but  $3.5\mu\text{m}$  was preferred for ease of fabrication.

A brief description of the device processing details are now given, full fabrication details are given in Chapter 3. The wafers used were 2 and 4 MQW AlGaAs MBE laser structures for operation around  $860\text{nm}$ , as detailed in Appendix I. Vertical confinement was provided by  $0.1\mu\text{m}$  thick  $\text{Al}_{0.2}\text{Ga}_{0.8}\text{As}$  separate confinement heterostructures surrounding the GaAs wells. Lateral confinement was provided by partially etching through the contact and upper cladding regions using reactive-ion etching to form a ridge waveguide structure. A diagram of a typical device cross section is shown in Fig. 6.5. A photograph of a complete Mach-Zehnder, prior to cleaving into individual chips, is shown below in Fig. 6.7. The light areas are the metal contacts, within which the waveguides are faintly visible.



*Fig. 6.7 SEM photograph of a fabricated AMZI prior to cleaving into individual chips.*

Additional SEM photos of the AMZI's are shown in Chapter 3. The straight section could also be cleaved into individual straight lasers to compare device thresholds. The devices facets were not AR coated because at transparency there are considerable linear losses due to free-carrier absorption, the presence of which should reduce any Fabry-Perot effects. Separate contacts were provided for the input and output waveguide sections and for the central section. Two mask variants were available, one which allowed the individual Mach-Zehnder arms to be biased independently of each other and one with a continuous contact for both. Isolation was achieved by leaving a 10 $\mu$ m gap between adjacent contacts. The resistance was measured to be 350  $\Omega$ . This allowed the whole device to be biased at transparency.

## **6.3 Linear characterisation of the AMZI's**

### **6.31 BPM model**

The linear properties of the AMZI fabricated, such as bending loss and splitting ratio, were modelled using Menufast, a public domain 2-D beam propagation method<sup>19,20</sup> (BPM) program from the University of Twente. This first required the waveguiding geometry to be broken down, using the effective index method<sup>21-24</sup>, to a slab providing lateral confinement.

The losses at the angle bends were first examined for the device geometries used. Bending losses occur when, because of a change in waveguide direction, part of the previously guided mode is no longer confined and therefore radiates. Fig. 6.8 shows an example of this; part of the mode continues to be guided in the new direction while part is radiated.

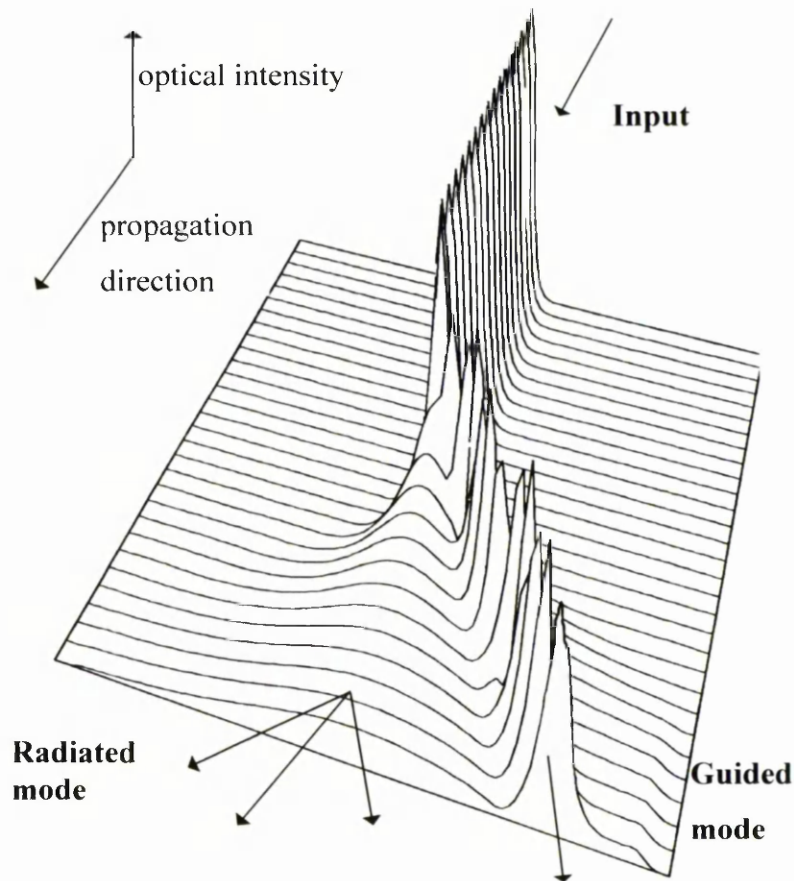


Fig. 6.8 BPM analysis of radiation losses at an angle bend. The signal is input from the top of the 'page', the apparent vertical axis represents intensity. The radiation losses can be seen to the left of the guided mode.

The calculated losses for the structures used are shown below in Fig. 6.9.

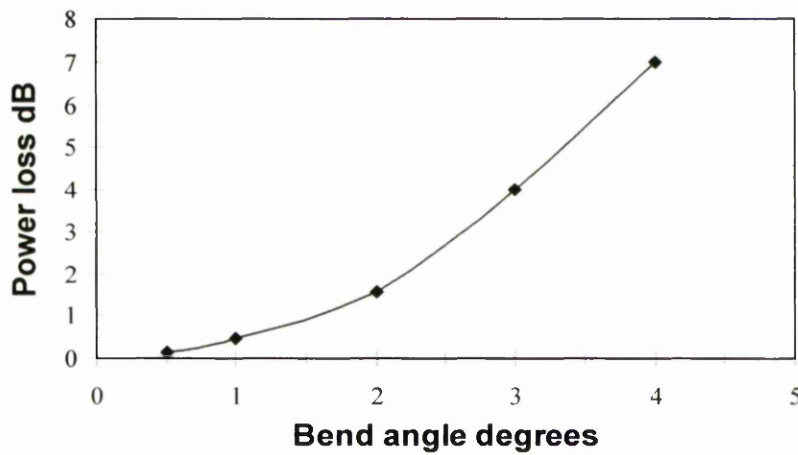
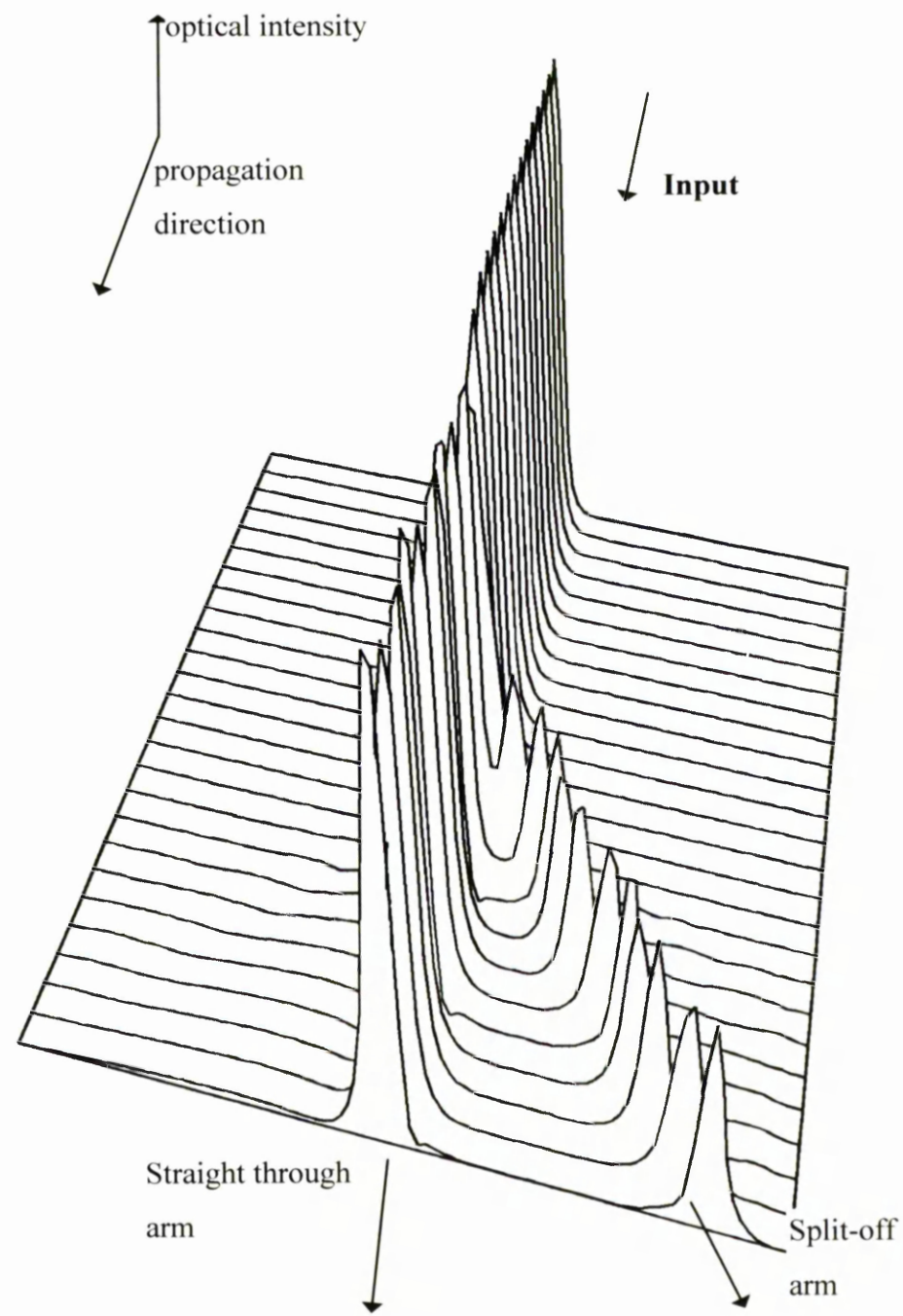


Fig. 6.9 Calculated power losses for various angle bends from the BPM analysis.

As can be seen the losses are modest for small angle bends but become large for angles of 3 and 4 degrees with most of the original power radiated.

The Y branch splitting ratios were calculated for a range of asymmetric Y branch angles, an example of the BPM output is shown in Fig. 6.10.



*Fig. 6.10 BPM analysis of a waveguide Y junction. The apparent vertical axis represents optical intensity.*

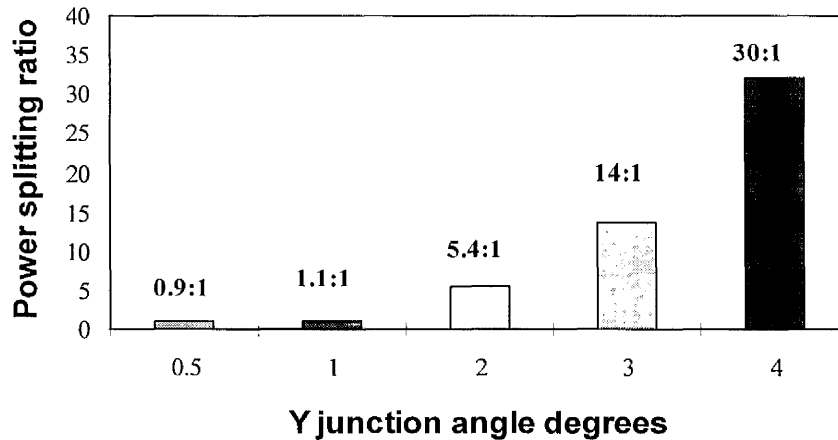


*Fig. 6.11 Modelled ratio of power travelling straight through to power coupled to the angled waveguide for various asymmetric Y branch angles.*

The results of the BPM analysis are shown above in Fig. 6.11. The obtained ratios vary from nearly symmetric for 0.5 and 1 degree splits to large ratios for the greater angles. Interestingly, for a 0.5 degree split the analysis suggests more signal would be coupled into the angled waveguide than the straight through Y branch section. This is because the guided mode redistributes itself in the region where the waveguide gradually widens before the split and more of the mode is on the side of the angled waveguide at the separation point.

The modelled power losses in the Y junctions were roughly similar at around 0.45 dB for all the geometries analysed, although in reality losses are likely to be larger due to fabrication practicalities. In particular the point of the Y branch, where the two waveguides split, will be blunted because of limited lithographic resolution. This can cause back reflections and scattering losses. The effects of a blunted AMZI tip were examined, again using a BPM approach. A blur of 1.5 $\mu\text{m}$  produced an additional modelled loss of 0.5 dB per Y junction, giving a total loss of 1dB at the Y combiner.

### 6.32 AMZI lasing characteristics

The AMZI's, because they were not AR coated, operated as lasers when driven sufficiently. This provided a convenient way of characterising their performance. For testing, devices were cleaved into chips containing straight Fabry-Perot lasers, Y

branches and complete AMZI's. In the first instance the chips were tested on a 200:1 duty cycle pulsed laser test rig. This allowed the devices' performance to be accessed without mounting. Any devices showing poor characteristics were abandoned.

As described in Appendix II, substantial information can be obtained from laser characterisation. When initially tested, the AMZI contacts, as shown in Fig. 6.4 and 6.7, were all biased together, which makes threshold comparisons with straight lasers of similar length complicated. Fig. 6.12 shows L-I characteristics for a complete AMZI, with a prominent kink. Kinked L-I characteristics occur when the laser mode hops either in wavelength or to higher order guided modes<sup>25</sup>. In this device the L-I curve kink is likely to be caused by asymmetries between the separate arms caused by fabrication inaccuracies.

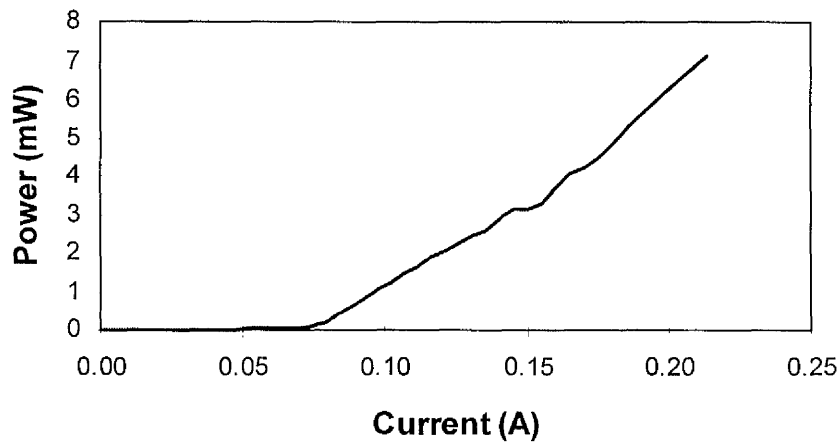


*Fig. 6.12 Kinked L-I characteristic for an AMZI laser amplifier.*

Fig. 6.13 shows the usually obtained unkinked AMZI L-I characteristics, the threshold is different than in Fig. 6.12 because the AMZI design is different. Table 6.3 shows a comparison of thresholds for different device geometries. The table confirms the BPM analysis that losses are significant, as illustrated by the higher thresholds for devices with greater bend angles. Straight Fabry-Perot ridge waveguide lasers were also cleaved from the straight portions of the AMZI mask, typical thresholds for 500 $\mu$ m devices were 8mA (corresponding to a current density of 457 A cm<sup>-2</sup>) with power outputs of 25mW per facet at 100mA.

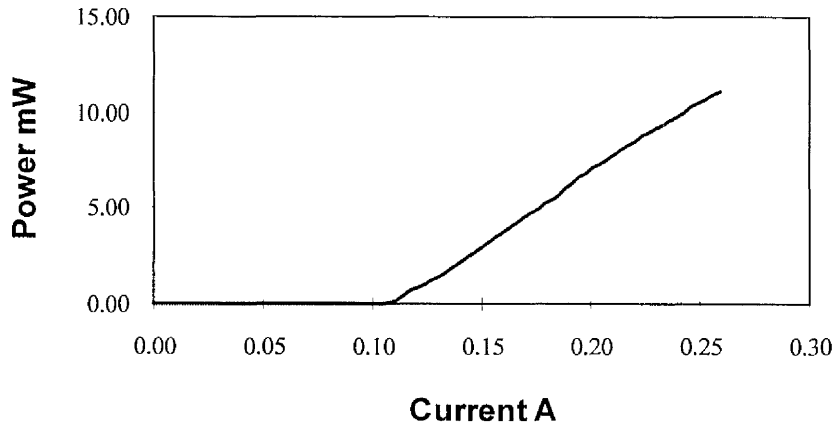


Fig. 6.13 Typical L-I characteristics for a complete AMZI.

Arm length (mm)	Y angle degrees	Input waveguide Length ( $\mu\text{m}$ )	Output waveguide Length ( $\mu\text{m}$ )	Threshold current (mA)	Threshold current density ( $\text{A cm}^{-2}$ )
1.5	2	100	100	90	818
1.5	3	100	100	101	901
1.5	4	100	100	130	1160
1	3	100	100	75	974
0.75	4	100	100	100	1680

Table 6.3 Average thresholds for comparable AMZI device geometries.

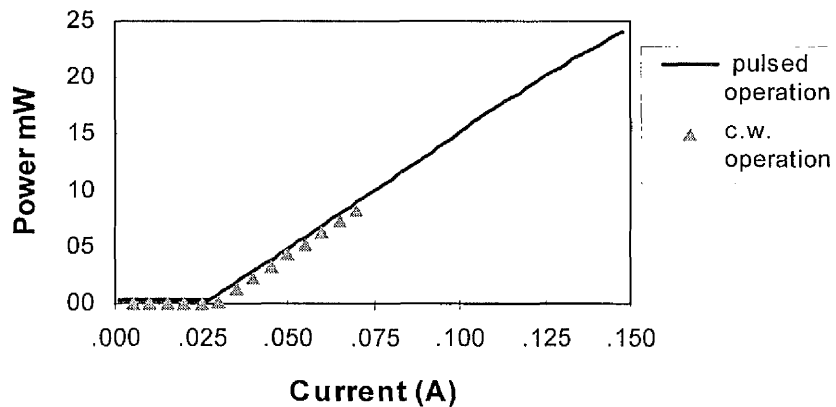


Fig. 6.14 Comparison between c.w. and pulsed operation for a  $400\mu\text{m}$  long AMZI Y junction segment.

The c.w. characteristics for selected devices were compared with their pulsed counter parts, the c.w. and pulsed thresholds showed little difference, as illustrated above in Fig. 6.14.

Devices showing good characteristics were mounted on individual gold plated copper blocks for c.w. operation and assessment.

## **6.4 All-optical switching of the AMZI -Experimental**

### **6.41 Experimental details**

The AMZI's, described previously, were tested for all-optical switching using a diode pumped self mode-locked Cr:LiSAF laser <sup>26</sup> at Strathclyde University Department of Physics and Applied Physics. The laser produced 100 fs pulses at a repetition rate of 80 MHz. The laser was tuned to 860 nm, which should be close to the gain peak in the AMZI laser amplifiers. Fig. 6.15 shows the spectrum of the Cr:LiSAF laser; the small ripples in the trace were due to a dielectric coated mirror used to align the beam to the spectrum analyser.

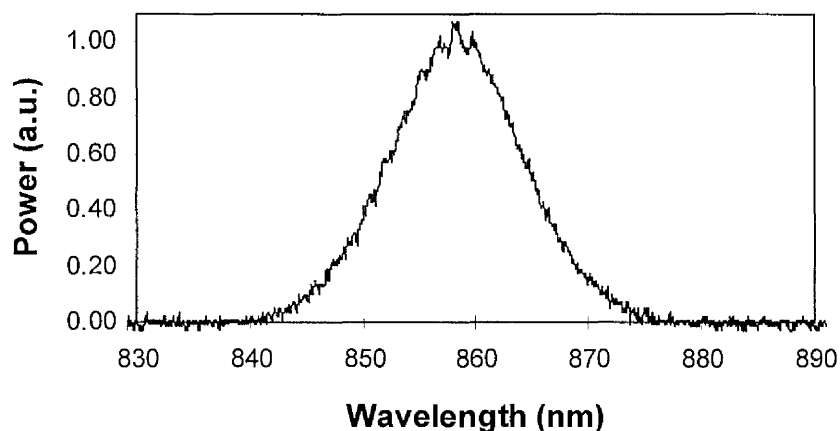


*Fig. 6.15 Spectra from the mode-locked Cr:LiSAF laser when producing 100fs pulses, bandwidth 13nm, FWHM.*

Because the pulses are significantly shorter than the anticipated recovery time of the

nonlinearity, little information can be obtained from the analysis of the spectra emerging from the laser amplifiers. It is not possible to use spectral broadening in amplifiers to measure the nonlinear index,  $n_2$ , for pulse durations this short.

The AMZI laser amplifiers were mounted p-side (ridge side) up on gold plated copper blocks, which were temperature stabilised with a thermo-electric cooler and thermistor. Coupling in and out of the devices was via microscope objective lenses. An experimental arrangement, similar to Fig. 5.7, was used to test the AMZI laser amplifiers for all-optical switching. The incident power level was adjusted using a  $\lambda/2$  waveplate on a rotating stage followed by a polariser. The power output was measured on a large area photodiode and a small percentage of the input was split off and measured in a similar fashion. The ratio of these two signals gave a measure of the AMZI transmission. A long 1500  $\mu\text{m}$  device (plus 500  $\mu\text{m}$  output waveguide) AMZI (from wafer B454) with a 2 degree Y-branch angle was used to minimise switching powers and because some of the higher angle devices exhibited greater attenuation, according to the BPM analysis.

The technique used to estimate input coupling efficiency was similar to that used in Chapter 5. For a given input power the output power can be measured, the relationship between input and output is expressed as,

$$\frac{P_o}{P_i} = (1 - R)^2 \cdot C_i \cdot e^{-\alpha l} \cdot C_o \quad (6.3)$$

where  $C_i$  and  $C_o$  are the input and output coupling overlap losses respectively.  $R$  is the facet reflectivity and the  $e^{-\alpha l}$  term represents any gain or loss in the device. In these uncoated devices the facet reflectivity is typically 0.3, the output coupling efficiency can be estimated by measuring the luminescence power, with the optical input blocked. A large area photodiode was used to measure the luminescence power close to the facet, this was then compared to the power obtained when the output was lensed on to the photodetector. Using this method the output coupling overlap was measured as 0.61 for a 40x objective. The only remaining unknown is the device's linear loss (or gain), at transparency the linear loss can be obtained from laser characterisation data, as described in Appendix II. Free carrier absorption losses are typically within the range of

7-  $35 \text{ cm}^{-1}$  (although a linear loss of  $35 \text{ cm}^{-1}$  would be a very poor for an AlGaAs laser), depending on the material structure and quality. Scattering loss, caused by etch roughness which scatters light into higher order modes, also contributes to the total propagation loss, but this is normally small compared to free carrier absorption.

Two  $500 \mu\text{m}$  long straight waveguide devices were measured at transparency, the fractional throughputs were 1.30% and 1.04 %. If an assumption is made as to the value of the free carrier absorption, an estimation of the coupling efficiency can be made. The estimates this gives are an overall input coupling efficiency of 4% for  $\alpha=7 \text{ cm}^{-1}$ , and 16% for  $\alpha=35 \text{ cm}^{-1}$  and a coupling efficiency of close to 10% for  $\alpha=25 \text{ cm}^{-1}$ . For the AMZI analysis a coupling efficiency of 10% (+/- 6%) is assumed.

#### 6.42 AMZI switching results and error analysis

Fig. 6.16 shows the all-optical switching characteristic obtained for a device with a 2 degree Y angle and a 1.5mm arm length. On the vertical axis is plotted the normalised device transmission. A  $\pi$  phase shift is achieved for a peak power of 30W in the device or a pulse energy of 3pJ, assuming a coupling efficiency of 10%. No similar effects were observed with c.w. input or for straight waveguides. Although other AMZI configurations were available, because of time pressures it was not possible to investigate them fully.

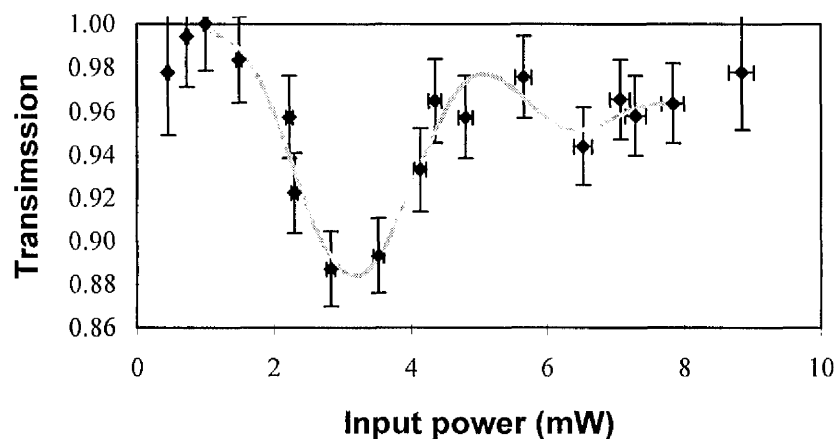


Fig. 6.16 All optical switching of the AMZI for 100fs pulse input. The switching point corresponds to a peak power of 30W in the device or a pulse energy of 3pJ.

The error bar analysis is described in detail in Appendix VI. Consecutive repeat measurements also indicated that the experimental uncertainties are significantly smaller than the measured switching contrast, showing that the response was due to genuine switching. Of relevance in optical switches is the contrast ratio, which is defined as the ratio of the maximum to the minimum transmission of the switch. The contrast ratio achieved here is poor, only 1 : 0.88. Another way of looking at this is the extinction ratio which is only 0.5dB or 12%. The possible reasons for this poor switching contrast are covered in the next section

## **6.5 All-optical switching of the AMZI- analysis and discussion**

In this section the performance of the AMZI is analysed, in particular the reasons for the poor switching contrast. Comparisons are also made with other published work on amplifiers at transparency. A program has been developed to model the switching characteristic of the AMZI and good agreement between the experimental and modelled data is seen.

### **6.51 Comparison with other work in amplifiers at transparency**

From the graph of the Mach-Zehnder switching characteristic, Fig. 6.16, the effective value of  $n_2$  can be calculated. The self induced phase shift between the two arms of an AMZI is given by Equation 6.4,

$$\Delta\phi = \frac{2 \cdot \pi \cdot n_2 \cdot I \cdot (1 - 2\delta)}{\lambda} \cdot \left[ \frac{1 - e^{-\alpha \cdot L}}{\alpha} \right] \quad (6.4)$$

where I is the switching intensity, L is the arm length,  $\lambda$  the optical wavelength,  $\delta$  is the

arm power splitting ratio,  $n_2$  is the nonlinear index and  $\alpha$  is the linear loss due primarily to free-carrier absorption. The switching intensity which corresponds to a  $\pi$  phase shift is expressed as,

$$I = \frac{\lambda}{2(1-2\delta)n_2} \cdot \frac{1}{\frac{\exp^{-\alpha L}}{\alpha} - \frac{1}{\alpha}} \quad (6.5)$$

The values assumed are  $\alpha = 25 \text{ cm}^{-1}$ , as estimated from laser threshold data and  $\delta = 0.16$ , from the BPM analysis. The modal area was calculated to be  $1.75 \text{ } \mu\text{m}^2$  for the 4MQW ridge waveguide structures used. The input coupling efficiency was estimated to be 10%, allowing for the overlap integral and facet reflectivity. Using these parameters the nonlinear index,  $n_2$  was calculated to be  $1.2 \times 10^{-12} \text{ W cm}^{-2}$ , neglecting two-photon absorption. If the two-photon absorption coefficient is assumed to be  $30 \text{ cm GW}^{-1}$  a  $n_2$  of  $2.0 \times 10^{-12} \text{ cm}^2 \text{ W}^{-1}$  is calculated. In reality the analysis is more complicated than Equation 6.4 suggests and for this reason a Mathematica program, described later, was used to include additional factors such as two-photon absorption. The effect of the initial attenuation that occurs before the Y junction split was included as was the modelled loss of 2 dB due to the angle bends, although this has only a small effect as significant absorption occurs before the bend. Not included in the calculation were the effects of losses due to blunting of the Y branch tip, which were modelled to be 1dB, which means the calculated  $n_2$  is likely to be slight underestimate. There are also significant uncertainties in derivation of the value of  $n_2$  from the results, this is discussed later.

The nonlinear index,  $n_2$ , has also been measured by other groups <sup>27-29</sup> and slightly larger values have been measured. Pump-probe measurement techniques in AlGaAs bulk laser material in the small signal regime point to  $n_2$  values of  $5 \times 10^{-12} \text{ cm}^2 \text{ W}^{-1}$ . The nonlinear index in InGaAsP has also been measured from small signal pump probe experiments to be  $\sim 1 \times 10^{-12} \text{ cm}^2 \text{ W}^{-1}$ , depending on the nature of the laser active region.

The AMZI described here is compared with the AlGaAs nonlinear directional coupler (NLDC) of Lee et al <sup>1</sup> which switched from the bar point to the 3 dB position for an input pulse energy of 6 pJ for TE polarisation, using pulses of 200 fs FWHM from a

self-mode-locked Ti-sapphire laser. The structure of the NLDC was similar to that used here, both employed 100Å thick GaAs quantum wells with Al<sub>0.2</sub>Ga<sub>0.8</sub>As barriers, however the AMZI used a thicker barrier layer, 100 Å compared to 50 Å. The AMZI structure used here employs fewer quantum wells, 4 compared to 10 in the directional coupler structure. Comparing the switching powers of these two similar structures, the directional coupler switches with an intensity 5 times smaller than the AMZI. These are several effects which could lead to this difference in switching intensity and the smaller  $n_2$ , which is calculated here.

- The AMZI fabricated here is a more lossy structure than the NLDC. Bending losses were modelled as 2dB. In addition the AMZI contains a small 10 μm long unpumped region which serves to isolate the electrical contacts between the input waveguide and the Mach-Zehnder region. This unpumped region will account for additional insertion losses.
- The directional coupler is excited by pulses of longer duration, There are several competing nonlinearities in amplifiers<sup>28,29</sup>. The dominant nonlinearity depends on pulse duration. In the regime of the AMZI operation, the net phase shift will be the sum of the negative  $\Delta n$  due to two-photon absorption and the positive  $\Delta n$  due to carrier heating. Shorter pulses will experience more two-photon absorption. The NLDC of Lee et al employs a 10MQW structure and would have a greater vertical confinement factor. This would enhance the carrier heating nonlinearity compared to the 4QW structures used here. Conversely a more poorly confined structure is likely to see more two-photon absorption, which occurs mainly in the cladding. It is difficult to make a definitive conclusion on the reasons for the higher switching intensity as the coupling efficiencies are not given in Lee et al's data, although it is suggested that such a device would see more carrier heating effects.

In summary the AMZI shows higher switching intensities than the NLDC of Lee et al. This is consistent with the higher insertion losses associated with its more elaborate structure. Consequently the  $n_2$  calculated is likely to be an underestimate. The

device is also likely to see more two-photon absorption than the NLDC of Lee et al, which would further increase switching powers, if TPA is excessive.

### **6.52 Analysis of the AMZI switching characteristics**

The AMZI devices show only weak switching behaviour, with a switching contrast of only 1 to 0.88. There are several possibilities that could account for this:

- 1. Pulse-break up:** A 1:0 switching contrast ratio will only be achieved by a perfectly square pulse, in a real pulse only the peak experiences the maximum phase shift, reducing switching contrasts.
- 2. Two-photon absorption:** If significant, two-photon absorption will preferentially attenuate the signal in the Mach-Zehnder arm with most power, limiting the all-optical switching performance. The detrimental effects of two-photon absorption on switching response have been observed in a passive Mach-Zehnder<sup>30</sup>.
- 3. Competing nonlinearities:** The nonlinearity at transparency when excited with pulses of 100fs duration has both positive and negative components<sup>28</sup>
- 4. Poor radiation of higher order modes:** In the AMZI it is crucial that the waveguide is single mode, otherwise the device will not switch off properly.
- 5. Additional asymmetry in the Mach-Zehnder arms:** Even if the Mach-Zehnder arms are fabricated perfectly symmetrically and two-photon absorption is neglected there are additional factors which may lead to degraded extinction ratios. The nonlinearity in amplifiers at transparency has a significant gain component, in addition to the nonlinear refractive index component which we wish to exploit. In Chapter 5 the gain dynamics were investigated using a pump-probe technique and the gain at transparency was shown to saturate due to heating of the carrier distribution. This leads to an intensity dependent transparency current which has also been observed elsewhere<sup>29</sup>. In the literature it has been observed that the gain changes associated with a  $\pi$  phase shift can almost totally extinguish the pulse<sup>28</sup>. This nonlinear gain will clearly complicate the Mach-Zehnder response from the

ideal case.

These points are now addressed in turn.

**Pulse break up:** Taking the first point, the area under a normalised gaussian distribution is given by,

$$\frac{1}{\sqrt{2\pi}} \int_{-\infty}^{+\infty} e^{-t^2/2} \cdot dt = 1 \quad (6.6)$$

where, t is time and  $\tau$  is a constant determined by the pulsewidth. This is analogous to the total pulse power in the AMZI, assuming a gaussian pulse shape. Taking into account the cosine squared switching characteristic of the Mach-Zehnder interferometer, Equation 6.6 can be amended to give the transmission for a ‘real’ device, which is limited by the pulse wings as shown below,

$$\frac{1}{\sqrt{2\pi}} \int_{-\infty}^{+\infty} e^{-t^2/2} \cdot \text{Cos}^2\left(\frac{\phi}{2} \cdot e^{-t^2/2}\right) \cdot dt \quad (6.7)$$

this expresses the AMZI transmission for a peak phase shift of  $\phi$  between arms. Equation 6.7 is equal to 0.26 for a  $\pi$  phase shift. Rather than switching from 1 to 0, even an ideal AMZI when excited with a gaussian pulse would only switch from 1 to 0.26 because of the pulse ‘wings’. Although the non-square pulse shape does limit the switching response partially, it does not fully account for the poor switching characteristic of the AMZI.

**Two-photon absorption:** There have been few experimental measurements of  $\beta$ , the two-photon absorption coefficient, in active laser structures at energies around the band gap. However TPA has received considerable attention in passive waveguides at wavelengths below the bandgap, because of its relevance to all optical nonlinearities in

waveguides and because of its role in producing efficient waveguide autocorrelators. Two-photon absorption together with free carrier effects influence semiconductor laser and amplifier performance. A brief review of the literature on TPA in GaAs/AlGaAs is now presented.

Two-photon absorption (introduced in Chapter 2) is a nonlinear process which gives a light intensity dependent loss mechanism. The process is significant for high intensity optical signals, which primarily occur in pulsed or mode-locked lasers. For low light intensities in a semiconductor material, at wavelengths below the band edge interband absorption is expected to be small. Therefore in a semiconductor waveguide the optical loss will just be given by the residual losses caused by scattering due to waveguide surface roughness. However at high intensities, two photon absorption becomes significant. In this process an electron can experience an interband transition through the absorption of two photons, i.e. transitions which would be forbidden with one-photon absorption are now possible.

In general TPA has a wavelength dependence, at photon energies at less than half the bandgap TPA is small, at around half the bandgap a strong resonance occurs and TPA becomes significant. The wavelength response for larger photon energies, away from the resonance features, is relatively flat. TPA also shows significant polarisation dependence. The two photon absorption coefficient in GaAs and GaAs/AlGaAs waveguides has been measured in a wide range of structures for a wide range of conditions. Some of the published work is summarised in Table 6.4 below.

<b>TPA coefficient (cm GW<sup>-1</sup>)</b>	<b>Structure and measurement conditions</b>	<b>Reference</b>
45 +/-10	Si doped bulk GaAs. $\lambda=1.06\mu\text{m}$ pulsewidth=5ps	<b>31</b>
26	Bulk GaAs, TE polarisation. $\lambda=1.06\mu\text{m}$ pulsewidth=80ps	<b>31</b> In bulk GaAs most quoted values lie between 20-30 cm GW <sup>-1</sup> at 1.06 $\mu\text{m}$ for picosecond pulse excitation.
23	Bulk GaAs , $\lambda=1.06\mu\text{m}$ , pulsewidth=80ps.	<b>32</b>

20 +/- 8	GaAs / Al <sub>0.2</sub> Ga <sub>0.8</sub> As MQW waveguide with 58 periods, TE polarisation. $\lambda=1.06\mu\text{m}$ pulsewidth=90ps	<b>33</b>
31 +/- 6	GaAs single QW laser with graded AlGaAs separate confinement heterostructure with a Lasing wavelength of 0.83 $\mu\text{m}$ . The laser was pumped optically not electrically. TE polarisation. $\lambda=0.86\mu\text{m}$ pulsewidth=50ps	<b>34</b> Obtained using a pump probe technique.
11 +/- 2	85 period Al <sub>0.1</sub> Ga <sub>0.9</sub> As / Al <sub>0.25</sub> Ga <sub>0.75</sub> As MQW waveguide with a band edge of 760nm. $\lambda=0.85\mu\text{m}$ pulsewidth=3.5ps	<b>35</b> The optical source was a Q-switched diode laser.
50 +/- 25	Double QW Al <sub>0.23</sub> Ga <sub>0.77</sub> As / Al <sub>0.55</sub> Ga <sub>0.45</sub> As LED with an emission peak of 670nm. TE polarisation $\lambda=0.810\mu\text{m}$ pulsewidth=115fs	<b>36</b> Obtained from photocurrent measurements from a range of reverse biased devices.
0.15	GaAs / Al <sub>0.45</sub> Ga <sub>0.53</sub> As MQW waveguide with 54 periods, the band edge for the LH transition is 770nm. $\lambda=1.55\mu\text{m}$ pulsewidth=250fs	<b>37</b> Measured for TM input at below half the bandgap, polarisation dependence of $n_2$ and $\beta$ is observed.
Ranges from 0.2 cm GW <sup>-1</sup> at 1.625 $\mu\text{m}$ to 10 cm GW <sup>-1</sup> at 1450 $\mu\text{m}$ .	85 period GaAs / Al <sub>0.32</sub> Ga <sub>0.68</sub> As MWQ waveguide. Strong polarisation anisotropy is observed together with exciton features. pulsewidth=5ps	<b>38,39</b> Measured for both polarisations across a wavelength region corresponding to half the band gap.
Ranges from 2	Bulk GaAs waveguide (band gap 0.87 $\mu\text{m}$ )	<b>40</b>

cm GW <sup>-1</sup> at 1.7μm to 32 cm GW <sup>-1</sup> at 1.45μm	with a 1.3μm thick guiding region. pulsewidth=8ps	
34	Theoretical calculation, a wavelength of 1.064 is assumed.	<b>41</b>
Close fit to experimental data.	Theoretical calculation.	<b>42</b>

Table 6.4 Summary of measured and theoretical values for the two-photon absorption coefficient,  $\beta$ , in GaAs / AlGaAs.

In this section the value of  $\beta$  assumed is that measured by Lee et al as 30 cm GW<sup>-1</sup> in an unbiased AlGaAs laser structure at 860nm<sup>34</sup>. Using this value of  $\beta$ , the influence of two-photon absorption can be accessed. The influence of linear losses and two-photon absorption experienced by a propagating optical signal in a straight waveguide is expressed by,

$$\frac{dI}{dz} = -\alpha \cdot I - \beta \cdot I^2 \quad (6.8)$$

where I is the intensity,  $\alpha$  is the linear absorption coefficient and  $\beta$  is the two-photon absorption coefficient. If this term is integrated Equation 6.9 is obtained.

$$I_{out} = \frac{I_m \cdot \alpha \cdot e^{-\alpha l}}{\alpha + \beta \cdot I_m \cdot (1 - e^{-\alpha l})} \quad (6.9)$$

Which can be simplified by introducing an effective length,  $l_{eff} = (1 - e^{-\alpha l}) / \alpha$ , giving Equation 6.10.

$$I_{out} = I_m \cdot \frac{e^{-\alpha l}}{1 + \beta \cdot l_{eff} \cdot I_m} \quad (6.10)$$

Clearly two-photon absorption becomes important when  $\beta \cdot l_{eff} \cdot I_m$  is not significantly less

than one. In the AMZI switching is obtained for 3mW average power. This corresponds to a peak power of 375W or 37.5 W peak power coupled into the device, assuming a coupling efficiency of 10% and an active area of  $1.75\mu\text{m}^2$ . In the AMZI this gives a value  $\beta \cdot L \cdot I_{\text{in}}$  of 9.63, although the inclusion of linear losses in the effective length term reduces this by a factor of 4. Even so two-photon absorption cannot be ignored.

The simple calculation, shown above, shows that two-photon absorption is not insignificant when pulses of this duration are used, and for this reason its effect on the Mach-Zehnder switching response is now more fully quantified. Firstly the nonlinear phase shift is considered, which is given by,

$$\phi = k \cdot \int_0^L n_2 I \cdot dz \quad (6.11)$$

where  $k$  is the vacuum wavenumber,  $n_2$  is the nonlinear index and  $L$  is the length over which the phase shift occurs. Upon integration, using Equation 6.9 to express  $I$ , Equation 6.12 is obtained for the self-induced phase shift.

$$\phi = \frac{k \cdot n_2}{\beta} \cdot \text{Log} \left[ \frac{-\alpha - I \cdot \beta + I \cdot \beta \cdot e^{-\alpha \cdot l}}{-\alpha} \right] \quad (6.12)$$

For simplicity the effects of the linear loss can be ignored, leading to Equation 6.13, the induced phase shift in a straight waveguide.

$$\phi = \frac{k \cdot n_2}{\beta} \cdot \text{Log}[1 + I \cdot \beta \cdot l] \quad (6.13)$$

The variation of the AMZI transmission, with intensity is given by the following expression,

$$\text{Transmission} = I_a - I_b \sin^2(\Delta\phi) \quad (6.14)$$

where  $I_a$  and  $I_b$  are the output intensities of each respective Mach-Zehnder arm and  $\Delta\phi$  is the difference in the self-induced phase shift in each arm, obtained from 6.13. Using Equation 6.9 and taking  $\delta:1-\delta$  to be the Mach-Zehnder split ratio, Equation 6.14 becomes,

$$Transmission = \frac{\delta \cdot I_m \cdot (1-\delta)}{1 + \beta I_m \delta} - \left[ \frac{\delta \cdot I_m \cdot (1-\delta)}{1 + \beta I_m (1-\delta)} \right] \cdot \sin^2(\Delta\phi) \quad (6.15)$$

where  $I_m$  is the input intensity. This is an expression for the transmission of an all-optical AMZI including the effects of two-photon absorption and linear losses.

A Mathematica program, listed in Appendix V was used to solve Equation 6.15 for various values of  $\beta$ , leading to the graphs of Fig. 6.17. The parameters used were  $n_2=2.5 \times 10^{-12} \text{ cm}^2 \text{ W}^{-1}$  and  $\delta=0.16$ , with the other parameter values as used previously.

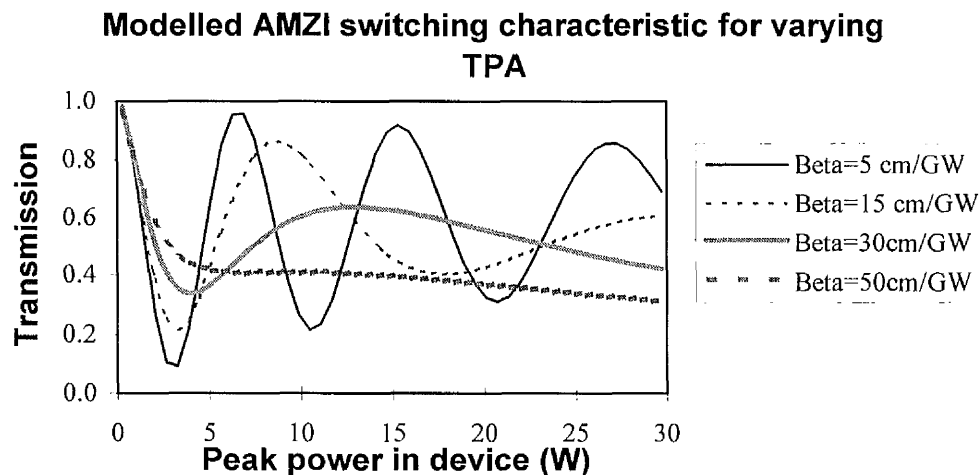


Fig. 6.17 Modelled effect of two-photon absorption on AMZI switching power and contrast ratio.  $\beta$  has been measured to be  $30 \text{ cm GW}^{-1}$  in AlGaAs lasers.

From the above graph it can be seen that two-photon absorption can significantly affect the switching characteristics. For the analysis of Fig. 6.17, the  $n_2$  value was adjusted to produce a switching intensity similar to that observed in the real device. Assuming  $\beta=30$

$\text{cm GW}^{-1}$ , the switching response is degraded, however the calculated characteristics are not similar to those observed. TPA would limit contrast ratios but not to the degree seen. Larger values of  $\beta$  than those plotted above lead to a  $1/\text{intensity}$  decay, as expected from Equation 6.9. Two-photon absorption alone cannot account for the obtained switching characteristics.

**Competing nonlinearities:** As mentioned previously the nonlinearities in amplifiers at transparency, when perturbed by pulses of  $<1\text{ps}$  duration, show nonlinear components with opposite signs<sup>1,28,29</sup>. The AMZI will see the net phase shift, whilst any competing effects would increase switching powers by cancelling each other out, they would not compromise contrast ratios. The NLDC of Lee et al was operated in a similar regime and switched from 0.8 to 0.4 in the cross state.

**Rejection of higher order modes:** Although the structures were modelled as single mode it is difficult to produce laser structures that are truly single mode. If the guides are slightly multimode this will have a marked effect on the switching response.

A 2-D BPM program, Prometheus from B.B.V. software was used to investigate the radiation of the higher order mode excited at the Mach-Zehnder recombination point. The index step between ridge and slab was calculated to be 0.0027 using a slab solver, this was later compared with a 2-D mode solver and a similar value was obtained. The plots of Fig 6.18 show the BPM analysis for a  $3.5\mu\text{m}$  guide width (the geometry used) and a  $1.5\mu\text{m}$  wide waveguide.

The BPM analysis of Fig. 6.18 reveals that for a  $3.5\mu\text{m}$  wide guide, as used, significant power remains in the vicinity of the waveguide. In a real device, following the mode profiles of Fig. 6.6, the 1<sup>st</sup> order mode is poorly confined and is largely out with the pumped region. When the AMZI was tested the output spot was imaged onto a CCD camera. Higher order guided modes were not observed, although stray light in the slab regions made observation difficult. The L-I characteristics of the amplifiers also did not show any large discontinuities associated with mode jumps. Although the modelling suggests that the 1<sup>st</sup> order mode does not decay quickly, it will present less of a problem in a real device and therefore poor mode rejection is unlikely to fully explain the observed switching characteristics.

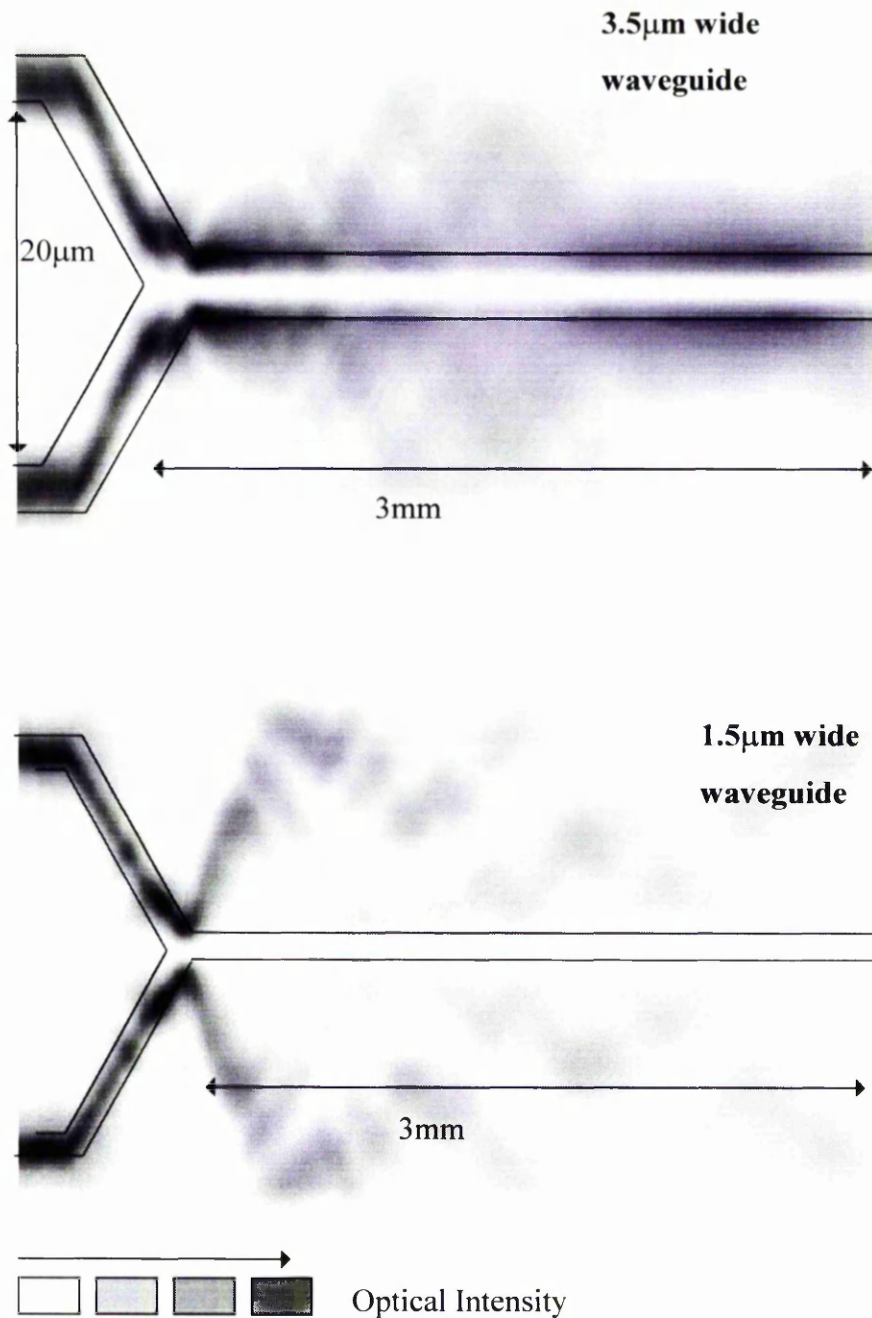


Fig. 6.18 BPM analysis of a Mach-Zehnder with a  $\pi$  phase shift between arms for a 3.5µm wide guide, top and a 1.5µm wide guide, bottom. The 1st order mode is radiated almost fully after 300µm in the case with the narrower guide but fails to radiate completely when a wider guide is used even after 3mm.

**Asymmetry in the Mach-Zehnder arms:** The data from other pump-probe studies<sup>28,29</sup>, conducted using similar pulse durations to the AMZI switching experiment described

here, show a significant gain nonlinearity is associated with a  $\pi$  phase shift. These pump-probe studies show that the gain nonlinearities can lead to an almost complete absorption of the pump signal. Similar modelled results are shown in Chapter 5. Hultgren et al <sup>27</sup> quote a linewidth enhancement factor of 2 for the dynamics associated with carrier heating in AlGaAs laser amplifiers and we can use this to estimate the gain reduction associated with a  $\pi$  phase shift, assuming the nonlinearity does not saturate. The linewidth enhancement factor was described in Chapter 1 and can be defined as,

$$\alpha = \frac{\text{Re}(\chi)}{\text{Im}(\chi)} = -2 \cdot k_0 \cdot \frac{\Delta n}{\Delta g} \quad (6.16)$$

where  $k_0$  is the wavenumber,  $\Delta n$  and  $\Delta g$  are the induced gain and index changes. In the AMZI, neglecting any additional loss mechanisms, a  $\pi$  phase shift for an arm length of 1.5mm leads to a  $\Delta g$  of  $2.1 \times 10^3 \text{cm}^{-1}$ . This leads to an attenuation of 95% of the original signal or a gain reduction of 13dB. The other arm, assuming a 5.4:1 split ratio sees a lesser gain reduction of 45%. In this case the switching contrast would be limited to 50%. The nonlinear gain due to carrier heating will have a similar effect on the switching response as TPA, because in both cases the light in the straight through arm is preferentially attenuated.

The transparency condition in amplifiers at transparency can be influenced by the light intensity <sup>29</sup>. If this is significant in the AMZI it would mean that the effective bias conditions seen by the pulses in each arm are different. This is not an additional effect but an artefact of the gain saturation phenomena described above.

A fabrication defect in one arm of the device could lead to a switching response similar to the one observed, however the devices were visually examined and no obvious defects were observed.

### **6.53 Unified AMZI switching model**

As described in the previous section, the AMZI switching characteristics are influenced by many factors and until now these have been dealt with in isolation. A Mathematica program, listed in Appendix V, was developed to model all of these competing effects.

The modelled switching powers are within 15% of the experimental data for a broad range of  $\beta$  and  $n_2$  values. This allows the boundaries within which  $n_2$  and  $\beta$  lie to be calculated for this GaAs/AlGaAs laser structure.

The model takes Equation 6.14 as its starting point and also provides a facility for the incorporation of the following effects:

- Linear losses,  $\alpha$ , which are mainly due to free-carrier absorption in amplifiers.
- Two-photon absorption. This is included using Equation 6.12 for the self-induced phase shift and Equation 6.9 which gives the attenuation due to two-photon absorption and free carrier absorption. The attenuation in the initial AMZI straight input section is also included.
- Pulse shape. In reality the AMZI is not switched by a ‘top hat’ shaped pulse and this leads to a decrease in the switching contrast. This is included using Equation 6.7 at all points in the switching characteristic.
- The program allows additional asymmetries in absorption and phase to be introduced between Mach-Zehnder arms. This could occur because of fabrication or material imperfections or because of the intensity dependent gain saturation, described in detail in Chapter 5. In the model Mach-Zehnder arm asymmetries can be introduced by allowing a difference in carrier densities between arms. Gain changes are then given by including the term  $a(N_1-N_0)$  where  $a$  is the gain coefficient,  $N_0$  is the carrier density in one arm and  $N_1$  is the carrier density in the other arm. Although these parameters are not accurately known, this approach allows the effect of asymmetries to be modelled. The linear loss / gain term now becomes  $e^{-a[(N_1-N_0)-\alpha]L}$ . If a value for the linewidth enhancement factor is assumed index asymmetries can also be included.

The table below shows values used in the AMZI switching model.

Parameter	Description	Value (estimated uncertainty limits)	Reference
$\lambda$	Wavelength	860nm	
$\beta$	Two-photon absorption coefficient. In the model this value is adjusted to give a best fit to the data.	30 cm GW <sup>-1</sup> (10-50 cm GW <sup>-1</sup> )	<b>34</b>
$\alpha$	Linear loss term	25cm <sup>-1</sup> (7-30)	<b>1</b> Also laser characterisation data in Appendix II.
$n_2$	Nonlinear coefficient	2.5x10 <sup>-12</sup> cm <sup>2</sup> W <sup>-1</sup> (0.5 - 5 cm <sup>2</sup> W <sup>-1</sup> )	<b>27,28</b>
area	Effective modal area	1.75 $\mu\text{m}^2$ (1.25-2.25 $\mu\text{m}^2$ )	From 2-D mode solver calculations using FWAVE as described in Section 6.21
$\delta$	Mach-Zehnder arm power splitting ratio $\delta:(1-\delta)$	0.156	From BPM modelling Section 6.31. This is a critical function of waveguide dimensions, but in the analysis is assumed to be accurately known.
L	Mach-Zehnder arm length	1.5 mm	
L <sub>input</sub>	Length of straight input waveguide	0.2mm	
P <sub>peak</sub> /P <sub>ave</sub>	Peak to average power ratio. For the Cr:LiSAF laser used. 80MHz repetition rate, 100fs pulse widths.	125 x 10 <sup>3</sup>	<b>26</b>

Table 6.5 Parameters used in the AMZI switching model, listed in Appendix V.

Many of the parameters in the model such as  $n_2$ ,  $\beta$ ,  $\alpha$  are not accurately known, the estimated uncertainties in these values are shown on Table 6.5. The approach taken was therefore to vary them in turn and compare the modelled switching characteristic with the experimental data. Some of the calculated switching responses are shown below.

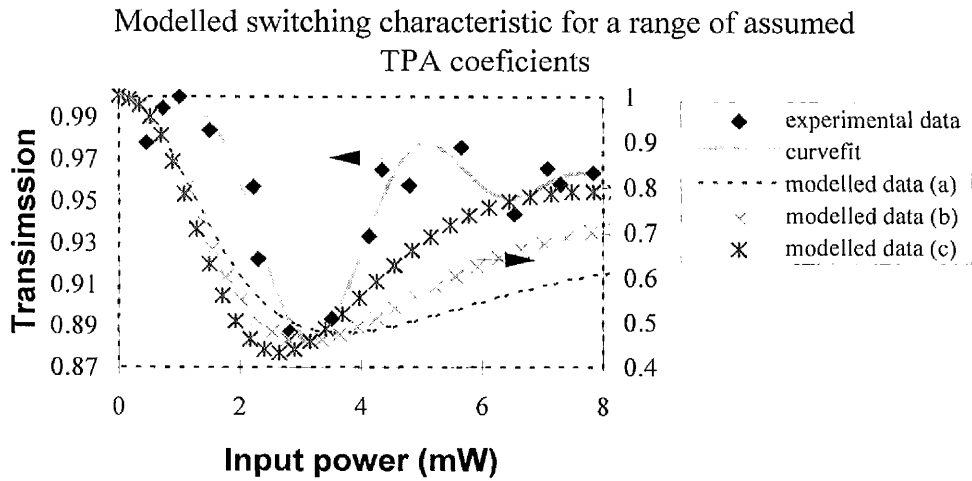


Fig. 6.19 Experimental (left side) and modelled data (right side). The parameters assumed are shown in Table 6.5, The TPA coefficient,  $\beta$  takes the values of a)  $30 \text{ cm GW}^{-1}$  b)  $25 \text{ cm GW}^{-1}$  c)  $20 \text{ cm GW}^{-1}$ .

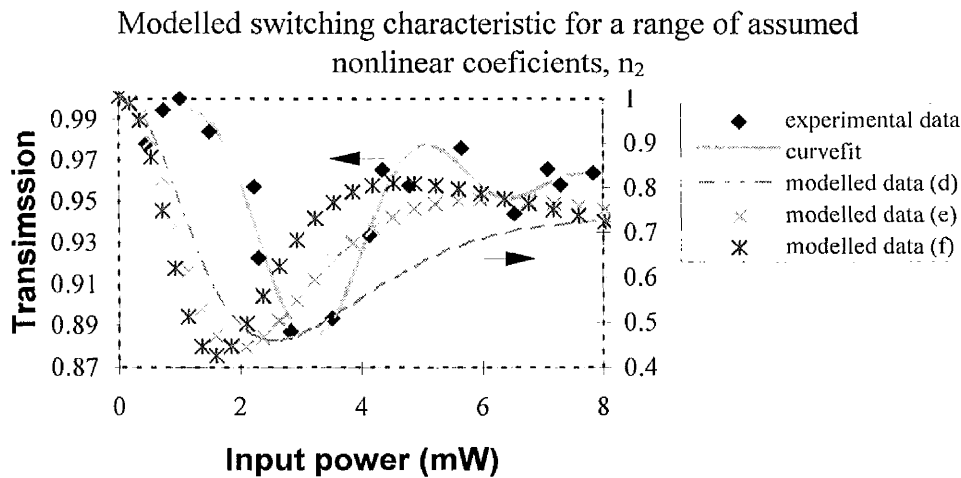


Fig. 6.20 Experimental and modelled data. The nonlinear index,  $n_2$  takes the values of d)  $3 \times 10^{-12} \text{ cm}^2 \text{ W}^{-1}$  e)  $3.5 \times 10^{-12} \text{ cm}^2 \text{ W}^{-1}$  f)  $4 \times 10^{-12} \text{ cm}^2 \text{ W}^{-1}$ . Other parameters are as in Table 6.5.

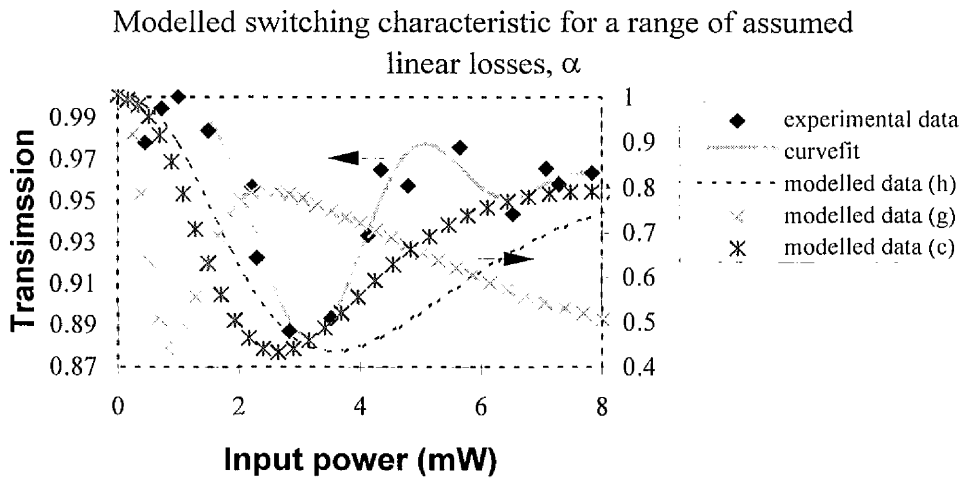


Fig. 6.21 Experimental and modelled data. The linear loss term,  $\alpha$  takes the value of c)  $20 \text{ cm}^{-1}$  g)  $10 \text{ cm}^{-1}$  and h)  $30 \text{ cm}^{-1}$ . The other parameters used were  $n_2=2.5 \times 10^{-12} \text{ cm}^2 \text{ W}^{-1}$ ,  $\beta=20 \text{ cm GW}^{-1}$ . The remainder as shown on Table 6.5.

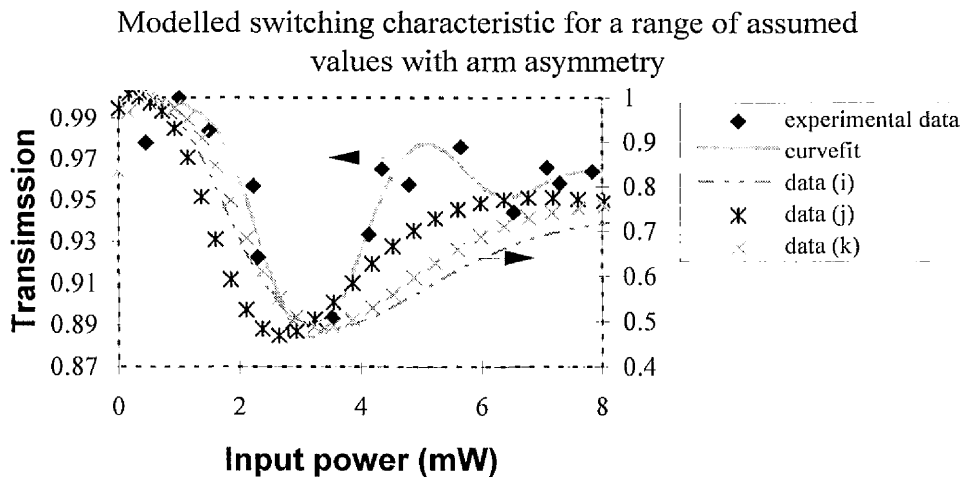


Fig 6.22 Modelled data for a AMZI with an initial phase offset between arms of i)  $\pi/3$  with an  $n_2=3.5 \times 10^{-12} \text{ cm}^2 \text{ W}^{-1}$ , j)  $\pi/3$  with an  $n_2=4 \times 10^{-12} \text{ cm}^2 \text{ W}^{-1}$  and k)  $\pi/2$  and  $n_2=4 \times 10^{-12} \text{ cm}^2 \text{ W}^{-1}$ . Other parameters as Table 6.5.

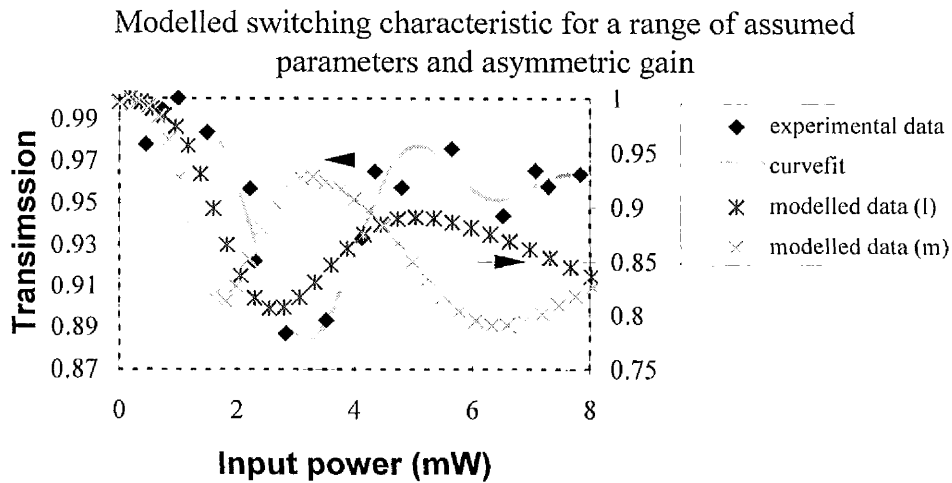


Fig 6.23 Modelled switching with different gain (loss) in each arm and an initial phase shift. The model makes the simple assumption that there is a different effective carrier density in each arm and the ratio of the carrier densities,  $N1/N2$  can be varied. It should be noted that this leads to decreased contrast ratios. The parameters used were l)  $\alpha= 30 \text{ cm}^{-1}$ ,  $\beta= 17 \text{ cm GW}^{-1}$ ,  $n_2= 4 \times 10^{-12} \text{ cm}^2 \text{ W}^{-1}$ ,  $N1/N2= 0.9$  m)  $\alpha= 25 \text{ cm}^{-1}$ ,  $\beta= 12 \text{ cm GW}^{-1}$ ,  $n_2= 4 \times 10^{-12} \text{ cm}^2 \text{ W}^{-1}$ ,  $N1/N2= 0.9$ . Otherwise parameters are as Table 6.5.

#### 6.54 Critical assessment of fit with model

Some of the data of Figures 6.19-6.23 show, subjectively a reasonable fit to the experimental data. However it is difficult to draw any definitive conclusions about the fit between model and theory, because of the large number of variables involved, many of which are not known to a high level of accuracy. A more objective method was subsequently adopted in order to determine how well the theory fits the experimental data and over what range of parameters. The degree of error between a given curve and a series of experimental data can be measured by the least squares method where the least squares rms error is given by,

$$\delta = \sqrt{\sum_{\text{data\_points}} (T - T_{fit})^2} \quad (6.17)$$

where  $T$  and  $T_{\text{fit}}$  are the experimental and modelled data values respectively. The existing AMZI Mathematica model was adapted to scan over a matrix of parameter values and perform a least squares fit to the experimental data (for input powers between 0.5 and 7mW), outputting the least squares fitting parameter as defined by Equation 6.17. The adapted programme is listed in Appendix V. In the AMZI model, the factors which influence the switching response are summarised in Table 6.5. The primary parameters are  $n_2$ ,  $\alpha$  and  $\beta$ , these are not known to a high level of accuracy, hence they are all allowed to vary in the search for the best fit. Although not accurately known, the coupling efficiency is taken to be fixed, it is assumed that the uncertainties in the coupling efficiency will lead to uncertainties in the accuracy with which  $n_2$ ,  $\alpha$  and  $\beta$  can be subsequently determined. Secondary parameters are the asymmetry in the Mach-Zehnder arms, in terms of both phase and gain.

When comparing the modelled and experimental data the contrast ratio of the switching response is ignored, both data sets are normalised. This is because a range of causes, as discussed in Section 6.52. could degrade the contrast ration.

A wide range of parameter values were scanned over. The estimated uncertainties in the parameters values, as listed on Table 6.5, defined the scan area. A phase asymmetry of up to  $0.5\pi$  was also allowed. Additional gain asymmetries although allowed for in the model were not investigated as this would have significantly increased the parameter space that was required to be scanned over.

The results of the least squares fit analysis is shown on Table 6.6. The results are divided into two, the upper data does not include a phase asymmetry, while the lower data does. The modelled curve fits are graded into 3 divisions; Division A- a good fit, Division B- a reasonable fit and Division C which encompasses everything else. A good fit corresponds to a least squares fitting parameter of less than 0.15, or in other words the average rms error between the modelled and the experimental data points is less than 15%. From the least squares fitting data the following conclusions are drawn:

- A significantly better fit is obtained if an initial arm asymmetry is allowed.
- The best fit is obtained for  $\alpha=40 \text{ cm}^{-1}$ ,  $\beta=10 \text{ cm GW}^{-1}$ ,  $n_2= 4 \times 10^{-12} \text{ cm}^2 \text{ W}^{-1}$
- A good fit of is obtained for a wide range of parameters (up to 100% variation), it is therefore not possible to determine the values of  $n_2$ ,  $\alpha$  and  $\beta$

unless one of the parameters is known to a high level of accuracy.

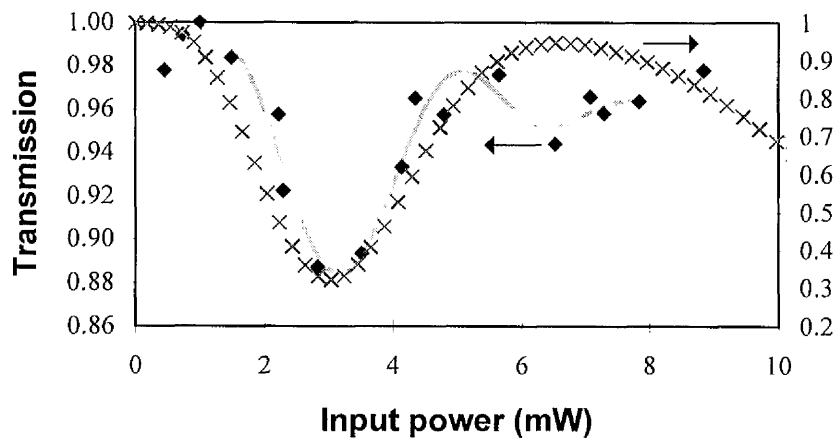


Fig 6.24 Graph showing the smallest least squares error between modelled and experimental data with no initial arm phase asymmetry. The parameters used are  $\alpha=30 \text{ cm}^{-1}$ ,  $\beta=5 \text{ cm G W}^{-1}$ ,  $n_2= 2 \times 10^{-12} \text{ cm}^2 \text{ W}^{-1}$ . The modelled data is indicated by the crosses.

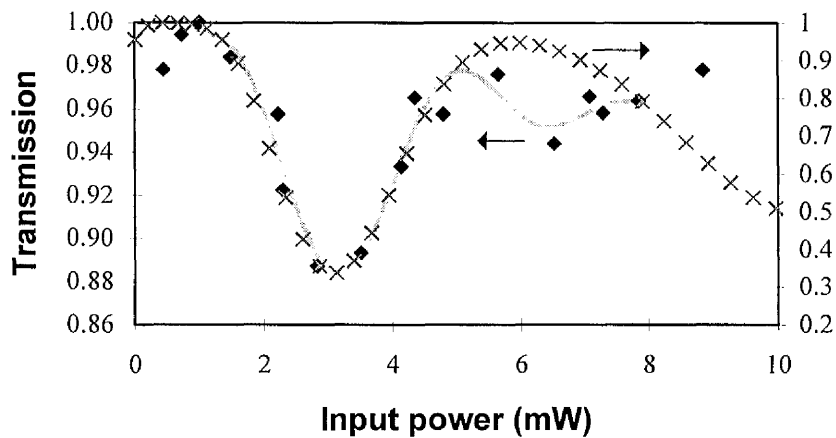


Fig 6.25 Graph showing the smallest least squares error between modelled and experimental data with no initial arm phase asymmetry. The parameters used are  $\alpha=40 \text{ cm}^{-1}$ ,  $\beta=10 \text{ cm G W}^{-1}$ ,  $n_2= 4.5 \times 10^{-12} \text{ cm}^2 \text{ W}^{-1}$ , with an initial path imbalance of  $0.36\pi$ .

Figures 6.24 and 6.25 show the best curve fits obtained with and without an initial phase shift.

alpha (cm-1)	beta (cm GW-1)	n2 (cm2 W-1)	phase asymmetry (1/π)	least squares rms error	fit quality	
30	5	2	0	0.17	B	
40	5	3	0	0.17		
35	10	3	0	0.21	C	
40	10	3	0	0.21		
45	5	4	0	0.22		
45	15	4	0	0.22		
30	10	2	0	0.25		
45	5	3	0	0.26		
40	25	4	0	0.27		
(with modeled initial phase asymmetry between arms)						
40	10	4.5	0.36	0.11	A	
30	10	3	0.36	0.12		
25	15	3	0.45	0.13		
35	20	4.5	0.36	0.13		
20	15	2.5	0.45	0.14		
45	10	4.5	0.18	0.14		
20	20	3	0.5	0.16	B	
25	15	3	0.36	0.16		
25	20	3.5	0.45	0.16		
25	20	3.5	0.5	0.17		
35	10	3	0.18	0.17		
15	20	2.5	0.5	0.18		
20	15	2.5	0.5	0.18		
40	20	4.5	0.18	0.18		
20	15	2.5	0.36	0.19		
20	20	3	0.45	0.19		
20	25	3.5	0.5	0.19		
30	20	4.5	0.5	0.19		
25	15	2.5	0.275	0.2		C
25	15	2.5	0.18	0.2		
25	15	3	0.5	0.21		
25	20	3	0.36	0.21		
25	20	3	0.275	0.21		
25	20	3.5	0.33	0.21		
25	25	3.5	0.45	0.21		
30	10	3	0.18	0.21		
30	30	4.5	0.36	0.21		
40	10	4.5	0.18	0.21		
25	20	3.5	0.36	0.22		
25	25	3.5	0.36	0.22		
15	20	2.5	0.45	0.23		
20	20	2.5	0.36	0.23		
20	25	3	0.45	0.23		
25	15	3	0.275	0.23		
35	20	4.5	0.18	0.23		
15	20	3	0.45	0.24		
20	25	3	0.36	0.24		
25	15	2.5	0.36	0.24		
25	25	3.5	0.275	0.24		
20	20	2.5	0.45	0.26		
20	20	3	0.33	0.26		
20	25	3	0.5	0.26		
25	15	3.5	0.5	0.26		
30	20	3	0.18	0.26		
30	30	4.5	0.5	0.26		
35	10	4.5	0.5	0.26		
40	20	4.5	0.36	0.26		
25	20	2.5	0.10	0.27		
15	25	2.5	0.45	0.28		
25	20	2.5	0.18	0.28		
25	20	3.5	0.25	0.28		
35	10	4.5	0.5	0.31		
25	20	2.5	0.25	0.32		
25	40	2.5	0.25	0.35		

Fit quality

A-good

B-reasonable

C-poor

Table 6.6 AMZI model output, for a selection of modelled values which gave the best fit. The lower part of the table allows an initial phase imbalance.

Taking the data from Table 6.6 it is possible to gauge how critically dependent the curve fit is on each of the parameters  $n_2$ ,  $\alpha$  and  $\beta$ , by plotting pairs of these parameters against each other. Taking the data points when the third parameter is constant, a series of graphs is obtained. The graphs are shown in Appendix VI. The gradient of these graphs is a measure of the variation in one parameter that is required to offset the variation in another, and return the modelled characteristic to what is a good fit. More data points would be required for a full analysis, but of note is the strong correlation between the two loss terms  $\alpha$  and  $\beta$ .

The effects of the uncertainties in the AMZI parameters are now considered. The key parameters which determine the switching response are assumed to be  $n_2$  and  $\alpha$ , while the coupling efficiency,  $\beta$  and the arm imbalance are regarded as secondary parameters which finely hone the modelled characteristic to the desired response. The coupling efficiency was estimated by assuming a value for  $\alpha$  in a similar, but shorter, device. From Table 6.5  $\alpha$ , is taken to be in the range  $7\text{-}30\text{ cm}^{-1}$ , which gives a coupling efficiency which could vary by up to a factor of 3, or  $\pm 100\%$ , this will lead to a corresponding uncertainty in  $n_2$ . Fig. A20, in the appendix, shows that the values of  $\beta$  and  $\alpha$  which give a good fit, for a fixed  $n_2$  show significant correlation. Any uncertainties in  $\alpha$  therefore mean that the TPA which the model predicts shows an uncertainty of up to 70% of the variation in  $\alpha$ .

The results of the AMZI model, curve fit and the significance of uncertainties in the AMZI parameters are now summarised.

By comparing the experimental and modelled data it is possible to gain more insight into the obtained switching response of the Mach-Zehnder. As observed previously, all the numerous effects which act to limit the switching response even when considered together do not limit the contrast ratio to the extent seen. The model described in this section did not include: poor radiation of higher order modes, carrier heating induced gain saturation and additional asymmetries- these effects are difficult to quantify. Compared to the passive Mach-Zehnder structures<sup>7,14,30</sup> that proved successful in AlGaAs at half the bandgap, the active AMZI response is susceptible to a great many more competing effects, all of which potentially limit its performance. Also compared to the directional coupler switches that have been demonstrated in amplifiers at

transparency, the AMZI will suffer more significantly from the effects of gain nonlinearities as it has two separate arms. It is therefore concluded that the AMZI should, and does, have a significantly worse response compared to comparable passive all-optical switches and active directional coupler devices.

From Fig. 6.19 it is observed that the AMZI switching is not catastrophically limited by the effects of two-photon absorption, although this prevents the Mach-Zehnder from showing further on/off cycles. An improved fit to the experimental data, as shown in Figures 6.22 and 6.25, can be obtained if an initial phase shift is allowed between arms, suggesting that the AMZI experiences some asymmetry in path length between arms. Fig. 6.23 includes some gain asymmetry between arms which reduces the contrast ratio to values similar to that observed. The approach used assumes that the linear losses in one arm are larger. This is obviously a simplification and would only accurately model asymmetries due to fabrication imperfection, for instance. A more complex model could also include an additional intensity dependent loss term, to more accurately model gain saturation due to carrier heating.

The model shows a good fit to the experimental data, the optimum fits were identified using the least squares method. However, the device parameters, cannot be accurately deduced from the best fit data, because for a range of values of  $n_2$ ,  $\beta$ , and  $\alpha$  we find the modelled switching characteristic within 15% of the experimental data. As none of these parameters are accurately known there exists a wide matrix of values over which  $n_2$ ,  $\alpha$ ,  $\beta$  could lie, up to +/- 100% typically. In order to deduce these parameters accurate measurements of  $\alpha$  and ideally another parameter would have been required.

## **6.5 Practical applications of semiconductor optical amplifiers at the transparency bias point**

In this section the practicalities of devices such as the all-optical AMZI are addressed. Initially, possible improvements to the AMZI switch are suggested and then its potential is compared with other competing devices.

The AMZI fabricated was designed to be a proof of principle, there is considerable scope for optimisation. Taking the case of a 1x1 switch, which could be adapted to form a routing / demultiplexing switch, the following areas can be improved:

- **Longer pulse widths:** Pulses of duration in the sub picosecond regime lead to competing nonlinearities in amplifiers <sup>28,29</sup> and enhanced two-photon absorption and carrier heating gain nonlinearities. This will degrade the switching response. Also pulses of this duration are unlikely to be available in a communications network employing semiconductor laser sources.
- **Reduction of bend losses:** The AMZI in its current form is lossy: the asymmetric power splitting Y branch will lead to a loss greater than 7dB at the recombination point, assuming a 5.4:1 split ratio. A better device could use different width waveguides in each arm to introduce asymmetry.
- **Reduction of coupling losses:** Insertion losses are also significant. These could be reduced using taper structures which have been recently developed in lasers to mode match to optical fibres <sup>43</sup>. Similarly AR coatings would improve throughput.
- **Active and passive sections:** In the AMZI demonstrated, the input and output sections were also biased at transparency and because of the linear losses due to free carrier absorption this leads to additional loss. A better solution would be to introduce active and passive sections using regrowth techniques or disordering. Alternatively gain in the input and output sections would also be possible, although at milliwatt power input levels gain saturation would be significant in the input section.
- **Optimised MQW's:** There is potential for optimising the amplifier structure: work by Roberts <sup>29</sup> suggests that if the carrier-heating nonlinearity is to be employed, a bulk structure or a structure with a large number of repeated quantum wells would be optimum as it enhances the confinement factor. This

is important because the nonlinear carrier heating interactions mainly occur in the active region. This would however increase the linear losses associated with free carrier absorption.

- **Gain saturation compensation:** If the asymmetric gain saturation seen in the arm with most power is known, a design can be developed to compensate for this allowing improved contrast ratios, limited only by the pulse shape.

In order to assess the practicalities of a switch using an amplifier at transparency the comparison is drawn with the TOAD <sup>44-52</sup> (terahertz optical asymmetric demultiplexer) and fibre loop mirror switches <sup>53,54</sup>, two other contenders for all-optical 100GHz routing switches and time division demultiplexers.

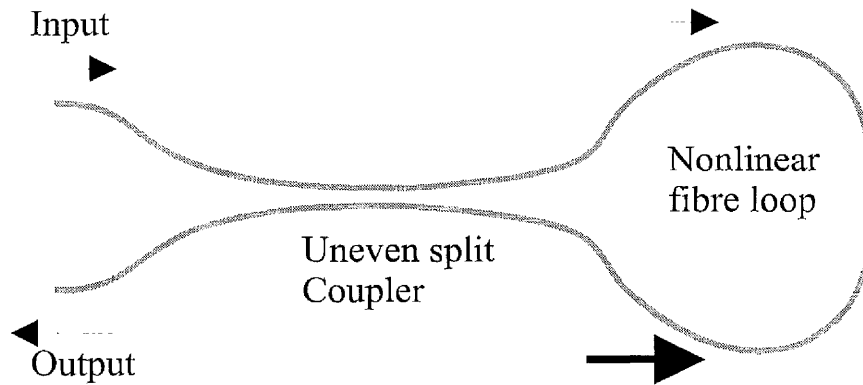


Fig. 6.26 The fibre loop mirror, a possible configuration.

A diagram of a fibre nonlinear-optical loop mirror is shown above in Fig. 6.26. The device works on a similar principle to the AMZI but is adapted so that the two pulses travel the same optical path. The nonlinearities in optical fibre are relatively weak necessitating long lengths of fibre. The loop mirror approach removes the problem of instability between interferometer arms, which would be significant for the fibre lengths used. With reference to Fig. 6.26, the input signal to the loop mirror is split asymmetrically by the coupler. If sufficiently intense, each pulse will experience a different nonlinear self phase modulation. When the pulses return to the coupler the split ratio will depend on the relative phase shift between pulses, so the device therefore forms an intensity dependent switch. A more practical application of the loop mirror

could employ a control pulse to switch the data signals.

A similar device called the TOAD (terahertz optical asymmetric demultiplexer) is shown below in Fig. 6.27. This device employs the strong interband nonlinearities present in optical amplifiers. In the TOAD a signal pulse is split in half, each half travels around the loop in opposite directions. An intense control pulse is used to induce an index change in the amplifier, which is displaced from the loop centre. Because of the asymmetry each pulse experiences the phase shift in the amplifier at a different time. The net result of this is that the control pulse changes the mirror transmission for a period of time determined by the amplifier's displacement from the loop centre. Although the interband nonlinearity has a slow recovery time of the order of hundreds of nanoseconds, it has a fast turn on time. The device does not need to fully recover between switching pulses so high switching speeds are possible. TOADs are expected to achieve bit rates of  $100 \text{ Gbs}^{-1}$  <sup>45,48,51</sup>.

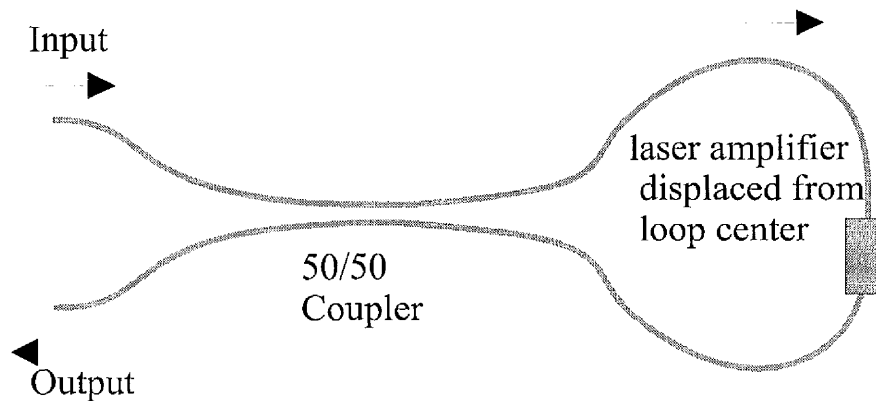


Fig. 6.27 TOAD (terahertz optical asymmetric demultiplexer).

As a means of addressing the practicality of utilising the nonlinearity at transparency in amplifiers, the projected performance parameters for a signal routing or demultiplexing switch are compared with those published for TOAD and Loop mirror devices. Table 6.7 lists these comparisons.

Device	Nonlinear loop mirror <sup>53,54</sup>	TOAD <sup>44-52</sup>	Optimised amplifier at transparency
<b>Likely performance specs.</b>	<p>&gt;50 GHz speeds</p> <p>Negligible attenuation.</p> <p>Power / length trade-off.</p> <p>1-100pJ pulses.</p>	<p>260 GHz Speed</p> <p>Attenuation limited by fibre laser coupling.</p> <p>&lt;2dB insertion loss possible.</p> <p>mW average powers possible.</p> <p>100 fJ pulses.</p>	<p>500 GHz</p> <p>Attenuation in device ~100dB cm<sup>-1</sup> at transparency so 10dB for 1mm device.</p> <p>sub Watt peak powers.</p> <p>100pJ pulses.</p>
<b>Advantages</b>	<p>Fibre compatible</p> <p>In principle length / power trade off is fairly flexible.</p> <p>Recovery times faster than TOAD as it exploits a Kerr-like nonlinearity.</p>	<p>Lower powers required.</p> <p>Small physical size.</p> <p>Possibility of adjusting the switching energies by changing the amplifier bias to account for intensity fluctuations in data.</p>	<p>Possibility of offsetting some of the loss with gain.</p> <p>Small physical size.</p> <p>In principle faster recovery times are possible than the inter-band effects used in the TOAD.</p>
<b>Disadvantages</b>	<p>Solitons possibly required to offset dispersion.</p> <p>Length reduction is possible but requires a speciality fibre.</p>	<p>Fibre to amplifier coupling limits insertion loss.</p> <p>Gain nonlinearities limit switching contrasts, requiring more complex geometries<sup>47,48</sup>.</p> <p>Switching pulse should have a regular clock.</p>	<p>The linear losses at transparency are large.</p> <p>Gain nonlinearities also limit performance.</p>

Table 6.7 Comparison between switching in an amplifier transparency and other alternative switching configurations.

As is shown in the table all the devices offer the potential for switching in the 100GHz regime. The clear disadvantage of the nonlinearity at transparency is the attenuation, which would be in excess of 10dB for a 1mm long active region. Insertion losses for most optical components are generally required to be small, <1dB. Amplification after the switching section could be possible, but for the intensities involved the amplifier may experience saturation.

To conclude, devices utilising nonlinearities present at transparency are limited because of their large insertion losses. At the moment TOAD like devices offer more hope for 100GHz routing switches because of their lower power requirements. Amplifiers at transparency could provide a role when faster switching is required, and also have other useful nonlinear properties which could be utilised in high speed switching networks. At the moment the main impetus in utilising the large bandwidth of optical fibres is dense wavelength division multiplexing (DWDM) schemes, where 16, 32 or 64 closely spaced channels are used to increase capacity<sup>55,56</sup>, but faster routing switches will have a role to play further into the future.

## **6.6 Conclusions**

To conclude, for the first time an active asymmetric Mach-Zehnder interferometer (AMZI) laser / amplifier all-optical switch has been fabricated in the GaAs/AlGaAs material system. Prior to this, to our knowledge, only all-optical switches based on the nonlinear directional coupler or polarisation rotation configurations had been demonstrated in amplifiers at transparency.

The AMZI devices have been tested as lasers and their linear characteristics have been analysed using a BPM technique, the results of which agreed with the data obtained from lasing thresholds. The devices were all-optically switched with pulses of 100fs duration, yielding an effective  $n_2$  of  $2 \times 10^{-12} \text{ cm}^2 \text{ W}^{-1}$ , which is consistent with values obtained elsewhere. The switching contrast ratio was poor. A range of effects including two-photon absorption and the non square pulse shape have been modelled

and were shown to significantly reduce contrast ratios, but only to 50%, which is significantly better than the 12% observed. An additional factor specific to current injected devices is carrier heating induced gain saturation, which will lead to an additional preferential attenuation of the signal in one arm. However the full reason for the poor contrast ratios is not entirely clear from the work done to date. Further experiments would be required to identify if its origin is related to a device imperfection, or fundamental property of the nonlinear AMZI. It is pointed out that compared to the passive Mach-Zehnder all-optical switches which proved successful, the active AMZI is susceptible to many more effects which degrade its performance. In particular amplifiers at transparency do not have an ideal Kerr-like nonlinearity. A significant gain nonlinearity exists, which in a nonlinear Mach-Zehnder configuration will reduce switching contrasts. This is less of a problem in an NLDC amplifier switch.

A model of the AMZI switching response was developed, which predicted a similar switching characteristic to that observed, and allowed the influence of the various limiting effects to be accessed together. The model however shows a close fit for a wide range of parameters. Additional analysis showed that the device parameters have an interrelated effect on the AMZI switching response, the uncertainty in one parameter results in subsequent uncertainty in deducing additional material properties using the model. Therefore without accurate knowledge of key material properties, other parameters such as  $n_2$  and  $\beta$  cannot be deduced accurately, the uncertainties are large, up to 100%. Further measurements would have been required to establish more conclusively how well the model and experimental data fit and to accurately deduce the values of key material parameters.

There have been few experimental studies on two-photon absorption in laser structures, quantifying and obtaining a more accurate measure of  $\beta$  would be a key requirement in producing an efficient switch. Similarly the nature of the carrier heating induced gain saturation requires further investigation

Improvements to the AMZI have been suggested, in particular a longer switching pulse duration is proposed, to reduce TPA and gain saturation, secondly a more optimised design could reduce optical losses. A more complicated Mach-Zehnder design could be employed to offset the gain nonlinearities, allowing the device to switch off fully. If future similar experiments are envisaged it is important to accurately

characterise the key material parameters, to help analyse device performance.

Similar devices could provide a role in all-optical signal routing and operate to speeds comparable with TOAD and loop mirror switches, but at the moment the device is limited by its large insertion losses, even if the other limitations discussed here can be overcome.

## References

- 1 S. G. Lee, B. P. McGinnis, R. Jin, J. Yumoto, H. M. Gibbs, R. Binder, S. W. Koch, N. Peyghambarian, "Subpicosecond switching in a current injected GaAs / AlGaAs multiple-quantum-well nonlinear directional coupler", *Appl. Phys. Lett.*, vol. 64, no. 4, p. 454, 1994
- 2 D. M. Atkin, M. J. Adams, "Optical switching in the twin-guide travelling-wave laser amplifier", *IEE Proc.*, vol.140, no. 5, p. 296, 1993
- 3 D. A. O. Davies, M. A. Fisher, D. J. Elton, S. D. Perrin, M. J. Adams, G. T. Kennedy, R. S. Grant, P. D. Roberts, W. Sibbett, "Nonlinear switching in InGaAsP laser amplifier directional couplers biased at transparency", *Electron. Lett.*, vol. 29, no. 19, p. 1710, 1993
- 4 R. J. Manning, D. A. O. Davies, "Three-wavelength device for all-optical signal processing", *Optics Lett.*, vol. 19, no. 12, p. 889, 1994
- 5 G. I. Stegeman, E. M. Wright, "All-optical waveguide switching", *Optical and Quantum Electronics*, vol. 22 , p. 95, 1990
- 6 K. Al-hemyari, C. N. Ironside, J. S. Aitchison, "Resonant nonlinear optical properties of GaAs/GaAlAs single quantum-well waveguide and an integrated asymmetric Mach-Zehnder interferometer", *IEEE Journal of Quantum Electronics*, vol. 28, no. 10, p. 2051, 1992
- 7 K. Al-hemyari, C. N. Ironside, J. S. Aitchison, G. T. Kennedy, R. S. Grant, W. Sibbett, "Ultrafast all-optical switching in GaAlAs integrated interferometer in 1.55 $\mu$ m spectral region", *Electron. Lett.*, vol. 28, p.1090, 1992
- 8 F. J. Leonberger, C. E. Woodward, D. L. Spears, "design and development of high speed electro-optic A/D converter", *IEEE Trans. Circuits Syst.*, CA 26, p. 1125, 1979
- 9 F. J. Leonberger, "High speed operation of LiNbO<sub>3</sub> electro-optic interferometric waveguide modulators", *Optics. Lett.*, vol. 15, p. 312, 1980
- 10 P. Liu, B. J. Li, Y. S. Trisno, " In search of a linear electrooptic amplitude modulator", *IEEE Photonics Tech. Lett.*, vol. 3, no. 2, p. 144 ,1991
- 11 F. Devaux, J. C. Harmand, I. F. L. Dias, T. Guettler, O. Krebs, P. Voisin, "High

- power saturation, polarisation insensitive electroabsorption modulator with spiked shallow wells”, *Electron. Lett.*, vol. 33, no. 2, p. 161, 1997
- 12** T. Ido, S. Tanaka, M. Suzuki, H. Inoue, “MQW electroabsorption optical modulator for 40Gbit/s modulation”, *Electron Lett.*, vol. 31, no. 24, p. 2124, 1995
- 13** R. M. Lammert, G. M. Smith, J. S. Hughes, M. L. Osowski, A. M. Jones, J. J. Coleman, “MQW wavelength-tunable DBR laser with monolithically integrated external cavity electroabsorption modulators with low-driving voltages fabricated by selective area MOCVD”, *IEEE Photonics Tech. Lett.*, vol. 8, no. 6, p. 797, 1996
- 14** C. N. Ironside, “Ultra-fast all-optical switching”, *Contemporary Physics*, vol. 34, no.1, p. 1, 1993
- 15** Y. Shani, C. H. Henry, R. C. Kistler, R. F. Kazarinov, K. J. Orlowsky, “Integrated optic adiabatic devices on silicon”, *IEEE Journal of Quantum Electronics*, vol. 27, no 3, p. 556, 1991
- 16** T. A. Ramadan, R. Scarmozzino, R. M. Osgood, “Adiabatic couplers: design rule and optimisation”, *Journal of Lightwave Technology*, vol. 16, no. 2, p. 277, 1998
- 17** W. K. Burns, F. Milton, “Mode conversion in planar-dielectric separating waveguides”, *IEEE Journal of Quantum Electronics*, vol. 11, no. 1, p. 32, 1975
- 18** L. D. Hutcheson, I. A. White, J. J. Burke, “Comparison of bending losses in integrated optical circuits”, *Optics Lett.*, vol. 5 no. 6, p. 276, June 1980
- 19** R. März, “Integrated optics: design and modelling”, Chapter 4, Artech House, 1994
- 20** L. Thylen, D. Yevick, “ Beam propagation method in anisotropic media”, *Appl. Optics*, vol. 21, p. 2751, 1982
- 21** G. B. Hocker, W. K. Burns, “Mode dispersion in diffused channel waveguides by the effective index method”, *Appl. Optics*, vol.16, no. 1, p. 113, 1977
- 22** D. Lee, “Electromagnetic principles of integrated optics”, Wiley, 1986
- 23** M. J. Adams, “An introduction to optical waveguides “, Wiley, 1981
- 24** R. A. Sammut, I. M. Skinner, “Effective index method for MQW waveguides”, *Optics Comm.*, vol. 76, no. 3/4, p. 213, 1990

- 25 G. P. Agrawal, N.K. Dutta, "Semiconductor lasers", 2nd ed., Van Nostrand Reinhold, 1993
- 26 M. J. P. Dymott, A. I. Ferguson, "Self-mode-locked diode-pumped Cr:LiSAF laser", *Optics Lett.*, vol. 19, no. 23, p. 1988, 1994
- 27 C. T. Hultgren, E. P. Ippen, "Ultrafast refractive index dynamics in AlGaAs diode laser amplifiers", *Appl. Phys. Lett.*, vol. 59, no. 6, p. 635, 1991
- 28 K. L. Hall, G. Lenz, A. M. Darwish, E. P. Ippen, "Subpicosecond gain and index nonlinearities in InGaAsP diode lasers", *Optics Comm.*, vol. 111, p. 589, 1994
- 29 P. D. Roberts, "Ultrafast nonlinearities in InGaAsP waveguide Devices", Ph.D. Thesis, University of St. Andrews, 1996
- 30 J. Bell, K. Al-hemyari, J. S. Aitchison, C. N. Ironside, G. T. Kennedy, W. Sibbett, " Demonstration of all-optical switching in a symmetric Mach-Zehnder interferometer", *Electron. Lett.*, vol. 31, p.2095, 1995
- 31 D. N, Nikogasyan, "Handbook of properties of optical and laser-related materials", John Wiley, 1997
- 32 E. W. Van Stryland, H. Vanherzeele, M. A. Woodall, M. J. Soileau, A. L. Smirl, S. Guha, T. F. Boggess, "Two-photon absorption, nonlinear refraction, and optical limiting in semiconductors", *Optical Engineering*, vol. 24, no. 4, p.613, 1985
- 33 F. R. Laughton, J. H. Marsh, J. S. Roberts, "Intuitive model to include the effect of free carrier absorption in calculation the two-photon absorption coefficient", *Appl. Phys. Lett.*, vol. 60, no. 2, p. 166, 1992
- 34 H. Q. Lee, H. K. Choi, C. A. Wang, "Measurement of the two absorption coefficient in a GaAs/AlGaAs quantum well laser", *Appl. Phys. Lett.*, vol. 57, no. 3, p. 212, 1990
- 35 H. K. Tang, P. P Vasil'ev, I. H. White, R. V. Penty, J. S. Aitchison, "First demonstration of two photon absorption in a semiconductor waveguide pumped by a diode laser", *Electronics Lett.*, vol. 29, no. 18, p. 1660, 1993
- 36 P. M. W. Skovgaard, R. J. Mullane, D. N. Nikogosyan, J. G. McInerney, "Two-photon absorption in semiconductor waveguide autocorrelators", *Optics Communication*, vol. 153, p. 78, 1998
- 37 H. K. Tsang, R. S. Grant, P. V. Penty, I. H. White, J. B. D. Soole, E. Colas, H.

- P. Leblanc, N. C. Andreadakis, M. S. Kim, W. Sibbett, "GaAs/GaAlAs multi-quantum well waveguides for all-optical switching at 1.55 $\mu$ m", *Electronics Lett.*, vol. 27, no. 22, p 1993, 1991
- 38 C. C. Yang, A. Villeneuve, G. I. Stegeman, C-H Lin, H-H Lin, "Anisotropic two-photon transitions in GaAs/AlGaAs multiple quantum well waveguides, *IEEE Journal of Quantum Electronics*, vol. 29, no. 12, p 2934, 1993
- 39 C. C. Yang, A. Villeneuve, G. I. Stegeman, C-H Lin, H-H Lin, "Measurements of two-photon absorption coefficient and induced refractive index in GaAs/AlGaAs multi-quantum well waveguides", *Electronics Lett.*, vol. 29, no. 1, p. 37, 1993
- 40 A. Villeneuve, C. C. Yang, G. I. Stegeman, C. N. Ironside, G. Scelsi, R. M. Osgood, "Nonlinear absorption in a GaAs waveguide just above half the band gap", *IEEE Journal of Quantum Electronics*, vol. 30, no. 5, p. 1172, 1994
- 41 H. S. Brandi, C. B. de Araujo, "Multiphoton absorption in solids: a universal curve", *J. Phys. C*, vol 16, p 5929, 1983
- 42 M. Sheik-Bahae, D. C. Hutchings, D. J. Hagan, E. W. Van Stryland, "Dispersion of bound electronic nonlinear refraction in solids", *IEEE Journal of Quantum Electronics*, vol. 27, no. 6, p. 1296, 1991
- 43 R. Zengerle, W. Weirshausen, "Tapered two-layer InGaAsP / InP waveguides for highly efficient chip coupling to single mode fibres", *Optics Comm.*, vol 115, p. 453, 1995
- 44 K. L. Deng, I. Glesk, K. I. Kang, P. R. Prucnal, "Unbalanced TOAD for optical data and clock separation in self-clocked transparent OTDM networks", *IEEE Photonics Technology Letters*, vol. 9, no. 6, p. 830, 1997
- 45 J. K. Blow, R. J. Manning, A. J. Probst, "Nonlinear optical loop mirrors with feedback and a slow nonlinearity", *Optics Comm.*, vol. 134, no. 1-6, p. 43, 1997
- 46 I. Glesk, J. P. Solokoff, P. R. Prucnal, "All-optical address recognition and self routing in a 250Gb/s packet-switched network", *Electron. Lett.*, vol. 30, no. 16, p. 1322, 1994
- 47 J. Leuthold, P. A. Besse, J. Eckner, E. Gamper, M. Dülk, H. Melchior, "All-optical space switches with gain and principally ideal extinction ratios", *IEEE Journal of Quantum Electronics*, vol. 34, no 4, p. 622, 1998

- 48 N. S. Patel, K. L. Hall, K. A. Rauschenbach, "Interferometric all-optical switches for signal processing", *Applied Optics*, vol. 37, no. 14, p. 2831, 1998
- 49 N. S. Patel, K. L. Hall, K. A. Rauschenbach, "40-Gbit/s cascaded all-optical logic with an ultrafast nonlinear interferometer", *Optics Lett.*, vol. 21, no. 18, 1466, 1996
- 50 N. S. Patel, K. L. Hall, K. A. Rauschenbach, "40-Gb/s demultiplexing using an ultrafast nonlinear interferometer (UNI)", *IEEE Journal of Photonics Technology Letters*, vol. 8, no 12, p. 1695, 1996
- 51 A. J. Proustie, K. J. Blow, R. J. Manning, "Storage threshold and amplitude restoration in an all-optical regenerative memory", *Optics Comm.*, vol. 146, p. 262, 1998
- 52 K. J. Blow, R. J. Manning, A. J. Proustie, "Model of longitudinal effects in semiconductor optical amplifiers in a nonlinear loop mirror configuration", *Optics Comm.*, vol. 148, p. 31, 1998
- 53 N. J. Doran, D. Wood, "Nonlinear-optical loop mirror", *Optics Lett.*, vol. 13, no. 1, 1988
- 54 W. S. Man, H. Y. Tam, M. S. Demokan, "Optimal loop length of a nonlinear optical loop mirror in switching solitons", *IEEE Journal of Lightwave Technology*, vol. 16, no 1, p. 100, 1998
- 55 K. Okamoto, K. Takiguchi, Y. Ohmori, "16-channel optical add / drop multiplexer using silica-based arrayed-waveguide gratings", *Electron. Lett.*, vol.31, no.9, p.22, 1995
- 56 K. Okamoto, H. Yamada, "Arrayed-waveguide grating multiplexer with flat spectral response", *Optics Lett.*, vol. 20, no. 1, p. 43 , 1995

# Chapter 7

## Conclusions and summary

In this section a summary of the work presented in this thesis and the reasons why it was undertaken is given. The main achievements of this thesis are summarised, suggestions for future work are made, together with the outlining of some of the problems that impeded this research.

Chapters 1 & 2 presented the background to this thesis, the relevance and possible applications of the ultrafast nonlinear effects in semiconductor laser amplifiers. A review of the recent literature was presented, concentrating on pump-probe, four-wave mixing and other studies designed to investigate the magnitude and origin of these nonlinearities. The majority of these studies were conducted in the small signal regime with very short pulse durations. Little published material was available on the effects of these nonlinearities upon excitation with longer pulse widths in the large signal regime, which would be more practical for a real device. In particular, attention was drawn to the possibility of utilising the ultrafast nonlinearities in amplifiers at transparency to form an all optical switch, this had previously been demonstrated in the nonlinear directional coupler configuration and a polarisation rotation switch.

Chapter 3 presented the fabrication techniques used to produce the integrated GaAs/AlGaAs asymmetric Mach-Zehnder interferometer all-optical switch, the ridge waveguide laser geometry was used which is relatively easy to fabricate. Separate contacts were provided, allowing each portion of the Mach-Zehnder to be biased separately. Originally the intention was to fabricate this device in the InGaAsP material system allowing it to be tested in-house using the F-centre laser, described later. However at the time a partial dry etch / wet etch process was used to form the ridge waveguide laser structure, only later did it become apparent that this process, because of the high r.f. powers used in the dry etch, caused damage to the quantum wells even though they were 100's of nm from the etched surface. Later it was also shown that, the

hydrogen ions in the etch also passivated the Zn dopants in structure resulting in poor contact resistance which could cause the diode to fail catastrophically. Subsequently a wet etch technique was developed as well as an improved dry etch using a lower r.f. power. These improvements were too late to be of benefit to this project. Much time was spent trying to fabricate the AMZI structure in InGaAsP, but because of the reasons described above this proved unsuccessful. It was only possible to produce the AMZI structure in GaAs/AlGaAs, this meant it had to be tested externally, at Strathclyde University.

Chapter 4 concerns the development of the experimental laser system, later used to perform experiments on InGaAsP/InP amplifiers. The system employed a prototype diode-pumped Nd:YLF laser from Microlase Optical Systems which pumped a St. Andrews University built F-centre laser. This was, to our knowledge, one of the first diode-pumped F-centre systems demonstrated. The Nd:YLF laser produced 2.2 W output and was FM mode-locked at 77.77 MHz producing pulses of 20ps FWHM duration. When synchronously pumped the F-centre produced pulses of 10ps FWHM duration with a maximum average power of 200 mW, wavelength tuning was over the range 1.45 to 1.55 $\mu$ m. An interesting property of the pump laser was its ability to Kerr lens mode-lock, producing pulses of duration 6ps FWHM, this allowed pulses as short as 4ps FWHM to be produced from the F-centre, when synchronously pumped. The cavity was analysed and the LiNbO<sub>3</sub> phase modulator was identified as the Kerr medium, which has a larger  $n_2$  than the Nd:YLF rod, and is longer. The modulator is also positioned in a place where the beam size is near the minimum. The cavity is close the instability limit and calculations, give a 0.5% Kerr induced beam waist reduction,  $dw/w$ , in the rod, which is assumed to be the effective aperture. The exact cavity dimensions are however not known exactly and the  $dw/w$  may be as low as 0.2% or high as 1.5%. This weak Kerr lensing explains why the KLM is not self starting. Experimental trials with a slit, to enhance KLM, were unsuccessful, analysis showed that this was because the optimum slit position in the cavity is close to the rod, which was impossible to access. The Kerr lensed mode-locking and FM operation was prone to slow drifts over time and required constant adjustment to optimise it, this was attributed to thermal instabilities.

Further analysis showed that the pump induced thermal lensing is strong, a lens with a focal length of 1.06 m was calculated. The inclusion of this lens in the resonator analysis moves it closer to the instability limit. These thermal instabilities meant that the Nd:YLF pump laser and therefore the F-centre laser could not realise their full potential, as a reliable source of tuneable ultrashort pulses.

Suggestions are made to improve the system, in particular it is pointed out that the standard Microlase Nd:YLF system, which employs a shorter cavity, designed to mode-lock at 122 MHz suffers far less from any thermal lens fluctuations as it employs a stronger focusing mirror.

Chapter 5 concerned the probing of InGaAsP/InP semiconductor optical amplifiers, obtained from BNR using the synchronously pumped F-centre laser. Initially the linear amplifier properties such as gain peak, gain ripple, transparency current, and threshold were characterised. The nonlinear index,  $n_2$  was measured as  $2.39 \times 10^{-11} \text{ cm}^2 \text{ W}^{-1}$ , by spectral broadening for pulses of 20ps duration. The main focus of this work was a pump-probe experiment to identify the ultrafast gain nonlinearities and to look into the saturation of the nonlinearities when excited out with the small signal regime. By biasing the amplifier at transparency it was possible to just observe the ultrafast nonlinear components. The dominant nonlinearity is shown to be carrier heating for pulses of 20 picosecond duration, significant two-photon absorption was not observed. The carrier heating nonlinearity is observed to saturate for excitation in the milliwatt regime, a saturation effect which has not been reported before, elsewhere. Further information such as the recovery time of the nonlinearity could not be obtained because this was smaller than the minimum pulse duration of the experimental laser system.

A model of the carrier heating induced gain saturation at transparency was developed, this showed good agreement with the experimental data from the pump-probe study. The nonlinearity is expected to saturate for power levels in the mW regime, the mechanism of saturation is an attenuation of the signal, caused by a heating of the temperature distribution. It is pointed out that the gain nonlinearities which complement the index nonlinearities could degrade the performance of optical switches utilising this nonlinearity.

Chapter 6 describes the design of an integrated asymmetric Mach-Zehnder interferometer (AMZI) laser amplifier in GaAs/AlGaAs. Similar structures have proved highly successful all-optical switches in AlGaAs at half the bandgap. This was, to our knowledge, the first time such a switch had been constructed using an amplifier at transparency. The AMZI configuration should, in principle offer reduced switching powers compared to other configurations.

This structure was fabricated to allow different regions to be biased separately. The structures were characterised as lasers. The geometries used were analysed using a BPM method to give a picture of the asymmetric splitting ratios used and the losses of the structure. A 1.5mm long AMZI was switched with pulses of 100fs, from a self mode-locked Cr:LiSAF laser. The pulse energy for switching was 3pJ, or a peak power of 30W, in the device. This is a slightly larger switching power than seen in similar structures, but the AMZI is a more complex structure and has more inherent losses. The switching contrast obtained was poor, in order to identify the reasons, the various factors limiting switching performance were considered, including; two-photon absorption, non ideal pulse shape and linear losses. The inclusion of these factors does not fully account for the observed response. Although with their inclusion a switching contrast of only 50% is obtained, compared to the observed contrast of 12%. Other effects such as asymmetries between arm bias conditions and carrier heating induced gain nonlinearities, as discussed in Chapter 5, are likely to further limit switching. Compared to passive all-optical switches which have proved successful in AlGaAs at long wavelengths and fibre loop mirrors, the AMZI switching extinction is poor. It is noted that switching of the active AMZI is influenced by many more effects than for similar passive structures and does not have an ideal Kerr-like nonlinearity, instead a significant gain nonlinearity accompanies the index nonlinearity. Compared to the active NLDC configuration the AMZI's switching contrast is expected to be degraded more by arm asymmetries caused by gain nonlinearities, fabrication inaccuracies or current bias differences. If the comparison is made with similar active NLDC switches a poorer switching contrast is indeed observed in the AMZI. Further work is required to understand fully the interplay between the numerous factors which restrict the AMZI's performance.

A model of the AMZI was developed. In order to identify which parameters gave

the best fit a least squares technique was used, which revealed that a good fit was achieved for a wide range of material parameters. Modelled variations of up to 100% were possible in  $\alpha$ ,  $\beta$  and  $n_2$ , whilst still achieving a good fit. The coupling efficiency was estimated assuming a value for the linear losses,  $\alpha$ , which was not known accurately. This consequently lead to an uncertainty in the power in the device. Without detailed knowledge of key material parameters such as  $\alpha$  or  $\beta$  as it was not possible to accurately predict the value of  $n_2$  from the model. An improved experiment would measure these parameters.

Finally suggestions are made for an improved AMZI type switch and the potential of such a device is compared with other candidates for ultra-fast routing switches, although the gain nonlinearities can be compensated for, the large insertion losses will remain as a major problem.

# Appendix I

## Wafers used

### B 337 MBE GaAs/AlGaAs lattice matched 4 MQW structure grown 4/93

Layer	Material	Doping	Thickness	Comments
7	GaAs	p $2 \times 10^{18} \text{ cm}^{-3}$	0.1 $\mu\text{m}$	contact layer
6	Al <sub>0.4</sub> Ga <sub>0.6</sub> As	p $9 \times 10^{17} \text{ cm}^{-3}$	0.9 $\mu\text{m}$	upper cladding
5	Al <sub>0.2</sub> Ga <sub>0.8</sub> As	-	0.1 $\mu\text{m}$	SCH
MQW	GaAs/AlGaAs	-		
3	Al <sub>0.2</sub> Ga <sub>0.8</sub> As	-	0.1 $\mu\text{m}$	SCH
2	Al <sub>0.4</sub> Ga <sub>0.6</sub> As	n $5 \times 10^{17} \text{ cm}^{-3}$	1.5 $\mu\text{m}$	lower cladding
1	-	n	1 $\mu\text{m}$	buffer
substrate	GaAs	-	-	-

MQW Layer	Material	Thickness	Periods
well	GaAs	10nm	4
barrier	AlGaAs	10nm	3

**B 452 MBE GaAs/AlGaAs lattice matched 2 QW structure  
grown 5/94**

Layer	Material	Doping	Thickness	Comments
7	GaAs	$p\ 5 \times 10^{18}\ \text{cm}^{-3}$	$0.1\ \mu\text{m}$	contact layer
6	$\text{Al}_{0.4}\text{Ga}_{0.6}\text{As}$	$p\ 5 \times 10^{17}\ \text{cm}^{-3}$	$1\ \mu\text{m}$	upper cladding
5	$\text{Al}_{0.2}\text{Ga}_{0.8}\text{As}$	-	$0.1\ \mu\text{m}$	SCH
MQW	GaAs/AlGaAs	-		
3	$\text{Al}_{0.2}\text{Ga}_{0.8}\text{As}$	-	$0.1\ \mu\text{m}$	SCH
2	$\text{Al}_{0.4}\text{Ga}_{0.6}\text{As}$	$n\ 5 \times 10^{17}\ \text{cm}^{-3}$	$1.5\ \mu\text{m}$	lower cladding
1	-	n	$1\ \mu\text{m}$	buffer
substrate	GaAs	-	-	-

MQW Layer	Material	Thickness	Periods
well	GaAs	10nm	2
barrier	$\text{Al}_{0.2}\text{GaAs}_{0.8}$	10nm	1

**B 454 MBE GaAs/AlGaAs lattice matched 4 QW structure  
grown 5/94**

Layer	Material	Doping	Thickness	Comments
7	GaAs	$p\ 5 \times 10^{18}\ \text{cm}^{-3}$	$0.1\ \mu\text{m}$	contact layer
6	$\text{Al}_{0.4}\text{Ga}_{0.6}\text{As}$	$p\ 5 \times 10^{17}\ \text{cm}^{-3}$	$1\ \mu\text{m}$	upper cladding
5	$\text{Al}_{0.2}\text{Ga}_{0.8}\text{As}$	-	$0.1\ \mu\text{m}$	SCH
MQW	GaAs/AlGaAs	-		
3	$\text{Al}_{0.2}\text{Ga}_{0.8}\text{As}$	-	$0.1\ \mu\text{m}$	SCH
2	$\text{Al}_{0.4}\text{Ga}_{0.6}\text{As}$	$n\ 5 \times 10^{17}\ \text{cm}^{-3}$	$1.5\ \mu\text{m}$	lower cladding
1	-	n	$1\ \mu\text{m}$	buffer
substrate	GaAs	-	-	-

MQW Layer	Material	Thickness	Periods
well	GaAs	10nm	4
barrier	$\text{Al}_{0.2}\text{GaAs}_{0.8}$	10nm	3

**B 456 MBE GaAs/AlGaAs lattice matched 4 QW structure**

Layer	Material	Doping	Thickness	Comments
7	GaAs	p $1 \times 10^{19} \text{ cm}^{-3}$	0.2 $\mu\text{m}$	contact layer
6	Al <sub>0.4</sub> Ga <sub>0.6</sub> As	p $2 \times 10^{17} \text{ cm}^{-3}$	1.1 $\mu\text{m}$	upper cladding
5	Al <sub>0.2</sub> Ga <sub>0.8</sub> As	-	0.1 $\mu\text{m}$	SCH
MQW	GaAs/AlGaAs	-		
3	Al <sub>0.2</sub> Ga <sub>0.8</sub> As	-	0.1 $\mu\text{m}$	SCH
2	Al <sub>0.4</sub> Ga <sub>0.6</sub> As	n $1.4 \times 10^{17} \text{ cm}^{-3}$	1.8 $\mu\text{m}$	lower cladding
1	-	n	0.5 $\mu\text{m}$	buffer
substrate	GaAs	-	-	-

MQW Layer	Material	Thickness	Periods
well	GaAs	10nm	4
barrier	Al <sub>0.2</sub> GaAs <sub>0.8</sub>	10nm	3

**A 948 MBE GaAs/AlGaAs lattice matched 2 QW structure  
grown 6/95**

Layer	Material	Doping	Thickness	Comments
7	GaAs	$p\ 5 \times 10^{18}\ \text{cm}^{-3}$	$0.1\ \mu\text{m}$	contact layer
6	$\text{Al}_{0.4}\text{Ga}_{0.6}\text{As}$	$p\ 5 \times 10^{17}\ \text{cm}^{-3}$	$1\ \mu\text{m}$	upper cladding
5	$\text{Al}_{0.2}\text{Ga}_{0.8}\text{As}$	-	$0.1\ \mu\text{m}$	SCH
MQW	GaAs/AlGaAs	-		
3	$\text{Al}_{0.2}\text{Ga}_{0.8}\text{As}$	-	$0.1\ \mu\text{m}$	SCH
2	$\text{Al}_{0.4}\text{Ga}_{0.6}\text{As}$	$n\ 5 \times 10^{17}\ \text{cm}^{-3}$	$1.5\ \mu\text{m}$	lower cladding
1	-	n	$1\ \mu\text{m}$	buffer
substrate	GaAs	-	-	-

MQW Layer	Material	Thickness	Periods
well	GaAs	10nm	2
barrier	$\text{Al}_{0.2}\text{GaAs}_{0.8}$	10nm	1

**MR 398- Sheffield MOCVD InGaAsP lattice matched 5 QW structure grown 6/94**

Layer	Material	Doping	Thickness	Comments
11	In <sub>(0.53)</sub> GaAs	p $8 \times 10^{18} \text{ cm}^{-3}$	0.1 $\mu\text{m}$	contact
10	GaInAsP (Q1.18)	p $5 \times 10^{18} \text{ cm}^{-3}$	0.05 $\mu\text{m}$	
9	InP	p $7 \times 10^{17} \text{ cm}^{-3}$	1 $\mu\text{m}$	upper cladding
8	GaInAsP (Q1.05)	-	80nm	SCH
7	GaInAsP (Q1.18)	-	50nm	SCH
6	GaInAsP (Q1.26)	-	12nm	
MQW	In <sub>(0.53)</sub> GaAs/GaInAsP	-		
4	GaInAsP (Q1.26)	-	12nm	
3	GaInAsP (Q1.18)	n $5 \times 10^{17} \text{ cm}^{-3}$	50nm	SCH
2	GaInAsP (Q1.05)	n $5 \times 10^{17} \text{ cm}^{-3}$	80nm	SCH
1	InP	n $2 \times 10^{18} \text{ cm}^{-3}$	1 $\mu\text{m}$	lower cladding
substrate	InP	-	-	-

MQW Layer	Material	Thickness	Periods
well	In <sub>(0.53)</sub> GaAs	4.5nm	5
barrier	GaInAsP (Q1.26)	12nm	4

**MR 598- Sheffield MOCVD InGaAsP lattice matched 5 QW structure grown 8/95**

Layer	Material	Doping	Thickness	Comments
11	In <sub>(0.53)</sub> GaAs	p $8 \times 10^{18} \text{ cm}^{-3}$	0.1 $\mu\text{m}$	contact
10	GaInAsP (Q1.18)	p $5 \times 10^{18} \text{ cm}^{-3}$	0.05 $\mu\text{m}$	
9	InP	p $7 \times 10^{17} \text{ cm}^{-3}$	1 $\mu\text{m}$	upper cladding
8	GaInAsP (Q1.05)	-	80nm	SCH
7	GaInAsP (Q1.18)	-	50nm	SCH
6	GaInAsP (Q1.26)	-	12nm	
MQW	In <sub>(0.53)</sub> GaAs/GaInAsP	-		
4	GaInAsP (Q1.26)	-	12nm	
3	GaInAsP (Q1.18)	n $5 \times 10^{17} \text{ cm}^{-3}$	50nm	SCH
2	GaInAsP (Q1.05)	n $5 \times 10^{17} \text{ cm}^{-3}$	80nm	SCH
1	InP	n $2 \times 10^{18} \text{ cm}^{-3}$	1 $\mu\text{m}$	lower cladding
substrate	InP	-	-	-

MQW Layer	Material	Thickness	Periods
well	In <sub>(0.53)</sub> GaAs	4.5nm	5
barrier	GaInAsP (Q1.26)	12nm	4

## Appendix II

### Laser characterisation

It is important that the characteristics of laser wafers are objectively assessed to determine the quality of the material. To these ends broad area lasers were fabricated with a range of facet lengths with 75 $\mu\text{m}$  stripe widths. The devices were tested on a pulsed laser test rig with a 1:200 duty cycle. By measuring slope efficiencies and thresholds for various lengths useful characterisation data could be obtained<sup>1,2,3</sup>. The V-I characteristics were also obtained. Typically devices of lengths 400 $\mu\text{m}$ -1200 $\mu\text{m}$  were fabricated.

By plotting a graph of threshold density against the reciprocal of device length it is possible by extending the graph to calculate the threshold density for infinite length, which gives a measure of how good the material is. Table A1 shows the obtained thresholds for the AlGaAs MBE structures used and Table A2 shows the characteristics for the quaternary structures used.

Structure	Threshold current density for infinite length (A cm <sup>-2</sup> )	Comments
B337	400	4QW
B452	284	2QW
B454	318	4QW
B456	not characterised	4QW
A948	370	2QW

*Table A1 Characterisation data for the AlGaAs MBE laser structures used*

Structure	Threshold current density for infinite length (A cm <sup>-2</sup> )	Comments
MR398	637	5QW
MR598	563	5QW
E1192	385	BNR 6 QW strained layer

*Table A2 Characterisation data for the quaternary laser structures used*

From the slope efficiency data for various device lengths it is possible to extract information about the internal quantum efficiency and the losses at transparency. Extracting this data from the experimental results can be difficult if there are not sufficient data points. Table A3 shows the available quantum efficiency and linear loss data. The test data from the other wafers was scattered and it was not possible to establish what the internal quantum efficiencies or linear losses were. The value used in Chapter 6 is therefore an estimate based on a wafer grown at a similar time, B452 with some allowance made for the increased free carrier absorption likely because of the larger number of quantum wells.

Wafer	Internal quantum efficiency	$\alpha$ (cm <sup>-1</sup> )
B337	0.39	8
A948	0.43	6.4
B452	0.61	17

*Table A3 Additional characterisation data*

The approach taken was not to exhaustively characterise each wafer but identify if it was of reasonable quality and worthy of further use, or if it was poor. The wafers shown here showed acceptable characteristics, although in general the wafers with lower thresholds

were used preferentially. The technique of characterising broad area lasers is important because fabricating more complicated structures is time consuming and not the most efficient way to establish if a wafer is poor.

## **References**

- 1 Internal memo 11th December 1992, Stephen Ayling, "Follow up on characterisation of old MBE material"
- 2 Internal memo February 1994, B. Vögele, "growth of laser structures"
- 3 J. F. Martins-Filho, "Monolithic colliding pulse mode-locked quantum-well lasers", Ph.D. Thesis, University of Glasgow

## Appendix III

### Details of the BNR devices selected for this thesis

In Chapter 5 of this thesis, long wavelength InGaAsP amplifiers were investigated, these devices were supplied by BNR. The devices were available from a range of wafers which were originally grown as part of a development program for 1480 nm erbium doped fibre amplifier pump lasers. In total eleven wafers were available, from which four suitable wafers were chosen. Laser Bars from these four wafers were AR coated. The selection gave a range of gain peak wavelengths and acceptable single mode characteristics. Some of the data considered is shown in the table below.

Wafer	L-I characteristics	Room temperature Photo-luminescence (nm)	Lasing wavelength (nm)	Acceptable (on the basis of L-I characteristics and threshold and centre wavelength)
E467	kinky	1482	1506	
E470	smooth, 1st order	1493	1467	√, selected
E475	smooth, 1st order	1461	1500	√, selected
E481	smooth, 1st order	1479	1496	√, selected
E512	single mode		1496	√
E515	single mode		1495	√
E516	kinky	1483	1500	
E526	smooth, 1 st order		1491	√, selected
E529	smooth, but some 1st order		1492	
E541	kinky		1493	
E543	single mode		1499	√

Table A4. Characteristics of the BNR wafers, out of which four bars were selected for AR coating.

The optical spectrum of lasers from these wafers was captured, to give an indication of the likely peak of the material gain. The devices were measured above threshold at 70mA drive current. Selected devices were also measured at 30mA, around threshold and below threshold, as this should give a better indication of where the gain peak of an AR coated amplifier would lie. The spectra are shown below.

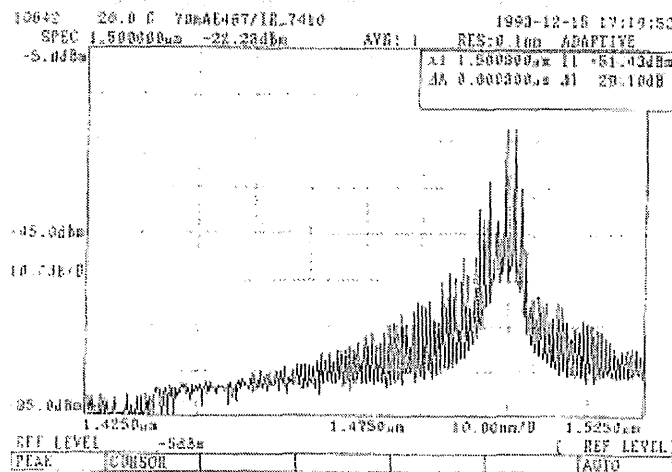


Fig. A1 Spectrum of E467 at 70mA.

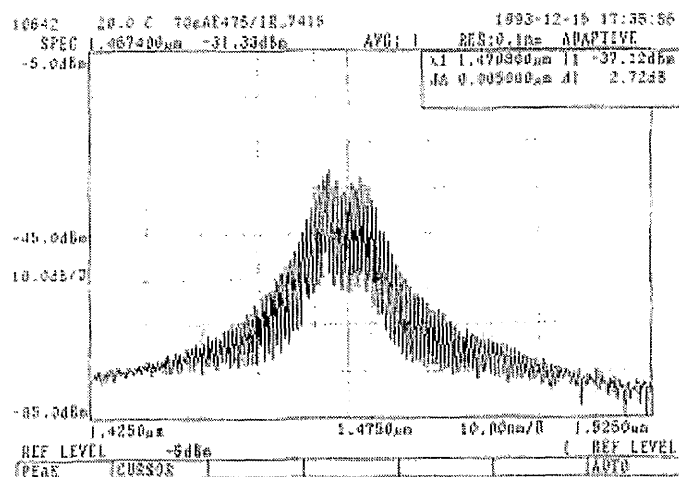


Fig. A2 Spectrum of E475 at 70mA.

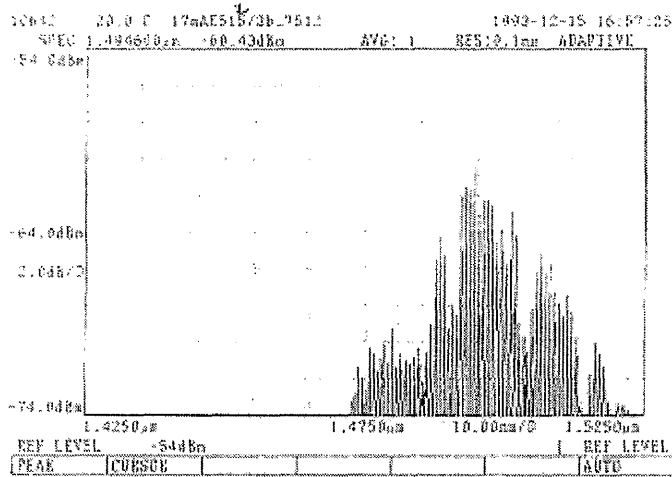


Fig. A3 Spectrum of E512 at 17mA.

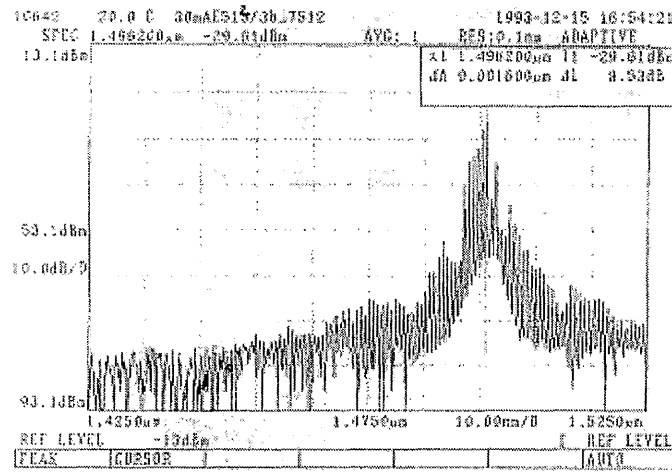


Fig. A4 Spectrum of E512 at 30mA.

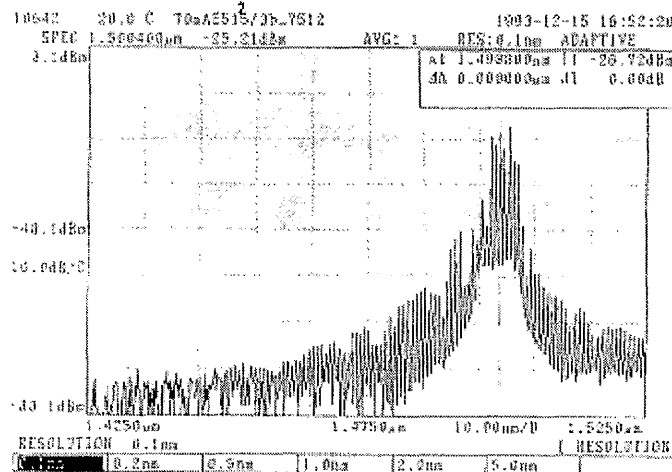


Fig. A5 Spectrum of E512 at 70mA.

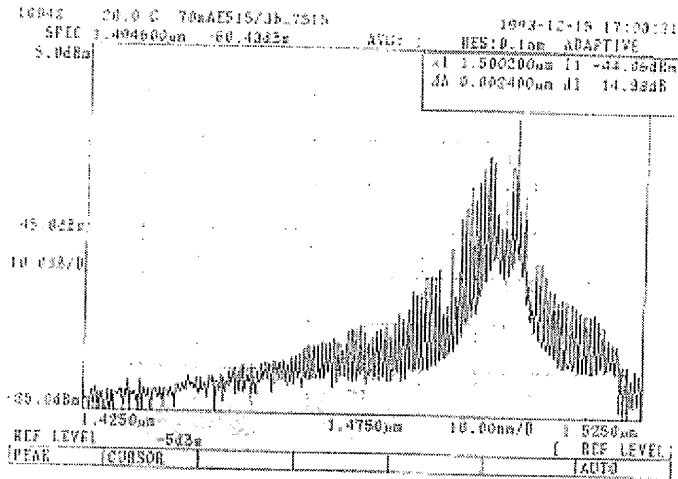


Fig. A6 Spectrum of E515 at 70mA.

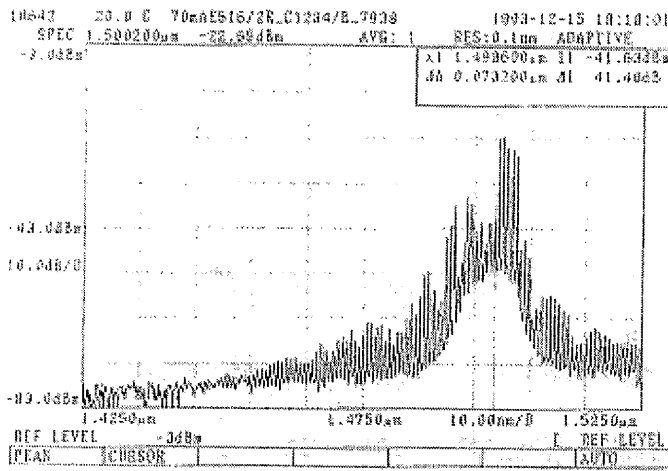


Fig. A7 Spectrum of E516 at 70mA.

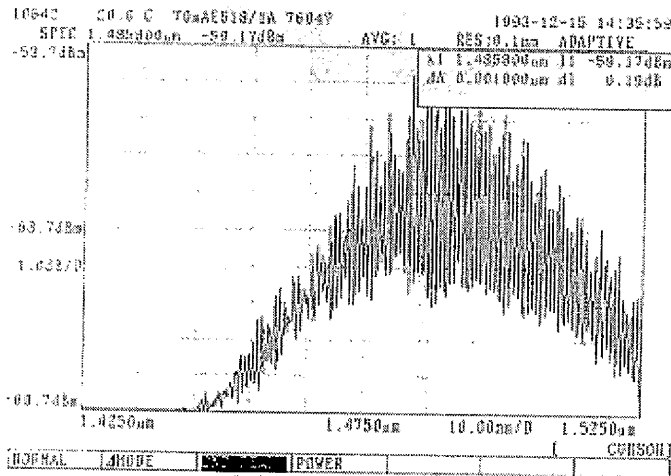


Fig. A8 Spectrum of E518 at 70mA.

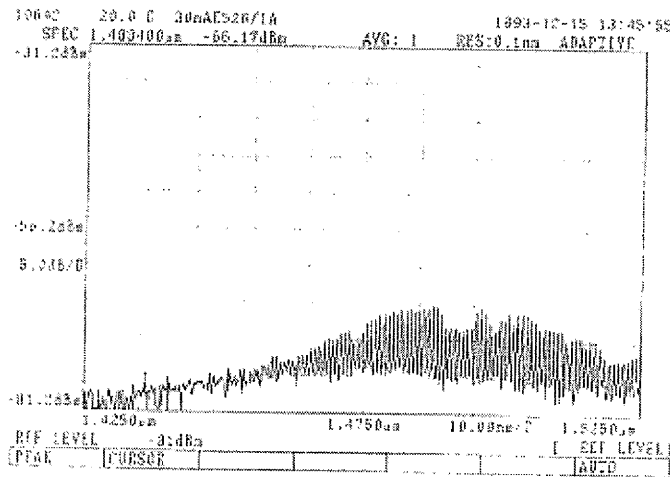


Fig. A9 Spectrum of E526 at 30mA.

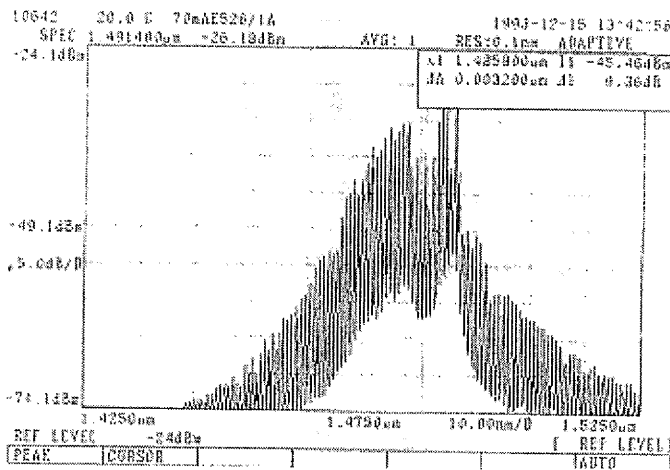


Fig. A10 Spectrum of E526 at 70mA.

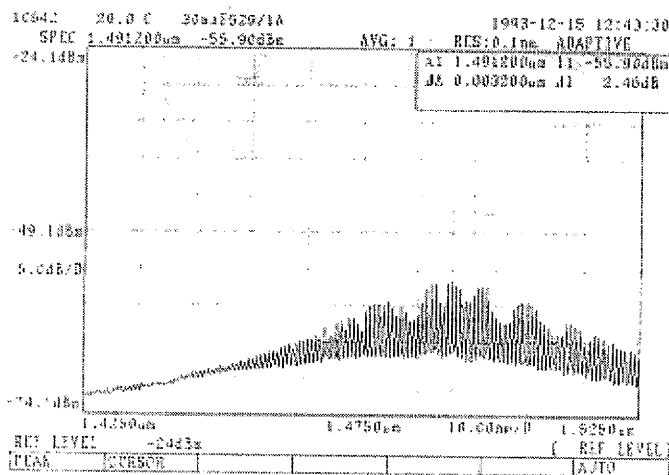


Fig. A11 Spectrum of E529 at 30mA.

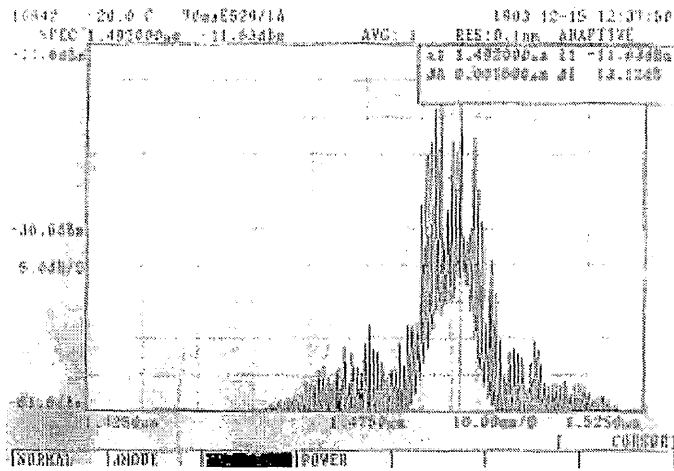


Fig. A12 Spectrum of E529 at 70mA.

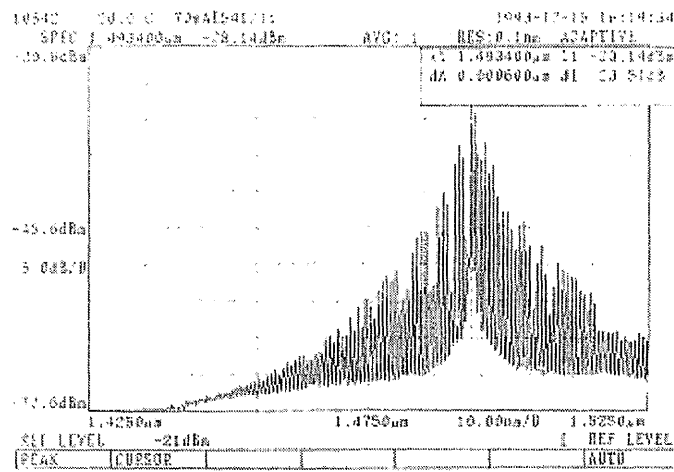


Fig. A13 Spectrum of E541 at 70mA.

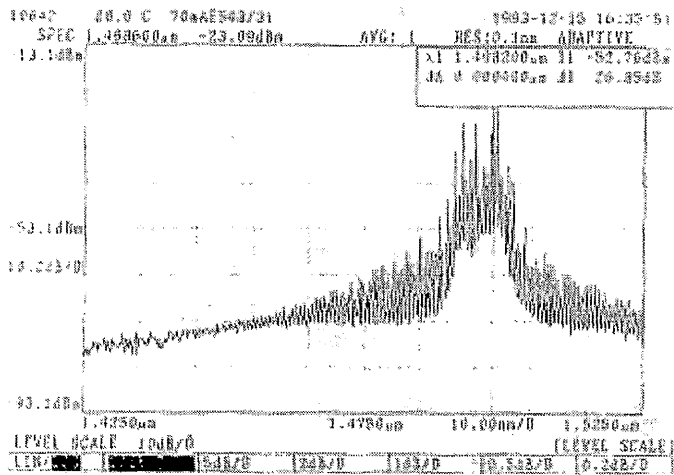


Fig. A14 Spectrum of E543 at 70mA.

## Appendix IV

### ABCD matrix method for the modelling of gaussian beams in laser cavities

The ABCD matrix method is a powerful technique, allowing the path of a gaussian beam (for example a laser beam in a cavity or a beam emerging from an optical waveguide) to be calculated through an assembly of optical components. These components could include lenses, mirrors, dielectrics or many others which are not discussed here. The technique is particularly useful because it allows the effect of multiple components to be represented by a single matrix, allowing the easy calculation of beam parameters and their dependence on variations in the laser cavity. In this section the technique is summarised with reference to its application in Chapter 4, to analyse Nd:YLF laser cavity. The computer model that performs this analysis is listed in Appendix V.

A beam of light which is gaussian in profile can be characterised at a given position by two parameters, the beam radius and the phase front curvature. The beam electric field profile, at a given position along the optical axis, can be represented by,

$$E(z) = \exp\left(-\frac{r^2}{w^2} + i \cdot k \frac{r^2}{2R}\right) \quad (\text{A.1})$$

where  $r$  is the transverse distance from the beam centre,  $z$  is the beam position along the propagation axis,  $w$  represents the beam radius or spot size at a particular position,  $R$  is the phase front curvature and  $k$  is the wavenumber. The spot size,  $w$ , corresponds to the distance in the transverse direction from the beam centre to the point where the light intensity falls to  $1/e^2$  of its peak value. The position along the propagation axis where the beam radius is smallest is termed the beam waist. For convenience, instead of the form of Equation A1 a gaussian beam is usually expressed in terms of a complex beam parameter,  $q(z)$ , as shown in Equation A2.

$$\frac{1}{q(z)} = \frac{1}{R} + i \cdot \left( \frac{\lambda}{\pi \cdot w^2} \right) \quad (\text{A.2})$$

As a gaussian beam propagates from the beam waist it expands. This is analogous to waves diffracting through a narrow slit, the matrix method allows this together with the effect of optical elements such as lenses to be readily modelled.

In the ABCD matrix method optical components are described by a 2x2 matrix as shown below.

$$\begin{bmatrix} a & b \\ c & d \end{bmatrix} \quad \text{general matrix form}$$

The matrices of some common optical elements are shown below.

$$\begin{array}{ll} \begin{bmatrix} 1 & d \\ 0 & 1 \end{bmatrix} & \text{uniform medium of length, } d \\ \begin{bmatrix} 1 & 0 \\ -1/f & 1 \end{bmatrix} & \text{thin lens of focal length, } f \\ \begin{bmatrix} 1 & 0 \\ -2/R & 1 \end{bmatrix} & \text{curved mirror with radius of curvature, } R \\ \begin{bmatrix} 1 & 0 \\ 0 & n_1/n_2 \end{bmatrix} & \text{dielectric interface from medium } n_1 \text{ to } n_2 \end{array}$$

The effects of generic optical system on a gaussian beam are described by,

$$q_2 = \frac{A \cdot q_1 + B}{C \cdot q_1 + D} \quad (\text{A3})$$

where  $q_1$  and  $q_2$  are the input and output beam parameters, as given in Equation A2. The matrix of a complete optical system is obtained from its individual components, as shown below,

$$\text{total matrix, } \begin{bmatrix} a_t & b_t \\ c_t & d_t \end{bmatrix} = \begin{bmatrix} a_n & b_n \\ c_n & d_n \end{bmatrix} \cdot \begin{bmatrix} a_{n-1} & b_{n-1} \\ c_{n-1} & d_{n-1} \end{bmatrix} \cdot \begin{bmatrix} a_{n-2} & b_{n-2} \\ c_{n-2} & d_{n-2} \end{bmatrix} \cdot \dots$$

The combined matrix is obtained by multiplying the matrices of the elements that make up the optical system in reverse, i.e. the last element is multiplied “first”. By using this technique the effects of an optical system on a known input beam can be calculated. Generally systems can be analysed independently in the two orthogonal planes, allowing for cylindrical lenses and birefringence.

In a laser resonator the situation is slightly different. The beam waist and radius are initially unknown, apart from at the mirror or lens, where the beam radius is required to be equal to the mirror curvature or determined by the lens focal length (a lens of focal length,  $f$  is equivalent to a curved mirror of radius  $R=2f$ ). It is the lens and mirror combinations and the optical distances which define the beam dimensions within the cavity. In order to analyse this, it is assumed for a stable cavity that the beam parameter,  $q$ , at a given position, in  $z$ , is identical for consecutive cavity round trips. Equation A3 then becomes,

$$q(z) = \frac{A \cdot q(z) + B}{C \cdot q(z) + D} \tag{A4}$$

where  $q(z)$  describes the beam at a particular position within the cavity, and the ABCD matrix here describes a complete round trip starting from the position where the beam parameters are to be calculated. Equation A4 can be solved and equated into real and complex components to give the beam width and curvature. Considering the following 3 element system,

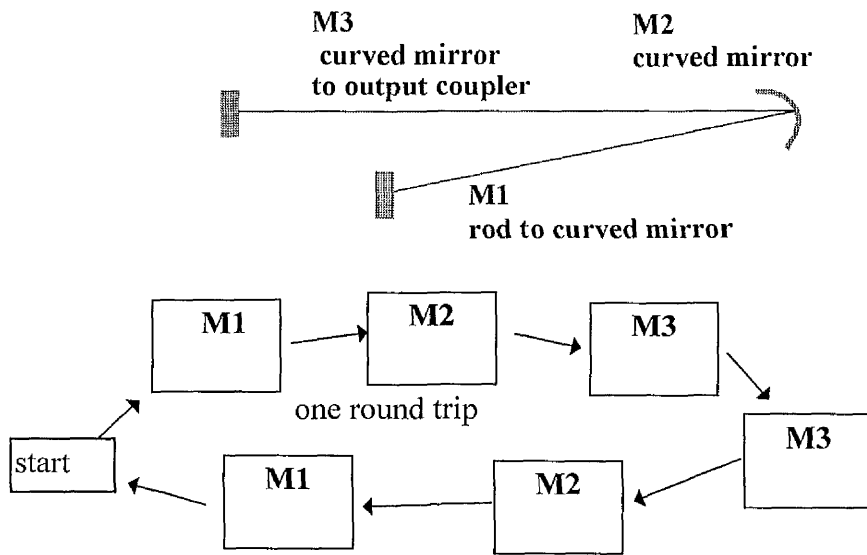


Fig. A15 Matrix multiplication order for resonator analysis.

In ABCD matrix analysis the matrices are multiplied in reverse order, to give the matrix of the total element assembly,  $M_T = M_1.M_2.M_3.M_3.M_2.M_1$ . Because a complete round trip is being considered, the matrices can effectively be multiplied in any order because the forward and reverse path involve a traverse through the same matrix elements.

## **References**

- 1 H. Kogelnik, "Imaging of optical modes-resonators with internal lenses", The Bell system technical journal, p. 455, March 1965
- 2 A. E. Siegman, "Lasers", Oxford University Press, 1986, Chapters 12-23
- 3 A. Yariv, "Quantum electronics", John Wiley, 3rd ed, 1989, Chapter 6
- 4 D. R. Hall, P. E. Jackson, "The physics and technology of laser resonators", Adam Hilger / IOP publishing, 1989, Chapter 1
- 5 N Yu, J. L. Passman, Dae M. Kim, "Coupling of a single-mode laser diode to single-mode fibre via etched conical microlenses", Report from the Oregon Graduate Centre, Beaverton.
- 6 P. W. Milonni, J. H. Eberly, "Lasers", John Wiley, 1988

# Appendix V

## Computer programs

### 1 Beam waist calculation for Nd:YLF cavity as used in Chapter 4

```

ClearAll[a,b,c,d,l,r,x]a
lt=1.948;
r1=500;          (**6.6*2 for kerr lens**)
r2=1.5;
l1=0.8025
l2=lt-l1;
x=0.0;
lamda=1.047*10^-6;
m1={{1,l1-x},{0,1}};
m2={{1,0},{-2/r2,1}};
m3={{1,l2},{0,1}};
m4={{1,0},{0,1}};
m5={{1,l2},{0,1}};
m6=m2;
m7={{1,l1},{0,1}};
m8={{1,0},{-2/r1,1}};
m9={{1,x},{0,1}};
mr=m1.m2.m3.m4.m5.m6.m7.m8.m9;
{{a,b},{c,d}}=mr
m=(a+d)/2;
t=Solve[q==((a*q)+b)/((c*q)+d),q]
sol=q /.t
sol=1/sol
(** solution for 1/q**)

```

```
w=Sqrt[Abs[(lamda*b)/(3.14*Sqrt[1-((d+a)/2)^2]])]
```

```
N[%]
```

```
Print["for l1= ",l1," m is ",m, " beam size is ",w]
```

**2 Beam waist with Kerr lens for the Nd:YLF laser cavity- Chapter 4**

```
ClearAll[a,b,c,d,l,r,x];
```

```
lt=1.948;          (**total cavity length**)
```

```
fm=77.74*10^6     (**pulse repetition rate**);
```

```
tp=6*10^-12      (**measured FWHM pulsewidth**);
```

```
n2=9*10^-20      (**nonlinear index in the kerr material**);
```

```
P=20             (**average power in the cavity in watts**);
```

```
Lkerr=2.5*10^-2   (**kerr material length m**);
```

```
fm=77.74*10^6     (**pulse repetition rate**);
```

```
Print[" l1  m  waist(um)  dw/w  fkerr"];
```

```
(**calculate the waist for a range of mirror positions**)
```

```
Do[
```

```
    wo=100000     (**set the initial kerr lens value to zero **);
```

```
    wnew=wo;
```

```
    rthermal=-2*1 (**thermal 'mirror' ROC = 2*fth in meters**);
```

```
(** loop around the cavity until the beam waist converges**)
```

```
Do[
```

```
    fkerr= N[ ( (wnew^4) *Pi*fm*tp)/(4*n2*2*P*Lkerr)];
```

```
    r1=N[1/ ( (1/rthermal)+1/(fkerr*2) )]      ;(**kerr lens and thermal lens**)
```

```
    r2=1.5;
```

```
    l2=lt-l1;
```

```
    x=0;
```

```
    lamda=1.047*10^-6;
```

```
    m1={{1,l1-x},{0,1}};
```

```

m2={{1,0},{-2/r2,1}};
m3={{1,l2},{0,1}};
m4={{1,0},{0,1}};
m5={{1,l2},{0,1}};
m6=m2;
m7={{1,l1},{0,1}};
m8={{1,0},{-2/r1,1}};
m9={{1,x},{0,1}};

mr=m1.m2.m3.m4.m5.m6.m7.m8.m9;
{{a,b},{c,d}}=mr;
m=(a+d)^2/4;;
t=Solve[q==((a*q)+b)/((c*q)+d),q];
sol=q /.t;
sol=1/sol;
(** solution for 1/q**);
wold=w;
w=Sqrt[Abs[(lamda*b)/(3.14*Sqrt[1-((d+a)/2]^2)]]];
(** remember the beam waist for the c.w. case with no Kerr lensing**)
If[ i==1,wcw=w];

wnew=w;

,{i,1,8}};
(** output the results of each iteration**)
dw=N[100*(wcw-wnew)/(wnew)]; (**% waist decrease**)
diff=Abs[(wnew-wold)/wnew]; (**check if the solution has converged**)
If [diff > 0.00001, Print["the solution has not converged"],

Print[l1," ",m, " ",w*10^6," ",dw," ",fkerr] ];

,{l1,0.608,0.908,0.02}}]

```

### 3 C.W. amplifier gain vs current and input power version 1, linear gain approximation -Chapter 5

```

ClearAll[h,f,q,alpha,gamma,slope,nt,l,d,w,v,a,b,c,smax,s,s1,n1,steps];
h=6.625*10^-34;
f=0.19608*10^15;
q=1.6*10^-19;
alpha=30;
gamma=0.07;
slope= 7*10^-16;
nt=1.0*10^18;
l=500*10^-4;
d=0.1*10^-4;
w=3.5*10^-4;
v=w*l*d;
a=10^8;
b=10^-10;
c=4*10^-29
smax=3*10^-3;
s=0.000025*10^-3;
s1=s;
n1=6*10^18;
steps=10;

Calcun[m_]:=FindRoot[m==q*v(n(a+b*n +c*n*n)+slope*(n-nt)*s/(h*f*w*d)),{n,n1}]
i=0.030
lstep=l/steps
While[s<smax,
  s1=s;
  Do[
    t=Calcun[i] ;
    den=n /.t;

```

```
gain= Exp[(slope*gamma(den-nt)-alpha)*lstep];  
s=s*gain;  
,{num,lstep,l,lstep}];  
gain=s/s1;  
smw=s1*1000;  
Print[smw," ",i," ",gain];  
s=s1*2
```

]

#### 4 C.W. amplifier gain vs current and input power version 1, logarithmic gain approximation -Chapter 5

(\*\*with recommended alterations now includes a logarithmic expression for gain in terms of carrier density\*\*)

```
ClearAll[h,f,q,alpha,gamma,slope,nt,l,d,w,v,a,b,c,smax,s1,n1,steps];
```

```
h=6.625*10^-34;
```

```
f=0.19608*10^15;
```

```
q=1.6*10^-19;
```

```
alpha=30;
```

```
gamma=0.07;
```

```
slope= 7*10^-16;
```

```
nt=1.0*10^18;
```

```
slope2=1424; (** gain parameter for the logarithmic expression for gain**)
```

(\*\*obtained by equating the two expressions at a given drive current (100mA) for a low input power\*\*)

```
l=500*10^-4;
```

```
d=0.1*10^-4;
```

```
w=3.5*10^-4;
```

```
v=w*l*d;
```

```
a=10^8 (**small enough to ignore**);
```

```
b=10^-10;
```

```
c=4*10^-29
```

```
smax=3*10^-3;
```

```
s=0.000025*10^-3;
```

```
s1=s;
```

```
n1=6*10^18;
```

```
steps=100;
```

```
(**Logg[m_]:= (2*(n/nt-1)/(n/nt+1)+(1/3)*((n/nt-1)/(n/nt+1))^3)**)
```

```

Calculun[m_]:=FindRoot[m==q*v(n(a+b*n
+c*n*n)+slope2*Log[n/nt]*s/(h*f*w*d)),{n,n1}]

```

```

i=0.2

```

```

lstep=l/steps

```

```

While[s<smax,

```

```

    s1=s;

```

```

    Do[

```

```

        t=N[Calculun[i]] ;

```

```

        den=n /t;

```

```

        gain=N[ Exp[(slope2*gamma*Log[den/nt]-alpha)*lstep]];

```

```

        s=s*gain;

```

```

    ,{num,lstep,l,lstep}];

```

```

    gain=s/s1;

```

```

    smw=s1*1000;

```

```

    (**Print[smw,"    ",i,"    ",gain," n=",den];**)

```

```

    Print[gain];

```

```

    s=s1*2

```

```

]

```

## 5 Amplifier pulse amplification -Chapter 5

```

(** calculate the effects of pulse amplification **)
(**units mostly in cm**)
(**from agrawal 1989 paper**)

q=1.6*10^-19; (**electron charge**)
d=0.1*10^-4; (**active region thickness**)
w=3.5*10^-4; (**active reigion width**)
l=500*10^-4; (**device length**)
no=1*10^18; (**cm-3**)
nt=no
n1=6*10^18 (** trial solution **)
gamma=0.07; (**confinement factor**)
a=10^8; (**recombination constants**)
b=10^-10; (**cm3 . s-1**)
c=4*10^-29; (**cm6. 2-1 **)
slope=7*10^-16; (** gain coeficient cm-2**)
f=0.196*10^15; (**optical frequency**)
h=6.625*10^-34;
alpha=30
v=w*I*d

stepno=100;
pin=Table[1,{100}];
pout=Table[1,{100}];
gain=Table[1,{100}];
ampli=Table[1,{100}];
tpulse= 2; (**in pico seconds**)
span=2; (**no of times greater that pulse width to calc**)
tstart=-tpulse*span;

```

```

tstep=(tpulse*span*2)/stepno;
epulse=1;    (**input pulse energy PJ**)
Calcun[m_]:=FindRoot[m==q*v(n(a+b*n+c*n*n)),{n,n1}]

(**Read in input pulse**)
t=tstart;
count=1;
Print["input power"]

Do[
    pin[[count]]=N[epulse/tpulse*(E^(-(t*t)/(tpulse*tpulse)))] (** Watts**);
    t=t+tstep;
    Print[pin[[count]]];
, {count, 1, stepno, 1}];

(**next bit**)
(** get the value of n**)
i=0.05;
t=Calcun[i];
den=n /.t;
n=den;

trec=1/(a+b*n+c*n*n);

esat=h*f*w*d/(gamma*slope);    (**units Joules**)

i0=q*w*d*I*no/trec; (**units**)
go=gamma*slope*no/(i0-1);

(** calculate the gain**)
area=0;
count=1;

```

```

esat=esat*10^12      ;(** convert to PJ**)
Print["output powers"];
Do[

    area=area+(pin[[count]]*tstep); (**time in ps**)
    gain[[count]]=N[go*E^(-area/(esat))];
    pout[[count]]=pin[[count]]*E^((gain[[count]]-alpha)*1);
    ampli[[count]]=pout[[count]]/pin[[count]];
    Print[pout[[count]]];

, {count,1,stepno,1}];

(** calculate the net gain**)
inp=0;
out=0;
count=1;
Do[
    inp=inp+pin[[count]];
    out=out+pout[[count]];

, {count,1,stepno,1}];

totalgain=out/inp

Print["net gain=",totalgain]

```

**6 Calculate the carrier heating induced gain saturation-Chapter 5**

(\*\* calculate the carrier heating induced change in the temperature of the carrier distribution for various pulse widths and intensities \*\*)

ClearAll[h,f,pulsewidth,reprate,lamda,tc,tp,TL,beta,pav,Hi,vgroup,sigma,d,w,length,area];

h=6.625\*10^-34; (\*\*Plancks constant\*\*)  
 f=0.196\*10^-15; (\*\*frequency of the light\*\*)  
 pulsewidth=30; (\*\*FWHM pulsewidthin ps \*\*)  
 reprate=77\*10^6; (\*\*pulse repetition rate\*\*  
 period=1/reprate; (\*\*time between pulses\*\*)  
 pav=5\*10^-3; (\*\*average optical power in the device Watts\*\*)  
 beta=800; (\*\*free carrier absorption coefficient m-1\*\*);  
 Hi=(6.26\*10^-21)/(1.6\* 10^-19); (\*\*1/h = dependence of enegry wrt temperature\*\*)  
 Gi=-108; (\*\*gain coeficient m-1 K-1\*\*)  
 vgroup=(3\*10^8)/3.5; (\*\*group velocity\*\*)  
 tc=0.65\*10^(-12); (\*\*intra-band relaxation time in ps\*\*)  
 TL=300; (\*\*equalibrium lattice temp K\*\*)  
 sigma=N[( pulsewidth/2 )/(2\*Log[2])]; (\*\*pulswidth parameter\*\*\*)  
 tp=N[((pulsewidth/2)^2)/Log[2]]; (\*\*pulswidth parameter 1/ps squared\*\*\*)  
  
 d=0.1; (\*\*active region dimensions um\*\*)  
 w=3.5;  
 length=500;  
 area=d\*w\*length\*10^-18;  
  
 tstart=-45; (\*\*starting time ps\*\*)  
 stepno=1000; (\*\*number of steps\*\*)  
 H=-tstart\*2/stepno; (\*\*step size\*\*)  
 Tnew=300; (\*\*output this number of points\*\*)  
 steptest=stepno/300;

```

steptest1=steptest;
k= beta*vgroup*pav*period*Hi/( area*sigma*( 2*Pi)^(1/2) );
sumold=0;
sum=0
deriv[t_]:=N[k*( E^(-t*tp) )-(Told-TL)/tc];
gain[t_]:=N[H* E^( Gi*length*(10^-6)*(Tnew-TL ) ) * ( E^(-t*tp) ) /
(sigma*(2*Pi)^(1/2) )];
Print["*****OUTPUT STARTS*****"];

Print["time (ps)          temperature (K)"];
Do[                          (**step over the pulse**)
Told=Tnew;
sumold=sum;
Tnew=Told+(H*10^-12)*deriv[j];          (**solve the temperature at each point
across the pulse**)
                                (**by Eulers method**)
sum=N[sumold+ gain[j]] ;          (**sum up the net gain over the pulse**)

If[j>(tstart+steptest1*H),          (**temperature output**)
Print[N[j],"          ",EngineeringForm[ Tnew,14]];
steptest1=steptest1+steptest;
,dummy=0;
];
,{j,tstart,-tstart,H}];

Print["total gain= ",sum];          (**output net gain**)
Print["*****calculations complete*****"];

```

**7 Calculate the nonlinear index,  $n_2$  from the AMZI switching power- Chapter 6**

As used in section 6.51. The effects of two-photon absorption, linear losses and bend losses can be included.

(\*\* calculate the  $n_2$  from the AMZI switching power\*\*)

(\*\*including TPA\*\*)

ClearAll [lamda,psplit,alpha,l1,l2,bdloss,a,ppeak,pinp,iin,isplit,leffang,leffstra,n2]

lamda=0.860\*10<sup>-6</sup>; (\*\*wavelength m\*\*)

psplit=0.1563; (\*\*modeled MZ arm split ratio\*\*)

alpha=25\*10<sup>2</sup>; (\*\*estimated FCA loss m<sup>-1</sup>\*\*)

l1=716 \*10<sup>-6</sup>; (\*\* angled arm length m\*\*)

l2=784\*10<sup>-6</sup>; (\*\*straight arm length m\*\*)

bdloss=1; (\*\* bend loss\*\*)

a=0.5\*3.5\*10<sup>-12</sup>; (\*\* calculated modal area m<sup>2</sup> \*\*)

ppeak=3\*125; (\*\* peak power watts 80MHz, 100fs pulses\*\*)

pinp=ppeak\*0.7\*0.15; (\*\* input coupling efficiency estimated\*\*)

iin=pinp/a; (\*\*input intensity W/m<sup>2</sup> \*\*)

isplit=iin\*E<sup>(-alpha\*200\*10<sup>-6</sup>)</sup>; (\*\* initial attenuation before the splittinh Y branch\*\*)

beta=(30\*10<sup>-9</sup>)\*10<sup>-2</sup>; (\*\*TPA coefficient m / GW\*\*)

leffang=N[(1-E<sup>(-alpha\*l1)</sup>)/(alpha)]; (\*\* effective length\*\*)

leffstra=N[(1-E<sup>(-alpha\*l2)</sup>)/(alpha)] ;

(\*\* calculate the expression for the phase shift/Pi\*n<sub>2</sub> in each arm\*\*)

n2a=N[( (2/lamda)\*(1-psplit)\*isplit\*leffstra)+ ((2/lamda)\*(1-psplit)\*bdloss\*isplit\*E<sup>(-alpha\*l2)</sup>\*leffang)];

n2b=N[ ((2/lamda)\*psplit\*isplit\*leffang) + ((2/lamda)\*psplit\*bdloss\*isplit\*E<sup>(-</sup>

```

alpha*11)*leffstra)];
n2=N[1/(( n2a-n2b )*10^-4)];
Print["simple calc, n2= ",n2];

(** now include TPA**)

phase[i_,l_]:= (2/(lamda*beta))*Log[ ( -alpha-i*beta+i*beta*E^( -alpha*1 ) ) / ( -alpha )];
tpaatten[i_,l_]:= ( alpha*E^( -alpha*1 ) ) / ( alpha+beta*i*( 1-E^( -alpha*1 ) ) );

(** calculate the expression for the phase shift/Pi*n2 in each arm including TPA**)

n2a= phase[(1-psplit)*isplit,l2]+ phase[ tpaatten[ ( 1-psplit )*isplit,l2] *(1-
psplit)*bdloss*isplit,l1];
n2b= phase[psplit*isplit,l1]+ phase[tpaatten[ (psplit
)*isplit,l1]*(psplit)*bdloss*isplit,l2];
n2=N[1/(( n2a-n2b )*10^-4)];

Print["with tpa calc, n2= ",n2]

```

## 8 Calculate the effects of two-photon absorption on the AMZI switching characteristic- Chapter 6

Used in section 6.52 to produce the data shown in Fig 6.17. The program was intended to determine the effects of excessive two-photon absorption on the switching characteristic.

```

(** calculate The AMZI switching characteristic including beta**)
(** ignoring linear losses**)
(** all units in m etc., no prefixes**)
ClearAll[d,lamda,area,length,beta,alpha,k,n2,a,Beta,out,b,inten,ppeak,i,out,phase,val];
d=0.156;          (** AMZI split ratio**)
lamda=0.86*10^-6; (**wavelength**)
area=1.75*10^-12; (** device modal area**)
length=1.5*10^-3; (** arm length in m**)
beta=(50 *10^-9)*10^-2; (**TPA coeficien 30 cm2/GWt**)
alpha=25*10^2;    (**linear losses**)
k=2*Pi/lamda;    (** wave number**)
n2=(2.5*10^-16);  (**nonlinear coefficient n1*10-12 cm2/W**)
ppeak=30;        (** peak power watts**)

(**ignoring the bending losses**)

inten=ppeak/area

(** calculate the power in each arm at the recombination point**)

a[i_]:= d*i*(1-d)/(1+beta*i*length*d);          (** arm with least power**)
b[i_]:= (1-d)*i*d/(1+beta*length*i*(1-d));      (** arm with most power**)

phase[i_]:= (k*n2/beta)*(Log[1+(1-d)*(i*beta*length)]-Log[1+d*i*beta*length]);

out[i_]:= (a[i]-b[i]*(Sin[phase[i]/2])^2)/i;

```

```
Table[out[val]/0.13,{val,inten/100,inten,inten/50}];  
ListPlot[%,PlotJoined->True];  
  
Print["intensity --- peak power --- transmission ----- phase shift "];  
  
Do[  
  
Print[val/(1*10^12)," ",val*area," ",N[out[val]/0.13]," ",phase[val]]  
  
,{val,inten/100,inten,inten/50}]
```

## 9 A unified model of the AMZI switching characteristics- Chapter 6

Used in section 6.53 to model the AMZI switching including a range of effects. The modelled responses are shown in Fig. 6.19-6.21.

```

(**modelled AMZI switching characteristic **)
(**including two-photon absorption and linear losses **)
(** include a d.c. offset in gain and phase shift between arms**)
(** include the effects of the pulse wings **)
(**bending losses are ignored**)
(** all units in m etc., no prefixes**)
Print[" CALCULATION IN PROGRESS "];
ClearAll[d,lamda,area,length,tpa,alpha,k,n2,a,out,b,atten,inten,ppeak,i,out,phase,val,b1,
N0,N1,lef,slope];

d=0.156;                (** AMZI split ratio**)
lamda=0.86*10^-6;       (**wavelength m**)
area=1.75*10^-12;      (**effective modal area**)
length=1.5*10^-3;      (**length of AMZI arms**)
tpa=(30 *10^-9)*10^-2; (**TPA coeficien 30 cm2/GWt**)
alpha=25*10^2;         (**linear losses**)
k=2*Pi/lamda;          (*wave number**)
n2=(4*10^-16);         (**nonlinear coefficient n1*10-12 cm2/W**)
ppeak=60;              (**max peak power to scan to in watts**)
leff=(1- E^( -alpha*length ))/alpha; (** effective length**)
inten=ppeak/area;      (**optical intensity in device**)

atten[i_]:= N[ alpha*( E^( -alpha*200*10^-6 ) )/(alpha+tpa*i( 1-E^( -alpha*200*10^-6)
))] (**include initial attenuation before Mach Zehnder**)

(** setup parametres for a d.c. offset in one of the arms**)

```

slope=3.1\*(10<sup>-17</sup>)\*10<sup>-4</sup> ; (\*\*slope of the gain characteristic m2  
check \*\*)

lef=5 ; (\*\*linewidth enhancement factor\*\*)

b1=lef\*slope/(2\*k); (\*\*phase coefficient\*\*)

N0=1\*(10<sup>18</sup>)\*10<sup>6</sup> ; (\*\*carrier density m-3\*\*)

gain=0 (\*\* gain set to one to allow asymmetric gain in each arm.  
set to zero to forbid\*\*)

(\*\* calculate the power in each arm at the recombination point\*\*)

a[i\_]:=d\*i\*(1-d)\*E<sup>-alpha\*length</sup>/(1+tpa\*i\*lef\*d); (\*\* arm with least power\*\*)

b[i\_]:= (1-d)\*i\*d\*Exp[gain\*slope\*(N1-N0)\*length]\*E<sup>-alpha\*length</sup>/(  
1+tpa\*lef\*i\*(1-d)); (\*\* arm with most power\*\*)

(\*\* calculate the effect of the pulse wings for a given power\*\*)

wings[ph\_]:=NIntegrate[(1/(2\*Pi))<sup>1/2</sup> \* (Sin[ph\*E<sup>-(x<sup>2</sup>/2)</sup>])<sup>2</sup> \* E<sup>-1\*(x<sup>2</sup>/2)</sup>,{ x,-4,4},WorkingPrecision->10];

(\*\* calculate the phase shift between arms for a given power\*\*)

phase[i\_]:=k\* b1\*(N1-N0)\*length + ((n2\*k)/tpa) \* ( Log[( -alpha-(1-d)\*i\*tpa+ (1-d)\*i\*tpa\*E<sup>-alpha\*length</sup> )/(-alpha) ] - Log[( -alpha -d\*i\*tpa+d\*i\*tpa\*E<sup>-alpha\*length</sup> )/(-alpha) ] ) ;

(\*\* calculate the transmission for zero power\*\*)

N1=1\*N0;

start=out[inten/100];

N1=0.85\*N0; (\*\*nominal carrier density in 2nd arm\*\*)

(\*\* calculate the AMZI transmission for a given power\*\*)

```

out[i_]:= (a[i]- wings[phase[i]/2] *b[i]*(Sin[phase[i]/2])^2)/i;

(** build a table to plot results and also output as text**)

Table[out[va]/start, {val/atten[val],inten/1000,inten,inten/( ppeak ) } ];
ListPlot[%,PlotJoined->True, PlotRange->{{0, (ppeak) },{0,1}}];
Print["intensity --- peak power --transmission - phase shift "];

Do[

Print[N[ val/(atten[val]*1*10^12)],"          ",N[ val*area/atten[val] ],"
",N[out[val]/start],"    ",N[ phase[ val ]/Pi ]," Pi" ]

,{val,inten/1000,inten,inten/50}]

```

## 10 A unified model of the AMZI switching characteristics with least squares fit to experimental data- Chapter 6

(\*\*modelled AMZI switching characteristic \*\*)  
 (\*\*2000 for thesis corrections quantify fit between the modelled and experimental dat\*\*)  
 (\*\* file: Characdc4\*\*)  
 (\*\*including two-photon absorption and linear losses \*\*)  
 (\*\* include a d.c. offset in gain and phase shift between arms\*\*)  
 (\*\* include the effects of the pulse wings \*\*)  
 (\*\*bending losses are ignored\*\*)  
 (\*\* all units in m etc., no prefixes\*\*)

ClearAll[d,lamda,area,length,tpa,alpha,k,n2,a,out,b,atten,inten,ppeak,i,out,phase,val,b1,  
 N0,N1,lef,slope,error,counter,error1,fit,,leff];

d=0.156; (\*\* AMZI split ratio\*\*)  
 lamda=0.86\*10<sup>-6</sup>; (\*\*wavelength m\*\*)  
 area=1.75\*10<sup>-12</sup>; (\*\*effective modal area\*\*)  
 length=1.5\*10<sup>-3</sup>; (\*\*length of AMZI arms\*\*)

tpa=(13 \*10<sup>-9</sup>)\*10<sup>-2</sup>; (\*\*TPA coeficien 30 cm<sup>2</sup>/GWt\*\*)  
 alpha=25\*10<sup>2</sup>; (\*\*linear losses\*\*)  
 k=2\*Pi/lamda; (\*wave number\*\*)  
 n2=(3.7\*10<sup>-16</sup>); (\*\*nonlinear coefficient n1\*10<sup>-12</sup> cm<sup>2</sup>/W\*\*)

ppeak=60; (\*\*max peak power to scan to in watts\*\*)  
 leff=(1- E<sup>( -alpha\*length )</sup>)/alpha; (\*\* effective length\*\*)  
 inten=ppeak/area; (\*\*optical intensity in device\*\*)  
 intstep=inten/20; (\*\*step to take in the power domain\*\*)  
 (\*\*fit to experimental data points\*\*)

fit[i \_]=N[0.739716+1.184541969\*i-2.284412085\*i<sup>2</sup>+2.401955273\*i<sup>3</sup>-

```
1.499128734*i^4+0.5719715323*i^5-0.1362115307*i^6+0.02030536377*i^7-
0.001841020121*i^8+0.0000928408846*i^9-1.997576115*(10^-6)*i^10];
```

```
atten[i_]:=N[alpha*(E^(-alpha*200*10^-6))/(alpha+tpa*i(1-E^(-alpha*200*10^-6)))];
(**include initial attenuation before Mach Zehnder**)
```

```
(** setup parametres for a d.c. offset in one of the arms**)
```

```
slope=3.1*(10^(-17))*10^(-4) ; (**slope of the gain characteristic m2
check **)
```

```
leff=5 ; (**linewidth enhancement factor**)
```

```
b1=leff*slope/(2*k); (**phase coefficient**)
```

```
N0=1*(10^18)*10^6 ; (**carrier density m-3**)
```

```
gain=0 ; (** gain set to one to allow asymmetric gain in each arm.
set to zero to forbid**)
```

```
(** calculate the power in each arm at the recombination point**)
```

```
a[i_]:=d*i*(1-d)*E^(-alpha*length)/(1+tpa*i*leff*d); (** arm with least power**)
```

```
b[i_]:=((1-d)*i*d*Exp[gain*slope*(N1-N0)*length])*E^(-alpha*length)/(
1+tpa*leff*i*(1-d)); (** arm with most power**)
```

```
(** calculate the effect of the pulse wings for a given power**)
```

```
wings[ph_]:=NIntegrate[(1/(2*Pi))^(1/2) * (Sin[ph*E^(-(x^2)/2)])^2 * E^(-
1*(x^2)/2),{x,-4,4},WorkingPrecision->10];
```

```
(** calculate the phase shift between arms for a given power**)
```

```
phase[i_]:=k*b1*(N1-N0)*length + ((n2*k)/tpa) * (Log[(1-alpha*(1-
```

```
d)*i*tpa+ (1-d)*i*tpa*E^( -alpha*length ) )/(-alpha) ] - Log[( -alpha -d*i*tpa+d*
i*tpa*E^( -alpha*length ) )/(-alpha) ] ) ;
```

```
(** calculate the transmission for zero power**)
```

```
N1=1*N0;
```

```
start=out[inten/100];
```

```
N1=1*N0;          (**nominal carrier density in 2nd arm**)
```

```
(** calculate the AMZI transmission for a given power**)
```

```
out[i_]:= (a[i]- wings[phase[i]/2] *b[i]*(Sin[phase[i]/2])^2)/i;
```

```
(** build a table to plot results and also output as text**)
```

```
(**
```

```
tp1=N[Table[out[val]/start,{val,inten/1000,inten,inten/20 } ]];
```

```
ListPlot[%,PlotJoined->True, PlotRange->{{0, (ppeak) },{0,1}}];
```

```
**)
```

```
pmw=Table[100,{60}];
```

```
trans=Table[1,{60}];
```

```
transexp=Table[1,{60}]; (**experimental curve fit**)
```

```
itensity=Table[1,{60}];
```

```
(**perform the least squares curve fit for a range of parametres**)
```

```
Print["calculations underway, light blue touch paper....."];
```

```
Print["data appears alpha__Tpa__n2__N1/N0__gain__phase "];
```

```
Do[
```

```
    Do[
```

```
        Do[
```

```
            Do[
```

```

(**main body of programme - really should fill up the array with the real experimental
data outside this loop**)
counter=1;          (**set up a counter to build an array of the results**)
Do[
    trans[[counter]]=N[out[val]/start];          (**transmission**)

    pmw[[counter]]=(N[ val*area/atten[val] ]*10)/(125);    (**average power
mw**)
    intensity[[counter]]=N[ val/(atten[val]*1*10^12)];
    transexp[[counter]]=N[fit[pmw[[counter]]]];    (**fill an array with the
experimental response**)
    counter=counter+1;
, {val,inten/1000,inten,inten/50}];
phasval=N[phase[inten/1000]];    (**phase offset**)
transl=trans;    (**define a new array to contain the normalised response**)
(** normalise the transmission between 1 and 6mw**)
counter=1;
minel=1;          (**find the minimum transmission**)

While [pmw[[counter]]<7,
    If [ trans[[counter]]<minel,
        minel=trans[[counter]];    ];
    counter=counter+1;    ];
(**normalise the array**)
trnasexpold=transexp;
Do [
    transl[[counter]]=(trans[[counter]]-minel)/(1-minel);
    transexp[[counter]]=(transexp[[counter]]-0.884336)/(1-0.884336); (**normalise
the experimental data**)
, {counter,1,60,1}];

```

```

(**perform the lease squares error analysis for pin > 0.5 but <8 **)
(** and >0.5 and < 5**)
cnt=1;
error=0;
error1=0;
pl=0;
pl1=0;

Do[
  If [ (pmw[[counter]]<7) && (pmw[[counter]]>0.5),
    error1=error1+(trans1[[counter]]-transexp[[counter]])^2;
    pl1=counter;
    If[ pmw[[counter]]<5,
      error=error+(trans1[[counter]]-transexp[[counter]])^2;
      pl=counter;
    ];
  ];
  cnt=cnt+1;
,{counter,1,50,1} ];

(**get the rms error**)
error2=error1/pl1;
error1=(error1/pl1)^(1/2);
error=(error/pl)^(1/2);
Print[alpha,"_",tpa*10^11,"_",n2*10^16," ",N1/N0," ",gain," ",phasval,"_ewi=",error1,
" ena=", error];

(**
ListPlot[transexp,PlotJoined->True, PlotRange->{{0, (30)},{0,1}}];
Print["model"];
ListPlot[trans1,PlotJoined->True, PlotRange->{{0, (30)},{0,1}}];
**)

```

```
,{alpha,1500,2500,1000}];  
  ,{tpa,20*10^-11,40*10^-11,10*10^-11}];  
    ,{n2,2.5*10^-16,4.5*10^-16,1*10^-16}];  
      ,{N1,N0,0.9*N0,-0.025*N0}];  
        ,{gain,0,0,0}];
```

## Appendix VI

### Error analysis of AMZI switching response and uncertainty in the modelled AMZI response

It is important that the experimental errors are considered particularly in complicated experiments such as the AMZI switching experiment of Section 6.4, where the experimental uncertainty is not insignificant. In this section that data of Fig 6.16 are reconsidered with respect to experimental errors. The interpretation and fitting of the data with the modelled responses and the uncertainties in deducing parameter values from the experimental results are covered in Section 6.54, although the accuracy with which the AMZI model can be used to deduce device parameters is partially considered here.

Gaussian or normal distributions, have various useful properties which simplifies their analysis, only distributions with a large number of independent factors approach a gaussian. It is however a widely used assumption, in this section the error distributions are assumed to be gaussian.

The uncertainties in the data of Fig 6.16 are first considered and are summarised in Table A5, below.

parameter	assumed value, symbol
power stability, $\epsilon_{cw}$	+/-2% variation in average power (Chapter 6 reference 26)
pulsewidth variation , $\epsilon_p$	assumed to be small for a diode-pumped regeneratively stabilised KLM system
coupling stability, $\epsilon_c$	+/- 2%
input power reading, $\epsilon_{in}$	determined by the lockin amplifier used, +/- 0.01mV uncertainty
output power reading accuracy, $\epsilon_{out}$	determined by the lockin amplifier used, +/- 0.01mV uncertainty
bias current and temperature drift	assumed to be negligible over the short duration of the experiment

*Table A5 Experimental uncertainties in the AMZI switching experiment*

The transmission of the device can be expressed as,

$$T = \frac{\text{output}}{\text{input}} \quad (\text{A5})$$

The total uncertainty in the input reading is obtained by considering the components described in the table above. If a gaussian error distribution is assumed with 3sigma distributions given by the values  $\epsilon$  ( $3\sigma = \epsilon$ ), described in the table above, then the total standard deviation in the input readings is given by Equation A6.

$$\sigma_{input} = \sqrt{\sigma_{cw} + \sigma_{in}} \quad (\text{A6})$$

For the purposes of the initial error analysis the output and input variables are treated as independent, the standard deviation of the output power is given by.

$$\sigma_{output} = \sqrt{\sigma_{cw} + \sigma_c + \sigma_{out}} \quad (\text{A7})$$

The standard deviation in the transmission is therefore<sup>1</sup>,

$$\begin{aligned} \sigma_{transmission} &= \sigma_{input}^2 \cdot \left( \frac{\delta T}{\delta P_{input}} \right)^2 + \sigma_{output}^2 \cdot \left( \frac{\delta T}{\delta P_{output}} \right)^2 \\ &= \sigma_{input}^2 \cdot \left( \frac{1}{P_{input}^2} \right)^2 + \sigma_{output}^2 \cdot \left( \frac{1}{P_{output}} \right)^2 \end{aligned} \quad (\text{A8})$$

where T is the transmission and  $P_{input}$  and  $P_{output}$  are the input and output powers respectively, the calculated error is around +/-3% for most of the data points, These errors are shown in Fig. A16.

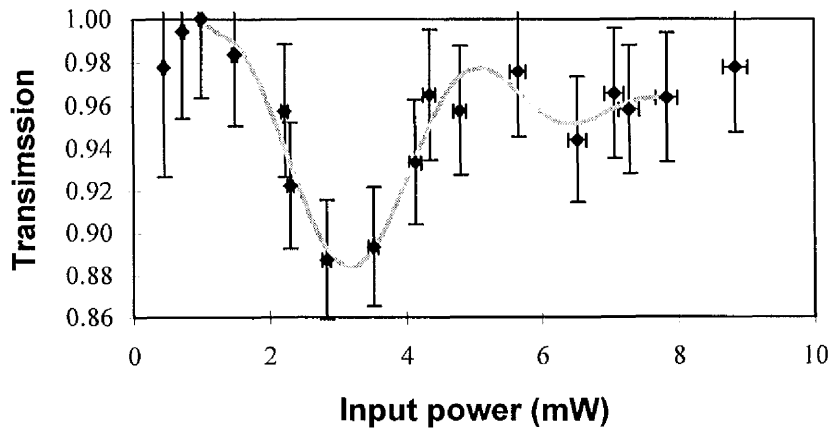
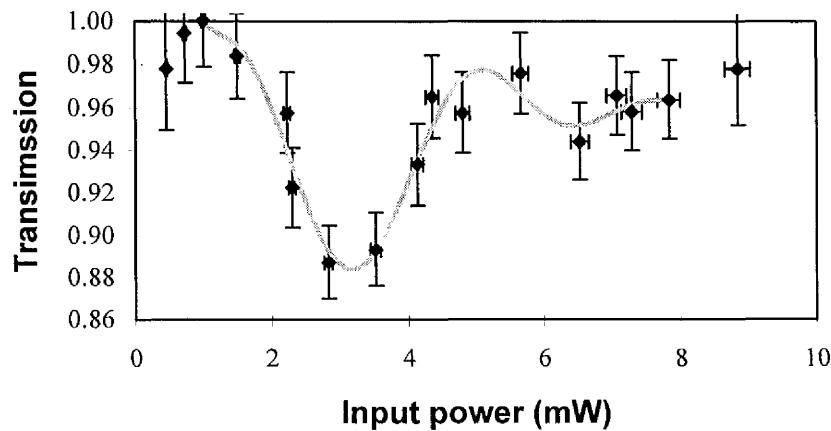


Fig. A16 All-optical switching of the AMZI for 100fs pulse input. The switching point corresponds to a peak power of 30W in the device or a pulse energy of 3pJ. The error bars indicate the estimated  $3\sigma$  limits using a simplified error analysis.

Following the simple analysis, treating the errors in the output and input powers as independent a more detailed analysis was used, to estimate the experimental uncertainty. Instead of deriving an analytical expression for the conditional errors in the transmission, a Monte Carlo technique was used. In Excel several random gaussian noise distributions are generated, one for each error term; each distribution has 1000 random values. For each of these 1000 points the individual unique errors are added to the input signal, this is then used to calculate the output signal, using the equation found from the curve fit to the experimental data. The errors in the output are then added, allowing the transmission to be calculated. Because a large sample size is used, the standard deviation of the resulting transmission with error data gives the experimental error. This technique gives a  $3\sigma$  value for the transmission of around 2% for most of the data points, in other words the uncertainty is within  $\pm 2\%$ , except for low input powers. This is lower than was estimated by the simplified analysis. A graph of the AMZI switching with the error distribution predicted by this method is shown below in Fig. A7, which is also presented in Chapter 6.



*Fig. A17 All optical switching of the AMZI for 100fs pulse input. With detailed error analysis, the uncertainty in transmission is  $<2\%$  for most of the data points.*

Figures A16 and A17 neglect any pulsewidth variation which would have a big effect on the error analysis, for example a  $\pm 5\%$  pulsewidth variation leads to a  $\pm 6\%$  uncertainty in the AMZI transmission, but the pulsewidth variations in regeneratively mode-locked and actively stabilised KLM systems should be small<sup>2,3</sup>.

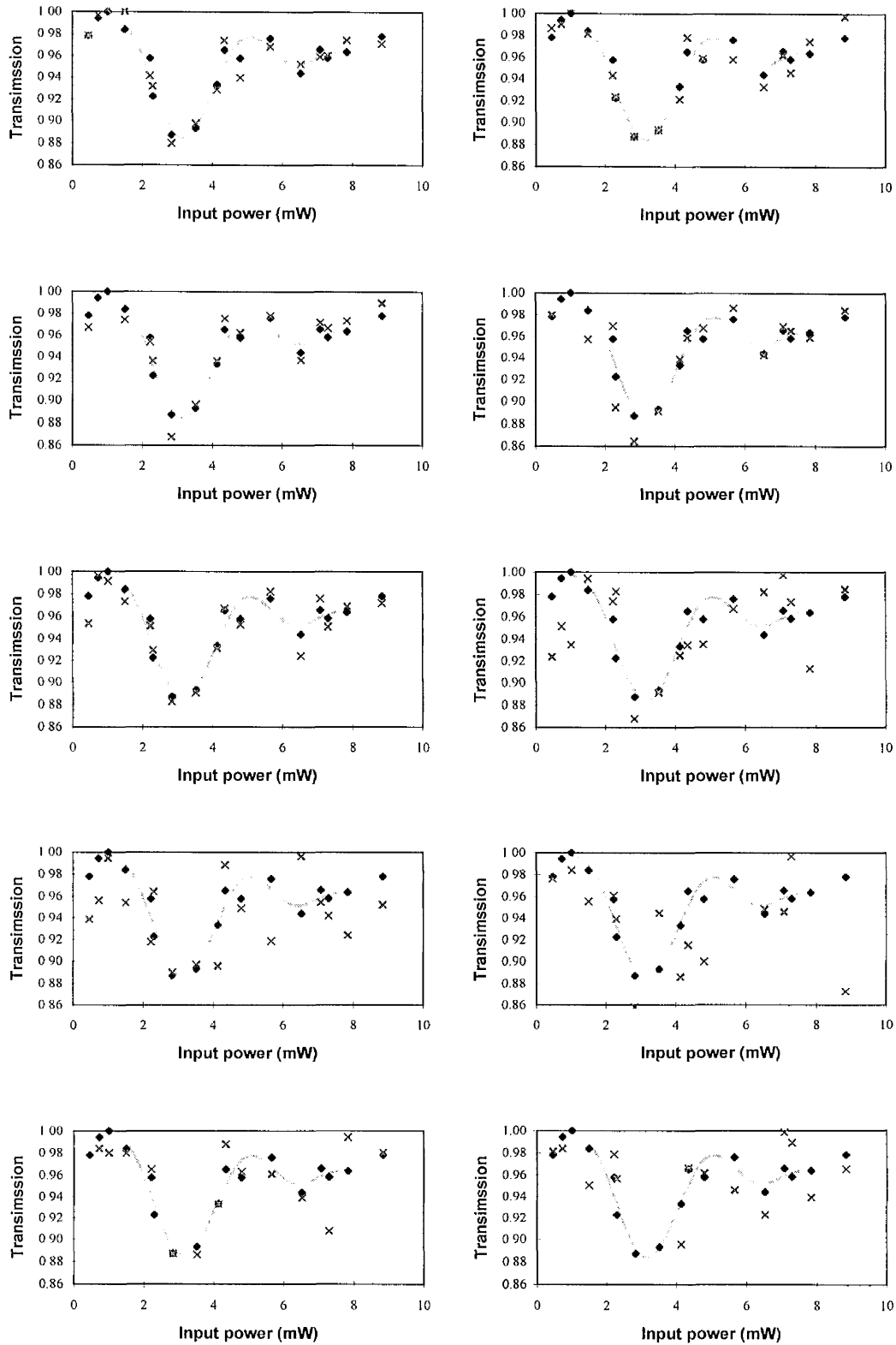


Fig A18 The crosses indicate the AMZI switching data with random gaussian noise applied. Figures 1-5 use noise with the estimated standard deviation and Graphs 6-10 use an error distribution three times bigger.

The influence of the experimental uncertainties are illustrated in Fig A18 which plots the experimental data with the addition of random noise. If a  $3\sigma$  of 3% is taken which is worse than predicted. The nature of the switching distribution is largely unchanged as illustrated in Graphs 1-5 (at the top of the page). A much larger error of 9%, as illustrated in graphs 6-10 alters the characteristic significantly.

In summary, the biggest uncertainty is in the transmission data, a simplified analysis gave an error of  $\pm 3\%$  ( $3\sigma$ ), a more detailed analysis estimated the error in the transmission to be  $<2\%$ . Errors of this magnitude, although not negligible are not expected to alter the measured AMZI switching characteristic significantly.

The output from the least squares fit AMZI model was used to produce the series of graphs shown below in Fig A19-21. The best fitting data from Table 6.6 were used to establish how the values of  $n_2$ ,  $\alpha$  and  $\beta$  are traded off in the model. Pairs of parameters are plotted for a fixed third parameter. The gradient of the fits to the graphs give a measure of how accurately one parameter can be determined for a given uncertainty in another, from the best fit modelled data.

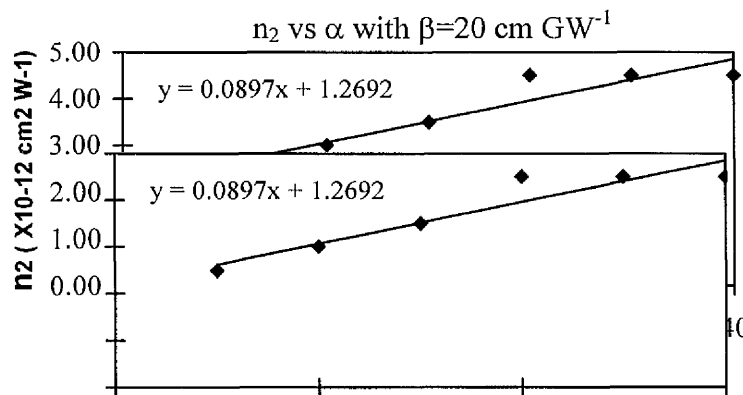


Fig. A19 Correlation of  $n_2$  and  $\alpha$ , taken from the best fit modelled data. Each point on the graphs corresponds to one for the modelled runs from Table 6.6.

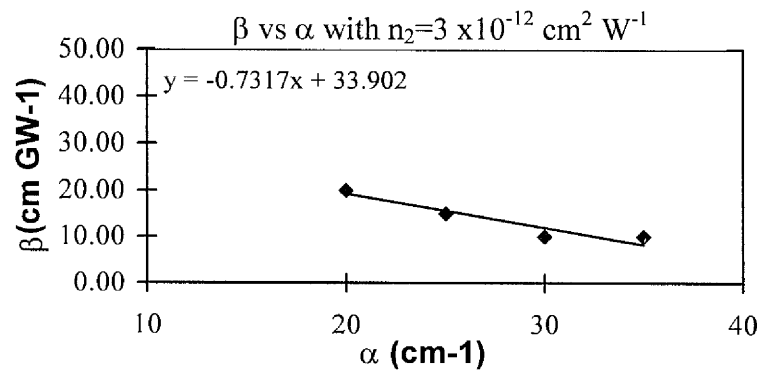


Fig. A20 Correlation of  $\beta$  and  $\alpha$ , taken from the best fit modelled data. Each point on the graphs corresponds to one for the modelled runs from Table 6.6.

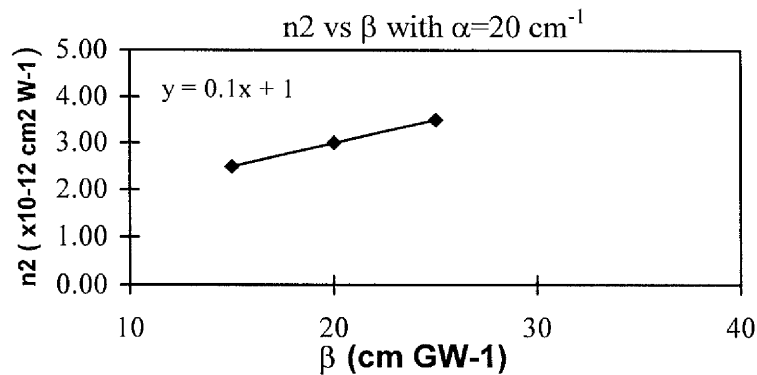


Fig. A21 Correlation of  $n_2$  and  $\beta$ , taken from the best fit modelled data. Each point on the graphs corresponds to one for the modelled runs from Table 6.6.

## References

- 1 M. R. Spiegel, "Statistics", 3rd Ed., McGraw-Hill International
- 2 Reference 26, Chapter 6
- 3 Reference 23, Chapter 4